

ACTA

UNIVERSITATIS OULUENSIS

Risto Laitinen

IMPROVEMENT OF
WELD HAZ TOUGHNESS
AT LOW HEAT INPUT
BY CONTROLLING
THE DISTRIBUTION OF
M-A CONSTITUENTS

FACULTY OF TECHNOLOGY,
DEPARTMENT OF MECHANICAL ENGINEERING,
UNIVERSITY OF OULU

C
TECHNICAL



ACTA UNIVERSITATIS OULUENSIS
C Technica 234

RISTO LAITINEN

**IMPROVEMENT OF WELD HAZ
TOUGHNESS AT LOW HEAT
INPUT BY CONTROLLING
THE DISTRIBUTION OF
M-A CONSTITUENTS**

Academic Dissertation to be presented with the assent of
the Faculty of Technology, University of Oulu, for public
discussion in Raahensali (Auditorium L10), Linnanmaa, on
March 4th, 2006, at 12 noon

OULUN YLIOPISTO, OULU 2006

Copyright © 2006
Acta Univ. Oul. C 234, 2006

Supervised by
Professor Pentti Karjalainen

Reviewed by
Doctor Pekka Nevasmaa
Doctor Casper van der Eijk

ISBN 951-42-8000-8 (nid.)
ISBN 951-42-8001-6 (PDF) <http://herkules.oulu.fi/isbn9514280016/>
ISSN 0355-3213 <http://herkules.oulu.fi/issn03553213/>

OULU UNIVERSITY PRESS
OULU 2006

Laitinen, Risto, Improvement of weld HAZ toughness at low heat input by controlling the distribution of M-A constituents

Faculty of Technology, University of Oulu, P.O.Box 4000, FI-90014 University of Oulu, Finland,
Department of Mechanical Engineering, University of Oulu, P.O.Box 4200, FI-90014 University of
Oulu, Finland

Acta Univ. Oul. C 234, 2006

Oulu, Finland

Abstract

This research work focuses on how to improve the toughness of heat affected zones (HAZs) of low heat input welds in the case of high strength thermomechanically processed (TMCP) and recrystallization controlled rolled and accelerated cooled (RCR) plates with yield strengths of 355–500 MPa.

Experimental work was aimed at the investigation of the intragranular nucleation of acicular ferrite or bainite in hot-rolled plates and the evaluation of the Charpy V and CTOD toughness of the most critical sub-zones of the weld HAZ using simulated specimens with a cooling time $t_{8/5} = 5$ s. The zones studied were the coarse grained HAZ (CGHAZ), the intercritically reheated coarse-grained HAZ (ICCGHAZ) and the intercritical HAZ (ICHAZ), the metallographical analyses consisted of microstructural investigations complemented with hardness measurements. Optical, scanning and transmission electron microscopy techniques were employed together with image and electron backscatter diffraction (EBSD) analysis.

The test results showed that the toughness of the various sub-zones of the HAZ is improved by promoting intragranularly nucleated ferritic-bainitic (acicular) microstructure in both the CGHAZ and in the base plate. In this way, the sub-zones subjected to intercritical thermal cycles (the ICCGHAZ and the ICHAZ) develop evenly distributed M-A constituents between ferrite and bainite laths. These favourable microstructures can be achieved by using titanium killing or by avoiding niobium microalloying by using copper plus nickel alloying instead.

In the laboratory experiments titanium killed steel, containing titanium-manganese oxide/manganese sulphide inclusions with a number density of 300–750 particles/mm², develops a largely acicular ferritic microstructure in the base plate provided the austenite grain size is greater than about 120 µm and the cooling rate is in the range 6–11 °C/s down to 500 °C. Under plate mill conditions, no significant amount of acicular ferrite could be obtained, because it was not possible to achieve austenite grain sizes larger than about 70 µm after rolling. However, a significant fraction of acicular ferritic-bainitic microstructure was achieved in the CGHAZ, when the austenite grain size exceeded 90 µm.

When achieved, a uniform distribution of M-A particles in an acicular ferritic-bainitic microstructure improves toughness. Cracks nucleate at numerous sites on M-A/ferrite boundaries or bainite packet interfaces, but they are initially arrested in the acicular matrix. Crack growth finally occurs by linking of the numerous arrested microcracks.

Keywords: acicular ferrite, hardness, intragranular nucleation, low heat input welding, M-A constituents, packet size, RCR, simulated HAZ, steel, Ti killing, TMCP, toughness

Acknowledgements

This research work was carried out at the Research Centre of Ruukki Production (formerly: Rautaruukki Steel) and the Material Engineering Laboratory, Department of Mechanical Engineering, University of Oulu, during 1999–2003. Additionally, the quantitative characterisation of non-metallic inclusions was performed at CSM in cooperation with a European Coal and Steel (ECSC) R&D project "*Heterogenous nucleation of acicular ferrite for toughness improvement of HSLA steels*".

I would like to express my sincerely gratitude to my supervisor Prof. Pentti Karjalainen and Dr. David Porter for their guidance, encouraging attitude and countless valuable scientific comments and advices regarding the analytical work. I am very grateful to Mr. Seppo Järvenpää, Mrs Raija Peura and Mr. Tero Oittinen, for their assistance in SEM/EDS, TEM and EBDS examinations and Mr. Jussi Paavola, Mr. David Martin and Martti Korhonen for the heat treatment and weld HAZ simulation tests.

I wish to thank my colleagues and all of the staff for their contribution and help to the various parts of the work during its lifetime, without whom this all would not have been possible. Particularly, I would like to thank Mr. Esa Karjaluoto and Mr. Esko Petäjäsoja for their work in testing of materials, Mrs Anja Maaninka and Mrs Maire Manninen for the metallographical experiments and Mrs Hely Kultala for her assistance in the secretarial work.

Financial support by the Graduate School of Metallurgy within the University of Oulu and the European Coal and Steel (ECSC) in cooperation of the above-mentioned collaborative project is gratefully acknowledged.

Finally, my personal thanks are due to my sister and brothers and their families for motivation throughout the work, particularly Dr. Raimo Soininen for his interest and valuable advice, the members of Sportclub/T and many friends for the mental encouragement during the course of this research work.

Raahe, January 2006

Risto Laitinen

List of symbols and abbreviations

α	ferrite
a_α	lattice constant of ferrite (Å)
a_0	lattice constant in cubic crystal (Å)
a_{ppt}	lattice constant of precipitate (Å)
A_5	elongation (%)
A_{c1}	temperature at which austenite begins to form upon heating (°C)
A_{c3}	temperature at which transformation from ferrite to austenite is completed upon heating (°C)
A_{e3}	temperature at which transformation from ferrite to austenite is at equilibrium (°C)
A_{r3}	temperature at which transformation from austenite to ferrite begins upon cooling (°C)
AF	acicular ferrite
AIA	automatic image analysis
AlF	alloy factor for formation of M-A constituent
B	bainite
B_s	bainite transformation start temperature
B-N	Baker-Nutting relationship
bcc	body centred cubic lattice structure
CEV	carbon equivalent (IIW)
CE_{II}	carbon equivalent for the calculation of microhardness of bainite
CCT	continuous cooling transformation (diagram)
CFS	cleavage facet size (μm)
CGHAZ	coarse grained heat affected zone
Charpy V	Charpy V impact test
CTOD	crack tip opening displacement
c	size of a critical microcrack or carbide (μm)
c_0	lattice constant in c-axis of hexagonal crystal (Å)
δ_c	crack tip opening displacement value in the CTOD test (mm)
ΔG^0	standard free energy (J/mol)
DWT	drop weight tear test

d	grain, packet size (μm)
d_A	two-dimensional particle diameter or length (μm)
d_{eff}	effective grain, packet size (μm)
d_V	three-dimensional particle diameter (μm)
df	degree of freedom in statistical analyses
ε_F	strain in finish rolling deformation
E	Young's modulus = 2×10^5 MPa
EB	electron beam welding
EBSD	electron backscatter diffraction
EDS	energy dispersive spectrometer
F	F-value in variance test
FC	ferrite carbide aggregate including pearlite
FGHAZ	fine grained heat affected zone
FS(A)	ferrite with aligned second phase
FS(NA)	ferrite with non-aligned second phase
fcc	face centred cubic lattice structure
γ	austenite
γ_{eff}	effective surface energy (J/m^2)
γ'	retained austenite
GB(B)	grain boundary nucleated bainite
GB(PF),GBF	grain boundary nucleated polygonal ferrite
GB(WF)	grain boundary nucleated Widmannstätten ferrite
GMAW	gas metal arc welding (i.e., MIG/MAG welding)
GTAW	gas tungsten arc welding (i.e. TIG welding)
H_B	microhardness of bainite (HV)
H_M	microhardness of martensite (HV)
HAZ	heat affected zone
HSLA	high strength low alloy steel
HT	high tensile steel
HV	Vickers hardness
HV_{M-A}	Vickers hardness of M-A constituent (HV)
IAF	intragranular acicular ferrite
IFPI	acicular ferrite, type I
IFPII	acicular ferrite, type II
ICHAZ	intercritical heat affected zone
ICCGHAZ	intercritically reheated coarse grained heat affected zone
IF(B)	intragranularly nucleated bainite
IF(PF)	intragranularly nucleated primary ferrite
IF(Wf)	intragranularly nucleated Widmannstätten ferrite
IIW	International Institute of Welding
K_{IC}	plane strain fracture toughness
K-S	Kurdjumow-Sachs orientation
KV_T	transverse impact energy (J)
k_y	Hall-Petch coefficient
L	length of M-A constituent
LB	lower bainite

L.P.R.	lattice constant ratio $a_{\text{ppt}}/a_{\alpha}$
μ	shear modulus
M, α'	martensite
M_s	martensite transformation start temperature
M-A, M^*	martensite-austenite constituent (island) (%)
\overline{MS}	mean squares
$\frac{N}{A}$	number of particles per unit area (No/mm^2)
$\frac{N}{V}$	number of particles per unit volume (No/mm^3)
N-W	Nishiyama-Wasserman orientation
NDT	nil-ductility temperature
OM	optical microscope
P	pearlite
P_L	degenerated pearlite
P_{cm}	Japanese welding carbon equivalent
PF; F_1	polygonal (or equiaxed) ferrite
PF(G), F_p	primary grain boundary (or alltriomorphic, FA) ferrite
PF(I)	intragranular polygonal ferrite
PWHT	post weld heat treatment
p -value	significance of probability in statistical analyses
QT	quenched and tempered
R	relative interfacial energy
R	stress intensification around the crack tip
R^2	correlation coefficient
R_{eH}	yield strength (N/mm^2)
R_m	tensile strength (N/mm^2)
$R_{p0.2}$	0.2% proof stress (N/mm^2)
RKR	Ritchie-Knott-Rice model
RCR	recrystallization controlled rolled
r_M	CTOD deterioration factor ($1/\text{wt}\%$)
σ	standard deviation
σ_F, σ_F	critical cleavage stress (MPa)
σ_{max}	maximum achievable stress around a crack tip (MPa)
σ_y	uniaxial yield stress (MPa)
SAW	submerged arc welding
SEM	scanning electron microscope
SCHAZ	subcritical heat affected zone
SMAW	shielded metal arc welding (manual metal arc welding)
SS	sum of squares
τ_1	friction stress on dislocation
$t_{8/5}$	cooling time between 800 to 500 °C (s)
T	temperature (K)
T_{27J}	27 J impact energy transition temperature (°C)
T_{50}	50% transformation temperature (°C)
$T_{50\%}$	50% fibrous fracture transition temperature (°C)
$T_{0.1\text{mm}}$	0.1 mm crack tip opening transition temperature in CTOD test (°C)
T_{NR}	austenite recrystallization temperature

T_s	transformation start temperature
$T_{p1,p2}$	peak temperatures (°C)
T_{PRTT}	peak rate transformation temperature (°C)
TEM	transmission electron microscope
TK_{28J}	28 J energy transition temperature Charpy V test (°C)
$TK_{50\%US}$	50% upper self energy (°C)
TMCP	thermomechanically processed
t Stat	ratio of coefficient and standard error in statistical analyses
UB	upper bainite
ν	Poisson's ratio = 0.3 for steels
$\nu_{Trs/}$	
$FATT_{50\%}$	50% fracture appearance transition temperature (°C)
V_v	inclusion volume fraction
W	width of M-A constituent (μm)
WF	Widmannstätten ferrite
X	critical distance ahead a macrocrack tip (μm)

Contents

Abstract	
Acknowledgements	
List of symbols and abbreviations	
Contents	
1 Introduction	17
2 Intragranular nucleation of ferrite	19
2.1 Competition between the intergranular and intragranular nucleation of ferrite during the austenite-ferrite transformation	20
2.1.1 Summary of paragraph 2.1	22
2.2 Intragranular nucleation of acicular ferrite	22
2.2.1 Summary of paragraph 2.2	24
2.3 Oxide inclusions and their influence on the nucleation of acicular ferrite	24
2.3.1 Type of the inclusions	24
2.3.2 Size and number distribution of inclusions	25
2.3.3 Formation of titanium oxide inclusions and the nucleation of acicular ferrite on them	28
2.3.4 Summary of paragraph 2.3	29
2.4 Acicular ferrite formation mechanisms	30
2.4.1 Local variation of the chemical composition around the inclusion	30
2.4.2 Favourable crystallographic lattice match for the nucleation of ferrite	32
2.4.3 Increased stress-strain fields around the inclusion	33
2.4.4 Reduction of the nucleation free energy barrier for the ferrite embryo	34
2.4.5 Summary of paragraph 2.4	34
2.5 Factors affecting the nucleation of acicular ferrite	34
2.5.1 Chemical composition of steel	35
2.5.1.1 Titanium and oxides	35
2.5.1.2 Aluminium and oxides	36

2.5.1.3 Sulphur	36
2.5.1.4 Nitrogen	37
2.5.1.5 Niobium	38
2.5.1.6 Vanadium	38
2.5.1.7 Manganese, nickel and carbon	39
2.5.1.8 Silicon	39
2.5.1.9 Molybdenum and chromium	40
2.5.1.10 Boron	40
2.5.1.11 Rare earth elements	41
2.5.2 Austenitizing temperature and austenite grain size	42
2.5.3 Hot deformation	44
2.5.4 Cooling rate and finish cooling temperature	45
2.5.5 Summary of paragraph 2.5	47
3 Influence of acicular ferrite, M-A constituents and the effective grain and packet sizes on the toughness of the HAZ	48
3.1 Fracture mechanism of acicular ferrite	49
3.1.1 Role of acicular ferrite for crack initiation	49
3.1.2 Influence of acicular ferrite on the effective grain and packet size and crack propagation	50
3.1.3 Summary of paragraph 3.1	51
3.2 Formation and properties of M-A constituents	51
3.2.1 Formation mechanism	51
3.2.2 Type and properties of M-A constituents	52
3.2.3 Summary of paragraph 3.2	53
3.3 Factors affecting the formation and properties of M-A constituents	53
3.3.1 Chemical composition of steel	53
3.3.1.1 Carbon and carbon equivalent	54
3.3.1.2 Nitrogen and boron	55
3.3.1.3 Niobium and vanadium	55
3.3.1.4 Aluminium and silicon	55
3.3.1.5 Manganese, chromium and molybdenum	56
3.3.1.6 Copper and nickel	56
3.3.2 Peak temperature	56
3.3.3 Cooling rate	57
3.3.4 Summary of paragraph 3.3	58
3.4 Influence of M-A constituents on the fracture mechanism	58
3.4.1 Ductile fracture	59
3.4.2 Brittle fracture	60
3.4.3 Summary of paragraph 3.4	62
3.5 Interrelation between acicular ferritic microstructure and M-A constituents	63
3.5.1 Formation of acicular ferrite and M-A constituents	63
3.5.2 Effect of the chemical composition of steel	64
3.5.2.1 Titanium and nitrogen	64
3.5.2.2 Vanadium	64
3.5.2.3 Niobium	65

3.5.2.4 Aluminium.....	66
3.5.2.5 Silicon.....	67
3.5.2.6 Boron.....	67
3.5.2.7 Manganese.....	67
3.5.2.8 Chromium, molybdenum, nickel and copper.....	67
3.5.3 Effect of a cooling rate.....	68
3.5.4 Influence of the effective grain size and M-A constituents on toughness.....	68
3.5.5 Summary of paragraph 3.5.....	70
3.6 Failure micromechanisms.....	70
3.6.1 Ductile-to-brittle transition temperature.....	70
3.6.2 Factors affecting the critical fracture stress.....	72
3.6.3 Cleavage fracture models.....	73
3.6.4 Summary of paragraph 3.6.....	74
3.7 Testing of ductile-to-brittle transition temperature.....	75
3.7.1 Charpy V impact energy transition temperature T_{27J}	75
3.7.2 50% ductile fracture transition temperature $T_{50\%}$ in Charpy V impact test.....	76
3.7.3 Crack tip opening displacement transition temperature $T_{0.1mm}$ in CTOD test.....	77
3.7.4 Summary of paragraph 3.7.....	77
3.8 Toughness improvement mechanisms of the ICCGHAZ and ICHAZ.....	78
3.8.1 ICCGHAZ.....	78
3.8.2 ICHAZ.....	80
3.8.3 Summary of paragraph 3.8.....	82
4 Novel features of this work.....	83
5 Experimental procedure.....	85
5.1 Test materials.....	85
5.1.1 Chemical composition and preparation of the test plates.....	85
5.1.2 Mechanical properties of the test plates.....	86
5.1.3 Rolling of the test plates.....	86
5.1.4 Analyses of the inclusions in the test plates.....	86
5.1.5 Heat treatments to obtain a significant amount of acicular ferritic microstructure contained test pieces.....	88
5.2 Simulation of the weld heat affected zones.....	89
5.2.1 Test specimens and simulation programmes.....	89
5.2.2 Mechanical testing of simulated specimens.....	89
5.2.3 Metallography.....	90
6 Test results.....	92
6.1 Simulation heat treatments and preparation of acicular ferritic microstructure contained test pieces.....	92
6.1.1 Summary of paragraph 6.1.....	93
6.2 Toughness of the simulated HAZ zones.....	94
6.2.1 Impact toughness.....	94
6.2.2 Fracture toughness.....	96
6.2.3 Summary of paragraph 6.2.....	98

6.3 Microstructures of the simulated HAZ zones and their influence on impact and fracture toughness	99
6.3.1 Microstructural analyses.....	99
6.3.2 Microstructural investigation on the basis of hardness measurements	100
6.3.3 Influence of microstructural constituents on the impact and fracture toughness of the simulated ICCGHAZ and ICHAZ specimens	102
6.3.4 Summary of paragraph 6.3	105
6.4 Grain sizes and their influence on impact and fracture toughness.....	106
6.4.1 Austenite grain size and ferrite grain and bainite packet sizes	106
6.4.2 Grain orientation analyses	108
6.4.3 Relationship between the largest ferrite grain and bainite packet sizes and the cleavage facet size.....	111
6.4.4 Influence of ferrite grain and bainite packet sizes on impact and fracture toughness.....	112
6.4.5 Summary of paragraph 6.4	114
6.5 Investigations of M-A constituents and their influence on impact and fracture toughness.....	115
6.5.1 Amount and size of M-A constituents	115
6.5.2 Type and distribution of M-A constituents	117
6.5.3 Influence of M-A constituents on impact and fracture toughness.....	121
6.5.4 Summary of paragraph 6.5	122
6.6 Crack initiation and propagation	123
6.6.1 Crack initiation mechanisms	123
6.6.2 Crack propagation mechanisms.....	127
6.6.3 Summary of paragraph 6.6	132
6.7 Multiple linear regression analyses.....	132
6.7.1 CGHAZ and ICCGHAZ.....	133
6.7.2 Plate and ICHAZ	135
6.7.3 Summary of paragraph 6.7	137
7 Discussion	139
7.1 Intragranular nucleation of ferrite and bainite	139
7.1.1 Chemical composition of steel	140
7.1.2 Type, amount, distribution and size of inclusions.....	141
7.1.3 Austenite grain size.....	142
7.1.4 Hot deformation and cooling rate.....	143
7.1.5 Finish cooling temperature	144
7.1.6 Summary of paragraph 7.1	144
7.2 Toughness of the CGHAZ and ICCGHAZ.....	145
7.2.1 Type of microstructures	145
7.2.2 Ferrite grain and bainite packet sizes.....	146
7.2.3 Amount, size, type and distribution of M-A constituents	147
7.2.4 Hardness	149
7.2.5 Summary of paragraph 7.2	149
7.3 Toughness of the ICHAZ.....	150

7.3.1 Type of microstructures	150
7.3.2 Ferrite grain and bainite packet sizes.....	151
7.3.3 Amount, size, type and distribution of M-A constituents	152
7.3.4 Hardness	153
7.3.5 Summary of paragraph 7.3	154
7.4 Evaluation of testing and analyzing methods	154
7.4.1 Simulated weld HAZ specimens	155
7.4.2 Microstructural investigations and hardness measurements.....	155
7.4.3 Charpy V impact energy transition temperature T_{27J}	156
7.4.4 50% ductile fracture transition temperature $T_{50\%}$ in Charpy V impact tests	157
7.4.5 Crack tip opening displacement (CTOD) tests	159
7.4.6 Summary of paragraph 7.4	160
8 Conclusions	161
9 Future research	163
9.1 Improvement of toughness of the most critical sub-zones CGHAZ, ICCGHAZ and ICHAZ of the low heat input weld HAZ.....	163
9.2 Practical consequences of this work for steelmaking	164
References	
Appendices	

1 Introduction

The weakest link in steel weldments regarding toughness is the heat affected zone (HAZ). Normally, the coarse grained HAZ (CGHAZ) or the intercritically reheated coarse grained HAZ (ICCGHAZ) is considered to possess the lowest toughness with the values decreasing as the weld heat input increases. However, the studies on normalized ferritic-pearlitic offshore steels and the recent studies on low-carbon thermomechanically processed steels have shown that the lowest toughness is sometimes found in the intercritical HAZ (ICHAZ) or subcritical HAZ (SCHAHAZ), if welding with a low heat input (Fairchild *et al.* 1991, Akselsen *et al.* 1987, Akselsen *et al.* 1988, Laitinen 1998). The overmatched weld metal and the overmatched and narrow HAZ at low heat input welding is apt to concentrate cracking on the lower hardness ICHAZ or SCHAHAZ.

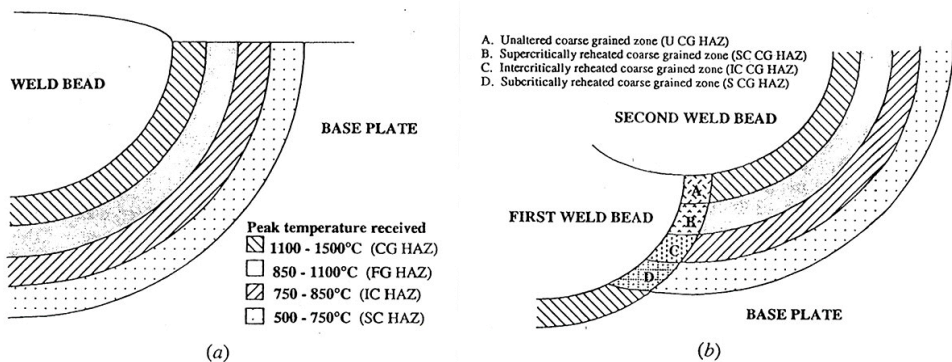


Fig. 1. Schematic presentation of microstructures in single (a) or multipass (b) weld (Davis & King 1994).

It has been observed that the intercritical thermal cycle of the ICHAZ does not remove all traces of microstructure of base plates as does the CGHAZ thermal cycle. In consequence, the technique used to manufacture steel can significantly affect the toughness of the ICHAZ (Fairchild *et al.* 1991). Modern steelmaking technology has opened up new possibilities for manufacturing high-strength TMCP steels. Such

improvements include a better control of titanium microalloying and nitrogen levels and even the use of titanium killing, both of which can be expected to improve the toughness of the base plate and the weld HAZ. In titanium killed plates, titanium oxide particles are known to nucleate acicular ferrite intragranularly improving the toughness of the ICHAZ as has been shown in laser welded joints (Senogles 1998).

The use of titanium killing to improve the toughness of steel is based on the usual manufacturing practices associated with weld metals. Normally, the high and intermediate oxygen content (200–800 ppm) in weld metals of the conventionally welded (SMAW, GMAW, SAW) joints can provide enough favourable inclusions for the nucleation of acicular ferrite. However, the recent development of titanium killed steels, with oxygen contents less than 80 ppm and titanium contained weld metals, have shown that acicular ferritic microstructure can be achieved in the low oxygen (15–30 ppm) TIG and even extremely low oxygen (about 10 ppm) EB weld metals, when the aluminium content of steel is less than 0.002% and the Al/O ratio does not exceed unity (Bhadeshia & Svensson 1993, Thewlis 1994, Francis-Scrutton 1995a, Francis-Scrutton 1995b, Ohkita & Hori 1995, Zhang & Farrar 1996, Koseki *et al.* 1997, Ohara & Wallach 1999). This has opened up the use of titanium killed steels for offshore structures and pipes, where a good fracture toughness of the coarse grained HAZ can be guaranteed after high heat input welds. However, in some applications of low heat input welding it is necessary to use for constructional reasons or to reduce the distortion of structures.

2 Intragranular nucleation of ferrite

The optimum strength and toughness for high strength steel plates and weldments has normally been considered to be achieved through grain refinement by using microalloying elements such as aluminium, niobium, vanadium and titanium, which form precipitates of carbides, nitrides and carbonitrides to prevent the grain coarsening of austenite. Generally, the fine ferrite grain size has been achieved in the plates and the HAZ of the welded joints as a result of the fine austenite grain size.

In thermomechanical plate rolling a strong deformation below the austenite recrystallization temperature T_{NR} forms deformation bands inside the austenite grains for the nucleation sites of ferrite in addition to the nucleation in austenite grain boundaries. The recent studies of ultrafine ferritic-bainitic TMCP plates have demonstrated that the best combination of strength and toughness properties was obtained with a microstructure comprising a high amount of intragranularly nucleated bainite (acicular ferrite) and small ($\sim 0.5 \mu\text{m}$) particles of dispersed M-A (Yakubtsov & Boyd 2001, Yakubtsov *et al.* 2004). The dominated acicular ferritic microstructure, as a result of the intragranular nucleation of ferrite, could be achieved with an industrially-realistic processing schedule using either a strong deformation ($\epsilon_F \sim 0.5$) of steel below the austenite recrystallization temperature T_{NR} , a relatively rapid cooling at $25 \text{ }^\circ\text{C/s}$ and a low finish cooling temperature of $400 \text{ }^\circ\text{C}$ (Yakubtsov & Boyd 2001, Yakubtsov *et al.* 2004). Or a two stage controlled rolling in the austenite recrystallization plus non-recrystallization regions followed by controlled cooling at a rate of $30 \text{ }^\circ\text{C/s}$ has also been investigated (Zhao *et al.* 2003).

The ultrafine ferritic-bainitic and acicular ferritic microstructures (ferrite grain size $< 1 \mu\text{m}$), at least in the surface layers of plates, have been achieved according to recent research work (Hickson *et al.* 1999, Akhlaghi *et al.* 2000, Boyd & Zhao 2000, Howe 2000, Priester & Ibraheem 2000, Weng & Dong 2000, Yang *et al.* 2000). The prior austenite grain size in ultrafine ferrite steel processes is even as low as $10 \mu\text{m}$ (Weng & Dong 2000, Leinonen 2001, Leinonen 2002). The recent studies on carbon-manganese, niobium and niobium plus titanium microalloyed steels have demonstrated that a high strain, a low deformation temperature close to A_{F3} and a fine prior austenite grain size promoted formation of ultrafine grains (Pan 2004). Rolling just at or above the austenite-ferrite transformation temperature has caused strain induced transformation of austenite into ferrite.

In weld metals the fine ferrite grain size has normally been achieved through the intragranular nucleation of ferrite on fine oxide inclusions without restricting the grain coarsening of austenite. This idea has been utilized in the development of titanium killed steels, where the improvement of weld HAZ toughness has been achieved through fine acicular ferritic microstructure as a result of the intragranular nucleation of ferrite on titanium oxide inclusions. Although titanium oxide inclusions have a minimal influence on austenite grain refining, recent studies have demonstrated that ultrafine oxides containing magnesium can also retard austenite grain coarsening near the weld fusion line (Terada *et al.* 2004). The main factors affecting intragranular nucleation of acicular ferrite on oxide inclusions has been explored in this research work on the basis of the weld metal, the weld HAZ and the base plates.

2.1 Competition between the intergranular and intragranular nucleation of ferrite during the austenite-ferrite transformation

Nucleation of ferrite during the austenite-ferrite transformation is normally intergranular, because the grain boundaries lower the free energy barrier for nucleation. The effectiveness of various heterogeneous sites for the nucleation of ferrite has been ranked in order of increasing free energy barriers as follows (Thewlis 1994, Thewlis *et al.* 1997):

- high energy boundary triple points (high angle boundary $> 25^\circ$ in corner)
- high energy boundary plus inclusions ($10 \mu\text{m}$)
- high energy boundaries (high angle boundary $> 25^\circ$ in edge)
- large inclusions (diam. $> 10 \mu\text{m}$)
- small inclusions (diam. $\approx 0.2 \mu\text{m}$)
- low energy boundary (5°)
- homogenous

Grain boundary sites have significantly lower free energy barriers for the nucleation of ferrite than intragranular inclusions, and large isolated inclusions are more efficient in nucleation of ferrite than small ones (Thewlis *et al.* 1997).

Conventionally, the different transformation structures in steels and weld metals in order of decreasing temperature are as follows (Grong 1994):

- primary grain boundary (or allotriomorphic) ferrite (PF(G))
- polygonal (or equiaxed) ferrite (PF) including intragranularly nucleated polygonal ferrite PF(I)
- Widmanstätten ferrite (WF)
- acicular ferrite (AF)
- upper bainite (UB)
- lower bainite (LB)
- martensite (M)

In this research work the used classification scheme for identification of microstructures by means of optical microscopy in steels and weld metals is recognized as the method of the International Institute of Welding (IIW) based on the above-mentioned

microstructures (Welding in the World 1991, Harrison & Webster 1994). However, it simplifies the classification procedure compared with the above-mentioned microstructures, since the distinction between acicular ferrite (AF) and the various side plate structures (FS(A) and FS(NA)) is based on features such as aspect ratio, relative lath size and number of parallel laths (Grong 1994).

In Figure 2 the microstructures have been schematically illustrated using a novel classification scheme based on two main transformation mechanisms: the diffusion controlled reconstructive reactions with slow cooling rates and the shear dominated displacive reactions with fast cooling rates (Thewlis *et al.* 1997, Thewlis 2000, Thewlis 2001, Thewlis 2004). The abbreviations of the microstructures in this classification scheme distinguish the grain boundary and intragranularly nucleated microconstituents corresponding to the above-mentioned microstructures as follows (Thewlis 2004):

- grain boundary microconstituents: GB(PF)=grain boundary primary ferrite corresponds to (PF(G)), GB(WF)=grain boundary Widmanstätten ferrite corresponds to (WF) and GB(B)=grain boundary bainite corresponds to (UB)
- intragranularly nucleated microconstituents: IF(Wf)=intragranular Widmanstätten ferrite plus IF(B)=intragranular bainite and intragranularly nucleated primary ferrite IF(PF) corresponds to (AF) and (PF(I)) respectively

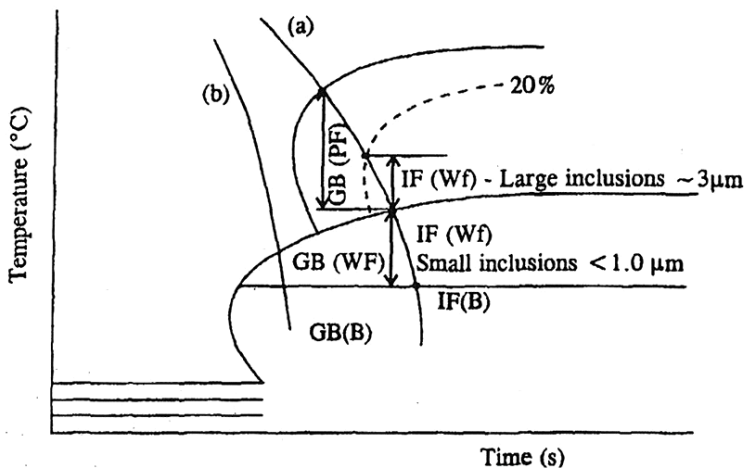


Fig. 2. Summary of the dynamics of the austenite-ferrite phase transformation in steels and weld metals as a function of undercooling (Thewlis 2001).

In Figure 2 a lower cooling rate (a) provides reconstructive transformation constituents such as grain boundary ferrite on austenite grain boundaries and intragranularly nucleated Widmanstätten ferrite and bainite on large ($\sim 3 \mu\text{m}$) and small inclusions ($< 1.0 \mu\text{m}$). A higher cooling rate (b) provides a transformation within the lower displacive nose of the diagram for the nucleation of Widmanstätten ferrite/bainite on austenite grain boundaries and intragranularly on small intragranular inclusions ($< 1 \mu\text{m}$). Ideally, acicular ferrite is formed within the displacive nose of the CCT diagram as a combination of intragranular Widmanstätten ferrite and bainite (Thewlis 2001).

2.1.1 Summary of paragraph 2.1

In summary, nucleation of ferrite during the austenite-ferrite transformation is normally intergranular because the austenite grain boundaries lower the energy barrier for the nucleation of ferrite. Strong deformation below the austenite recrystallization temperature in thermomechanical rolling and at or just above the austenite-ferrite transformation temperature in the rolling of ultrafine grain steels, forms deformation bands inside austenite grains for the intragranular nucleation of ferrite, in addition to the nucleation in austenite grain boundaries. Normally, a fine grain size in the plates and the HAZ of the welded joints is achieved by restricting austenite grain coarsening and a rapid cooling. However, a fine ferrite grain size in the weld metal, as well as in the HAZ of titanium killed steels, has been achieved through the intragranular nucleation of ferrite on small ($<1\ \mu\text{m}$) oxide inclusions within the lower displacive nose of the CCT diagram, or reconstructively on large ($\sim 3\ \mu\text{m}$) and small ($<1\ \mu\text{m}$) oxide inclusions without restricting austenite grain coarsening.

2.2 Intragranular nucleation of acicular ferrite

Acicular ferrite is ideally formed in low alloy steels, when austenite transforms during cooling in a temperature range, where diffusion controlled reconstructive transformations become relatively sluggish and give a possibility for phases (Widmanstätten ferrite, bainite and martensite) formed by displacive reactions within the lower displacive nose of the CCT diagram (Fig. 2). It is generally recognised that acicular ferrite has a three dimensional morphology of thin, lenticular or needle like laths, which are typically about $10\ \mu\text{m}$ long and about $1\text{--}2\ \mu\text{m}$ wide with the true aspect ratio likely smaller than 0.1. Its fine interlocking microstructure, with high angle boundaries between the ferrite laths, can deflect the propagation of cleavage cracks, thus enhancing toughness. Some authors have distinguished acicular ferrite (AF) in the weld metal as nucleated mainly on small inclusions displacively from intragranular acicular ferrite (IAF) in the base plate and the HAZ nucleated on small and large inclusions displacively and reconstructively. On the basis of microscopic investigation, acicular ferrite is similar to bainite or Widmanstätten ferrite and is therefore sometimes considered as intragranularly nucleated bainite or Widmanstätten ferrite, as seen in a novel microconstituent classification scheme (Fig. 2). The greatest difference between acicular ferrite and bainite or Widmanstätten ferrite is the nucleation and growth mechanism. Acicular ferrite nucleates intragranularly on the inclusions within large austenite grains and sympathetically on the surfaces of existing acicular ferrite laths, suppressing the growth of Widmanstätten ferrite or bainitic ferrite, which nucleate ideally within small austenite/austenite grain surfaces and grow in a sheaf morphology (Fig. 3) (Bhadeshia 1992, Bhadeshia & Svensson 1993, Grong 1994, Suh *et al.* 2000).

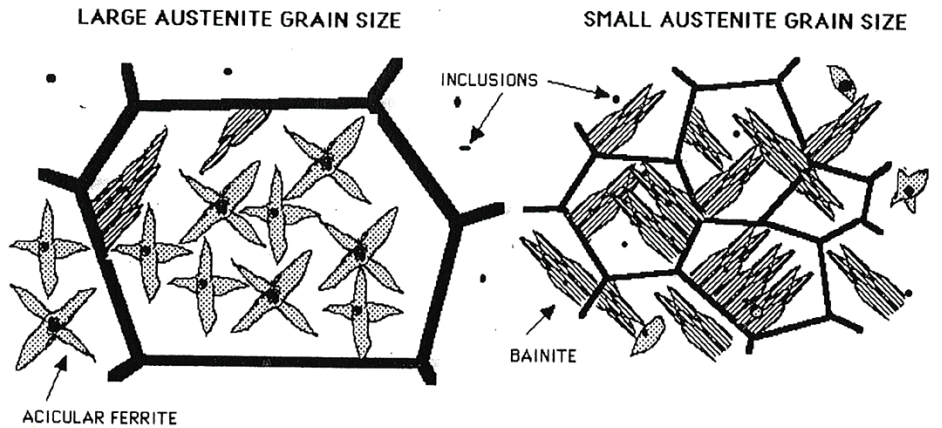


Fig. 3. Schematic illustration of the nucleation and growth mechanism of acicular ferrite and bainite (Bhadeshia 1992).

It has been observed that the acicular ferrite laths have an orientation relationship with the austenite grains and the prior delta ferrite columnar grains from which they grow. The orientation relationship lies within the Bain orientation region described as follows (Grong 1994 and Grong *et al.* 1995):

$$\begin{aligned} (101)_\alpha // (111)_\gamma \\ [11\bar{1}]_\alpha // [1\bar{1}0]_\gamma \end{aligned}$$

This orientation relationship corresponds to the well-known Kurdjumow-Sachs (K-S) and is close to Nishiyama-Wasserman (N-W) orientations and indicates that the growth of acicular ferrite occurs either by a ledge mechanism or by a pure shear mechanism (Grong 1994).

Acicular ferrite has been found to nucleate intragranularly as a result of a succession of competing nucleation and growth processes at the austenite grain boundary and intragranular nucleation sites during undercooling. The transformation start temperature T_s is generally regarded as a measure of grain boundary reaction, whereas the intragranular acicular ferrite formation is best described by temperatures at a later stage of the transformation, e.g. T_{50} (50% transformation temperature) or T_{PRTT} (peak rate transformation temperature). In weld metals the temperature range for the nucleation of acicular ferrite has been found to be 600–680 °C depending on the chemical composition of the steel and the cooling rate. Normally, the nucleation of acicular ferrite in weld metals is 40–70 °C higher than the formation of bainite (Thewlis *et al.* 1997). For example, the maximum rate of transformation in the optimised weld metal microstructure for X65 plates has been reported to be between 515 and 570 °C, indicating that acicular ferrite in these weld metals consisted of Widmanstätten ferrite and/or bainite (Thewlis 2000). It is reported that a peak rate transformation temperature between 500 and 625 °C gives a large amount of acicular ferrite. The upper end of this range coincides with the

onset of displacive transformation and the lower end a significant amount of ferrite side plate structures (Thewlis 2001). In the yield strength 420 MPa class TMCP steel intragranularly nucleated ferrite was found to form in the temperature range of 480–630 °C, when a cooling rate was 5 °C/s (Yoshida *et al.* 1998).

Formation of acicular ferritic microstructure, however, depends on the formation of the secondary acicular ferrite, which nucleates sympathetically in the austenite/ferrite interface on primary acicular ferrite laths. When the primary acicular ferrite laths nucleate on the inclusions, the austenite/ferrite interface area increases for further nucleation. Thus, the sympathetic nucleation of acicular ferrite at a new austenite/ferrite interface provides a possible explanation for the relatively evenly distributed acicular ferrite microstructure (Barbaro *et al.* 1989).

2.2.1 Summary of paragraph 2.2

In summary, acicular ferrite is an intragranularly nucleated microstructure for extreme improvement of toughness based on its three-dimensional, fine interlocking microstructure with high angle boundaries between ferrite laths. Formation of a large amount of acicular ferrite in the temperature range of 480–630 °C indicates that at least a part of it consists of Widmannstätten ferrite or bainite. The mechanisms and the factors influencing the formation of acicular ferrite such as the chemical composition of steel, the type, volume fraction and size distribution of inclusions, the austenite grain size, cooling rate, hot deformation and finish cooling temperature are investigated in the following paragraphs.

2.3 Oxide inclusions and their influence on the nucleation of acicular ferrite

The oxide inclusions for favourable intragranular nucleation sites are formed before or during solidification, and they can grow or transform their composition in a solid state. Non-metallic inclusions can also be inoculated into steel melt (Lou & Holappa, 2001).

2.3.1 Type of the inclusions

The stable titanium oxides formed in titanium killing of steels are TiO, Ti₂O₃, Ti₃O₅, TiO₂ and Fe₂TiO₂. Because these stable titanium oxides are formed in the steel melt they are joined on the core of inclusions formed at higher temperatures, such as Al₂O₃ (melting temperature 2015 °C), TiO (melting temperature 1800 °C), SiO₂ (melting temperature 1713 °C) and MnO (melting temperature 1650 °C), which are often in cores of titanium oxide inclusions. The main types of inclusions are MnOSiO₂, TiOMnOSiO₂, MnOTiO₂, MnOTi₂O₃, 2MnOTiO₂, 2SiO₂3Al₂O₃ (mullite) and MnOAl₂O₃ (galaxite) with MnS (melting temperature 1620 °C), CuS (melting temperature 1125 °C) and TiN on the

surface (Cochrane & Senogles 1994, Gladman & Senogles 1994, Thewlis 1994, Zhang & Farrar 1996, Haaland *et al.* 1997, Thewlis *et al.* 1997, Díaz-Fuentes *et al.* 1998, Díaz-Fuentes *et al.* 2000, Anelli *et al.* 2002).

During cooling of the high oxygen weld metals, glassy oxide $2\text{SiO}_2\cdot 3\text{Al}_2\text{O}_3$ (mullite) was formed first in addition to Ti_3O_5 , MnOTiO_2 and MnOTi_2O_3 . However, mullite is unstable in austenite and MnOAl_2O_3 (galaxite), having a spinel structure, becomes stable at lower temperatures. Titanium addition was found to be beneficial for the formation of acicular ferrite by decreasing the formation of ineffective glassy oxide mullite (Cochrane & Senogles 1994, Gladman & Senogles 1994, Koseki *et al.* 1997).

In the intermediate oxygen manual metal arc (SMAW) welds and in the low oxygen TIG (GTAW) welds, the types of inclusions MnOSiO_2 , TiOMnOSiO_2 , $\text{Al}_2\text{O}_3\cdot\text{MnOSiO}_2$, MnS and $(\text{Mn,Cu})\text{S}$ have been found around TiO (Zhang & Farrar 1996). In the low oxygen steels the Ti_2O_3 , TiO_2 type inclusions have been found and in higher oxygen steels MnOTiO_2 and MnOTi_2O_3 inclusions have been found (Cochrane & Senogles 1994, Gladman & Senogles 1994). In the extremely low oxygen (around 10 ppm) EB weld metals acicular ferrite has been found to nucleate intragranularly at inclusions of the dual structure consisting of oxide in the core and MnS on the surface (Ohara & Wallach 1999).

It has also been demonstrated that rare earth oxide and sulphide inclusions such as $(\text{La,Ce})_2\text{O}_3$, CeS , Ce_2S_4 and La_2S_3 are suitable nucleation sites for acicular ferrite. The favourable effects of CeS , Ce_2S_4 and La_2S_3 are explained as the cause for their multiplied lattice parameters (twice and three times) compared to ferrite (Shiga 1994, Lou & Holappa 2001, Thewlis 2001).

2.3.2 Size and number distribution of inclusions

The adequate number of active inclusions within the appropriate size range has been found to be the most significant controlling factor for the nucleation of acicular ferrite in the weld metals and in the HAZ. It has been reported that the appropriate size of inclusions for the intragranular nucleation of ferrite was $0.2\text{--}3\ \mu\text{m}$ and the probability for the ferrite nucleation increases with maximum sizes reaching $1.0\text{--}1.1\ \mu\text{m}$ (Shim J-H *et al.* 1999, Lou & Holappa 2001). However, it seems that acicular ferrite can nucleate to large intragranular inclusions ($> 3\ \mu\text{m}$) and grow reconstructively instead of in the normal shear dominated displacive reactions as undercooling increases (Fig. 2). On the other hand, the inclusions of diameters less than $0.1\text{--}0.2\ \mu\text{m}$ have been said to contribute insufficient free energy for the nucleation of acicular ferrite in the weld metals (Barbaro *et al.* 1989, Zhang & Farrar 1996, Shim *et al.* 2000).

In weld metals, increasing the oxygen content has increased the amount of inclusions and thus, the active nucleation sites for the displacive nucleation of acicular ferrite (Table 1). But the oxygen content has been found to have no significant influence on the size of the active inclusions. For example, in the high oxygen (300–800 ppm) (SAW) weld metals the size of active inclusions for the nucleation of acicular ferrite was $0.4\text{--}0.6\ \mu\text{m}$ and the number/unit volume $2.7\times 10^7\text{--}8.2\times 10^7$ particles/ mm^3 and in the intermediate oxygen (200–300 ppm) manual metal arc (SMAW) weld metals the corresponding diameter range was $0.3\text{--}0.9\ \mu\text{m}$ and the number/unit volume $3.1\times 10^7\text{--}4.9\times 10^7$

particles/mm³ (Barbaro *et al.* 1989, Zhang & Farrar 1996, Babu *et al.* 1999). In the low oxygen (15–30 ppm) TIG weld metals the most active inclusions were found to be within the diameter range 0.35–0.75 μm and the number/unit volume 1.8×10^7 particles/mm³. However, in the extremely low oxygen (about 10 ppm) EB weld metals, inclusion sizes of 0.32–0.47 μm and the number/unit volume 5×10^6 particles/mm³ have been reported. The inclusions formed during solidification of the rapidly cooled EB weld metal have been found to be smaller and their number density higher than in slower cooled weld metals (Zhang & Farrar 1996, Babu *et al.* 1999, Ohara & Wallach 1999).

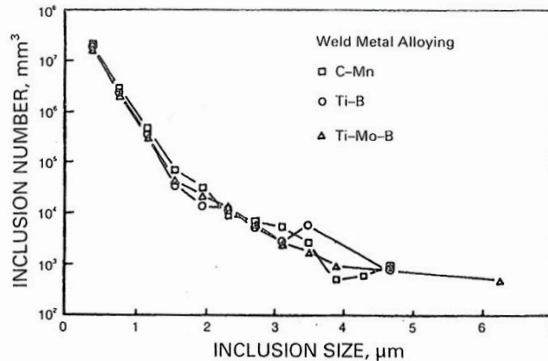


Fig. 4. Variation of inclusion number with size (Thewlis *et al.* 1997).

In titanium killed plates and in their HAZ, the size of titanium oxide particles was larger and their number density lower than in the weld metal (Table 1) being favourable nucleation sites also for reconstructive ferrite transformation. The size and number/unit volume of titanium oxide particles were increased with an increasing oxygen content being 0.5–4.0 μm in a low oxygen (20 ppm) steel and 1–10 μm and 1–18 μm in higher oxygen (120 ppm) and (230 ppm) test steels respectively (Gladman & Senogles 1997). In the HAZ of titanium killed steel, titanium oxide particles Ti_2O_3 with their diameter of 2–3 μm and their minimum number of 10 particles/mm² (2123 – 3185 particles/mm³) and MnS-SiO₂-oxysulphides with their diameter of 1–6 μm and their number of 52–250 particles/mm² (11×10^3 – 111×10^3 particles/mm³) were found (Chijiwa *et al.* 1988, Babu *et al.* 1999, van der Eijk *et al.* 2000). Yamamoto *et al.* (1989) and Yamamoto *et al.* (1996) reported Ti_2O_3 inclusions in titanium killed plates and their HAZ with a diameter of 0.2–3 μm and the number of 50–60 particles/mm² (10.6×10^3 – 191.1×10^3 particles/mm³). Anelli *et al.* (2002) reported that a high amount (50–80%) of acicular ferrite achieved in steels with an oxygen content of 40–100 ppm when the number of inclusions per unit area was equal to or greater than 200 particles/mm² and an average size of 3–4.5 μm .

Acicular ferrite has also been reported to nucleate on rare earth sulphide inclusions with a mean size between 0.6 and 1.7 μm and a number density of 0.5×10^6 – 6.0×10^6 particles/mm³ (minimum greater than 10^5 particles/mm³) as an example of displacive transformation (Thewlis 2001). This means that the rare earth plates in Table 1 do not contain high oxygen contents, but a high sulphur content, supporting the estimation that

the inclusion volume fraction depends on the total amount of oxygen and sulphur as follows (Grong 1994):

$$\text{Inclusion volume fraction} = 10^{-2} [5.0(\text{wt}\%O) + 5.4(\text{wt}\%S - 0.003)] \quad (1)$$

By including the following relationship

$$\text{Inclusion volume fraction} = V_v = \frac{\pi}{6} \overline{d_v}^3 \times \overline{N_v} \quad (2)$$

where $\overline{d_v}$ and $\overline{N_v}$ three-dimensional inclusion diameter and number density.

Table 1. Type, size and distribution of inclusion for the nucleation of acicular ferrite.

Specimen	Oxygen content (ppm)	Size of inclusions (μm)	Number of inclusions particle/mm ³	Reference
SAW weld	300–800	0.4–0.6	2.7x10 ⁷ –8.2x10 ⁷	Barbaro <i>et al.</i> 1989
SMAW weld	200–300	0.3–0.9	3.1x10 ⁷ –4.9x10 ⁷	Zhang & Farrar 1996
TIG weld	15–30	0.35–0.75	1.8x10 ⁷	Zhang & Farrar 1996
EB weld	≈ 10	0.32–0.47	5x10 ⁶	Ohara & Wallach 1999
Ti killed plate	≈ 20	0.5–4.0	-	Gladm. & Sen.1994
Ti killed plate	≈ 120	1–10	-	Gladm. & Sen.1994
Ti killed plate	≈ 230	1–18	-	Gladm. & Sen.1994
Ti killed plate	20–40	0.2–2.0	¹⁾ 50–60(15.9x10 ³ –191.1x10 ³)	Yamamoto <i>et al.</i> 1996
Ti killed plate	20–40	1.4–3.0	¹⁾ 52–250(11.0x10 ³ –113.7x10 ³)	van der Eijk <i>et al.</i> 2000
Ti killed plate	40–100	3.0–4.5	¹⁾ ≥ 200(28.3x10 ³ –42.5x10 ³)	Anelli <i>et al.</i> 2002
Rare earth sulphide plate	50–100	0.6–1.7	0.5x10 ⁶ –6.0x10 ⁶	Thewlis 2001
HAZ	-	2–3	¹⁾ ≥10 (2.1x10 ³ –3.2x10 ³)	Chijiwa <i>et al.</i> 1988
HAZ	17	0.5–3.0	¹⁾ 50 (10.6x10 ³ –63.7x10 ³)	Yamaoto <i>et al.</i> 1989

¹⁾ particle/mm² (calculated particles/mm³ according to Babu *et al.* 1999)

The measured two-dimensional arithmetic inclusion characteristics can be converted to three-dimensional values using the relations (Babu *et al.* 1999):

$$\overline{d_v} = 1.57x\overline{d_A} \quad (3)$$

and

$$\overline{N_v} = \frac{\overline{N_A}}{\overline{d_v}}, \quad (4)$$

where $\overline{d_A}$ and $\overline{N_A}$ are arithmetic average diameter and number density measured from optical micrographs.

2.3.3 Formation of titanium oxide inclusions and the nucleation of acicular ferrite on them

The formation of oxide inclusions in titanium killed steels can be evaluated according to the schematic representation based on the Thermo-Calc data (Fig. 5) (Haaland *et al.* 1997, van der Eijk *et al.* 2000).

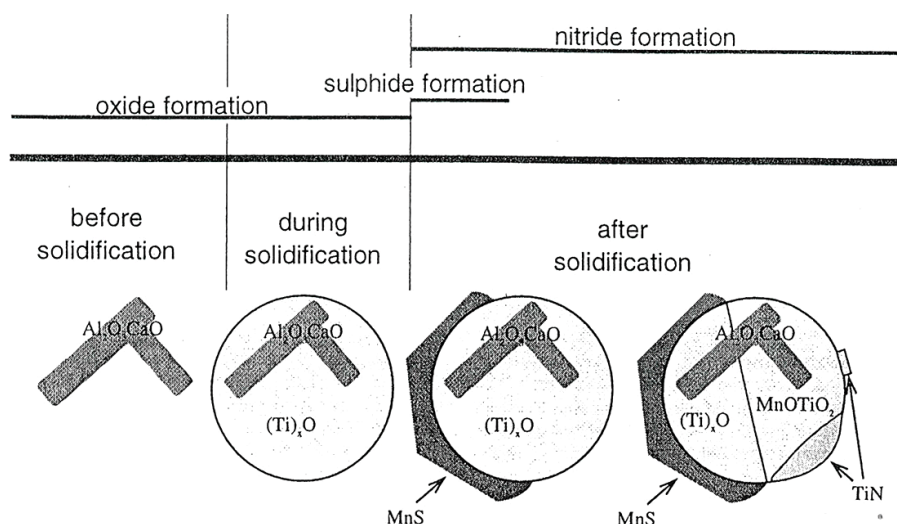


Fig. 5. Schematic representation of the sequence of inclusion formation in Ti killed steel (van der Eijk *et al.* 2000).

Before solidification oxide inclusions like Al_2O_3 and Ti_2O_3 were formed. In titanium killed steels, the remaining S precipitates on the surface of oxides as MnS in solid state. At lower temperatures TiN is formed through an exchange reaction with Ti_2O_3 , and the secondary reaction product is MnOTiO_2 according to the following reaction (Haaland *et al.* 1997, van der Eijk *et al.* 2000):



MnOTiO_2 in the inclusions has been found to be a very effective nucleant, producing up to 90% acicular ferrite (Powell *et al.* 1998).

Titanium addition has also been reported to decrease the size of MnS inclusions. This reduction of size is a result of the formation of liquid nuclei of $(\text{Ti},\text{Mn})\text{O}$ at the solid/liquid interface of iron, which act as heterogeneous nucleation sites for the formation of a liquid droplet of MnS during solidification. The successive nucleation of MnS, involving the nucleation of $(\text{Ti},\text{Mn})\text{O}$ particles, reduced the size of MnS inclusions in titanium killed steels compared to aluminium killed steels. As aluminium content was

increased, Al_2O_3 inclusions were formed in the melt and were the favourable nucleation sites for the rod-like MnS inclusions (Oikawa *et al.* 1997a,b).

Acicular ferrite can nucleate on the inclusion in three different ways depending on the size of the inclusion. Ferrite can envelope smaller inclusions ($<1\ \mu\text{m}$). A long ferrite needle can touch a larger inclusion on one side. A star like ferrite nucleation is typical for larger inclusions ($>1\ \mu\text{m}$), where the inclusion is located at the centre of the ferrite star growing in vertical directions to their nucleation surface (Fig. 6) (Zhang & Farrar 1996, Anelli *et al.* 2002).

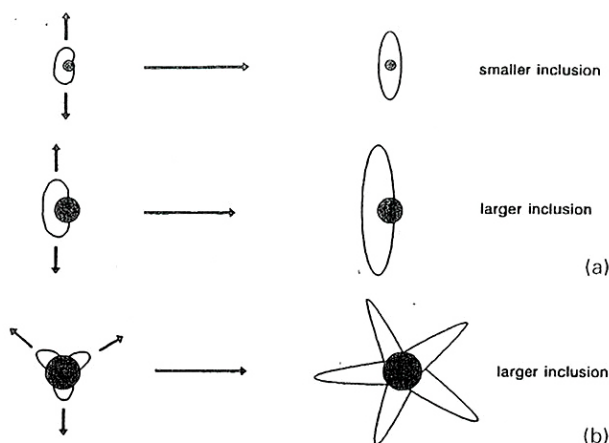


Fig. 6. Nucleation and growth models of acicular ferrite laths (Zhang & Farrar 1996).

2.3.4 Summary of paragraph 2.3

In summary, titanium killing of steel enhances the intragranular nucleation of acicular ferrite particularly in the low oxygen (15–30 ppm) TIG and extremely low oxygen (about 10 ppm) EB weld metals, when the types of inclusions Ti_2O_3 , TiO_2 were found. In the intermediate oxygen (200–300 ppm) and high oxygen weld metals (300–800 ppm) the types of inclusions MnOSiO_2 , TiOMnOSiO_2 , $\text{Al}_2\text{O}_3\text{MnOSiO}_2$, MnS and (Mn, Cu)S have been found around TiO.

In the weld metals the increase of oxygen caused an increase in the amount of inclusions and the active nucleation size for a displacive transformation of acicular ferrite being 2.7×10^7 – 8.2×10^7 particles/ mm^3 in the high oxygen (300–800 ppm) SAW welds and 1.8×10^7 particles/ mm^3 in the low oxygen (15–30 ppm) TIG welds. But the oxygen content had no significant influence on the size of the active inclusions for the intragranular nucleation of acicular ferrite being within a diameter range of 0.3–0.9 μm . In titanium killed plates and in their HAZ, the size of titanium oxide inclusions was higher and their number/unit volume was lower than in the weld metal, enhancing a

reconstructive transformation of acicular ferrite. The size of inclusions increased with an increasing oxygen content being 0.5–4.0 μm in low oxygen (20 ppm) steel and 1–10 μm and 1–18 μm in higher oxygen (120 ppm) and (230 ppm) test steels respectively. The minimum number of 10 titanium oxide (Ti_2O_3) particles/ mm^2 (2123–3185 particles/ mm^3) with diameters of 0.2–3 μm , the number of 50–60 particles/ mm^2 (10.6×10^3 – 191.1×10^3 particles/ mm^3) with diameters of 0.2–3 μm , equal or greater than 200 particles/ mm^2 (28.3×10^3 – 42.5×10^3 particles/ mm^3) with a diameter of 3.0–4.5 μm and the number of MnS-SiO₂-oxysulphides of 52–250 particles/ mm^2 (11.0×10^3 – 113.7×10^3 particles/ mm^3) with diameters of 1–6 μm were reported. The intragranular nucleation of acicular ferrite on rare earth sulphide inclusions CeS, Ce₂S₄ and La₂S₃ with diameters of 0.6–1.7 μm and their number density of 0.5 – 6.0×10^6 particles/ mm^3 has been reported as an example of a displacive transformation of acicular ferrite.

2.4 Acicular ferrite formation mechanisms

2.4.1 Local variation of the chemical composition around the inclusion

Local compositional inhomogeneity in steel matrix around inclusion can promote the nucleation of acicular ferrite due to an increase in the driving force of the austenite-ferrite transformation. Manganese depletion around the inclusions, as a result of the formation of MnS and galaxide (MnOAl_2O_3), has typically been thought to increase the ferrite nucleation temperature (Tomita *et al.* 1994, Mabuchi *et al.* 1996, Zhang & Farrar 1996, Enomoto 1997, Haaland *et al.* 1997, Koseki *et al.* 1997). Yamamoto *et al.* (1989) reported a manganese depletion of 0.02–0.2% at the interface between inclusions and austenite, but Mabuchi *et al.* (1996) evaluated the bottom of the manganese depleted zone to be deeper (-1.5%) and a 0.5% build-up of manganese on inclusions at the rim of a manganese depleted zone. Haaland *et al.* (1997) and Yamamoto *et al.* (1996) claimed that a 0.15% decrease in the manganese content at the interface increased the austenite-ferrite transformation temperature by about 8 °C. Also, Shim J-H *et al.* (1999) reported that a 1.84% manganese depletion increased the austenite-ferrite transformation start temperature by about 60 °C. A manganese depletion around the inclusions is believed to be one of the most important factors promoting the intragranular nucleation of ferrite, since the nucleation temperature of the grain boundary ferrite and ferrite side plate is 10 °C higher than the intragranular nucleation of ferrite. On the other hand, the increase of a driving force for ferrite transformation in a manganese depleted zone is estimated to be 100 J/mol, which is a half of the driving force (about 200 J/mol) for ferrite transformation at 700 °C according to thermo-calc (Mabuchi *et al.* 1996, Shim J-H *et al.* 1999).

The formation of a manganese depletion zone is associated with a diffusion of manganese from austenite into the titanium oxide inclusions or into the MnS precipitation on the surface of it. Thus, the width of the manganese depletion zone is proportional to the square root of the austenitizing time and to the cologarithm of the austenitizing temperature, i.e. the Arrhenius plot. The estimated activation energy for the formation of manganese depletion zones was 168 kJ/mol (Shim J-H *et al.* 1999). In addition to the

austenitizing temperature and time the formation of a manganese depletion zone depends on the cooling rate. According to Enomoto (1997), a cooling from 1200 °C to 850 °C or lower could cause a 500 nm wide manganese depletion zone at a cooling rate of 1 °C/s and 100–150 nm wide zone at a cooling rate 10 °C/s. Tomita *et al.* (1994) evaluated this using a simulated heat input of 20 kJ/mm and a peak temperature of 1400 °C. The width of a manganese depletion zone under these conditions would be 0.35–3.5 μm, if all manganese in the MnS inclusion with sizes of 0.01–0.1 μm is based on the matrix around the inclusion.

It has been shown that manganese atoms from steel matrices are absorbed into Ti_2O_3 inclusions by occupying the cation vacancies in Ti_2O_3 (Fig. 7). Precipitation of TiN lowers the interface energy for the formation of ferrite. In boron steels, diffusion of boron into cation vacancies of Ti_2O_3 provides a boron depleted zone around Ti_2O_3 promoting the intragranular nucleation of ferrite (Yamamoto *et al.* 1996, Shim J-H *et al.* 1999).

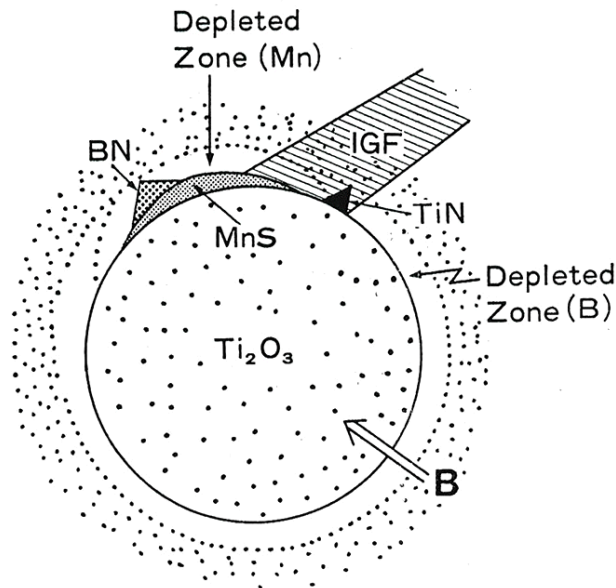


Fig. 7. Schematic illustration for the nucleation of intragranular acicular ferrite around Ti_2O_3 (Yamamoto *et al.* 1996).

A similar effect to that seen in relation to manganese is expected for the strong carbide and nitride forming elements such as titanium, niobium and vanadium. By holding at temperatures slightly above the A_{e3} temperature, carbonitride particles will start to precipitate and grow in size. The carbon and nitrogen profiles around the carbide and carbonitride precipitates cause a carbon depletion zone to form in austenite at the carbide interface. A decrease in the carbon content has been believed to increase the transformation temperature by 10–20 °C in this region (Enomoto 1997).

2.4.2 Favourable crystallographic lattice match for the nucleation of ferrite

A small lattice mismatch between inclusions and ferrite is expected to enhance the nucleation of ferrite because of a decrease in the interfacial energy in nucleation. A lattice mismatch is often measured determining a planar misfit between the inclusions or precipitations and ferrite. This lattice mismatch theory was first proposed by Bramfitt (1970). The planar misfits between the usual intragranular ferrite nucleation enhancing inclusions and ferrite are presented in Table 2 (Lee & Pan 1993, Lee & Pan 1995, Ohkita & Horii 1995).

Table 2. Planar misfits between inclusions and ferrite (Ohkita & Horii 1995, Lee & Pan 1995, Lou & Holappa 2001, Thewlis 2001).

Inclusion	Crystal structure	Lattice constant (Å)		Crystallographic relationship	Misfit (%)
		a_0	c_0		
TiN	Cubic (NaCl)	4.24	-	(100) n //(100) α [010] n //[011] α	3.8
TiO	Cubic (NaCl)	4.18	-	(100) n //(100) α [010] n //[011] α	3.0
TiO ₂	Tetragonal (SnO ₂)	4.59	2.96	(001) n //(110) α [010] n //[110] α	8.8
Ti ₂ O ₃	Hexagon.	5.14	13.66	(0001) n //(110) α [1000] n //[110] α	26.8
Al ₂ O ₃	Hexagon.(Cr ₂ O ₃)	4.76	12.99	(0001) n //(111) α [121] n //[110] α	16.0
γ - Al ₂ O ₃	Cubic	7.85	-	(100) n //(100) α [110] n //[110] α	3.2
SiO ₂	Hexagon.	4.91	5.45	(0001) n //(111) α [001] n //[110] α	21.0
MnOAl ₂ O ₃ Galaxite	Cubic (spinel)	8.27	-	(100) n //(100) α [110] n //[100] α	1.8
MnS	Cubic	5.23	-	(111) n //(111) α [110] n //[110] α	8.8
CuS	-	5.57	-	(111) n //(111) α [110] n //[110] α	2.8
CeS	Cubic	5.78	-	-	-
Ce ₃ S ₄	Cubic	8.37	-	-	-
La ₂ S ₃	Cubic	8.77	-	-	-
VN	Cubic (NaCl)	4.07	-	(100) n //(100) α [010] n //[011] α	0.7

There are a lot of differences among different research papers concerning the values of the lattice constants and misfits. According to Tomita *et al.* (1994) the lowest lattice misfits (1.1% and 1.3%) were found for VC and VN respectively and the highest (27.8%)

for MnS. On the other hand, vanadium nitride has a lattice misfit of 20% with austenite (Enomoto 1997). Díaz-Fuentes *et al.* (1998), Madariaga *et al.* (1998) and Díaz-Fuentes *et al.* (2000) have shown that the precipitation of the hexagonal CuS phase (*c/a* ratio 4.32) on the surface of the inclusions, with its base plane parallel to the surface of the inclusions, causes a low energy inclusion/ferrite interface. The nucleation of acicular ferrite was a result of a good lattice match with the base plane of the inclusion and the $\{111\}_\alpha$. However, CuS and austenite did not exhibit a low lattice mismatch, even in the most favourable situation when $\{111\}_\gamma$ and $(0001)_{\text{CuS}}$ were parallel.

Ishikawa and Takahashi (1995) observed a relative interfacial energy, R , as a function of lattice parameter ratio, $L.P.R. = a_{\text{ppt}}/a_\alpha$, where a_{ppt} was a lattice constant of precipitates of austenite iron and a_α was a lattice constant of ferrite. The interfacial energy calculation based on the habit planes $(111)_{\text{ppt}}/(110)_\alpha$ for the Kurdjumow-Sachs (K-S) relationship and $(001)_{\text{ppt}}/(001)_\alpha$ for the Baker-Nutting (B-N) relationship showed that the interfacial energy between vanadium nitride and ferrite was small according to this calculation if the B-N relationship held. Finally the precipitates, which were preferable nucleation sites for intragranular acicular ferrite, could develop coherent, low energy interphase boundaries with ferrite in austenite. Yamamoto *et al.* (1996) evaluated the increase of interfacial energy with the nucleation of ferrite of 0.85 J/m^2 at the coherent γ/γ interface, 0.20 J/m^2 at the semicoherent α/γ interface and 0.15 J/m^2 at the α/TiN interface.

2.4.3 Increased stress-strain fields around the inclusion

Differences in thermal expansion coefficients between inclusions and austenite can cause increased stress-strain fields around the inclusions. Ohkita and Horii (1995), Lee and Pan (1995) and Zhang and Farrar (1996) evaluated that $2 \text{ MnO} \cdot 2 \text{ Al}_2\text{O}_3 \cdot 5 \text{ SiO}_2$ inclusions were more favourable compared with, for example, TiO , TiO_2 , Al_2O_3 , MnOSiO_2 and MnS inclusions due to the largest thermal expansion difference with respect to austenite. Another possible factor is the increased arrays of dislocations around the inclusions. The dislocation structure may provide additional sites for ferrite nucleation and reduce the energy barrier for nucleation by reducing the total strain energy. (Thewlis 1994, Zhang & Farrar 1996, Enomoto 1997, Haaland *et al.* 1997.)

Enomoto (1997) evaluated that the strain energy around the inclusion may be insignificant compared to the chemical driving force unless nucleation occurs within $\sim 50^\circ\text{C}$ below A_{e3} temperature for an Fe-0.1 mass% C-1.5 mass% Mn alloy. Therefore, the strain energy might become significant for steels which have a low transformation temperature A_{f3} . Because the influence of the strain energy around the inclusion on the ferrite nucleation is low compared to the chemical driving force for ferrite nucleation, the stress-strain fields around the inclusions seem to be insignificant in the nucleation of acicular ferrite. This opinion is supported by the fact that the stress-strain field between MnS and austenite is low (Zhang & Farrar 1996, Haaland *et al.* 1997).

2.4.4 Reduction of the nucleation free energy barrier for the ferrite embryo

The nucleation of ferrite at inclusions is energetically more favourable than homogenous nucleation, but significantly less favourable than nucleation at grain boundaries. Thus, the reduction of a free energy barrier for nucleation follows the classical heterogenous nucleation theory (Zhang & Farrar 1996).

The intragranular nucleation of acicular ferrite on small inclusions within the displacive region of CCT diagram (Fig. 2) and the evidences concerning the limitations of the sizes (0.3–0.9 μm) of the preferable inclusions for the intragranular nucleation of ferrite, indicate a reduction of free energy caused by the nucleation of ferrite on inclusions. It has also been postulated that the intragranular nucleation of ferrite involves a manganese depletion at interface of MnS and inclusions and (V,Ti)(C,N) precipitations generating a dislocation substructure enhanced by deformation below T_{NR} temperature or a low lattice misfit between VN and ferrite (Furuhara & Maki 2000, Zhao & Boyd 2000).

2.4.5 Summary of paragraph 2.4

In summary, local variations in the chemical composition around inclusions, and a favourable lattice match for the nucleation of ferrite, are mostly accepted mechanism for the formation of acicular ferrite, although a measurement of very narrow depletion zones (≤ 500 nm) is very difficult to investigate. However, a manganese depletion around the inclusions in austenite grains as a result of formation of MnS and galaxite (MnOAl_2O_3) and absorbed manganese atoms into Ti_2O_3 inclusions by occupying the cation vacancies in Ti_2O_3 , is believed to increase the austenite-ferrite transformation temperature by over 10°C , when the intragranular nucleation of ferrite is possible instead of the intergranular nucleation of grain boundary ferrite and ferrite side plates. In several research works low lattice misfits of VC, VN and TiN and ferrite are also evidenced by promotion of the nucleation of acicular ferrite on them. Increased stress-strain fields around inclusions as a result of differences in the thermal expansion coefficient between the inclusion and austenite and a reduction of the free energy barrier for the nucleation of ferrite embryos are also suggested mechanisms from which the latter is evidenced by evaluations of the size of the inclusions. Most likely, the formation of acicular ferrite is caused by a combination of the mechanisms presented in this paragraph and enhanced by a deformation below T_{NR} temperature.

2.5 Factors affecting the nucleation of acicular ferrite

Many metallurgical factors in steelmaking and welding have a significant influence on the intragranular nucleation of acicular ferrite. The most important of these are the chemical composition of steel, the austenitization temperature, the austenite grain size, the type of hot deformation, the cooling rate and the finish cooling temperature.

2.5.1 Chemical composition of steel

The alloying elements of steel have a basic importance for the formation of acicular ferrite. In general their influence is threefold. Firstly, elements like titanium, aluminium, oxygen, nitrogen, manganese, sulphur and carbon affect the inclusions and factors, which contribute the nucleation of acicular ferrite on them. Secondly, elements like boron, niobium, aluminium and rare earth metals affect the nucleation site and growth of ferrite. Thirdly, elements like carbon, manganese, nickel and molybdenum, which decrease the austenite-ferrite transformation temperature subsequently enhancing intragranular nucleation of ferrite.

2.5.1.1 Titanium and oxides

The favourable effect of titanium oxide inclusions and titanium nitride precipitations on the nucleation of acicular ferrite has been evidenced in the previous paragraphs. Titanium oxides are normally more significant than titanium nitrides because of their superior thermodynamic stability assumed on the basis of the free energy change of formation, although they form later than titanium nitrides (Bhadeshia & Svensson 1993).



where ΔG° is the standard free energy of the formation of TiO_2 and TiN . Thus, the standard free energy of formation of TiO_2 is about 2.5 times larger than that of TiN at temperatures between 1000 and 1500 °C being similar as formation of Ti_2O_3 and TiN (2.1–2.4) (Homma *et al.* 1987).

The amount and the structure of nonmetallic oxide inclusions depend on the oxygen content of steel, which is normally less than 50 ppm in extremely low and low oxygen weld metals (EB, laser and TIG) less than 80 ppm in killed steel plates and even 200–800 ppm in the intermediate and higher oxygen weld metals (SMAW, GMAW and SAW). The oxygen content of steel has been found to influence the size and amount of the effective inclusions and the type of inclusions, as presented in paragraph 2.3.1–2.3.2 (Zhang & Farrar 1996, Ohara & Wallach 1999).

The formation of titanium oxides depends on the aluminium content in steel, because oxygen first binds with aluminium and then combines with titanium. Titanium oxide inclusions Ti_2O_3 and TiO_2 have been found in the low oxygen weld metals and MnOTiO_2 and MnOTi_2O_3 in the higher oxygen steels. In the low oxygen autogenous laser welds the formation of titanium oxide was possible, when the aluminium content is very low (<0.005%) (Cochrane & Senogles 1994, Gladman & Senogles 1994). The Acicular ferritic microstructure, for example in EB weld metals, has been found even in an oxygen content as low as 10 ppm, when the aluminium content in EB weld metals is restricted to

unusually low levels (from 0.003 to 0.009%) (Ohkita & Hori 1995, Ohara & Wallach 1999).

The role of titanium nitrides in the intragranular nucleation of ferrite is unclear. On one hand, titanium nitrides precipitated in a solid state are ineffective for the intragranular nucleation of ferrite due to their susceptibility to preventing austenite grain coarsening and their too small size ($<0.2 \mu\text{m}$) for preferable intragranular nucleation sites. On the other hand, titanium nitrides can contribute the intragranular nucleation of ferrite due to small lattice misfit between TiN and ferrite and formation of TiN-MnS complex precipitates for preferable nucleation sites (Tomita *et al.* 1994, Yamamoto *et al.* 1996).

2.5.1.2 Aluminium and oxides

Recent studies have shown that variations in the Al/O ratio have considerably influenced the formation of acicular ferrite. The optimum Al/O ratio would be about 0.6, and should not exceed unity due to a decrease in the amount of acicular ferrite and impact toughness. The maximum Al/O ratio of unity is valid in the extremely low and low oxygen weld metals (EB, laser, TIG), but in the intermediate and higher oxygen weld metals (SMAW, GMAW, SAW) the Al/O ratio of 1–1.2 is allowed without a decrease in the amount of acicular ferrite. When the Al/O ratio exceeds unity, the content of soluble aluminium is increased during austenite-ferrite transformation causing an aluminium concentration spike to build up in the austenite at the γ/α interface, which is believed to restrict carbon diffusion or to reject extra carbon into austenite retarding ferrite transformation. On cooling below bainite start temperature B_s , Widmanstätten ferrite and bainite laths grow rapidly from the austenite grain boundaries. It has also been presented that upper bainite is formed at high aluminium contents due to a stronger affinity of aluminium to oxygen than titanium and boron, when soluble titanium and boron increase followed by an increase in hardenability and a decrease of titanium oxide for the formation of acicular ferrite (Bhadeshia & Svensson 1993, Cochrane & Senogles 1994, Thewlis 1994, Francis-Scrutton 1995a, Francis-Scrutton 1995b, Ohkita & Hori 1995, Matsuda *et al.* 1996, Zhang & Farrar 1996, Koseki *et al.* 1997).

The presence of low levels of titanium (about 10–20 ppm) is found to be beneficial in preventing the deleterious effect of aluminium by refining microstructure. In steel, higher titanium contents (about 0.04%) and high aluminium and titanium contents simultaneously, can decrease the amount of acicular ferrite and increase the amount of Widmanstätten ferrite or upper bainite in microstructure as a result of increased soluble titanium (Francis-Scrutton 1995a, Francis-Scrutton 1995b and Ohkita & Hori 1995).

2.5.1.3 Sulphur

In several research works sulphur has been demonstrated to enhance intragranular nucleation of acicular ferrite by forming MnS on oxide inclusions during solid-state transformation over a temperature range of 1400–1050 °C, although the opposite opinions have also been presented in some investigations, for example Bhadeshia and

Svensson (1993). With increasing sulphur content, the size and density of inclusions increases and the inclusion phases change from predominantly oxides to oxysulfides and MnS. The formation of MnS on the oxide inclusions is believed to enhance the formation of a manganese depleted zone around the inclusion, increasing the driving energy for ferrite nucleation (Tomita *et al.* 1994, Mabuchi *et al.* 1996, Yamamoto *et al.* 1996, Haaland *et al.* 1997).

According to the research work of Tomita *et al.* (1994) concerning the TiN-MnS complex precipitates, MnS decreased the interfacial energy for nucleation due to the increase of the particle size or crystal coherency between TiN and ferrite. In low sulphur content (0.001%) steel many small TiN precipitates (0.01–0.1 μm) were found, but increasing the sulphur content by 0.003–0.004%, the particle size was increased 0.1–0.3 μm achieving the effective size (0.3–0.9 μm) for the nucleation of acicular ferrite in greater sulphur contents. When the sulphur content increased to 0.008%, the precipitates were coarsened up to 1 μm and increasing the size of the TiN-MnS complex precipitates decreased their number. Thus, the optimum sulphur contents of 0.003–0.008% stated on the basis of the HAZ toughness can be explained according to this nucleation mechanism.

Lee and Pan (1993) and Lee and Pan (1995) reported that the highest volume fraction of intragranular acicular ferrite and HAZ toughness was achieved at a higher sulphur content (102 ppm) than in the previous research works, whereas in calcium added steels the highest volume fraction was achieved at a sulphur content of 48 ppm due to the increased density and size of the inclusions caused by calcium addition in steel. The beneficial influence of the calcium addition in steel is based on the increase of the relative nucleation potential of intragranular acicular ferrite. In cerium added steels the optimum number density of inclusions was achieved with around 0.07% retained cerium corresponding with the region of 0.017% S according to stoichiometric sulphur contents of CeS and Ce₃S₄ (Thewlis 2001).

Díaz-Fuentes *et al.* (1998), Madariaga *et al.* (1998) and Díaz-Fuentes *et al.* (2000) observed that acicular ferrite nucleated on MnS inclusions covered with hexagonal CuS (with a c-axis about 4.5 times larger than lattice parameter of the austenite fcc lattice). The good lattice matching between ferrite and the hexagonal CuS phase adjusts the formation of low energy ferrite/inclusion interfaces aiding transformation.

2.5.1.4 Nitrogen

Free nitrogen in steel has a deleterious influence on toughness, increasing strain ageing and hardening of steel. In titanium-boron weld metals an increase in grain boundary ferrite with an increasing nitrogen content was found to decrease low temperature toughness (Matsuda *et al.* 1996). So, it is useful to bind nitrogen to niobium, vanadium, titanium and aluminium nitrides and niobium and titanium carbonitrides. In vanadium microalloyed steels, nitrogen is found to enhance the formation of a fine ferrite intragranularly nucleated ferritic microstructure due to vanadium nitrides, which have a low lattice misfit with ferrite. In addition, precipitation of vanadium carbides and nitrides enhance the intragranular nucleation of ferrite on precipitates due the formation of a

carbon and nitrogen depletion zone around the precipitates (Enomoto 1997, Kimura *et al.* 1997).

2.5.1.5 Niobium

Niobium microalloying of steel has been observed to increase the A_{r3} temperature of deformed austenite by about 10 °C, when the niobium content increases 0.01% due to the increase of Nb(CN) precipitates, which are suitable nucleation sites for ferrite. On the other hand, niobium has been found to slow the austenite-ferrite transformation due to a segregation of the niobium austenite-ferrite interface, which prevents the formation of ferrite. The ultralow niobium content up to 0.003% can prevent coarsening of primary grain boundary ferrite and enhance the formation of acicular ferrite. Higher niobium contents and a segregation of niobium to the high manganese areas promote the formation of upper bainite. The influence of niobium on the austenite-ferrite transformation is decreased by increasing the cooling rate. In titanium killed steels a niobium content of 0.01% has not been found to influence the nucleation of intragranular ferrite or a decrease of grain boundary ferrite, but the addition of the same amount of niobium to titanium microalloyed steel prevented almost all formation of it and induced the formation of coarse ferrite side plate microstructure (Yamamoto *et al.* 1989, Tomita *et al.* 1994, Manohar *et al.* 1996).

2.5.1.6 Vanadium

Vanadium microalloying (about 0.05%) of steel has been found to reduce colony size of bainite and to promote the formation of both a polygonal ferrite along austenite grain boundaries in the CGHAZ and acicular ferritic microstructure in the ICCGHAZ (Li *et al.* 2000). The addition of vanadium in an amount more than 0.1% has been found to increase vanadium segregation at the prior austenite grain boundaries preventing the formation of grain boundary ferrite and enhancing the formation of acicular ferrite. Thus, acicular ferrite content was found to increase from 50% to 80%, when the vanadium content increased from 0.1% to 0.25% (He & Edmonds 2000, He & Edmonds 2002). But the influence of vanadium on ferrite morphology tended to vary with the alloy content of steel.

The enhancement of the intragranular nucleation of ferrite due to the precipitation of VN has been demonstrated in many research works. Precipitation begins after the formation of VN at 700 °C and the precipitates continue to grow in size during cooling. They reach a sufficient size for the nucleation of ferrite between 650–600 °C. This nucleation of ferrite on VN precipitates refines ferrite grains remarkably, which has been utilised particularly in TMCP steels (Kimura *et al.* 1997).

The mechanism of the intragranular nucleation of ferrite on vanadium nitrides has been investigated in medium carbon steels. The small lattice mismatch of the interface between vanadium nitride and ferrite (Table 2) enhances the nucleation of intragranular ferrite plates due to a low energy interface between ferrite and the precipitate. Thus, the

presence of vanadium nitride precipitates can cause coherent low energy interphase boundaries to develop with ferrite in austenite (Ishikawa & Takahashi 1995).

2.5.1.7 Manganese, nickel and carbon

Manganese and nickel in steels decrease the austenite-ferrite transformation temperature of A_{r3} , which promotes the formation of intragranular acicular ferrite in addition to the positive influence of manganese on oxide and sulphide inclusions. Increasing the cooling rate decreases the austenite-ferrite transformation temperature and the duration of transformation (Manohar & Chandra 1997). According to Shim *et al.* (1999) the 95% volume fraction of acicular ferrite was achieved when the manganese content was about 2.5%. Ohkita and Horii (1995) reported that the microstructure mainly consisted of acicular ferrite with manganese contents of 1.4–1.8%, but the formation hardly occurred with less than 1.0%. Furthermore, acicular ferrite is refined by an increase in manganese content. Zhang and Farrar (1997) observed that the highest impact toughness in C-Mn-Ni weld metals was obtained with the contents of 1.6% Mn–1.0% Ni and 0.7% Mn–2.5 to 3.5% Ni, when the microstructure consisted of 50–75% acicular ferrite. However, a further increase of manganese and nickel contents decreased the toughness of weld metals due to the formation of martensite, the coarsened columnar grains, segregation structures and possible inherited structure in the reheated regions.

It is well known that carbon enhances the intragranular nucleation of acicular ferrite in steel decreasing the austenite-ferrite transformation temperature of A_{r3} , which prevents the formation of the primary grain boundary and Widmannstätten ferrite. In addition, the formation of carbide and carbonitride precipitates causes the formation of a carbon depleted zone around the precipitates to enhance the nucleation of acicular ferrite, as presented in paragraph 2.4.1 (Bhadeshia & Svensson 1993, Enomoto 1997). On the contrary, austenite grain size decreases with carbon content, which promotes intergranular transformation (Ohkita & Horii 1995).

2.5.1.8 Silicon

High silicon content in titanium containing steels was found to suppress the formation of acicular ferrite due to the deoxidization effect of silicon in molten steel, which decreases the absorbed manganese content in Ti_2O_3 inclusions followed by the insufficient development of a manganese depleted zone around Ti_2O_3 inclusions (Shim *et al.* 2001). Manohar and Chandra (1998) found that the high silicon content in steel promotes the formation of grain boundary ferrite, decreases the driving force for sympathetic nucleation of ferrite and increases of the carbon activity in austenite hindering the precipitation and diffusion controlled growth of ferrite. All of these conditions have a detrimental effect on the formation of acicular ferrite.

2.5.1.9 Molybdenum and chromium

The addition of 0.2–0.3% molybdenum in the weld metals is generally found to suppress the formation of grain boundary ferrite and to promote the formation of acicular ferrite in microstructure. This beneficial effect of molybdenum is based on a decrease of the austenite-ferrite transformation temperature and the enhancement of a displacive nucleation of ferrite instead of reconstructive nucleation on inclusions (Ohkita & Horii 1995, Thewlis *et al.* 1997). Zhang and Farrar (1996) observed that adding 0.25% Mo increased the amount of acicular ferrite by 10–16%.

The volume fraction of acicular ferrite in the weld metals has increased when the chromium and molybdenum content is increased to 1.0% and 0.5% respectively. At higher concentrations the columnar austenite grains of weld deposits transforms into bainite instead of acicular ferrite. Then bainite grows in the form of classical sheaves from the austenite grain boundaries. Probably, decreasing primary grain boundary ferrite while increasing the alloying of manganese, nickel, molybdenum and chromium, the austenite grain boundaries become free to nucleate bainite (Bhadeshia & Svensson 1993).

2.5.1.10 Boron

The significant beneficial influence of boron on the intragranular nucleation of acicular ferrite has been utilised for a long time in the weld metals due to the ability of soluble boron to retard the nucleation of primary grain boundary ferrite and to lower the austenite-ferrite transformation temperature. The effect of boron on the intragranular nucleation of acicular ferrite depends on the boron content and austenite grain size. At finer grain sizes significantly greater levels of soluble boron are required to achieve acicular ferritic microstructure because of the increased need of boron atoms to saturate a larger grain boundary surface area. A volume fraction of 80% acicular ferrite at 30 μm austenite grain size could be achieved with soluble boron levels between 0.0022 and 0.0028%, whereas at 120 μm austenite grain size with soluble boron levels between 0.0016–0.0022% was required (Fig. 8) (Thewlis 1994).

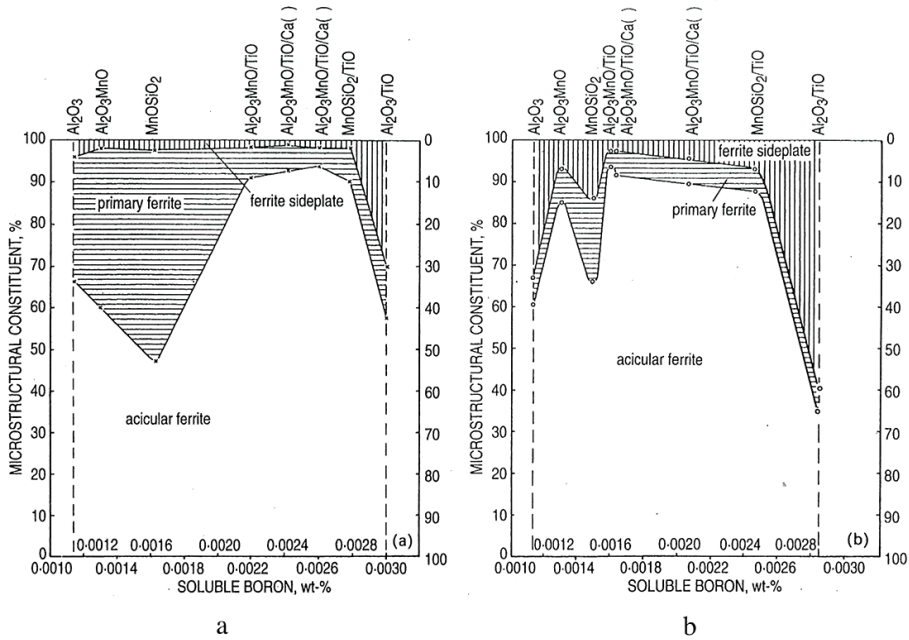


Fig. 8. Relationship between types of ferrite and inclusions and soluble boron content of weld metals having 30 μm (a) and 120 μm (b) austenite grain sizes (Thewlis 1994).

Boron in the weld metals is often used with titanium, which has a significant influence on the nucleation of acicular ferrite. Evans (1996) observed, according to his systematic evaluations, that the maximum amount of acicular ferrite in weld metals (aluminium, niobium and vanadium < 5 ppm) is achieved with titanium and boron levels of 250–400 ppm and 40–50 ppm respectively. Nitrogen and boron in steel can form boron nitrides, which decreases free boron and nitrogen contents in steel. An excess of boron in steel can also combine with carbon to form boron carbides or to increase soluble boron, which are detrimental for toughness (Bhadeshia & Svensson 1993).

Yamamoto *et al.* (1996) found that boron cannot retard the nucleation of ferrite around titanium oxide inclusions due to the formation of a boron depleted zone around the inclusions caused by the diffusion of boron into titanium oxide via cation vacancies.

2.5.1.11 Rare earth elements

The addition of rare earth elements, such as cerium and lanthanum, has been evidenced to enhance intragranular nucleation of acicular ferrite. This is due to the formation of the suitable sulphide and oxide inclusions, such as (La, Ce)₂O₃, CeS, Ce₂S₄ and La₂S₃, for the nucleation sites of acicular ferrite, as presented in paragraph 2.3.1. The suitable cerium content for the formation of cerium sulphides for the intragranular nucleation of acicular ferrite was demonstrated to be between 0.04% and 0.20% (Lou & Holappa 2001, Thewlis

2001). Besides this favourable effect of cerium sulphide inclusions, the addition of rare earth elements (cerium, neodymium, lanthanum and yttrium) in steel is believed to retard the formation of primary grain boundary ferrite involving segregation to the austenite grain boundaries. A mechanism similar to that used to examine boron has been focused on to explain the effect of cerium addition up to an amount of 0.15%. According to these investigations, cerium and boron retard the formation of primary grain boundary ferrite to a much greater extent than the formation of bainite. The effect of cerium is reduced drastically if the phosphorus content of steel exceeds 0.02%. The influence of other rare earth elements and their influencing mechanisms requires further investigations (Bhadeshia & Svensson 1993).

2.5.2 Austenitizing temperature and austenite grain size

A high austenitizing temperature enhances the intragranular nucleation of acicular ferrite due to the increase of the austenite grain size followed by a decrease of the most favourable nucleation corners and grain boundary sites. In addition, the large austenite grain size decreases the austenite-ferrite transformation temperature. If the grain size is not large enough, austenite transforms mainly to grain boundary ferrite, ferrite side plates and bainite.

The influence of the austenite grain size on the nucleation of acicular ferrite also depends on a volume fraction of the favourable inclusions in steel, the chemical composition of steel, a hot forming, a cooling rate and a finish cooling temperature. Lee and Pan (1991) reported that in titanium killed steels the existence of titanium oxides and the austenite grain sizes larger than 50 μm at peak temperatures higher than 1200 $^{\circ}\text{C}$, provided a favourable condition for the formation of intragranular ferrite. However, in aluminium killed steel bainite was a dominant microstructure. Zhang and Farrar (1996) evaluated that the amount of acicular ferrite increased notably in weld metals when the austenite grain size increased from 30 μm to 80 μm . However, a further increase of the austenite grain size up to 200 μm had no influence on the amount of acicular ferrite. Anelli *et al.* (2002) observed that the formation of significant amounts of acicular ferrite in titanium killed plates, with the number densities of favourable inclusions at about 200 particles/ mm^2 , was only possible if the austenite grain size was larger than about 100 μm .

As was presented in paragraph 2.5.1, the boron and manganese contents of steels in particular control the intragranular and grain boundary nucleation of ferrite. The minimum austenite grain size for the nucleation of acicular ferrite in weld metal was about 50–60 μm using a low boron content and about 20 μm using a high boron content (Thewlis 1994). In a Ti-B-Mo alloyed weld metal a very high fraction of acicular ferrite (96.4–99.5%) was achieved when the austenite grain sizes were between 30 and 124 μm (Thewlis 2000). In a 2.5% Mn contained wrought steel, an acicular ferritic microstructure of 95% was achieved after deformation of 50% at 1150 $^{\circ}\text{C}$, when austenite grain size was about 80 μm , but it was rarely observed after deformation of the same steel at temperatures less than 950 $^{\circ}\text{C}$, since the prior austenite grain size was too small to suppress the formation of intergranular ferrite (Shim *et al.* 2000). In cerium contained steel, 60% acicular ferrite was achieved on an austenite grain size of 84 μm , whereas in

conventional base steel without cerium addition, the same amount of acicular ferrite was achieved on an austenite grain size of $122\ \mu\text{m}$ (Thewlis 2001). It has been presented that the maximum austenite grain size affecting the nucleation of acicular ferrite was $140\text{--}200\ \mu\text{m}$, which also includes the evaluation of the austenite grain sizes of $180\text{--}190\ \mu\text{m}$ based on the highest nucleation potential of ferrite (Shim *et al.* 2000, Lee & Pan 1995).

In Figures 9 and 10 Barbaro *et al.* (1989) presented that in the weld metal deposits the amount of acicular ferrite was over 60% in the HAZ, when the austenite grain size was in the range of $40\text{--}100\ \mu\text{m}$ with a cooling time $t_{8/5}=4\ \text{s}$. With longer cooling times the amount of acicular ferrite was over 60%, when austenite grain size exceeded $100\ \mu\text{m}$.

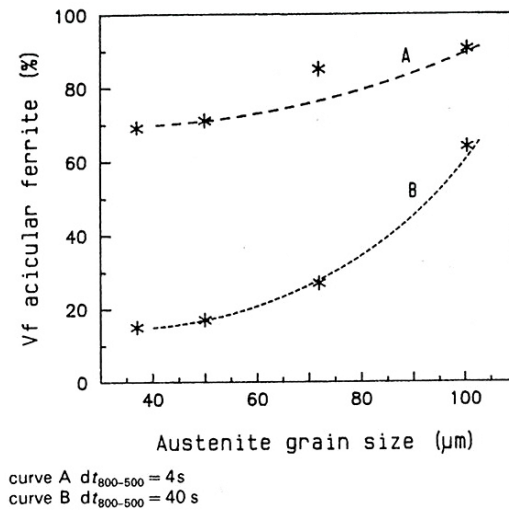


Fig. 9. Effect of austenite grain size on the formation of acicular ferrite (Barbaro *et al.* 1989).

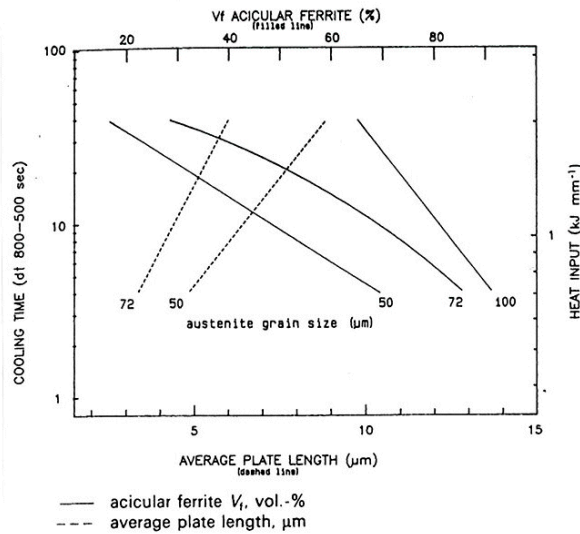


Fig. 10. Effect of weld heat input on the amount and plate size of acicular ferrite (Barbaro *et al.* 1989).

According to Figures 9 and 10 the larger austenite grain size increases the amount of acicular ferrite and decreases the average lath length of it. On this basis, the larger austenite grain size promotes the formation of more and finer acicular ferrite.

2.5.3 Hot deformation

A hot deformation is expected to decrease the formation of acicular ferrite due to a reduction of the prior austenite grain size, as was previously stated in paragraph 2.5.2. Many research works have provided evidence that a hot deformation raises austenite-ferrite transformation temperature and delays the transformation during the final 30% of the transformation temperature range. This enhances the formation of grain boundary ferrite, polygonal ferrite, bainite and acicular ferrite with M-A constituents (Manochar & Chandra 1998).

However, acicular ferritic microstructure was obtained in 2–2.5% Mn wrought steel after 50% hot deformation at temperatures of 1050–1150 °C, but was not believed to be obtained in the conventional production of plates and strips, since the finishing rolling temperatures are normally under 950 °C and deformation is limited (Shim J-D *et al.* 1999, Shim *et al.* 2000). In the recent research works of ultrafine grained TMCP steels, acicular ferritic microstructure was obtained after a strong deformation ($\epsilon_F \sim 0.5$) below the austenite recrystallization temperature caused by an increased density of deformation bands for the intragranular nucleation sites and increasing thermodynamic driving forces for the intragranular nucleation of ferrite (Yakubtsov & Boyd 2001, Yakubtsov *et al.* 2004). Austenite deformation below its recrystallization temperature has been found to

enhance the ferrite nucleation at inclusions in medium carbon, titanium and vanadium steel (Zhao & Boyd 2000). However, only a slight (10–30%) hot deformation of austenite has also been observed to enhance ferrite and pearlite nucleation in high sulphur, vanadium and nitrogen steels contained MnS+V(C,N) complex precipitates (Furuhara & Maki 2000). Recent research work on TMCP steel (0.076%C–0.24%Si–1.33%Mn–0.014%P–0.0032%S–0.03%Al–0.0048%N–0.04%Nb–0.02%Ti–0.04%V) has evidenced that the dominated acicular ferritic microstructure could be achieved by a two stage controlled rolling in the austenite recrystallization region plus the non-recrystallization region followed by a controlled cooling at a rate of 30 °C/s (Zhao *et al.* 2003).

2.5.4 Cooling rate and finish cooling temperature

The intragranular nucleation of acicular ferrite in titanium killed steels was possible to obtain in a wide cooling rate range of 0.3–54 °C/s ($t_{8/5}$ =1000–5.6 s) according to (Fig. 11) Yamamoto *et al.* (1989) likewise at cooling rates 0.3–50°C/s ($t_{8/5}$ =1000–6 s) according to Chijiwa *et al.* (1988), Terada *et al.* (1992) and Yoshida *et al.* (1998). However, Barbaro *et al.* (1989) proposed shorter cooling times $t_{8/5}$ = 40–4 s. In conventional hot rolling and controlled rolling processes acicular ferrite microstructure was achieved in a low carbon wrought steel at relatively slow cooling rates 1–30 °C/s and mainly at cooling rates 1–10 °C/s. This range depends on, for example, the chemical composition of steel and a hot deformation before cooling (Shim J-D *et al.* 1999). Yakubtsov *et al.* (2004) proposed that intragranularly nucleated bainitic (acicular ferrite) microstructure is achieved with an industrially-realistic processing schedule at a cooling rate of 25 °C/s. According to Zhao *et al.* (2003) the dominated acicular ferritic microstructure in TMCP plates, mentioned previously in paragraph 2.5.3, was achieved at cooling rates of 1–10 °C/s without a hot deformation and at cooling rates of 10–30 °C/s after a two stage hot deformation.

Yamamoto *et al.* (1989) found that a density of acicular ferrite in the simulated CGHAZ increased to a cooling time $t_{8/5}$ =30 s, but decreased at larger cooling times of $t_{8/5}$, due to the formation of grain boundary and Widmannstätten ferrite. At the same time, the length of acicular ferrite laths (IFPII) increased. However, acicular ferrite was formed in the HAZ of titanium killed steels even at a high cooling time $t_{8/5}$ = 161 s, whereas Widmannstätten ferrite dominated in the microstructure of the HAZ of aluminium killed steels at the same cooling time of $t_{8/5}$. The density of acicular ferrite was greater and the length of the ferrite laths shorter in a titanium killed steel than in an aluminium killed steel. At the same time, the length of ferrite side plates in an aluminium killed steel increased when the cooling time increased, but it stopped growing in a titanium killed steel when the cooling time $t_{8/5}$ exceeded 30 s.

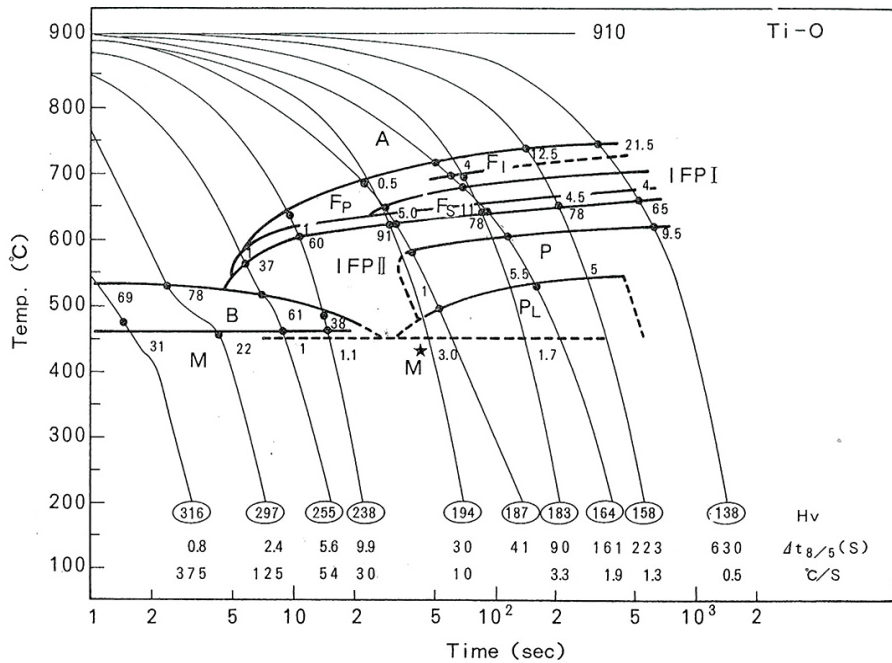


Fig. 11. CCT curves of a Ti killed steel (heating temperature 1400 °C (Yamamoto *et al.* 1989) (F_p = grain boundary ferrite, F₁ = polygonal ferrite, IFPI = acicular ferrite, type I, IFPII = acicular ferrite, type II, P = pearlite, P_L = degenerated pearlite, B = bainite and M = martensite).

A finish cooling temperature for the formation of a significant amount of acicular ferrite was reported to be between 480 and 630 °C, but a peak rate transformation temperature of between 500 and 625 °C has been demonstrated. The upper end of this range coincides with the onset of a displacive transformation and the lower end for the formation of ferrite side plate and bainite. In the weld metals the upper end of a displacive transformation of 630 °C and the maximum rate of transformation at temperatures 515–610 °C was found depending on the chemical composition and a cooling rate. Accordingly, the maximum rate of transformation temperatures are 40–70 °C above the theoretical and experimentally observed bainite start temperatures, when significant amounts of ferrite side plates are in acicular ferrite (Thewlis *et al.* 1997, Thewlis 2000, Thewlis 2001). In titanium killed TMCP steel, intragranularly nucleated ferrite begins to form at about 630 °C and its formation is completed at about 480 °C at cooling rates 5–10 °C/s (Fig. 11) (Chijiwa *et al.* 1988, Yamamoto *et al.* 1989, Yoshida *et al.* 1998). However, even at temperatures of 200 °C and 400 °C was proposed for ultrafine bainitic steels (Yakubtsov & Boyd 2001, Yakubtsov *et al.* 2004).

2.5.5 Summary of paragraph 2.5

In summary, the chemical composition of steel, the austenite grain size and a cooling rate are the main factors completed by a hot deformation and a finish cooling temperature affecting the nucleation of acicular ferrite. Elements like titanium, aluminium, oxygen, nitrogen, manganese, sulphur and carbon significantly affect the nucleation of ferrite on inclusions in addition to the type, size and distribution of inclusions. It is possible to achieve intragranular nucleation of acicular ferrite even in the extremely low oxygen weld metals (EB), when the maximum Al/O ratio is unity. A minimum austenite grain size for nucleation of acicular ferrite in the weld metals is 50–60 μm and 80–140 μm in the base plates and the HAZ, where the highest nucleation potential was achieved with austenite grain sizes of 180–190 μm . Elements like carbon, manganese, nickel and molybdenum enhance austenite grain coarsening, therefore decreasing the austenite-ferrite transformation temperature. When a soluble boron content of steel is between 0.0016–0.0022%, a volume fraction of 80% acicular ferrite microstructure is achieved with the austenite grain size of 30 μm . A hot deformation in plate and strip rolling and titanium microalloying of steel decrease the austenite grain size diminishing the intragranular nucleation of ferrite despite a favourable cooling rate of 0.3–54 $^{\circ}\text{C}/\text{s}$. It is possible to achieve acicular ferritic microstructure in the weld HAZ in a wide heat input range with cooling times $t_{8/5}=4\text{--}1000$ s being maximum, with a cooling time $t_{8/5}=30$ s. Finish cooling temperatures for the formation of a significant amount of acicular ferrite has been reported to be between 480 and 630 $^{\circ}\text{C}$ at cooling rates of 5–10 $^{\circ}\text{C}/\text{s}$.

3 Influence of acicular ferrite, M-A constituents and the effective grain and packet sizes on the toughness of the HAZ

It is desirable to provide microstructure in steel including acicular ferrite with minimal primary grain boundary ferrite and ferrite side plates. The significant improvement of toughness with increasing acicular ferrite content is attributed by the chaotic arrangement of fine ferrite laths. It is generally believed that the acicular ferrite content of 80–90% in the as-deposited weld metal is necessary to obtain satisfactory toughness at low temperatures, i.e. –50 to –60 °C. On the other hand, the best combination of properties of low alloy weld metals has been found to be obtained when there was 50–75% acicular ferrite with other proeutectoid ferrite. Only 50% acicular ferrite has been found to improve toughness significantly (Svensson & Gretoft 1990, Zhang & Farrar 1997). Grong (1994) evaluated that a volume fraction of acicular ferrite in weld metal beyond 25 vol% will generally be sufficient to meet the impact toughness requirement of 35 J at –40 °C. Increasing the acicular ferrite content from 25% to 70% decreased the 35 J transition temperature by about 25 °C (Fig. 12).

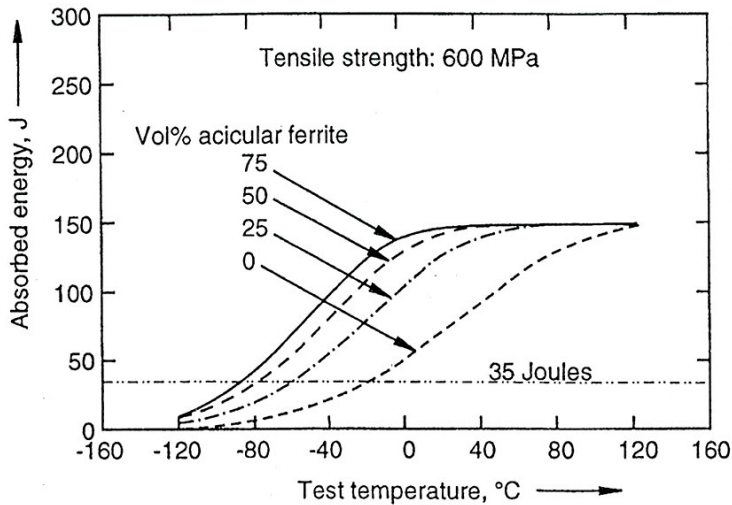


Fig. 12. Influence of weld metal acicular ferrite content on Charpy V impact toughness transition curves (Grong 1994).

An optimum microstructural combination regarding the toughness of the HAZ is dominated by acicular ferrite with evenly dispersed M-A constituents between acicular ferrite plates rather than the highest level of acicular ferrite. In addition to acicular ferrite, the toughness of the HAZ depends on the amount, type and distribution of M-A constituents due to their formation in the intercritical heating of the previous weld bead (ICCGHAZ) and the base plate (ICHAZ). M-A constituents have a fundamental influence on the initiation of cracks, but their influence on the propagation of cracks is unclear. The propagation of cracks is mainly dependent on the effective grain size of ferrite and the packet and lath size (width) of bainite.

3.1 Fracture mechanism of acicular ferrite

3.1.1 Role of acicular ferrite for crack initiation

Acicular ferrite has an indirect influence on crack initiation, which mainly depends on the amount, size and distribution of M-A constituents. A decrease of the ferrite grain size caused by acicular ferrite reduces stress concentration between the M-A/matrix interface due to a decrease a sharpness of M-A constituents as a result of the formation at a higher temperature (about 600 °C) compared to the formation of ferrite side plates (about 560 °C) (Homma *et al.* 1987, Tian 1998). Thus, the formation of M-A constituents is believed to reduce as the austenite-ferrite transformation temperature increases. Chijiwa *et al.* (1988) and Yamamoto *et al.* (1989) evidenced that intragranular nucleation of acicular ferrite prevents the formation and growth of ferrite side plates, refines the effective grain

size and suppress the formation of M-A constituents, which were polygonal in shape between intragranularly nucleated acicular ferrite laths, but needle like between ferrite side plates.

In weld metals, intragranularly nucleated acicular ferrite can improve toughness due to a decrease of grain boundary ferrite, but inclusions with diameters greater than 1–1.5 μm can nucleate cracks (Ricks *et al.* 1982, McRobie & Knott 1985, Tweed & Knott 1987, Grong 1994). However, acicular ferrite nucleates preferentially on the surfaces of the inclusions with diameters of 0.3–0.9 μm , which are not the potential nucleation sites for cracks. But there are no evidences that titanium oxide inclusions with diameters of 2–5 μm enhance nucleation of cracks in titanium killed steels, as calcium aluminate inclusions with diameters of 2–3 μm have been found to nucleate cracks in CTOD tests (Harrison & Hart 1990).

3.1.2 Influence of acicular ferrite on the effective grain and packet size and crack propagation

The crystallographic grains or packets correspond to grains or sets of neighbouring units which have the same crystallographic orientation. In body centred cubic (bcc) iron like acicular ferrite a cleavage fracture is typically propagated along $\{100\}$ planes, which means that the cracks must be deflected at high angle grain or packet boundaries as shown in Figure 13. Gourgues *et al.* (2000) have found that in acicular ferrite nearly all boundaries between acicular ferrite laths were high angle boundaries with misorientation angles greater than 45° .

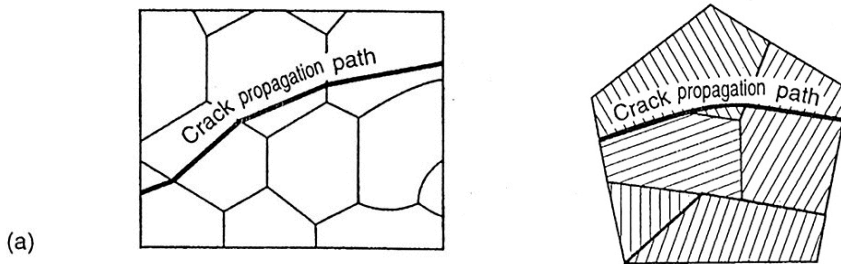


Fig. 13. Schematic illustration showing crack deflection at interfaces: a) high angle ferrite-ferrite grain boundaries and b) high angle packet boundaries (bainitic microstructure) (Grong 1994).

3.1.3 Summary of paragraph 3.1

In summary, acicular ferrite has an indirect influence on crack initiation, which mainly depends on the amount, size and distribution of M-A constituents. The intragranular nucleation of acicular ferrite suppresses the formation of M-A constituents decreasing their sharpness. Thus, they are mainly polygonal in shape reducing a stress concentration between the M-A/matrix interface. Small effective packet sizes and high angle grain boundaries in acicular ferrite laths are the main factors preventing cleavage crack propagation.

3.2 Formation and properties of M-A constituents

In high strength low alloy steels, M-A constituents can form in the coarse grained HAZ (CGHAZ), intercritically reheated coarse grained HAZ (ICCGHAZ) and intercritical HAZ (ICHAZ). During intercritical heating of low carbon microalloyed steel plates, austenite grows rapidly into pearlite until the dissolution process is completed continuing into ferrite at a rate controlled by either carbon diffusion in the austenite or diffusion of substitutional elements (for example manganese) in ferrite (Akselsen *et al.* 1987, Akselsen *et al.* 1988). In intercritical reheating the CGHAZ consisted of upper bainite with a large prior austenite grain size austenite nucleates and grows preferentially along the prior austenite grain boundaries and bainite lath boundaries. These austenite areas become carbon enriched and transformed to hard and brittle M-A constituents during cooling (Davis & King 1993). The formation mechanism, type and properties of M-A constituents depend on the chemical composition and manufacturing of steel and a thermal cycle.

3.2.1 Formation mechanism

The predominant transformation products in carbon rich austenite after cooling are lath and plate martensite and retained austenite. In addition, in the simulated underbead zone of HT 80 and HT 100 QT steels M-A constituents consisted of cementite precipitated from retained austenite and structurally free cementite precipitated from lath martensite during self tempering (Hrivnak *et al.* 1992a). The transformation of martensite is accomplished with the maximum expenditure of strain energy by a homogeneous distortion of austenite. The strain can occur either by slip at higher M_s temperature or twinning at lower M_s temperatures. The relationships between martensite (α') and retained austenite (γ') in M-A constituents were described by Kurdjumow and Sachs as follows (Tian 1998, Hrivnak *et al.* 1992a, Hrivnak *et al.* 1992b):

$$\begin{aligned} & \{111\}_{\gamma'} // \{110\}_{\alpha'} \\ & (111)_{\gamma'} // (110)_{\alpha'} \end{aligned}$$

Retained austenite is situated either inside M-A constituents or between the martensite laths. According to the recent studies in mixed M-A constituents, martensite was located in the centre and retained austenite in the periphery (Lambert *et al.* 2000a). Retained austenite has a lower dislocation density than surrounding ferrite and lath martensite. It has also been evidenced that small M-A constituents (0.5–1.0 μm) do not readily transform into martensite, but remain retained austenite. Thus, the elongated M-A constituents between bainite laths and packets consisted mainly of retained austenite. This is thought to be due to the stabilizing effect of the high carbon content, lack of nucleation sites for martensite and the volume restraint blocking effect of the surrounding matrix. The amount of retained austenite is usually close to 2–8 vol.% in the microstructure and its amount in M-A constituents decreases when the size of M-A constituents increases (Lanzilotto & Pickering 1982, Akselsen *et al.* 1987, Akselsen *et al.* 1988, Hrivnak *et al.* 1992a, Hrivnak *et al.* 1992b, Davis & King 1994, Hrivnak 1995, Tian 1998).

3.2.2 Type and properties of M-A constituents

Two following main types of M-A constituents are classified according to their shape: elongated (or string/rod like) M-A constituents with L (length) to W (width) ratio $L/W > 3$ and massive (or block/polygonal) M-A constituents with an $L/W < 3$. Elongated M-A constituents with approximately 0.2–1 μm in width and several microns in length develop preferentially between ferrite, bainite and martensite laths of the ICCGAZ and in the prior austenite grain boundaries of the CGHAZ in fast cooling ($t_{8/5}=20\text{--}40$ s). Blocky M-A constituents with a diameter of 3–5 μm preferentially form along the prior austenite grain boundaries in the ICCGAZ and between the ferrite laths in the CGHAZ in slow cooling rates ($t_{8/5} > 80$ s). Suzuki *et al.* (1996) found that in the lath type structure, plate like and rectangular plate like martensitic constituents were aligned with identical directivity transgranularly inside austenite grains, but in the blocky type structure lumpy martensite is randomly formed from the vicinity of ferrite grain boundaries (Hrivnak *et al.* 1992b, Davis & King 1993, Davis & King 1994, Hrivnak & Matsuda 1996, Liao *et al.* 1996).

The carbon content of M-A constituents was found to be almost independent of the carbon content of the base steel and was in the range of 0.6–2.2% in high strength low alloy steels. Since the hardness of martensite increases with carbon content, the hardness of the massive and elongated M-A constituents were measured from 800 to 1200 HV and from 600 to 800 HV respectively (Matsuda *et al.* 1991, Hrivnak *et al.* 1992a, Hrivnak *et al.* 1992b). Hardness of M-A constituents (HV_{M-A}) could be expressed as follows (Hrivnak *et al.* 1992b):

$$HV_{M-A} = 575xC + 15 \quad (8)$$

where C= carbon content of M-A constituents

The decomposition of M-A constituents depends on their shape, size and chemical composition and was observed to start at temperatures above 200 $^{\circ}\text{C}$ and to complete at

500 °C (Matsuda *et al.* 1991, Hrivnak *et al.* 1992a, Hrivnak *et al.* 1992b, Terada *et al.* 1992). Matsuda *et al.* (1991) found that the elongated M-A constituents were more easily decomposed than the massive M-A constituents and the decomposition of the massive M-A constituents started at the boundary between M-A constituents and the matrix indicating that the retained austenite decomposed first. After annealing 1 h at 350 °C the hardness of the M-A constituents was decreased to a range of 350–550 HV.

3.2.3 Summary of paragraph 3.2

In summary, M-A constituents are formed in the coarse grained HAZ (CGHAZ), intercritically reheated coarse grained HAZ (ICCGHAZ) and intercritical HAZ (ICHAZ). During the intercritical heating of the base plate of high strength low alloy steel with ferritic-pearlitic microstructure, austenite grows rapidly into pearlite until the dissolution process is completed. Then austenite continues to grow into ferrite at a rate controlled by either a diffusion of carbon in austenite or a diffusion of substitutional elements (for example manganese) in ferrite. In the intercritical heating of CGHAZ, with the large austenite grain size and upper bainitic microstructure austenite, preferentially nucleates and grows along the prior austenite grain boundaries and bainite lath boundaries. These carbon enriched (carbon contents 0.6–2.2%) austenite areas transform to hard (hardness 600–1200 HV) and brittle M-A constituents during cooling. Two main types of M-A constituents are classified according to their shape: elongated (or string/rod like) M-A constituents with L (length) to W (width) ratio $L/W > 3$ and massive (or block/polygonal) M-A constituents with an $L/W < 3$. Elongated M-A constituents with approximately 0.2–1 μm in width and several microns in length develop preferentially between ferrite, bainite and martensite laths in the ICCGHAZ and at the prior austenite grain boundaries in the CGHAZ during fast cooling ($t_{8/5}=20\text{--}40$ s). Blocky M-A constituents with a diameter of 3–5 μm preferentially form along the prior austenite grain boundaries in the ICCGHAZ and between the ferrite laths in the CGHAZ in slow cooling rates ($t_{8/5} > 80$ s).

3.3 Factors affecting the formation and properties of M-A constituents

3.3.1 Chemical composition of steel

Numerous research works have evidenced that many alloying elements in steel promote the formation of M-A constituents in the HAZ. Nitrogen, boron and carbon has been found to be the strongest, followed by the carbide forming elements such as niobium, vanadium, molybdenum and chromium. The effect of manganese, nickel and copper is less significant (Fig. 14) (Haze & Aihara 1987, Matsuda *et al.* 1996, Tian 1998). Moreover, the segregation of manganese, nickel and phosphorus during solidification and

carbon, nitrogen and boron during the austenite-ferrite transformation could enhance the formation of M-A constituents (Matsuda *et al.* 1996).

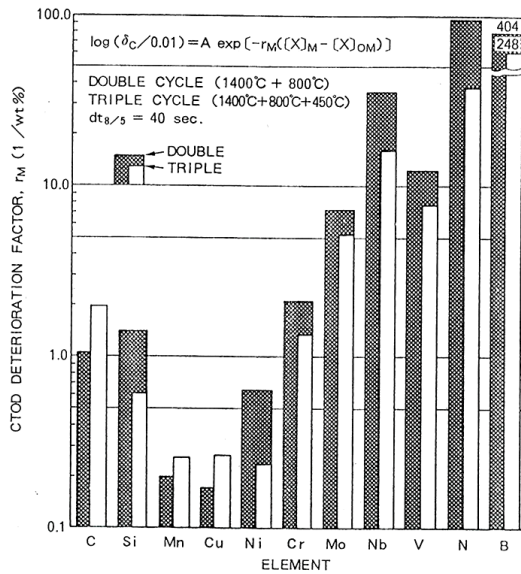


Fig. 14. CTOD deterioration factors for alloying elements: simulated HAZ (double and triple thermal cycle) (Haze & Aihara 1987).

3.3.1.1 Carbon and carbon equivalent

It is generally agreed that the amount of M-A constituents increases with the carbon content of steel, which has a small influence on the carbon content of M-A constituents (Matsuda *et al.* 1996). For the evaluation of the influence of the other alloying elements on the fraction of M-A constituents in the CGHAZ, the following alloy factor (AIF) was developed by Harrison and Webster (1994) and Harrison and Wall (1996):

$$\text{AIF} = (\text{Si} + \text{Mn})/6 + (\text{Cr} + \text{Mo} + \text{V})/5 + (\text{Ni} + \text{Cu})/15, \quad 0.06 \leq \text{C} \leq 0.11 \% \quad (9)$$

which is the same as the carbon equivalent of IIW (International Institute of Welding) plus Si/6 without carbon. If the AIF is less than 0.32, the fraction of M-A constituents is rather low, normally ≤ 6 vol.%.

3.3.1.2 Nitrogen and boron

The improvement of toughness of the base plate and weld metal is caused by reducing a nitrogen content, when M-A constituents between the ferrite laths change to pearlite. Evans (1998) evaluated that 10 ppm of free nitrogen in weld metal increased the impact transition temperature by 2–4 °C. However, the influence of nitrogen depends on the titanium and boron contents in the weld metal. The best impact toughness in weld metal was achieved by titanium and nitrogen contents of 400 ppm and 40 ppm respectively. The impact energy 100 J at –100 °C was possible to obtain in nitrogen contents of 25–35 ppm, according to Evans (1998). In HSLA steels the optimum ratio of Ti/N, to achieve high HAZ toughness, has been reported to be a stoichiometric ratio of TiN (3.4) and in aluminium and boron contained steels a ratio between 2.1 and 2.4 (Karjalainen *et al.* 1995, Tian 1998).

3.3.1.3 Niobium and vanadium

Carbide forming elements, such as niobium and vanadium, increase the hardenability of the re-austenitized area during the second thermal cycle promoting the formation of M-A constituents. In addition, these elements retard the decomposition of M-A constituents by preventing carbon diffusion during the third thermal cycle (Haze & Aihara 1987, Matsuda *et al.* 1996).

In high carbon steels the local amount of M-A constituents was enhanced by increasing niobium content because of promoted microsegregation of niobium and manganese in a higher region of enriched carbon (Furuya *et al.* 2000). Niobium has also been found to increase the hardenability of martensite (Lee *et al.* 1992).

It is evidenced that the volume fraction of M-A constituents increases in the simulated ICHAZ with increasing vanadium content (Fairchild *et al.* 1991). On the contrary, a lower area fraction of M-A constituents at the prior austenite grain boundaries of the ICCGAZ in 0.05% V steel was found (Li *et al.* 2000, Li *et al.* 2001).

3.3.1.4 Aluminium and silicon

High free aluminium content in steel has been found to enhance the formation of M-A constituents by preventing the diffusion of carbon and the precipitation of carbides from high carbon austenite (Matsuda *et al.* 1996). Namely, an excess of aluminium partitions in proeutectoid ferrite or bainitic ferrite retards austenite-ferrite transformation followed by formation of upper bainitic microstructure with carbon enrichment into retained austenite between bainitic ferrite plates. The enrichment of carbon during transformation has been found due to a repulsive force between Al-C in Mn-Mo and Mn-Mo-Ni steels (Mabuchi & Nakao 1981, Mabuchi & Nakao 1983).

Silicon has been found to promote the formation of twinned martensite and M-A constituents during intercritical heating. High silicon content in steel retards the precipitation of cementite, when carbon is enriched in austenite, promoting the formation

of M-A constituents (Fairchild *et al.* 1991, Matsuda *et al.* 1996). It has been explained that the rate control of silicon partitioning in bainitic ferrite can raise carbon activity in ferrite as a result of a change of carbide morphology and carbon enrichment into retained austenite left between bainitic ferrite laths during transformation through a repulsive force between Si-C (Mabuchi & Nakao 1983).

3.3.1.5 Manganese, chromium and molybdenum

The high manganese, chromium and molybdenum contents in steel decrease the B_s temperature promoting the formation of M-A constituents. Chromium and molybdenum, as carbide forming elements, increase the hardenability of the reaustenitized area during the second welding thermal cycle, which promotes the formation of M-A constituents (Matsuda *et al.* 1996). On the other hand, chromium has been explained to eliminate the influence of an excess of aluminium in steel due to an attractive force between Al-Cr in austenite as a result of lower bainitic microstructure after transformation (Mabuchi & Nakao 1983).

3.3.1.6 Copper and nickel

Reducing the copper and nickel content of high strength steel ($R_m = 500\text{--}600 \text{ N/mm}^2$) has been evidenced to decrease the amount of M-A constituents due to the reduced hardenability and upper bainite content. An addition of nickel has been found to lower the influence of excess aluminium on mechanical properties due to an attractive force between Al-Ni in austenite resulting in a reduction of carbon enrichment into retained austenite left between bainitic ferrite plates during transformation (Mabuchi & Nakao 1983). On the contrary, by addition of Ni and Mn in 780 MPa steel, the microstructure changes from upper bainite to lower bainite and martensite and M-A constituents don't form (Matsuda *et al.* 1996).

3.3.2 Peak temperature

The peak temperature of the thermal cycle of the CGHAZ has been found to have a minor influence on the amount of M-A constituents, but it probably has a significant influence on their distribution. The polygonal M-A constituents formed between the intragranularly nucleated ferrite laths in titanium killed steels have been more homogeneously distributed compared to the needle-like M-A constituents formed between the aligned ferrite laths in bainite packets of aluminium killed steels (Yamamoto *et al.* 1989, Lee & Pan 1991).

The peak temperature of the second intercritical thermal cycle has been considered to have a great influence on the amount of M-A constituents in the ICCGHAZ. The volume fraction of M-A constituents was increased by increasing the temperature of the second cycle from 660 °C to 750 °C and achieved the maximum value from 750 °C to 770 °C (Terada *et al.* 1992). During the second thermal cycle between A_{c1} and A_{c3} temperatures,

the first nucleation and growth of austenite begins to form from carbides and pre-existing M-A constituents at the prior austenite grain boundaries (Matsuda *et al.* 1996, Lambert *et al.* 2000a). During cooling M-A constituents first form along the prior austenite grain boundaries and then at the interfaces of martensite and ferrite laths (Akselsen *et al.* 1988, Matsuda *et al.* 1996, Kweon *et al.* 2000). When the peak temperature of the second thermal cycle is less than the Ac_1 temperature, the microstructure is tempered after the first thermal cycle. At higher peak temperatures above the Ac_3 temperature, the microstructure changes from a mixture of ferrite and pearlite to upper bainite as the peak temperature increases (Matsuda *et al.* 1996).

During the intercritical thermal cycle of the ICHAZ, the maximum volume fraction of M-A constituents was found at 775 °C, when austenite was formed at the pearlite colonies and ferrite grain boundaries and the volume fraction of M-A constituents was close to the pearlite content of the base plate in rapid cooling ($t_{8/5} = 5$ s). The decomposition of M-A constituents was observed to start at temperatures above 200 °C and to complete fully at 500 °C (Akselsen *et al.* 1988, Matsuda *et al.* 1991, Hrivnak *et al.* 1992a, Hrivnak *et al.* 1992b, Terada *et al.* 1992).

3.3.3 Cooling rate

The influence of the cooling rate of the intercritical thermal cycle on the amount of M-A constituents has not been evidenced. The formation of M-A constituents, for example, in the ICCGHAZ depends on the microstructure formed in the CGHAZ, which further depends on the cooling rate. In high strength steels the amount of M-A constituents increased rapidly when $t_{8/5}$ became longer than 10–20 s achieving the maximum values and then decreasing due to decomposition into carbides in ferrite, which begins when $t_{8/5} \geq 50$ s (Ikawa *et al.* 1980, Matsuda *et al.* 1996). For example, in low alloy (0.19% C, 0.62% Ni, 0.56% Mo) steel SQV-2A according to JIS G3120, the M-A constituents began to form when the cooling time $t_{8/5}$ exceeds 20 s. By increasing the cooling time $t_{8/5} = 20$ –40 s elongated M-A constituents were formed near the prior austenite grain boundaries of martensite and lower bainite contained microstructure. When the cooling time $t_{8/5}$ exceeded 40 s, M-A constituents formed between the prior austenite grain boundaries and transgranular ferrite laths of microstructure consisting of upper bainite, M-A constituents, bainitic ferrite, acicular ferrite and ferrite plus carbides or granular bainite. Elongated M-A constituents dominated until the cooling time $t_{8/5}$ exceeded 80 s, when massive M-A constituents formed (Liao *et al.* 1996). Yamamoto *et al.* (1989) reported that in titanium killed TMCP steels the area fraction of M-A constituents increased to the maximum until cooling times $t_{8/5} = 10$ –30 s corresponding to a cooling time of the maximum formation of the intragranularly nucleated ferrite laths, whereas in aluminium killed steel the area fraction of M-A constituents was high over a wide cooling time range ($t_{8/5} = 10$ –100 s) decreasing with longer cooling times (Fig. 15).

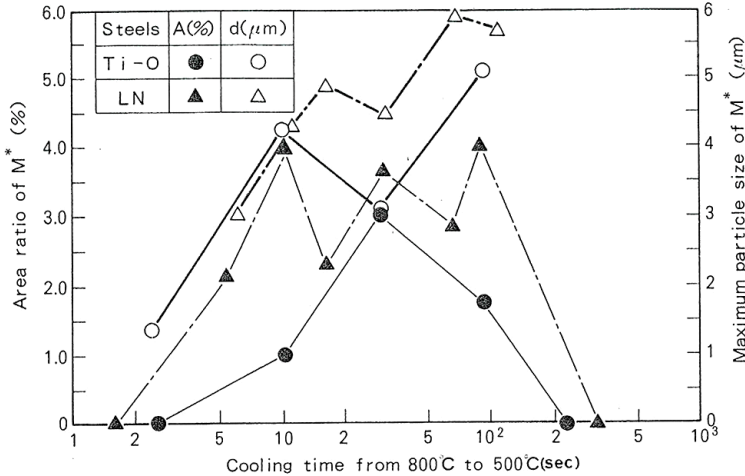


Fig. 15. Effect of a cooling time on area fraction of M-A constituents and maximum particle size (Yamamoto *et al.* 1989).

3.3.4 Summary of paragraph 3.3

In summary, it is generally agreed that the amount of M-A constituents increases with carbon and alloy contents of steel. In addition, nitrogen, boron, niobium, vanadium and aluminium enhance the formation of M-A constituents. The peak temperature of the thermal cycle of the CGHAZ and the prior austenite grain size have a minor influence on the amount of M-A constituents, but they probably have a significant influence on their distribution being polygonal in shape between intragranularly nucleated plates of titanium killed steels compared with needle like structure between aligned ferrite laths in bainite packets of aluminium killed steels. The amount of M-A constituents increases rapidly with cooling times $t_{8/5} = 10-20$ s achieving a maximum value and then decreasing due to decomposition into carbides in ferrite. In titanium killed TMCP steels the area fraction of M-A constituents was increased until a cooling time achieved the maximum $t_{8/5} = 30$ s and decreased with longer cooling times, whereas in aluminium killed TMCP steels the area fraction of M-A constituents was large over a wide cooling time range $t_{8/5} = 10-100$ s decreasing with longer cooling times.

3.4 Influence of M-A constituents on the fracture mechanism

It has been postulated in numerous papers that M-A constituents cause crack initiation both in ductile and brittle fracture. De-bonding of M-A/matrix interface and cracking of M-A constituents are generally accepted for initiation sites of fracture. A crack can

nucleate at three positions: inside M-A constituents, in the matrix near M-A/matrix interfaces or right at the interface. The generally explained mechanism for crack initiation caused by M-A constituents is based on the concentration and triaxility of internal stresses in regions near M-A/matrix interfaces and is presented as follows (Tian 1998):

- M-A constituents crack readily as a brittle phase and initiate a microcrack. The elongated stringer-type M-A constituents have been shown to crack readily, but the blocky-type M-A constituents do so quite seldom (Davis & King 1994).
- Unrelieved transformation stresses as a result of volume expansion with the decomposition of austenite into M-A constituents may increase the elastic and plastic strain at the interface and inside ferrite (Akselsen *et al.* 1988, Davis & King 1994, Tian 1998).
- Strength mismatch between M-A constituents and the matrix (hardness of 800–1200 HV for massive M-A constituents and about 200 HV for ferrite matrix) can cause dislocations pile up in front of M-A constituents during loading, exerting a high dislocation stress on it and further to crack it (Chen *et al.* 1984, Akselsen *et al.* 1988, Xu *et al.* 1993).
- A difference in elastic strain between M-A constituents and the matrix during loading and further strain partitioning between M-A constituents and ferrite causes strain accumulation only in ferrite (Akselsen *et al.* 1988, Tian 1998).
- A microcrack formed at the M-A/matrix interface through interfacial decohesion initiates a crack (Davis & King 1994).
- Connection or near connection among M-A constituents enables an array of de-bonded M-A constituents to produce a constrained region in high stress fields, where a cleavage crack may be formed (Davis & King 1993, Davis & King 1994, Tian 1998).
- A decrease of the interfacial energy of the M-A/matrix interface by carbon segregation at the interface (Davis & King 1993, Davis & King 1994, Tian 1998).

The role of M-A constituents in crack propagation is not clear. On the one hand, M-A constituents assist crack propagation along the interface between the M-A constituents and the matrix contributing to cleavage fracture reinitiation either in cracked M-A particles or small cracks at the M-A/matrix interface. On the other hand, M-A constituents can cause kinks on the fracture surface and thus hinder fracture propagation (Hrivnak *et al.* 1992a, Hrivnak *et al.* 1992b, Hrivnak 1995, Hrivnak & Matsuda 1996, Tian 1998).

3.4.1 Ductile fracture

At moderately high temperatures ferrite can yield easily and has a great capability to tolerate deformation under stress. When a heavy deformation of the ferrite matrix causes a high stress concentration on an M-A/matrix interface, it cracks or de-bonds. With increasing strain, cracks grow voids and further develop deep holes. Then a main crack forms and propagates by lateral growth and coalescence of deep holes due to internal necking and lead to a rupture of the specimen (Chen *et al.* 1984, Hrivnak *et al.* 1992a, Hrivnak *et al.* 1992b, Davis & King 1994, Hrivnak 1995, Hrivnak 1996). It has also been

evidenced that microvoids formed on M-A/matrix interfaces can more easily form on interfaces of elongated stringer-type M-A constituents orientated at a 40–50 degree angle to the tensile axis than blocky-type M-A constituents, when the martensite stringers were parallel to the tensile axis (Fig. 16) (Kim *et al.* 1991, Tian 1998).

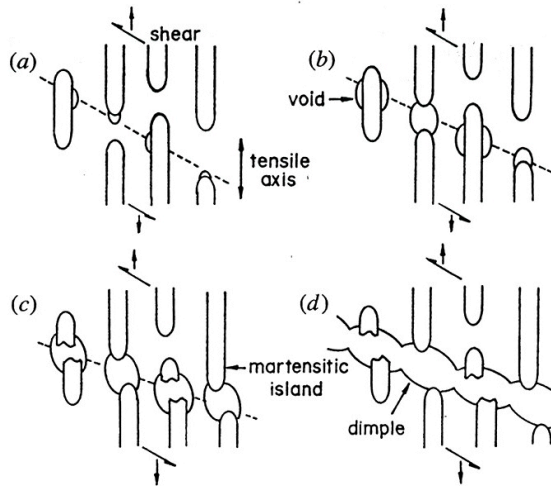


Fig. 16. Schematic illustration of the ductile fracture mechanism in the coarse grained HAZ (CGHAZ) of a HSLA steel weld. The examples tested at a temperature above the ductile to brittle transition temperature exhibit ductile rupture (Kim *et al.* 1991).

This type of microvoid formation at M-A constituents can be explained by the "shear cracking process" described for pearlite colonies by Miller and Smith. Ferritic-pearlitic steels voids were observed to initiate pearlite colonies, in particular at cementite lamellae parallel to the tensile axis, grain boundary carbides and sulphides. The initial microvoids become larger along the interfaces as the surrounding ferrite matrix undergoes plastic deformation and then martensitic constituents break in the later stages of void growth (Kim *et al.* 1991, Tian 1998).

3.4.2 Brittle fracture

The initiation mechanism of a brittle fracture has been found to be similar to that of a ductile fracture. In the case of cleavage fracture, the microvoids formed at M-A/matrix interfaces as a result of triaxial stresses propagate as a cleavage crack rapidly reaching prior austenite grain boundaries (Fig. 17) (Chen *et al.* 1984, Kim *et al.* 1991).

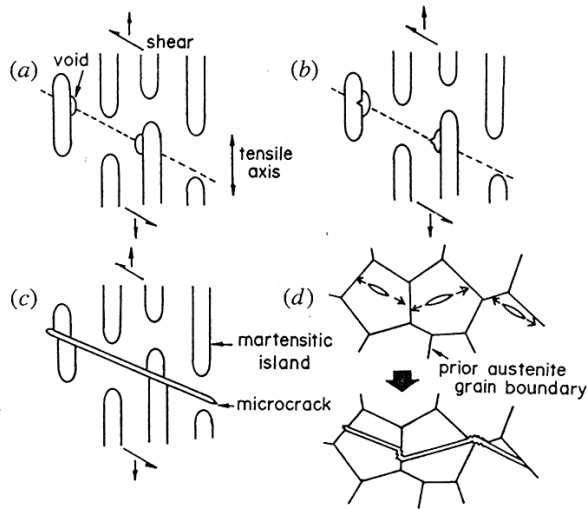


Fig. 17. Schematic illustration of the cleavage fracture mechanism in the CGHAZ of a HSLA steel weld (Kim *et al.* 1991).

A significant reduction in toughness has been found when M-A constituents form in a connected or nearly connected network of the blocky-type M-A constituents along the prior austenite grain boundaries, suggested to be caused by a series of de-bonded M-A constituents. Two closely spaced blocky-type M-A constituents produce a constrained region under a high stress field that form a small crack which initiates local cleavage (Fig. 18). It was suggested that an isolated de-bond M-A constituent was insufficient to cause a cleavage fracture (Chen *et al.* 1984, Davis & King 1993).

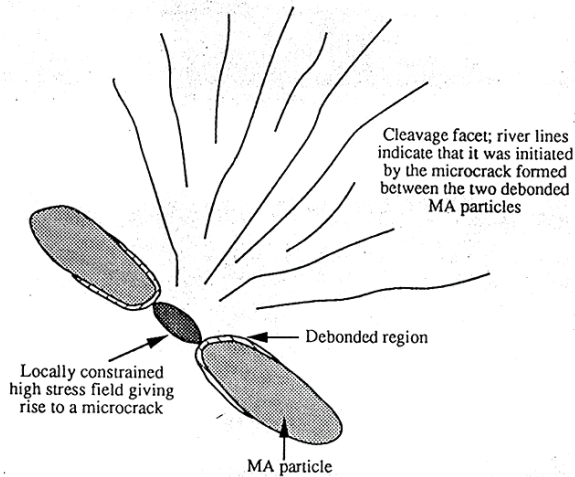


Fig. 18. Schematic diagram showing proposed mechanism by which connected or nearly connected M-A constituents initiate a cleavage fracture (Davis & King 1993).

Lambert *et al.* (2000b) and Lambert *et al.* (2000c) have shown that the mechanism of a cleavage fracture depends on the temperature. At very low temperatures (below $-150\text{ }^{\circ}\text{C}$), cleavage fracture was claimed to be nucleation controlled, but at higher temperatures, it involved the nucleation of a microcrack in M-A constituents (or at M-A/matrix interfaces) followed by its propagation into the surrounding matrix, where a crack arrest took place at high angle boundaries (misorientation over 40°). Lower angle boundaries (misorientation around 20°) were found to induce only a slight crack deviation. In numerous research works M-A constituents were evidenced to assist the propagation of cleavage fracture due to the fact that a cleavage fracture preferentially propagates along the interface between the M-A constituents and matrix. On the other hand, M-A constituents were found to hinder cleavage crack propagation and to create steps (river patterns) on the fracture surface or to kink out from its original path. The cleavage fracture path is found to follow a transgranular $\{100\}_{\alpha}$ (Hrivnak *et al.* 1992a, Hrivnak *et al.* 1992b, Hrivnak *et al.* 1996).

3.4.3 Summary of paragraph 3.4

In summary, M-A constituents enhance a crack initiation both in a ductile and brittle fracture. Cracks can nucleate at three positions: inside M-A constituents, in matrices near the M-A/matrix or right at the interface. In a ductile fracture strong deformation of the ferrite matrix causes a high stress concentration at the M-A/matrix interface causing it to crack or de-bond. With increasing strain cracks grow voids, leading to deep holes, their coalescence and rupture of the specimen. In the case of a cleavage fracture, microvoids

formed at the M-A/matrix interfaces, as a result of high triaxial stresses, propagate as a cleavage crack rapidly reaching prior austenite grain boundaries, where the nearly connected blocky-type M-A constituents can cause a series of de-bonded M-A constituents. In numerous research works M-A constituents were evidenced to assist cleavage crack propagation, but on the other hand, they have been found to hinder cleavage crack propagation.

3.5 Interrelation between acicular ferritic microstructure and M-A constituents

As presented in the earlier paragraph 2.5, the chemical composition of steel, the prior austenite grain size, the austenization temperature, the cooling rate and the type of hot deformation are the main factors affecting the intragranular nucleation of acicular ferrite on the surface of titanium oxide inclusions. Most of the same factors are also affect the formation of M-A constituents, as presented in the paragraph 3.3.

3.5.1 Formation of acicular ferrite and M-A constituents

The formation of acicular ferrite during welding is normally possible in the coarse grained HAZ (CGHAZ) due to the minimum requirement of the prior austenite grain size of 50–60 μm and inclusions for their nucleation, whereas M-A constituents are mainly formed during cooling after heating within the intercritical temperature range between A_{c1} and A_{c3} . During the nucleation and growth of acicular ferrite in the temperature range of 600–680 °C polygonal blocky-type M-A constituents are formed between the acicular ferrite laths as a result of the increased carbon content (Verrier *et al.* 1989, Yamamoto *et al.* 1989, Liao *et al.* 1996). Thus, the prior austenite grain size caused by the austenization temperature and austenite grain coarsening during cooling has an indirect influence on the formation of M-A constituents. The initial coarse grained HAZ formed after a single weld pass consists of upper bainite having a large prior austenite grain size in many high strength low alloy steels. During the intercritical heating of the second welding pass, newly formed austenite nucleates and grows at first at the prior austenite grain boundaries and then at the ferrite, bainite or martensite lath interfaces. During cooling new high carbon austenite was transformed into bainite or a mixed structure of high carbon bainite and M-A constituents. Then massive M-A constituents are formed at the prior austenite grain boundaries and elongated M-A constituents at ferrite, bainitic ferrite and martensite lath boundaries in the ICCGHAZ (Akselsen *et al.* 1988, Davis & King 1993, Kweon *et al.* 2000).

During the intercritical heating of the base plate, newly formed austenite nucleates and grows at high carbon microstructures such as pearlite, bainite and martensite. These newly austenitized high carbon areas transform into M-A constituents between the ferrite grains. Thus, the volume fraction of M-A constituents in the ICHAZ is dependent on the carbon or pearlite content of steel (Akselsen *et al.* 1988).

3.5.2 Effect of the chemical composition of steel

The influence of an individual alloying element on the toughness properties of weldments mainly depends on its influence on microstructure of the steel matrix and M-A constituents. It also depends on the other alloying elements and a weld cooling rate. In paragraphs 2.5.1 and 3.3.1 the significant influence of the deoxidation, microalloying and strengthening elements on formation of intragranular acicular ferrite and M-A constituents has been presented.

3.5.2.1 Titanium and nitrogen

Titanium killing and microalloying of steel has been found to enhance the nucleation of intragranular acicular ferrite and even distribution of M-A constituents. On one hand, Ti_2O_3 inclusions and TiN precipitates assist the nucleation of intragranular acicular ferrite in refining the effective grain size. However, on the other hand they prevent the growth of austenite grain size and the formation of acicular ferrite (Harrison & Webster 1994, Harrison & Wall 1996, Tian 1998). Reduction of free nitrogen and/or carbon by fixing titanium suppresses the formation of M-A constituents especially in low aluminium (0.005% Al), Ti-B and Ti-bearing (for example pipeline steel API 5LX-80) steels (Harrison & Webster 1994, Harrison & Wall 1996, Tian 1998). For example, a reduction of the nitrogen content causes M-A constituents between the ferrite laths to transform into pearlite (Matsuda *et al.* 1996). The area ratio of M-A constituents has been found to be 1–2% lower and a maximum M-A particle size about 1 μm smaller in the simulated CGHAZ of titanium killed than aluminium killed TMCP steel (Yamamoto *et al.* 1989).

On the contrary, the addition of titanium (0.010–0.014%) into relatively high aluminium (0.064–0.073%) steels has been found to increase the formation of M-A constituents (Harrison & Webster 1994, Harrison & Wall 1996). It has been reported that the optimum ratio of Ti/N to achieve high HAZ toughness in HSLA steels was the stoichiometric ratio of TiN (3.4). However, a ratio between 2.2 and 2.4 is suggested for TMCP steels containing the elements with a high affinity to nitrogen, such as aluminium and boron (Tian 1998). Karjalainen *et al.* (1995) showed that the optimum Ti/N ratio can be between 3 and 5 for TMCP steels with a yield strength ≥ 355 MPa at cooling times $t_{8/5}$ of 80–200 s if the carbon equivalent is ≤ 0.33 and the niobium content is $\leq 0.02\%$. When the ratio of Ti/N is greater than the optimum range, an excess of titanium will remain in liquid steel promoting the formation of large TiN precipitation in the CGHAZ, which can act as an initiation site for cleavage fracture deteriorating toughness. Thus, it is suggested that the alloying of titanium should be kept below 0.015% (Tian 1998).

3.5.2.2 Vanadium

The precipitation of VN and the nucleation of intragranular acicular ferrite on them increase the amount of acicular ferrite and decrease free nitrogen in a solution decreasing

the formation of M-A constituents due to a reduced hardenability of the reaustenized area during the second thermal cycle (Matsuda *et al.* 1996).

An addition of 0.05% V to carbon-manganese boron free steel has been found to promote the formation of polygonal ferrite along the prior austenite grain boundaries and intragranular acicular ferrite in the CGHAZ, reducing reaustenization sites along the prior austenite grain boundaries during the second thermal cycle, followed by a reduction of the area fraction and the size of M-A constituents (Li *et al.* 2000, Li *et al.* 2001). A slightly higher vanadium content (0.08–0.10%) tended to increase the amount of intragranular polygonal ferrite reducing Widmanstätten side plate structures. In the titanium-boron low aluminium steel, vanadium has been found to reduce polygonal ferrite and increase acicular ferrite, but in the titanium-boron high aluminium steel, vanadium had a little effect the ferrite morphology. At high heat input welds, vanadium has been observed to promote the formation of M-A constituents (Harrison & Webster 1994, Harrison & Wall 1996).

3.5.2.3 Niobium

Niobium has been reported to deteriorate HAZ toughness due to martensite hardening, although it increases the strength and improves the toughness of the base plate (Lee *et al.* 1992, Tian 1996). It promotes the formation of coarse upper bainitic microstructure at long cooling times ($t_{8/5} \geq 50$ s) and limits the heterogenous nucleation of ferrite on TiN by forming unstable (Ti,Nb)N or (Ti,Nb)(C,N) precipitates (Verrier *et al.* 1989, Tian *et al.* 1996). It has also been evidenced that the microsegregation zones of manganese and niobium coincide increasing with carbon content. In higher carbon and niobium steels the carbon enrichment in untransformed austenite near grain boundaries and microsegregation of manganese and niobium have been stated to cause a local concentration of M-A constituents (Fig. 19) (Yamamoto *et al.* 1989, Furuya *et al.* 2000).

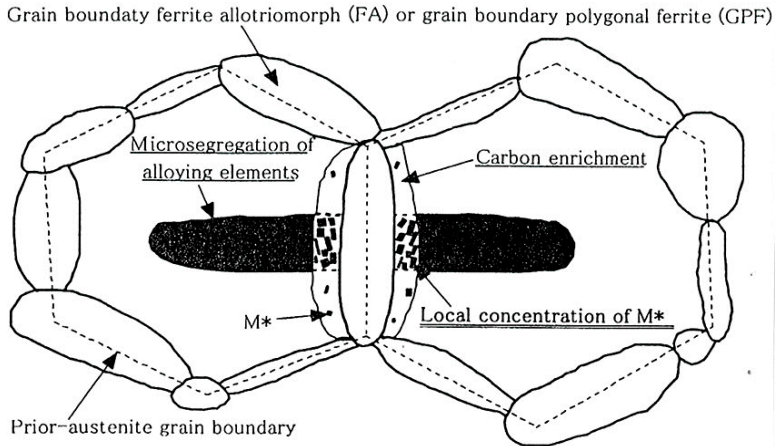


Fig. 19. Schematic illustration appearing formation of local concentration of M-A constituents (Furuya *et al.* 2000).

However, the influence of niobium on the toughness of the HAZ depends on the contents of niobium and carbon. Low niobium content ($\leq 0.02\%$) has been suggested to provide good HAZ toughness in normalized and TMCP steels with yield strength $\geq 355 \text{ N/mm}^2$. When the carbon content of steel is kept as low as $0.03\text{--}0.04\%$, niobium contents up to 0.04% can be used without any detrimental effect on HAZ toughness and is often required in TMCP steels to prevent and retard HAZ softening, for example, in X80 class pipe steels (Tian 1998).

3.5.2.4 Aluminium

Aluminium and oxides have a significant role in the formation of intragranular acicular ferrite. As stated in paragraph 2.5.1, that the Al/O ratio should not exceed unity due to the fact that soluble aluminium restricts a carbon diffusion in austenite during austenite-ferrite transformation causing a rapid growth of Widmannstätten ferrite and upper bainite laths from austenite grain boundaries. An excess of aluminium in austenite tends to cause the partition of proeutectoid ferrite (or ferrite in bainite), retarding ferrite transformation because of the rate control of aluminium partitioning during continuous cooling transformation. Retained austenite left between the bainitic ferrite laths has a higher carbon content during the transformation, since aluminium in bainitic ferrite rejects carbon into austenite due to a repulsive force between aluminium and carbon at higher temperatures. By reducing the aluminium content the formation of ferrite and a diffusion of carbon have been reported to be easier and promote carbide precipitation from high carbon austenite at lower temperatures, which prevents the formation of M-A constituents (Mabuchi & Nakao 1981, Mabuchi and Nakao 1983, Fukada & Komizo 1992, Matsuda *et al.* 1996, Zhang & Farrar 1996).

3.5.2.5 Silicon

Silicon has no significant influence on the formation of acicular ferrite. In upper and lower bainite transformation, silicon has been reported to retard the precipitation of cementite and enhance the enrichment of carbon in austenite (Matsuda *et al.* 1996). Fairchild *et al.* (1991) claimed that a silicon content in the range of 0.5% in the presence of about 0.08% vanadium promotes the formation of twinned martensite and M-A constituents during intercritical heating. By reducing the silicon content of steel the precipitation of cementite is promoted and the width of the ferrite laths become narrower followed by a reduction of M-A constituents (Matsuda *et al.* 1996).

3.5.2.6 Boron

It is well known that boron enhances the intragranular nucleation of acicular ferrite due to a saturation of soluble boron atoms along the austenite grain boundaries retarding the formation of grain boundary ferrite (Bhadeshia & Svensson 1993, Thewlis 1994). On the other hand, boron can form borides along the prior austenite grain boundaries and enhances the formation of coarse martensite laths. In order to prevent precipitation, boron is often alloyed with titanium because titanium has a stronger affinity to interstitial elements like carbon and nitrogen (Tian 1998).

3.5.2.7 Manganese

Manganese has a significant role in the nucleation of acicular ferrite due to a decrease in the austenite-ferrite transformation temperature and the formation of manganoxide inclusions and mangansulfides on inclusions for the favourable nucleation places of acicular ferrite (Ohkita & Horii 1995, Zhang & Farrar 1996, Manohar & Chandra 1997, Shim J-H *et al.* 1999). The high manganese content in steel has been stated to promote the formation of M-A constituents, because it decreases the bainite start temperature B_s (Matsuda *et al.* 1996).

3.5.2.8 Chromium, molybdenum, nickel and copper

From other elements chromium and molybdenum has been found to promote the formation of acicular ferrite in the weld metals and to decrease the bainite start temperature B_s promoting the formation of M-A constituents (Matsuda *et al.* 1996, Zhang & Farrar 1996, Thewlis *et al.* 1997).

Nickel and copper have been stated to promote the formation of acicular ferrite due to a decrease in the austenite-ferrite transformation temperature. However, the amount of M-A constituents decreases by reducing nickel and copper in 500–600 MPa steel because of a decrease of hardenability and the content of upper bainite. The addition of nickel and manganese in 780 MPa steel has been found to change the microstructure from upper

bainite to lower bainite and martensite and thus to prevent the formation of M-A constituents (Matsuda *et al.* 1996).

3.5.3 Effect of a cooling rate

Influence of weld cooling rate on the formation of acicular ferrite and M-A constituents depends on the chemical composition of steel and the thermal cycle of the weld. In low carbon TMCP steels, acicular ferritic microstructure and M-A constituents have been found to form in the CGHAZ in a wide cooling rate range, i.e. acicular ferrite in cooling times $t_{8/5} = 5.6\text{--}1000$ s and M-A constituents in cooling times $t_{8/5} = 10\text{--}100$ s (Ikawa *et al.* 1980, Verrier *et al.* 1989, Yamamoto *et al.* 1989, Hrivnak *et al.* 1992a, Liao *et al.* 1996). The maximum amount of acicular ferrite and M-A constituents into the CGHAZ was formed at the same cooling time $t_{8/5} = 30$ s (Yamamoto *et al.* 1989, Davis & King 1993). As a cooling time $t_{8/5}$ increases, the amount of M-A constituents increases rapidly in small cooling times up to $t_{8/5} \approx 30$ s, but was saturated or slightly decreased in larger cooling times $t_{8/5}$ due to its decomposition into ferrite and carbides, when cooling time $t_{8/5}$ was more than 50 s (Matsuda *et al.* 1996).

3.5.4 Influence of the effective grain size and M-A constituents on toughness

The correlation of toughness and grain size is well known. The prior austenite grain size was generally used to evaluate the relationship between toughness and grain size, because the size of sub-grains or subunits was related to that of the austenite grains in some lath type microstructures, such as bainite and lath martensite (Kim *et al.* 1991, Tian 1998). However, measuring of the cleavage facet or microcrack size has shown that the size of packets consisted of separate laths or lath bundles separated by high-angle boundaries was a controlling factor for cleavage fracture. Determination of the effective grain size has been conducted by measuring the cleavage facet or microcrack size. It has been pointed out that the effective grain size should be used only for evaluation of crack propagation and was found to be a dominant factor affecting impact toughness (Harrison & Webster 1994, Harrison & Wall 1996, Tian 1998).

HAZ toughness was observed to improve by increasing a fraction of intragranularly nucleated acicular and polygonal ferrite and was shown to reduce, by increasing a fraction of primary grain boundary ferrite, ferrite with second phase (Widmannstätten side plates) and upper bainite, which evidences the above-mentioned relationship between the effective grain and packet sizes (10) (Fig. 20) (Yamamoto *et al.* 1989, Lee & Pan 1991).

It has been assumed that ductile-brittle transition temperature is the inverse square root of the grain and packet diameter or the cleavage facet size (Yamamoto *et al.* 1989, Lee & Pan 1991, Harrison & Webster 1994, Yurioka 1995, Harrison & Wall 1996, Li *et al.* 2001). Thus, for the relationship between the effective grain size and fracture appearance

temperature $vTrs/FATT_{50\%}$ the following linear regression equation has been performed (Lee & Pan 1991):

$$FATT_{50\%} (^{\circ}C) = 80.9 - 16d^{-1/2} \quad (10)$$

where d = effective grain size (μm). The coefficients of d ranged from 10 to $19^{\circ}C\sqrt{mm}$ in different references (Lee & Pan 1991, Harrison & Webster 1994, Yurioka 1995, Harrison & Wall 1996, François 2001).

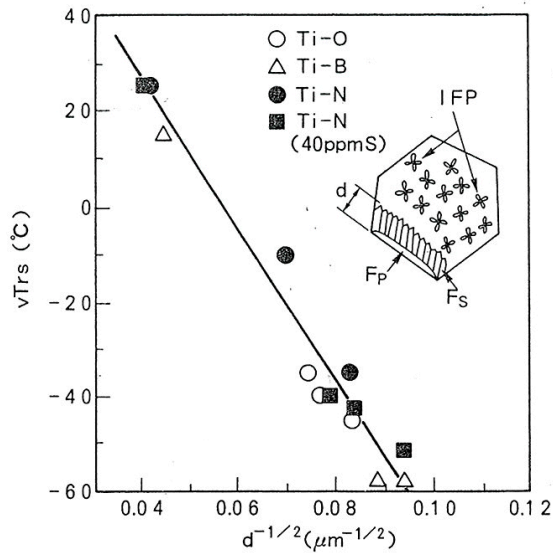


Fig. 20. Relationship between impact fracture appearance transition temperature ($vTrs$) and effective grain size of coarse grained HAZ (peak temperature = 1350, 1400, 1450 $^{\circ}C$, $t_{8/5} = 161$ s) (Yamamoto *et al.* 1989).

According to Fig. 20 the effective grain size has a significant influence on fracture appearance transition temperature, evaluated using the simulated specimens without M-A constituents, which has been found to have a significant influence also on the initiation of cleavage fracture. When a welding heat input was high (5.0–12.5 kJ/mm), brittle fracture was found to initiate at the intersection of a bainitic ferrite packet, where inhomogeneous microstructure rises to intense strain localization due to the constraint of plastic deformation followed by accumulation of defects for the brittle fracture. The relationship between the effective grain size and the toughness of the ICCGHAZ has been found to depend on the type of loading. The distance from the initiation site to the crack tip and fracture toughness of the ICCGHAZ was found to decrease with strain rate. With increasing strain rate, the number of large cleavage facets increased, but the area of dimple zones connecting cleavage facets decreased (Yokoyama & Nagumo 1998, Qiu *et al.* 2000).

3.5.5 Summary of paragraph 3.5

In summary, the formation of acicular ferrite and M-A constituents between acicular ferrite plates is influenced by the same main factors such as the chemical composition of steel, the prior austenite grain size and a cooling rate. It was suggested that free boron, nitrogen and carbon efficiently promote the formation of M-A constituents, but the binding of nitrogen and carbon with the microalloying elements such as titanium and vanadium, in addition to boron, enhances the formation of acicular ferrite and reduces the amount of free elements. Niobium promotes the formation of coarse upper bainitic microstructure, and a local concentration of M-A constituents, by microsegregation of manganese and niobium. Aluminium and silicon enhance the enrichment of carbon and the formation of M-A constituents. Aluminium in low oxygen plates and welds enhances formation of ferrite side plates and upper bainite. Manganese, chromium, molybdenum, nickel and copper promote the formation of acicular ferrite, but on the other hand, they increase the amount of M-A constituents mainly by decreasing the bainite start temperature B_s . The prior austenite grain size has a significant influence on the formation of acicular ferrite, but has a minor influence on the formation of M-A constituents. The cooling rate has a significant influence on the formation of both acicular ferrite and M-A constituents being the same maximum amount in the CGHAZ of TMCP steel at a cooling time $t_{8/5} = 30$ s.

3.6 Failure micromechanisms

In recent years there has been significant development in the area of fracture assessment approaches to predict the integrity of larger scale engineering structures using the results of fracture toughness tests carried out on the simulated coarse grained (CGHAZ), intercritically reheated coarse grained (ICCGHAZ) and intercritical HAZ (ICHAZ) specimens. In the approaches, fracture mechanical test results from these most critical microstructures in the welded joints have been transferred to the fracture assessment parameters using finite element analysis coupled with statistical models, for example the Gurson ductile damage model based on a normal distribution of the volume fraction of voids nucleating particles and the Beremin cleavage fracture model based on a weakest link concept applied by a Weibull distribution. According to the weakest link cleavage fracture concept, independent microcracks in the unit volume of steels are initiated at second phase particles scattered in size, orientation and shape and propagate unstably extending to the most critical crack.

3.6.1 Ductile-to-brittle transition temperature

The main factors affecting the ductile-to-brittle transition temperature of steels and weld metals are a critical cleavage stress, yield stress and stress intensification of specimens with crack. Thus, the cleavage mechanisms including cleavage crack initiation and

propagation have a significant influence on the investigation. In crack initiation dislocation pile-ups and twins, stress on carbide particles can become concentrated and cause cleavage cracks, which propagate the size of particles. This model of Smith reveals the critical cleavage stress σ_f as follows (François 2001):

$$\sigma_f^2 = \frac{4\gamma_{eff}\mu}{\pi(1-\nu^2)c} - \frac{k_y^2}{c} \left(1 + \frac{4\sqrt{c}\tau_i}{\pi k_y} \right) \quad (11)$$

where μ = shear modulus, ν = Poisson's ratio = 0.3 (for steels), γ_{eff} = an effective surface energy for cleavage = 11.2 J/m² (for M-A constituents), 14 J/m² (for carbides), 120 J/m² (for bainite packets), 500 J/m² (for ferritic-pearlitic microstructure), c = size of the carbide, k_y = Hall-Petch coefficient and τ_i = friction stress on the dislocations. The first term represents the stress needed to propagate a long crack of width c and the second one the influence of pile-up of dislocations which produces stress concentrations. When γ_{eff} is very low, for example for cementite, of order from 1 to 2 J/m² and $c = 1 \mu\text{m}$, $\tau_i = 100$ MPa and $k_y = 0.33 \text{ MPa}\sqrt{\text{m}}$, the first term is close the second one and the fracture stress value is very low corresponding to the initiation of a crack in a platelet. In the case of twinning the friction stress on dislocations is very low, when the second term in equation (11) can be neglected (Chen *et al.* 1984, San Martin & Rodriguez-Ibabe 1999, Zhang & Knott 1999, François 2001).

When the crack, once initiated in a carbide particle, must cross the cementite-ferrite interface, the effective surface energy γ_{eff} has been estimated to be 14 J/m². Thus, cleavage fracture is propagation controlled when the critical cleavage stress σ_f can be expressed according to the following Griffith criterion (Couque *et al.* 1988, Xu *et al.* 1993, San Martin & Rodriguez-Ibabe 1999, Zhang & Knott 1999, Lambert *et al.* 2000b):

$$\sigma_f = \sqrt{\frac{4E\gamma_{eff}}{\pi(1-\nu^2)c}} \quad (12)$$

where E = Young's modulus = 2×10^5 MPa (for steels)

The evaluation of cleavage-fibrous fracture transition temperature is based on the fact that the maximum achievable stress σ_{max} around a crack tip increases with decreasing temperature and becomes greater than the temperature independent cleavage strength (Xu *et al.* 1993):

$$\sigma_{max} = R\sigma_y \quad (13)$$

where σ_y = uniaxial yield stress and R = stress intensification around the crack tip is temperature dependent.

Schematic illustration (Fig. 21) of the temperature dependence of fracture type based on the formula (13) (Xu *et al.* 1993).

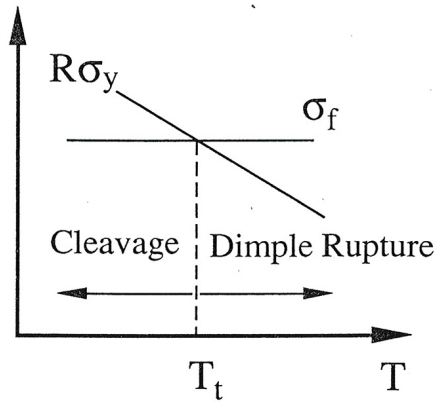


Fig. 21. Schematic illustration of fracture type (Xu *et al.* 1993).

3.6.2 Factors affecting the critical fracture stress

The main factors affecting the critical fracture stress σ_f are grain size and M-A constituents. Fig. 22 shows that the critical fracture stress decreases with increasing the grain size and amount of M-A constituents.

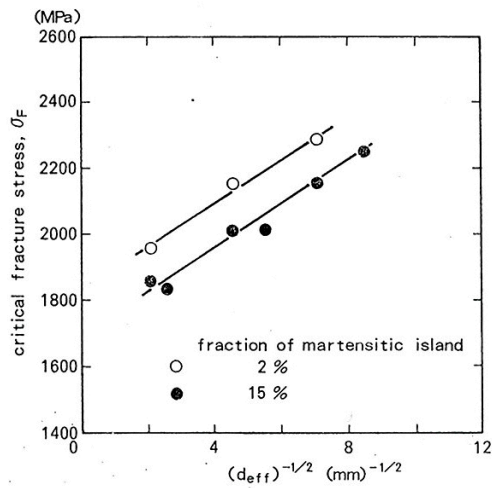


Fig. 22. Change of a critical fracture stress with effective grain size and amount of M-A constituents: simulated HAZ ($T_{p1}=900-1400$ °C, $T_{p2}=800$ °C) (Haze & Aihara 1988).

Although σ_f decreased with increasing the effective grain size and with increasing the volume fraction of M-A constituents, influence of the grain size was relatively small. The

influence of M-A constituents on σ_f is expected to be significant. When CTOD values decrease with decreasing σ_f or increasing the yield strength, decrease in the CTOD value with increasing peak temperature is mainly due to the increase in yield strength than due to an increase in the effective grain size (Haze & Aihara 1988).

3.6.3 Cleavage fracture models

Fracture mechanical test results are explained according to the RKR (Ritchie-Knott-Rice) model, which involves a local cleavage stress σ_f and a critical distance ahead of a macrocrack tip, X . This critical distance relates to a stress field, in which the local tensile stress is available to propagate a microcrack (Zhang & Knott 1999).

It was found that carbides or carbide colonies and an M-A/ferrite interface about $0.3\ \mu\text{m}$ to ferrite act as critical microcrack nuclei and therefore play a key role in determining fracture toughness. On the other hand, the variation in fracture toughness caused by material inhomogeneity was found to be very much larger than any experimental errors. In high strength low alloy steels containing M-A constituents, a value of γ_{eff} of $11.2\ \text{J/m}^2$ for the evaluation of the local fracture stress, but lath auto-tempered martensitic and bainitic microstructures, the local fracture stress has been found to depend on the microstructural packet size, when a value for γ_{eff} of $120\ \text{J/m}^2$ has been proposed (Chen *et al.* 1984, Zhang & Knott 1999).

The lath crystallographic orientations within any individual martensite and bainite packet are such that there are low angle boundaries between neighbouring laths. This means that crack deviation is small for a crack propagating across the packet. On reaching a high angle packet boundary, however, a significant change in crack direction may be required (Zhang & Knott 1999).

Cleavage fracture initiation in the ICCGHAZ has been observed to occur between two closely spaced blocky-type M-A particles, which requires the attainment of a critical level of imposed strain in addition to exceeding a critical cleavage fracture stress. When the stress level rises extremely quickly ahead of the crack tip, there is insufficient time for the strain levels to exceed the level required for crack initiation by this mechanism. Then cleavage fracture initiation can occur by a different operating mechanism, such as cracking of the interlath M-A particles, which does not require the attainment of a significant critical imposed strain (Davis & King 1996). In submerged arc welded joints welded using a relatively high heat input, cleavage initiation has been stated to occur at the intersection of bainitic ferrite packets with different orientations (Qiu *et al.* 2000).

Crack propagation depends on the type of loading. Under static loading, a crack propagates in the packet and extends to the packet boundary. At the boundary, fracture is induced again and continues to propagate in another packet along a certain plane having a low resistance to fracture (Fig. 23). Under dynamic loading, since failure takes place in a very short time, there is not sufficient time for cracks to find the weakest planes in adjacent grains and packets. Consequently, cracks propagate from one grain or packet to another on the same cleavage plane until a prior austenite grain boundary is reached. Cracks in different planes are connected by shear or ductile fracture (Fig. 23) (Qiu *et al.* 2000).

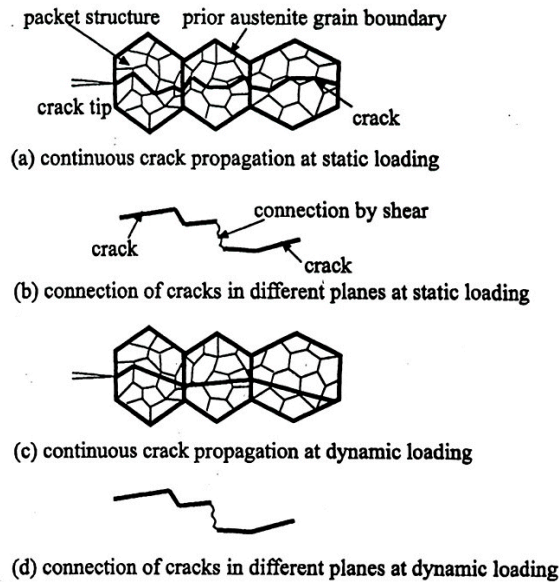


Fig. 23. Crack propagation mechanism under (a) and (b) static and (c) and (d) dynamic loading (Qiu *et al.* 2000).

3.6.4 Summary of paragraph 3.6

In summary, in recent years the new fracture assessment approaches were developed based on a weakest link concept using the statistical evaluation of independent microcracks in the unit volume and unstable propagation of the most critical crack, if the stress perpendicular to the crack surface surpasses a critical stress for cleavage fracture σ_f derived from the Griffith criterion. In these models fracture assessment parameters for engineering structures were calculated from fracture mechanical test results on simulated coarse grained HAZ (CGHAZ), intercritically reheated coarse grained HAZ (ICCGHAZ) and intercritical HAZ (ICHAZ) specimens using finite element analysis coupled with statistical models, such as the Beremin cleavage fracture model and the Gurson ductile damage model. The critical microstructures in the HAZ such as M-A constituents and carbides can induce local stresses surpassing the critical cleavage fracture stress σ_f , but a cleavage fracture initiation requires the attainment of a critical level of strain in addition to the exceeding of a critical cleavage fracture stress. Cleavage fracture propagation depends on a type of loading. Under static loading, fracture propagation continues along packets having low resistance to fracture, whereas under dynamic loading fracture propagation takes place from one packet to its neighbour on the same cleavage plane extending to the prior austenite grain boundaries.

3.7 Testing of ductile-to-brittle transition temperature

Practical evaluation of the ductile-to-brittle transition temperatures is generally based on the standard Charpy V test, which has become the common quality control toughness test for steel products because of its fast and simple application. However, a relatively large notch root radius (0.25 mm) in the Charpy V specimens has a limited capability to take micromechanical features into consideration and does not contribute to the increase of the stress-strain state for the formation of microcracks as effective as CTOD specimens with a smaller root radius. Nevertheless, the instrumented Charpy V impact test allows micromechanical modelling of static, as well as dynamic, initiation fracture toughness trends and has opened up possibilities to evaluate ductile crack initiation and propagation features (Li *et al.* 2001, Chaouadi & Fabry 2001). This has promoted the development of tools used for structural integrity assessments (for example SINTAP) based on Charpy V test results (Wallin *et al.* 2001). However, each test has its own characteristics concerning the ductile-to-brittle transition temperatures, such as 27 J and 50% transition temperatures (T_{27J} and $T_{50\%}$) in the Charpy V test and 0.1 mm crack tip opening transition temperature ($T_{0.1mm}$) in the CTOD test, as is presented in the following paragraphs.

3.7.1 Charpy V impact energy transition temperature T_{27J}

In the impact test, the absorbed energy including the initiation and propagation of the crack of the whole specimen is recorded. With the increase of material ductility, both the crack initiation and propagation energies grow. So, the impact test can be regarded as more versatile and better for the ranking of materials from the viewpoint of resistance to brittle fracture (Dziubin'ski & Adamiec 2001).

In crack nucleation the Charpy V specimens with a relatively large notch root radius (0.25 mm) have a limited capability to take micromechanical features into consideration and do not contribute to the increase of the stress-strain state for the formation of microcracks. Furthermore, dynamic loading in impact tests takes place so fast, as there is not sufficient time for cracks to find the weakest planes in adjacent grains and packets. Consequently, cracks propagate from one grain or packet to another on the same cleavage plane until a prior austenite grain boundary is reached (Qiu *et al.* 2000). The impact energy transition temperature T_{27J} has been observed to preferentially take ferrite grain size and bainite packet size into consideration (Harrison & Webster 1996, Harrison & Wall 1996, Matsuda *et al.* 1996).

In recent years, in Charpy V testing of laser welded joints, there have been problems due to a fracture path deviation in a ductile temperature range. Although the alternative test methods including side grooved, oversized and longitudinal specimens have been carried out for the characterisation of toughness, properties of the overmatched weld and narrow HAZ of laser welded joints will be doubtful. However, in a ductile-to-brittle transition temperature range failure of the laser welds it is recommended to select brittle fracture avoidance using the transition temperature T_{27J} (Nagel *et al.* 2001).

3.7.2 50% ductile fracture transition temperature $T_{50\%}$ in Charpy V impact test

Fracture appearance transition temperature $T_{50\%}$ ductile fracture is assumed to provide a safeguard against fracture propagation in the structure. Usually, the transition temperature $T_{50\%}$ is higher than the impact energy transition temperature T_{27J} and is regarded as over conservative, for example in ship structures, where a conventional criterion of a minimum Charpy impact energy of 47 J and a maximum of 70% crystallinity (30% ductile fracture) at 0 °C is applied (Wistance *et al.* 2001). Thus, the transition temperature $T_{50\%}$ represents more crack arresting of material than the transition temperature T_{27J} . The load-time test record from the instrumented Charpy V tests in Fig. 24 illustrates ductile crack initiation and propagation, cleavage fracture initiation, propagation and arrest and final shear lips formation (Chaouadi & Fabry 2001).

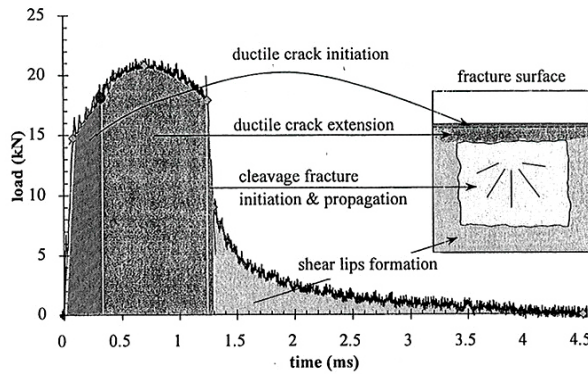


Fig. 24. Energy partitioning and correspondence with the fracture surface (Chaouadi & Fabry 2001).

In Figure 24 the energy is first spent for the nucleation of microvoids and shear crack with cavities and formation of a ductile crack front after general yielding. Then, ductile crack growth occurs in a stable manner by coalescence of microvoids linking the initiated shear cracks with cavities until an unstable cleavage fracture occurs up to an arrest of propagation followed by shear lip formation (Chaouadi & Fabry 2001, Tanguy *et al.* 2001).

The transition temperature $T_{50\%}$ correlates with the nil ductility temperature (NDT) in the Pellini test and 50% DWT temperature due to crack arrest properties. Wallin *et al.* 2001 have found that the transition temperature $T_{50\%}$ correlates the 50% of upper shelf energy ($TK_{50\%US}$) which was about 8 °C lower than $T_{50\%}$. Crack arrest occurs when the local crack driving force at the crack tip decreases below the local arrest toughness over a sufficiently large portion of the crack front.

3.7.3 Crack tip opening displacement transition temperature

T_{0.1mm} in CTOD test

The aim of the CTOD test is to evaluate ductile crack growth into the critical length for cleavage crack and is usually carried out according to BS 7448-1:1991 and BS 7448 Part 2:1997. The CTOD test has conventionally been used for offshore structures, where the common minimum crack tip opening displacement of 0.25 mm in the as-welded and 0.20 mm in the PWHT conditions at $-10\text{ }^{\circ}\text{C}$, have been specified in standards (Norsok MDS M-120 Rev. 4 2004, EN 10225 2000). The fatigue notched full size specimens of Bx2B (B = plate thickness) were used. The CTOD test with through thickness fatigue notched specimens has been regarded as too conservative due to the fact that in many applications cracks were mainly nucleated in the surface. But even more conservative are the CTOD test results on small size BxB specimens from the simulated HAZ, when the evaluation of toughness is commonly carried out according to the transition temperature $T_{0.1\text{mm}}$.

The sharp notch tip in the fatigue notched CTOD specimens characterizes a more sensitivity of microstructure such as M-A constituents on crack initiation in the CTOD tests than in the Charpy V tests. Thus, a great scattering is characteristic for the CTOD test results particularly in a ductile-to-brittle transition temperature range (Haze & Aihara 1988, Li *et al.* 2001). It has been observed in numerous studies that M-A constituents have a significant role for deterioration of toughness by decreasing crack initiation and propagation energies (Okada *et al.* 1994, Harrison & Webster 1994, Harrison & Wall 1996, Matsuda *et al.* 1996, Tian *et al.* 1996, Tian 1998).

Crack propagation depends on the type of loading. Under static loading in the CTOD test, a crack propagates in the packet boundary and continues to propagate in another packet along a certain plane having a low resistance to fracture (Fig. 23).

Since CTOD tests from the welded joints are very difficult and expensive to carry out, the correlations between the CTOD and Charpy V impact tests have been conducted and used in numerous design codes. The correlations are based on the parabolic relationship between the results of Charpy V and CTOD tests (Dziubin'ski & Adamiec 2001). The most well-known correlation is the Master Curves, based on the general brittle fracture correlation between $K_{IC} = 100\text{ MPa}\sqrt{\text{m}}$ and TK_{28J} . The application of the Master Curve concept allows the investigation of the scatter in the lower shelf of the base material as well as the welded joints statistically (Wallin *et al.* 2001, Mannsfeld *et al.* 2001).

3.7.4 Summary of paragraph 3.7

In summary, the standard Charpy V impact test has maintained its dominant position for evaluation of steel and welded joints in spite of its relatively large notch root radius (0.25 mm) in the specimens compared with the CTOD test specimens with smaller root radii. The absorbed energy in the impact test, including the initiation and propagation of the crack of the whole specimen, can be regarded as more versatile and better for the ranking of materials from the viewpoint of resistance to brittle fracture. The instrumented

Charpy V impact test has opened up possibilities to evaluate ductile crack initiation and propagation including a crack arrest capability using the ductile fracture transition temperature $T_{50\%}$ and to develop design codes based on correlations of Charpy V transition temperature $T_{27/28J}$ and fracture toughness CTOD test. A sharp notch tip in the fatigue notched CTOD specimens characterizes more sensitivity of microstructure on crack initiation in the CTOD test than in the Charpy V test.

3.8 Toughness improvement mechanisms of the ICCGHAZ and ICHAZ

Several studies concerning the toughness of the HAZ of high strength steel weldments have shown that a degradation of toughness is caused by M-A constituents formed during the cooling from the heating in the intercritical temperature range (A_{c1} and A_{c3}). Microstructure and the formation of M-A constituents during heating in the intercritical temperature range depend on the microstructure before the intercritical heating, the peak temperature in the intercritical heating and the cooling rate.

3.8.1 ICCGHAZ

The toughness of the ICCGHAZ is strongly influenced by metallurgical factors such as the amount, type and distribution of M-A constituents and the microstructure of the matrix. The characteristics (amount, hardness and size) of the M-A constituents were found to be strongly correlated with the peak temperature and a cooling rate of the previous pass, which have a great influence on the prior austenite grain size of the previous pass. During heating to the intercritical temperature range, austenite forms first along the prior austenite grain boundaries and martensite or bainite lath boundaries depending on the microstructure after the previous thermal cycle. This high carbon austenite transforms into bainite or a mixed structure of high carbon brittle bainite and some retained austenite contained martensite (M-A constituents).

The amount of M-A constituents has been considered a dominant factor influencing the toughness of the ICCGHAZ only when the cooling time is short. When the cooling time was increased, the hardness differences between M-A constituents and the softened matrix have been found to be the dominant factors (Fig. 25) (Kweon *et al.* 2000).

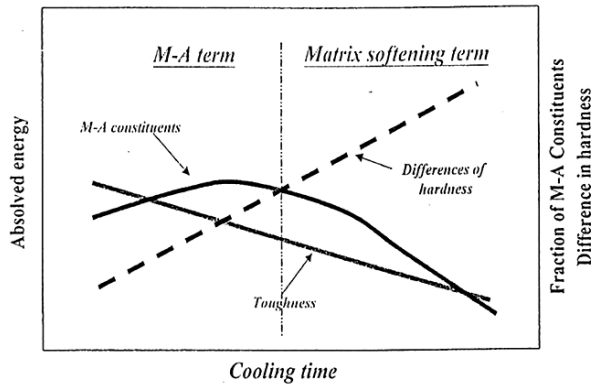


Fig. 25. Effect of the toughness of M-A constituents and differences in hardness (Kweon *et al.* 2000).

In short cooling times, the toughness deterioration mechanism caused by M-A constituents is based on high stress fields between two M-A particles at the prior austenite grain boundary followed by the formation of microvoids and their growth into the matrix (Kim *et al.* 1991, Davis & King 1993). In longer cooling times microvoids can nucleate around hard and coarsened M-A constituents or carbides after their separation from the prior austenite grain boundaries, lath boundaries and the softer matrix (Kweon *et al.* 2000).

In the recent studies the amount, type and distribution of M-A constituents and the packet size of bainite or the grain size of ferrite side plates have been found to be the main factors affecting the toughness of the HAZ of high strength low alloy steels. High carbon, blocky-type martensite located at the prior austenite grain boundaries have been claimed to be more deleterious than retained austenite mainly located between the laths of bainite packets or grains of ferrite side plates. In mixed M-A constituents martensite has been found to be located at the centre and retained austenite in the periphery as a result of chemical and/or mechanical stabilisation mechanisms (Lambert *et al.* 2000a).

When the packet size of bainite or grain size of ferrite side plates control a cleavage unit as the effective grain size and M-A constituents the initiation of a brittle fracture, the intragranularly nucleated acicular ferritic or fine bainitic microstructure in the CGHAZ can significantly improve the toughness of the ICCGHAZ. During intercritical heating, austenite forms at the prior austenite grain boundaries and homogeneous distributed M-A constituents between fine acicular ferrite laths. The M-A constituents formed during the subsequent rapid cooling are also more evenly distributed at the prior austenite grain boundaries and between acicular ferrite laths. Toughness improvement is based on both fracture initiation and propagation. In a crack initiation, small homogeneously distributed M-A constituents can distribute the loading and transformation stresses more evenly than the massive M-A constituents at the prior austenite grain boundaries or elongated M-A constituents between large bainite packets or ferrite grains and retard the nucleation of the microvoids. The intragranularly nucleated acicular ferritic microstructure can retard crack

propagation more effective than a coarse bainitic-ferritic microstructure due to numerous high angle boundaries between acicular ferrite laths.

3.8.2 ICHAZ

The toughness of the ICHAZ has been found to affect the same metallurgical factors as that of the ICCGHAZ, namely the amount, type and distribution of M-A constituents and the microstructure of the matrix. By comparing the toughness features of the ICHAZ with those reported from the ICCGHAZ or CGHAZ, the M-A constituents are a primary factor in controlling toughness. The strong influence of base plate microstructure is characteristic of the microstructure and the toughness of the ICHAZ. So, the steel manufacturing and rolling technique can significantly affect the toughness of the ICHAZ (Fairchild *et al.* 1991).

During intercritical heating austenite forms at high carbon pearlite/carbide colonies and ferrite grain boundaries. In a subsequent cooling these high carbon austenite areas decompose to M-A constituents or a wide variety of microstructures varying from twinned martensite to pearlite, depending on the hardenability of steel, the initial size of the austenized colonies and the cooling rate. It is evident that the carbon content of austenized colonies is close to the level of carbon in austenite at the temperature of dissolution (A_{c1}). Consequently, in the case of rapid cooling the volume fraction of M-A constituents in the ICHAZ of the low carbon microalloyed ferrite-pearlite steels is close to the initial pearlite content of the base plate. When the high carbon pearlite/carbide areas in the base plate are located in isolated colonies, for example at the ferrite grain boundaries, the austenized colonies formed during intercritical heating are small (below 0.5–1 μm) and M-A constituents formed during subsequent cooling remain retained austenite (Akselsen *et al.* 1987, Akselsen *et al.* 1988, Fairchild *et al.* 1991). In general, M-A constituents in the ICHAZ are preferably formed at the ferrite grain boundaries.

In the research works focusing on the low carbon microalloyed ferritic-pearlitic steel the toughness of the ICHAZ can be linked to the volume fraction of pearlite in the base plate and the volume fraction of M-A constituents in the ICHAZ. The volume fraction of M-A constituents above six percent by volume starts to become critical for impact toughness of the ICHAZ (Figs 26 and 27) (Akselsen *et al.* 1987, Akselsen *et al.* 1988).

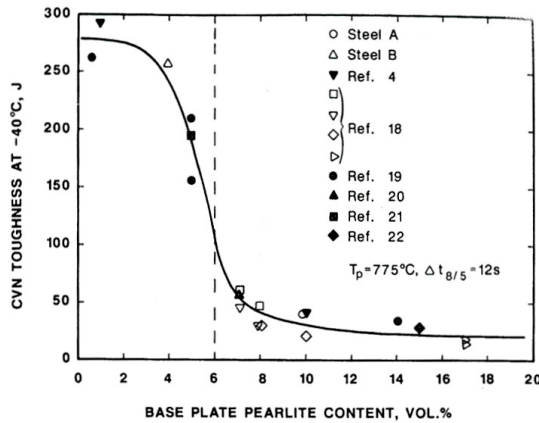


Fig. 26. Effect of base plate volume fraction of pearlite on ICHAZ toughness at -40°C (Akselsen *et al.* 1988).

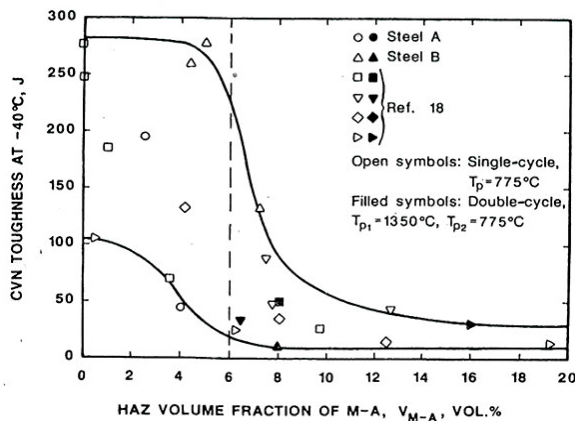


Fig. 27. Effect of M-A volume fraction on ICHAZ and ICCGAZ toughness at -40°C (Akselsen *et al.* 1988).

The embrittlement mechanism of ICHAZ caused by M-A constituents can be expected to introduce considerable stress concentrations at the M-A/ferrite interface due to the significant difference in the yield strength between these phases. In decomposition of austenite to M-A constituents and mechanical testing stress concentrations between M-A constituents and ferrite is conducted, strain accumulation can be caused in ferrite only. In the mechanical testing (for example impact testing) at subzero temperatures the local stress level at the M-A/ferrite interface exceeds the cleavage fracture stress of ferrite and causes the initiation of brittle fracture (Akselsen *et al.* 1987, Akselsen *et al.* 1988).

When M-A constituents at the ferrite grain boundaries, as earlier presented, have a dominating influence on the toughness of the ICHAZ, the intragranularly nucleated ferritic or bainitic microstructure can significantly improve toughness of the ICHAZ in rapid cooling of the weld. If the acicular ferritic microstructure with small high carbon

pearlite/carbide areas is homogeneously distributed between acicular ferrite laths in the base plate, it would be possible to achieve a homogeneous distribution of M-A constituents between slightly coarsened acicular ferrite laths into the ICHAZ after the intercritical thermal cycle. Thus, the homogeneously distributed M-A constituents can retard crack nucleation and the propagation of fine acicular ferritic microstructure with the same mechanism as described in the ICCGHAZ (previous paragraph 3.8.1).

3.8.3 Summary of paragraph 3.8

In summary, the toughness of the ICCGHAZ and ICHAZ is strongly influenced by metallurgical factors such as the amount, type and distribution of M-A constituents and the microstructure of the matrix. In the ICCGHAZ, massive blocky-type M-A constituents at the prior austenite grain boundaries and large ferritic-bainitic packets with elongated M-A constituents between ferrite or bainitic ferrite laths, are the dominant factors affecting the degradation of toughness. However, in the ICHAZ the amount of M-A constituents and high ferrite or bainite grain size mainly caused a degradation of toughness. Thus, acicular ferritic microstructure, with evenly distributed M-A constituents between ferrite plates, would be the ideal microstructure for the improvement of toughness of the ICCGHAZ and ICHAZ.

4 Novel features of this work

The increased interest in the low heat input welding applications and strict fracture toughness requirements for structures has led demands to improve HAZ toughness. But this has not previously been studied systematically. Other research works have concentrated on high heat inputs which are generally more interesting from an economical viewpoint and, at the same time, are more problematic due to increasing amounts of coarse ferrite side plate microconstituents in conventional niobium microalloyed steels as the cooling rate decreases.

The purpose of this research work was to see if the toughness problems that occur as a result of low heat input welding can be solved using titanium killing and by avoiding microalloying with niobium using copper and nickel alloying instead. The approach was based on the following assumptions:

- A significant improvement of the toughness of the HAZ in low heat input welding can be expected in the ICHAZ if the base plate is titanium killed and, provided there are enough fine titanium oxide inclusions, the prior austenite grain is large enough, and that the cooling rate and finish cooling temperature of the base plate are suitable for intragranular nucleation of ferrite and bainite.
- For the most part intragranularly nucleated acicular and fine polygonal ferritic or bainitic microstructures, together with evenly distributed high carbon microconstituents between fine interlocked ferrite grains or bainite laths, can be achieved in titanium killed plate and their CGHAZs. Consequently, the formation of evenly distributed M-A constituents (M-A islands) as a result of the intercritical thermal cycle can be expected to improve the toughness of the ICCGHAZ and ICHAZ.

The main tasks that have been undertaken in order to investigate the above hypotheses are as follows:

- Clarification of the theoretical background regarding the intragranular nucleation of acicular ferrite in the weld metal, the HAZ and the base plate.
- Preparation of test pieces from titanium killed plates containing as much intragranularly nucleated acicular ferrite as possible and a comparison of their

toughness with ferritic-pearlitic and ferritic-bainitic microstructures using simulated ICHAZ specimens.

- Investigation of the toughness of simulated CGHAZ, ICCGHAZ and ICHAZ test specimens in the as-simulated and post weld heat treated (PWHT) conditions.
- Evaluation of impact and CTOD toughness by multiple linear regression analyses using the microstructures, area fraction of M-A constituents, largest ferrite-bainite packet size and hardness as independent variables.

The main novel findings in this research work systematically evidenced the significant influence of the ICHAZ, as well as the distribution of M-A constituents plus microstructure of the matrix, on toughness of the low heat input weld HAZ as follows:

- A uniform distribution of M-A particles between intragranularly nucleated ferritic-bainitic laths, achieved using titanium killing of steel, improves the toughness of the overall low heat input weld HAZ far more than a low area fraction ($\leq 6\%$), small size and preferable type of these as emphasized in the previous research works. The improvement of the toughness of the ICCGHAZ is caused by a uniform distribution of M-A constituents. The distribution of M-A constituents also depends on the surrounding matrix microstructure. A uniform distribution of M-A constituents can markedly reduce their embrittling effect on the ICCGHAZ. These features emphasize the significance of the ICHAZ, rather than the ICCGHAZ, on the toughness of the low heat input weld HAZ.
- By avoiding microalloying with niobium and using copper and nickel improves the toughness of the ICCGHAZ significantly due to a tempering of martensitic-bainitic microstructure as a result of the second thermal cycle. This, in conjunction with stress relaxation of the matrix and the increase of ferritic-bainitic microstructures at the expense of bainitic-martensitic structures (a consequence of the intercritical thermal cycle), makes the ICHAZ the most critical sub-zone instead of the CGHAZ and ICCGHAZ, when it comes to low heat input weld HAZ.

5 Experimental procedure

5.1 Test materials

5.1.1 Chemical composition and preparation of the test plates

The test plates A, B and C were chosen for looking at alternative ways of producing steel grade S420ML at a thickness of 50 mm from the point of view of HAZ toughness at low heat input. Since thermomechanically controlled rolled and accelerated cooled (TMCP) and niobium microalloyed plates, like plate A (plate no. 82912-31), are known to be problematic from the point of view of ICHAZ toughness at low heat input ($t_{8/5} \approx 5$ s). The recrystallization controlled rolled and accelerated cooled (RCR) and copper and nickel alloyed plates B and C were chosen for the test plates. Plate B (plate no. 37642-11) was titanium microalloyed and plate C (plate no. 11172-21) was a vanadium microalloyed plate from vacuum degassed titanium killed charge from which normalized rolled and air cooled alternative test plate D (plate no. 11172-13) also originated. Steel for plates A and B was calcium treated with contents of 0.0015% and 0.0034% respectively. All test plates were produced by Rautaruukki Oyj at Raahe Steel Works. The chemical composition of the test plates are given in Table 3.

Table 3. Chemical composition (wt-% in ladle analysis and ppm in product analysis) of the test plates.

Plate	C	Si	Mn	P	S	Al	Nb	V	Ti	Cu	Ni	N ¹⁾ ppm	O ¹⁾ ppm	CEV
A	.074	.24	1.50	.015	.002	.041	.039	.012	.016	.01	.21	49	14	.35
B	.10	.21	1.58	.017	.007	.035	.001	.020	.013	.30	.34	51	37	.41
C&D	.087	.16	1.57	.012	.005	<.002	.004	.074	.014	.29	.40	46	48	.41

$$\text{CEV} = \text{C} + \text{Mn}/6 + (\text{Cr} + \text{Mo} + \text{V})/5 + (\text{Ni} + \text{Cu})/15$$

¹⁾ Determined from the test specimens.

5.1.2 Mechanical properties of the test plates

The mechanical properties of test plates A and B fulfilled the requirements specified for steel grades S460M/ML and titanium killed plate C the requirements specified for steel grades S420M/ML in EN 10025-4 respectively. Plate D fulfilled the requirements specified for steel grades S355N/NL in EN 10025-3 (Table 4).

Table 4. Tensile, impact and CTOD test results from the test plates.

Plate	Thickn. (mm)	Tensile tests			Impact tests ¹⁾			CTOD tests ¹⁾	
		R _{eH} (N/mm ²)	R _m (N/mm ²)	A ₅ (%)	KV _T (+23°C) (J)	T _{27J} (°C)	T _{50%} (°C)	CTOD(+23°C) (mm)	T _{0.1mm} (°C)
A	50	468	587	26	>281	-78	-56	0.42	-103
B	50	518	623	19	164	-95	-13	0.14	-40
C	50	420	537	22	259 (0 °C)	-92	-84	0.28	-99
D	12	379	493	29	227	-68	-32	0.41	-99

¹⁾ 10x10 mm specimens

5.1.3 Rolling of the test plates

Recrystallized controlled rolled and accelerated cooled test plates B and C were manufactured using a slab heating temperature of 1160 °C, a finish rolling temperature of 1000 °C, a finish cooling temperature of 580 °C and an accelerated cooling rate of 7 °C/s. Not considering the very last pass, the normal recrystallized rolling schedule consisted of the three last passes with reductions of 19–24%. The test plate A was a conventional thermomechanically rolled and accelerated cooled plate using a finish rolling temperature of 770 °C, a finish cooling temperature of 580 °C and an accelerated cooling rate of 8 °C/s. The normalized rolled test plate D was rolled in the normalizing temperature range and cooled in air.

5.1.4 Analyses of the inclusions in the test plates

The quantitative characterization of non-metallic inclusions was carried out at CSM in cooperation with a European Coal and Steel (ECSC) R&D project “*Heterogenous nucleation of acicular ferrite for toughness improvement of HSLA steels*”, in which Rautaruukki Oyj, Raahel Steel Works manufactured and tested titanium killed plate C and an aluminium killed plate from the same charge as plate A (Anelli *et al.* 2002). However, the quantitative characterization of non-metallic inclusions of plate B and the comparative analyses of plate C were carried out at the University of Oulu.

The analyses of inclusions were carried out using SEM/EDS and automatic image analysis (AIA) of CSM using a magnification of x1000. The analysed area was 6400 µm² for each field, and about 100 fields for each plate were analysed covering the total

measured area between 0.6 and 2.5 mm² per steel. Inclusions with an area larger than 0.5 μm² were characterized. In the SEM/EDS analysis at the University of Oulu, a scanning electron microscope Jeol JSM-6400 with an accelerated voltage of 20 kV and a magnification of x1000 was applied. The chemical composition of inclusions was measured using the EDS analyzer INCA and they were characterized using the automatic image analysis (AIA) program INCAFeature. The analysed area was 8540 μm² for each field, and the total amount of 141 fields for plate B and 156 fields for plate C was analysed covering the total measured area of 1.3 and 1.2 mm² respectively. Inclusions with a length larger than 0.12 μm were characterized. In the optical microscopy analysis a magnification of x500 was applied. The analysed area was 68352 μm² for each field, and about 100 fields for each plate were analysed covering the total measured area of 6.8 mm² per plate. Inclusions with an area larger than 0.5 μm² were characterized using automatic image analysis (AIA) program Image Processing Tool Kit v. 5. The number per unit area N_A and length as diameter d_A were measured for a calculation of a volume fraction of inclusions V_v using equations (2)-(4) (Table 5).

Table 5. Measured and calculated data from the characterization of non-metallic inclusions of test plates.

Plate	SEM/EDS at CSM				SEM/EDS at Oulu			Optical at Oulu		
	V_v ¹⁾ (10 ⁻⁴)	V_v ²⁾ (10 ⁻⁴)	N_A (no/mm ²)	d_A (μm)	V_v ²⁾ (10 ⁻⁴)	N_A (no/mm ²)	d_A (μm)	V_v ²⁾ (10 ⁻⁴)	N_A (no/mm ²)	d_A (μm)
A	0.2	5.5	119	1.9	-	-	-	-	-	-
B	4.0	-	-	-	17.0	249	2.3	13.4	142	2.7
C	3.5	53.5	303	3.7	6.2	751	0.8	6.5	69	2.7

¹⁾ Calculated according to equation (1). ²⁾ Calculated according to equations (2)-(4).

The analyses of inclusions in titanium killed plate C showed that titanium and manganese oxides were situated in the core of the inclusions and manganese sulphides around the inclusions or on one side of them (Fig. 28). The chemical composition of inclusions consisted of 34% TiO₂, 34% MnS and 32% MnO (Anelli *et al.* 2002).

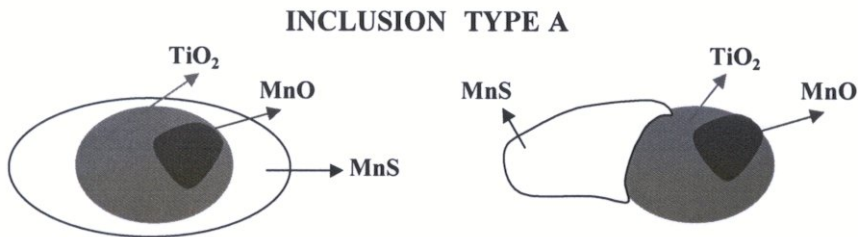


Fig. 28. Type of inclusions in titanium killed plate C (Anelli *et al.* 2002).

In inclusions of aluminium killed plates from the same charge as plate A contained 30–35% Al₂O₃, 20–30% TiO₂, 20–25% MnS and 15–25% MnO (Anelli *et al.* 2002). Aluminium oxides (Al₂O₃) were situated in the core and manganese and titanium oxides

(MnO and TiO₂) on the surface of the aluminium oxides and finally manganese sulphides around the inclusions (Fig. 29).

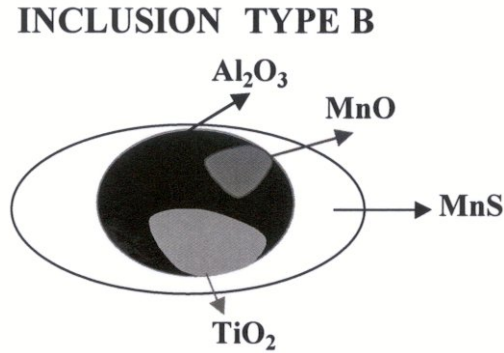


Fig. 29. Types of inclusions in aluminium killed plate from the same charge as plate A (Anelli *et al.* 2002).

The average chemical composition of inclusions (8.3% Al, 2.4% Si, 22.9% S, 11.2% Ca, 5.8% Ti and 49.4% Mn) in aluminium killed plate B analysed using EDS at the University of Oulu showed that aluminium, calcium, manganese and titanium oxides and manganese sulphides were the main components in the inclusions. The comparison with the average chemical composition of inclusions (2.5% Al, 1.9% Si, 19.6% S, 0.7% Ca, 11.4% Ti and 63.9% Mn) in titanium killed plate C revealed that the inclusions in plate C consisted of more titanium and manganese oxides and less aluminium and calcium oxides than those in plate B.

5.1.5 Heat treatments to obtain a significant amount of acicular ferritic microstructure contained test pieces

The optimal heat treatment of the test pieces from titanium killed plate D needed to achieve a significant amount of acicular ferritic microstructure was based on physical simulations carried out using a Gleeble 1500 simulator at the University of Oulu. Heating for 1h at 1300 °C to increase the prior austenite grain size and cooling at 10 °C/s to 500 °C was found to cause the intragranular nucleation of acicular ferrite in plates C and D. Then some 150x250 mm size test pieces from plate D were heated for 1 hour at 1300 °C in the argon flow furnace (at the University of Oulu), followed by cooling at 6–12 °C/s to 500 °C to obtain a significant amount of acicular ferrite in microstructure. This test was also conducted at the University of Oulu.

5.2 Simulation of the weld heat affected zones

5.2.1 Test specimens and simulation programmes

The test specimens were taken 2 mm under a plate surface transverse to the rolling direction of each test plate and test piece. Simulations were carried out using a Gleeble 1500 simulator at the University of Oulu with an evacuated chamber and a free span of 10 mm for $t_{8/5} = 5$ s ($t_{8/5}$ is the cooling time from 800 to 500 °C), when the size of the specimen was 10x10x70 mm. Simulation of the coarse grained HAZ (CGHAZ), intercritically reheated coarse grained HAZ (ICCGHAZ) and intercritical HAZ (ICHAZ) using a cooling time $t_{8/5} = 5$ s were carried out (Table 6).

Table 6. The thermal cycles for the simulations of HAZs.

	CGHAZ	ICCGHAZ	ICHAZ
Heating for first peak	100 °C/s to 1300 °C	100 °C/s to 1300 °C	n.a.
1st Peak Tp1	50 °C/s to 1350 °C	50 °C/s to 1350 °C	n.a.
Holding time at 1350 °C	1 s	1 s	n.a.
Cooling time $t_{8/5}$	5 s	5 s	n.a.
Min. temp. between peaks	n.a.	300 °C	n.a.
Heating for second peak		100 °C/s	100 °C/s
2nd Peak Tp2	n.a.	770 °C	770 °C
Holding time at peak	n.a.	1 s	1 s
Cooling programme	3D	3D	3D
Cooling time " $t_{8/5}$ "	n.a.	5 s	5 s
Free cooling below	300 °C	300 °C	300 °C

5.2.2 Mechanical testing of simulated specimens

The testing programme of simulated specimens consisted of the following mechanical tests:

- Impact tests at +60...–120 °C using Charpy V 10x10 mm through thickness notched specimens. The transition curves of the impact energy and the ductile fracture as an average value of two specimens in each temperature and the transition temperatures T_{27J} and $T_{50\%}$ were determined.
- CTOD tests at +40...–120 °C according to BS 7448-1:1991 using 10x10 mm through thickness notched specimens. The transition curves of the crack opening displacement as a lowest value of two specimens in each temperature and the 0.1 mm transition temperature $T_{0.1mm}$ were determined.
- Hardness measurements (HV 10) over the heat treated zone close to the surfaces and along the centre of it. The test results were the average values measured along the centre of the heat treated zone.

- Charpy V and CTOD tests and hardness measurements on the simulated ICCGHAZ and ICHAZ specimens were also carried out on post weld heat treated (PWHT) specimens (4 h at 600 °C).

5.2.3 Metallography

Metallographical investigations were carried out using optical microscopes (OM) Nikon Epiphot 300 and Olympus BH-2-UMA, a scanning electron microscope (SEM) JEOL JXA-8600 and an image analyses (AIA) Leco 486 with a program Image Analysis 3005 at the Research Centre of Rautaruukki Oyj. The electron backscatter diffraction (EBSD) device Link, Opal, was used for the investigation of grain orientations and a transmission electron microscope (TEM) LEO 912 OMEGA for the examination of precipitations at the Institute of Electron Optics of the University of Oulu. The following microstructural observations and quantitative analyses were performed:

- Investigation of basic microstructures such as ferrite, bainite, pearlite and martensitic constituents was carried out in the optical microscope using 2% Nital (2% nitric acid HNO_3 in ethyl alcohol) etching.
- Prior austenite grain sizes from the slab and rolling simulation specimens were evaluated using 2% picral (2% picric acid $\text{C}_6\text{H}_2(\text{NO})_3\text{OH}$ in ethyl alcohol). Etching revealed the prior austenite grain boundaries and estimated comparative charts using ASTM. Austenite grain sizes of the base plate and the ICCGHAZ were measured on the basis of primary grain boundary ferrite and M-A constituents along the prior austenite grain boundaries. The diameters of the three largest and mean grains from six different fields (sizes $605 \times 468 \mu\text{m}^2$ and $712 \times 530 \mu\text{m}^2$) in the specimens were measured, and the results were calculated as an average value of 18 measurement points of each test specimen.
- Evaluation of the relative proportions of the microstructural constituents such as primary grain boundary ferrite (PF(G)), intragranular polygonal ferrite (PF(I)), acicular ferrite (AF), ferrite with aligned second phase (FS(A)), ferrite with non-aligned second phase (FS(NA)), ferrite carbide aggregate included pearlite (FC) and martensite (M) were counted from 2% Nital etched specimens on a monitoring head using a magnification of x1400 connected with an optical microscope with a magnification of x500. Overall, six hundred points were measured from each specimen consisting of 100 counting points in each field (size $128.57 \times 128.57 \mu\text{m}^2$) (Welding in the World 1991, Harrison & Webster 1994).
- Investigation of the misorientation angles between the adjacent grains or packets from cross-sections and sides of the simulated ICCGHAZ and ICHAZ specimens were carried out using electron backscatter diffraction (EBSD) analyses. Specimens were polished electrochemically in the following solutions: 70% ethanol, 12% distilled water, 10% butanol and 8% perchloric acid, operating at 30 V and -30 °C and 32.5% nitric acid (60% HNO_3), 67.5% methanol, operating at 8 V and -35 °C. The misorientation line plot histograms were measured using a pixel size of 1145 nm and a grid size of 507x3 including 1536 points. The misorientation area plot histograms and

grain size distributions were measured using a pixel size of 1832 nm and a grid size of 53x34 including 1802 points.

- The amount of M-A constituents were measured using LePera etching (LePera 1980) consisting of a mixture of 1% sodium metabisulphite ($\text{Na}_2\text{S}_2\text{O}_5$) in distilled water and 4% picric acid $\text{C}_6\text{H}_2(\text{NO})_3\text{OH}$ in ethyl alcohol. After etching, the area fraction of white coloured M-A constituents was measured on a monitoring head using a magnification of x1400 and x2800 connected with an optical microscope with magnifications of x500 and x1000 respectively. Twelve different fields were analysed from each specimen covering $139650 \mu\text{m}^2$ with a magnification of x1000 and $541985 \mu\text{m}^2$ with a magnification of x500. The type and distribution of M-A constituents were evaluated using 1% sodium bisulphite (Na_2HSO_3) etching. This preparation made retained austenite appear white and martensite appear brown in M-A constituents.
- Measurements of the largest cleavage facet sizes (CFS) and the largest ferrite grain and bainite packet sizes were performed from the profiles of the brittle cracked specimens using 2% Nital etched specimens with an optical microscope. Twenty great cleavage fractured sides (ten from each fractures surface) and the fifty largest ferrite grains and bainite packets from ten different fields (five from each field) were measured from a crack initiation point of each specimen.
- Crack nucleation and propagation mechanisms were evaluated using an optical (OM) and scanning electron microscope (SEM) from 2% Nital etched specimens.
- The characterization of precipitates was examined using carbon extraction replicas and a transmission electron microscope (TEM) at the University of Oulu.
- Metallography from the simulated ICCGHAZ and ICHAZ specimens was carried out using the as-simulated and post weld heat treated (PWHT) specimens (4 h at 600 °C).

6 Test results

6.1 Simulation heat treatments and preparation of acicular ferritic microstructure contained test pieces

Microstructure of titanium killed plate C and rolling simulated specimens showed that acicular ferritic microstructure was not achieved and was probably due to a too small prior austenite grain size of 50–90 μm (average about 70 μm and the largest 116 μm). Therefore, coarsening of the austenite grain up to about 120–180 μm was carried out using simulated heat treatments for 20 min at 1250 $^{\circ}\text{C}$ and 3 min at 1300 $^{\circ}\text{C}$ and cooling at 10 $^{\circ}\text{C}/\text{s}$ to 500 $^{\circ}\text{C}$, when mainly acicular ferritic microstructure was achieved.

Consequently, two test pieces (size 12x150x250 mm) from test plate D were prepared on the accelerated cooling line at the University of Oulu. By heating for 1 h at 1300 $^{\circ}\text{C}$ the largest and the average-sized austenite grains coarsened up to 323 μm and up to 212 μm in the test piece D1 and up to 293 μm and up to 183 μm in the test piece D2 respectively. The accelerated cooling rates between 1000 and 500 $^{\circ}\text{C}$ were 11.2 $^{\circ}\text{C}/\text{s}$ for test piece D1 and 6.8 $^{\circ}\text{C}/\text{s}$ for test piece D2.

Microstructure of the test pieces contained over 60% intragranularly nucleated ferrite including 26–32% acicular ferrite (AF) and 32–36% polygonal ferrite (PF(I)) with the remaining being mainly ferrite with non-aligned second phase (FS(NA)) and primary grain boundary ferrite (PF(G)) (Figs 30 and 31). A star like nucleation of ferrite on some inclusions was found.

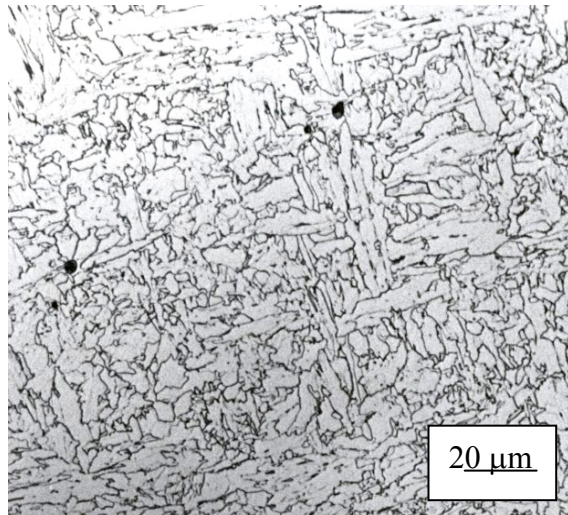


Fig. 30. Microstructure of the test piece D1 contained 15% PF(G), 32% PF(I), 32% AF, 3% FS(A), 17% FS(NA) and 1% Martensite.

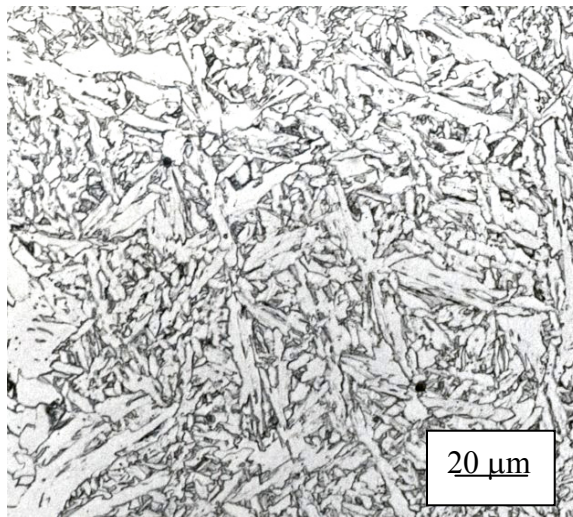


Fig. 31. Microstructure of the test piece D2 contained 16% PF(G), 36% PF(I), 26% AF, 2% FS(A), 19% FS(NA) and 1% Martensite.

6.1.1 Summary of paragraph 6.1

In summary, acicular ferritic microstructure was not achieved in the rolled test plate C and the rolling simulation specimens from it probably due to too small a prior austenite

grain size of 50–90 μm (average about 70 μm and the largest 116 μm). However, the simulation heat treatments showed that mainly acicular ferritic microstructure could be achieved in the specimens of plate C by heating for 20 min at 1250 $^{\circ}\text{C}$ or 3 min at 1300 $^{\circ}\text{C}$ and cooling at 10 $^{\circ}\text{C}/\text{s}$ to 500 $^{\circ}\text{C}$, when the prior austenite grain size was about 120–180 μm . Consequently, two test pieces were prepared using a furnace heat treatment by heating 1 h at 1300 $^{\circ}\text{C}$ followed by accelerated cooling at 6.8 $^{\circ}\text{C}/\text{s}$ and 11.2 $^{\circ}\text{C}/\text{s}$ to 500 $^{\circ}\text{C}$. Over 60% intragranularly nucleated ferrite including 26–32% acicular ferrite (AF) and 32–36% polygonal ferrite PF(I) was achieved in two test pieces, when the largest prior austenite grain sizes were 323 μm and 293 μm and the average of them 212 μm and 183 μm respectively.

6.2 Toughness of the simulated HAZ zones

Evaluation of toughness was carried out using Charpy V impact and fracture toughness CTOD testing. The test results were plotted as ductile-brittle transition temperatures T_{27J} and $T_{50\%}$ defined from the average transition curves of the Charpy V impact tests and $T_{0.1\text{mm}}$ defined from the lower bound transition curves of the CTOD tests. The test results are summarised in Figs 32–37 and in Appendix 1, Table 11.

6.2.1 Impact toughness

The transition temperatures T_{27J} and $T_{50\%}$ (Figs 32–35) showed that the ICHAZ was the weakest sub-zone in the weld HAZ at low heat input welding due to a remarkably high increase in the transition temperature resulting from the intercritical thermal cycle applied to the base plate. Even though plate A had a poorer toughness in the ICCGHAZ due to a significant elevation of the transition temperatures T_{27J} and $T_{50\%}$ as a result of the intercritical thermal cycle of the CGHAZ, in the real weld the ICHAZ showed a poorer toughness because the ICCGHAZ sub-zones are very limited in size, whereas the ICHAZ stretches through the whole thickness of the plate.

Plate D, with a ferritic-pearlitic microstructure, had the poorest toughness of the ICHAZ due to a considerable elevation of transition temperatures T_{27J} and $T_{50\%}$ caused by the intercritical thermal cycle. Toughness of the ICHAZ of the heat treated test piece D1 from plate D was a little lower than that of test plates A, B and C. But elevation of the transition temperatures T_{27J} and $T_{50\%}$, as a result of the intercritical thermal cycle of the heat treated test piece D1, was smaller than in the test plates except for the transition temperature $T_{50\%}$ of plate B because of the high transition temperature $T_{50\%}$ (-13 $^{\circ}\text{C}$) in the base plate.

Post weld heat treatment (PWHT) improved impact toughness of the ICCGHAZ and ICHAZ of all test plates roughly to the same level as that of the CGHAZ and the base plate respectively.

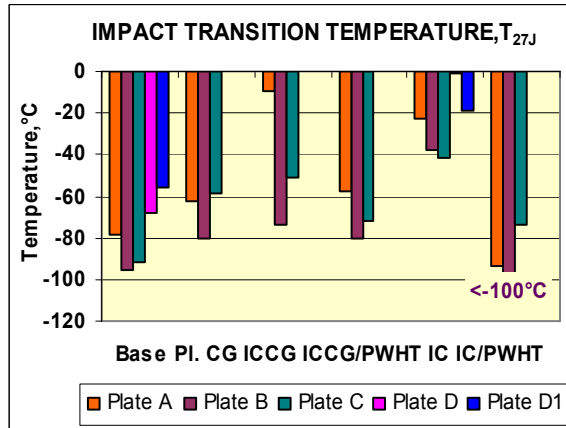


Fig. 32. Impact transition temperatures T_{27J} of base plates and the simulated HAZ zones (Base Pl.= Base plate, CG=CGHAZ, ICCG=ICCGHAZ, ICCG/PWHT=ICCGHAZ+PWHT, IC=ICHAZ and IC/PWHT=ICHAZ+PWHT).

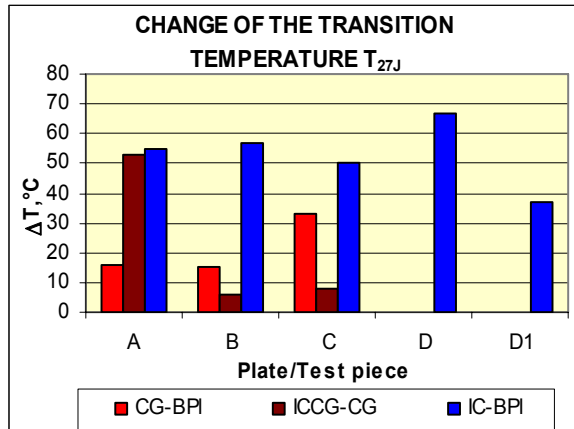


Fig. 33. Change of the impact transition temperature T_{27J} of the CGHAZ-base plate (CG-BPI), the ICCGHAZ-CGHAZ (ICCG-CG) and the ICHAZ-base plate (IC-BPI).

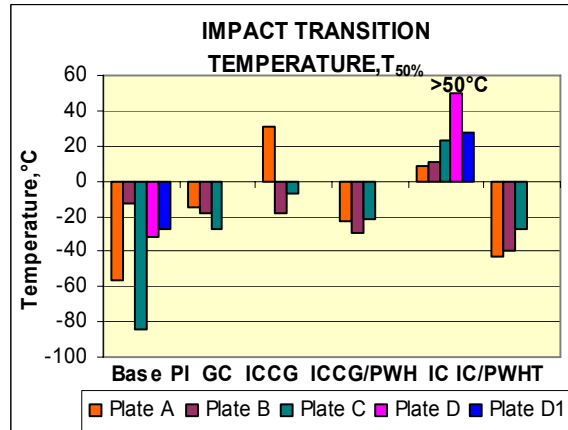


Fig. 34. Impact transition temperatures $T_{50\%}$ of base plates and the simulated HAZ zones (Base Pl.= Base plate, CG=CGHAZ, ICCG=ICCGHAZ, ICCG/PWHT= ICCGHAZ+PWHT, IC=ICHAZ and IC/PWHT=ICHAZ+PWHT).

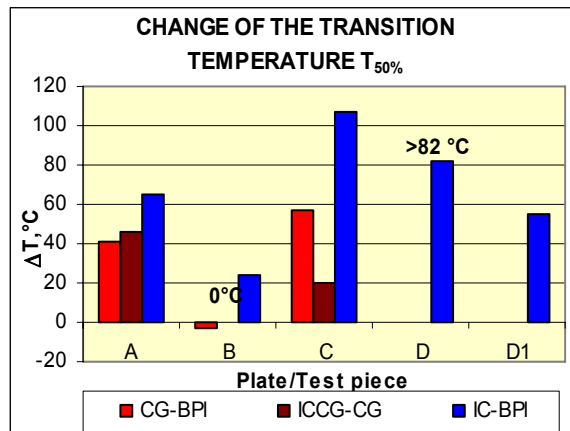


Fig. 35. Change of the impact transition temperature $T_{50\%}$ of the CGHAZ-base plate (CG-BPI), the ICCGHAZ-CGHAZ (ICCG-CG) and the ICHAZ-base plate (IC-BPI).

6.2.2 Fracture toughness

The CTOD transition temperatures $T_{0.1\text{mm}}$ (Figs 36–37) showed that the CGHAZ was the weakest sub-zone in the weld HAZ of plate B and the CGHAZ plus ICCGHAZ in that of plate A. The best fracture toughness in the CGHAZ was observed in plate C. The high CTOD transition temperature $T_{0.1\text{mm}}$ in the ICCGHAZ (+10 °C) emphasized an impairment of toughness of the HAZ in plate A, whereas the extremely low CTOD

transition temperature ($-66\text{ }^{\circ}\text{C}$) in the ICCGHAZ improved toughness of the HAZ in plate B. The high CTOD transition temperatures $T_{0.1\text{mm}}$ in the CGHAZ and particularly in the ICCGHAZ of plate A were caused by the high increase of transition temperature $T_{0.1\text{mm}}$ as a result of the CGHAZ thermal cycle of the base plate and the intercritical thermal cycle of the CGHAZ. Also, the ICHAZ of plate A had a poorer fracture toughness than that of plates B and C due to a higher increase of the transition temperature as a result of the intercritical thermal cycle of the base plate. The lowest changes of the CTOD transition temperature $T_{0.1\text{mm}}$, as a result of the intercritical thermal cycle of the CGHAZ and the base plate, were observed in plate B due to the high CTOD transition temperature $T_{0.1\text{mm}}$ of the CGHAZ and the base plate.

The poorest fracture toughness in the ICHAZ was shown in the ferritic-pearlitic plate D due to the highest elevation of the transition temperature $T_{0.1\text{mm}}$ ($99\text{ }^{\circ}\text{C}$) as a result of the intercritical thermal cycle. Also, the fracture toughness of the heat treated test piece D2 was poorer than that of test plates A, B and C, but elevation of the transition temperature $T_{0.1\text{mm}}$, as a result of the intercritical thermal cycle, was significantly smaller in the heat treated test piece D2 than in plate D and a little smaller than in plates A and C.

Post weld heat treatment (PWHT) improved the fracture toughness of the ICCGHAZ of plates A and B significantly, but impaired it in plate C. The fracture toughness of the ICHAZ was improved by post weld heat treatment (PWHT) roughly to the same level as that of the base plate in plate C and even better in plate B, but the improvement of fracture toughness in plate A was significantly smaller than in plates B and C.

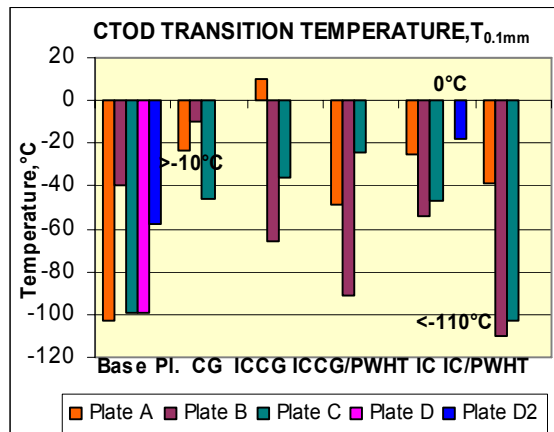


Fig. 36. CTOD transition temperatures $T_{0.1\text{mm}}$ of base plates and the simulated HAZ zones (Base Pl.= Base plate, CG=CGHAZ, ICCG=ICCGHAZ, ICCG/PWHT= ICCGHAZ+PWHT, IC=ICHAZ and IC/PWHT=ICHAZ+PWHT).

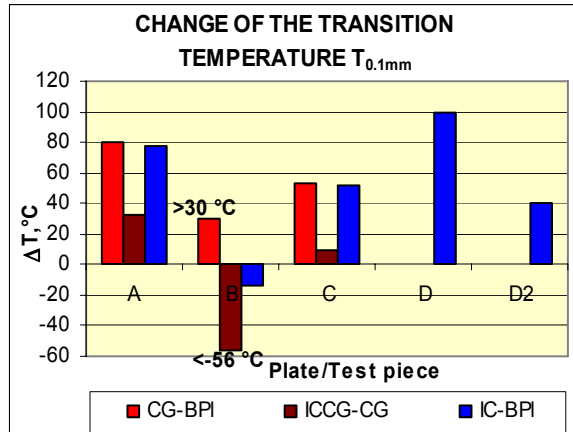


Fig. 37. Change of the CTOD transition temperature $T_{0.1mm}$ of the CGHAZ-base plate (CG-BPI), the ICCGHAZ-CGHAZ (ICCG-CG) and the ICHAZ-Base plate (IC-BPI).

6.2.3 Summary of paragraph 6.2

In summary, the impact and fracture toughness transition temperatures T_{27J} , $T_{50\%}$ and $T_{0.1mm}$ exhibited similar trends concerning a comparison of toughness of the most critical sub-zones of the weld HAZ in the test plates. In impact tests the ICHAZ was the weakest sub-zone of the weld HAZ due to a remarkably high increase of the transition temperatures T_{27J} and $T_{50\%}$ as a result of the intercritical thermal cycle of the base plate. In fracture toughness CTOD tests the CGHAZ was the weakest sub-zone of the weld HAZ in plate B and the CGHAZ plus ICCGHAZ in plate A, but the best fracture toughness in the CGHAZ of the weld HAZ was observed in plate C. A poor toughness in the ICCGHAZ, as a result of intercritical thermal cycle of the CGHAZ, emphasized an impairment of toughness of the CGHAZ plus ICCGHAZ in plate A, whereas an extremely good toughness in the ICCGHAZ improved toughness of the CGHAZ plus ICCGHAZ in plate B.

The poorest impact and fracture toughness of the ICHAZ was exhibited by ferritic-pearlitic microstructure containing plate D due to a remarkable elevation of transition temperatures T_{27J} , $T_{50\%}$ and $T_{0.1mm}$ as a result of the intercritical thermal cycle. Impact and fracture toughness of the ICHAZ of the heat treated test pieces D1 and D2 was a little poorer than test plates A, B and C. However, the elevation of transition temperatures T_{27J} , $T_{50\%}$ and $T_{0.1mm}$, as a result of the intercritical thermal cycle, was smaller than in plates A and C, but not in plate B where the intercritical thermal cycle even decreased the transition temperatures $T_{50\%}$ and $T_{0.1mm}$ due to their high temperatures in the base plate.

Post weld heat treatment (PWHT) improved impact toughness of the ICCGHAZ and ICHAZ of all test plates roughly to the same level as that of the CGHAZ and base plate respectively. Similarly, the improvement of fracture toughness was significant in the

ICCGHAZ and ICHAZ of test plates, except for the impairment of the ICCGHAZ in plate C.

6.3 Microstructures of the simulated HAZ zones and their influence on impact and fracture toughness

6.3.1 Microstructural analyses

Evaluation of the percentages of the microstructural constituents showed that primary grain boundary ferrite PF(G) was the main microconstituent in test plates A, B and C in addition to intragranularly nucleated polygonal ferrite PF(I) in plates A and C and ferrite with non-aligned second phases FS(NA) in plates B and C. However, intragranularly nucleated polygonal ferrite PF(I) and acicular ferrite (AF) dominated in the heat treated test pieces D1 and D2 from ferritic-pealitic microstructure containing plate D (Table 7, Appendices 2–5, Figs 87a–90a,c,e).

In the CGHAZ of test plates A, B and C, ferrite with non-aligned second phases (FS(NA)) and primary grain boundary ferrite PF(G) were the main microconstituents in addition to ferrite with aligned second phases FS(A) in plate A, martensite (M) in plate B and acicular ferrite (AF) in plate C (Table 7, Appendices 2–4, Figs 87b–89b).

The percentages of the microstructural constituents in the ICCGHAZ showed that plate A contained more primary grain boundary ferrite PF(G) plus ferrite with second phase microconstituents (FS(A)+FS(NA)) than plates B and C, where the microstructure consisted of more intragranularly nucleated microconstituents (AF+PF(I)) than in plate A. So, a relative proportion of ferrite with non-aligned second phases FS(NA) was decreased as a result of the intercritical thermal cycle of the CGHAZ in all test plates, whereas the percentages of intragranularly nucleated micro-constituents (AF+PF(I)) were increased particularly in plates B and C, but primary grain boundary ferrite PF(G) was increased in plate A (Table 7, Appendices 2–4, Figs 87c–89c).

The microstructural constituents in the ICHAZ of test plates A, B and C consisted mainly of primary grain boundary ferrite PF(G) and intragranularly nucleated polygonal ferrite PF(I), but the proportions of primary grain boundary ferrite PF(G) in plate A and acicular ferrite (AF) in plate B were higher than in the other test plates. So, the intercritical thermal cycle of the base plate increased a relative proportion of intragranularly nucleated polygonal ferrite PF(I) and decreased ferrite with second phase microconstituents (FS(A)+FS(NA)) in test plates A, B and C (Table 7, Appendices 2–4, Figs 87d–89d).

Table 7. Relative percentages of the microstructural constituents and hardness of the base plate, CGHAZ, ICCGHAZ and ICHAZ.

Test specimen	PF(G)	PF(I)	AF	FS(A)	FS(NA)	FC	M	M-A ¹⁾	Hardn. (HV)
Plate A	32	39	8	5	13	3	-	-	211
Plate B	26	16	11	10	28	1	8	-	245
Plate C	23	29	6	11	25	4	2	-	200
Plate D	-	-	-	-	-	-	-	-	180
Plate D1	15	32	32	3	17	-	-	1	202
Plate D2	16	36	26	2	19	-	-	1	202
A CGHAZ	19	5	11	23	34	-	8	-	262
B CGHAZ	21	6	14	6	29	-	24	-	295
C CGHAZ	24	6	20	13	27	-	10	-	280
A ICCGHAZ	27	12	14	21	17	3	-	6	237
B ICCGHAZ	14	14	37	15	12	4	-	4	235
C ICCGHAZ	26	19	28	8	13	3	-	3	240
A ICHAZ	42	44	3	-	1	-	-	10	213
B ICHAZ	25	46	17	1	-	1	-	10	197
C ICHAZ	31	50	5	-	3	2	-	9	200
D ICHAZ	-	-	-	-	-	-	-	-	197
D1 ICHAZ	5	50	27	-	8	-	-	10	210
D2 ICHAZ	18	35	15	1	21	-	-	10	202

¹⁾Evaluation of M-A constituents using 2% Nital etched specimens is only approximate.

In plate D the intercritical thermal cycle converted the pearlite bands in ferritic-pearlitic microstructure into M-A constituents (Appendix 5, Figs 90a and 90b). In the heat treated test piece D1, the intercritical thermal cycle increased relative proportions of intragranularly nucleated polygonal ferrite PF(I) and M-A constituents, but decreased primary grain boundary ferrite PF(G), ferrite with non-aligned second phase FS(NA) and a little acicular ferrite (AF) (Table 7, Appendix 5, Figs 90c and 90d). In the heat treated test piece D2, the intercritical thermal cycle decreased a relative proportion of acicular ferrite (AF) and increased that of M-A constituents using this evaluation, but did not increase it significantly using LePera etching and image analysis (Table 7, Appendix 1, Table 12, Appendix 5, Figs 90e and 90f).

6.3.2 Microstructural investigation on the basis of hardness measurements

Hardness measurement has normally been used for identification of microstructural constituents, but in addition it also reflects the contribution of dislocation, solid solution and precipitation strengthening. Normally, microhardness measurement has been used to identify individual microconstituents in the CGHAZ. Although the microhardness ranges of each microconstituent in the CGHAZ has been found to depend on heat input (welding

method), it is confirmed that primary grain boundary ferrite PF(G) and intragranularly nucleated polygonal ferrite PF(I) are softer than ferrite with aligned second phase FS(A) and acicular ferrite (AF). Microhardness of martensite H_M and bainite H_B can be calculated according to the following equations (Kojima *et al.* 1999):

$$H_M = 884xC(1-0.3xC^2)+294 \quad (14)$$

$$H_B = 197xCE_{II}+117 \quad (CE_{II} \ll 0.75) \quad (15)$$

$$CE_{II} = C+Si/24+Mn/5+Cu/10+Ni/18+Cr/5+Mo/2.5+V/5+Nb/3 \quad (16)$$

The hardness values of martensite and bainite based on the bulk carbon and alloy contents of the plates calculated according to equations (14)-(16) are shown in Table 8.

Table 8. Calculated hardness values of martensite and bainite in the test plates.

Test plate	Martensite	Bainite
Plate A	359	199
Plate B	382	212
Plate C	371	212

Comparison of hardness test results (Table 7) and the calculated hardness values (Table 8) showed that the microstructure in plates A and B was ferritic-bainitic and mainly ferritic in plates C and D and the heat treated test pieces D1 and D2. Local martensite in the microstructure of plate B probably increased hardness. The higher hardness values (202 HV) in the heat treated test pieces D1 and D2 than in the specimens (180 HV) from plate D showed that they contained higher hardness ferrite constituents such as ferrite with non-aligned second phase FS(NA) and acicular ferrite (AF) compared with the softer ferritic-pearlitic microstructure in the specimens from plate D.

Relatively high hardness in the CGHAZ of test plates A, B and C showed that their ferrite, with second phase microconstituents (FS(A)+FS(NA)), contained mainly bainite and also local martensite particularly in the specimens from plate B. Hardness of the ICCGAZ showed that the intercritical thermal cycle of the CGHAZ decreased it due to a stress relaxation and softening caused by formation of ferrite such as intragranularly nucleated polygonal ferrite PF(I), acicular ferrite (AF) and M-A constituents from ferrite with non-aligned second phase FS(NA) and local martensite.

Hardness of the ICHAZ showed that microstructure in all test plates contained mainly ferrite constituents, except for in plate A, which contained probably more bainite than the other test plates. A significant amount of M-A constituents in all test plates and acicular ferrite in the heat treated test piece D1 increased their hardness slightly. A significant decrease (48 HV) of hardness, as a result of the intercritical thermal cycle of plate B, was caused by the formation of intragranularly nucleated microconstituents PF(I), AF and M-A constituents from ferrite with second phase constituents (FS(A)+FS(NA)) and local martensite.

Post weld heat treatment (PWHT) of the ICCGHAZ decreased hardness from 4 to 18 HV and the ICHAZ from 11 to 22 HV being highest in plate B due to a decomposition of M-A constituents into carbides, which was indicated to increase hardness by an increase of M-A constituents (Appendix 1, Table 12).

Hardness measurements completed the investigation of microstructures and opened up a possibility to distinguish ferrite and bainite constituents, which belong to the same microconstituents in the microstructural analyses according to Welding in the World (1991).

6.3.3 Influence of microstructural constituents on the impact and fracture toughness of the simulated ICCGHAZ and ICHAZ specimens

Microstructural constituents are expected to have a significant influence on the toughness of the weld HAZ due to their direct influence on crack propagation and their indirect influence on crack initiation through M-A constituents in the most critical sub-zones ICCGHAZ and ICHAZ of the weld HAZ. Also, the test results in this and in a previous paragraph (6.2) show that the ICCGHAZ and ICHAZ were the most critical sub-zones in the HAZ in spite of the higher content of the intragranularly nucleated (AF+PF(I)) and the smaller content of primary grain boundary ferrite plus ferrite with second phase micro-constituents (PF(G)+FS) than in the CGHAZ (Figs 38–43). However, the very low fracture toughness of the CGHAZ of plate B (Fig. 40) was due to the presence of 24% martensite in the microstructure.

The diagrams of the relationship between the impact and fracture toughness transition temperatures T_{27J} , $T_{50\%}$ and $T_{0.1mm}$ of CGHAZ and ICCGHAZ and the microstructural constituents (Figs 38–40) showed that an increase of the intragranularly nucleated microconstituents (AF+PF(I)) and decrease of primary grain boundary ferrite, plus ferrite with second phase microconstituents, (PF(G)+FS) improved toughness.

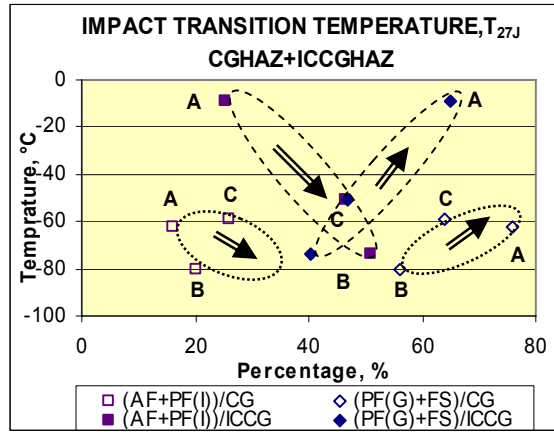


Fig. 38. Influence of the microstructural constituents ((AF+PF(I)) and ((PF(G)+FS) on the impact transition temperature T_{27J} of the CGHAZ (CG) and ICCGHAZ (ICCG) specimens.

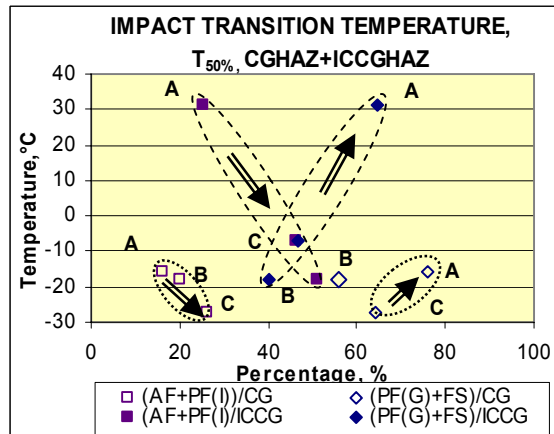


Fig. 39. Influence of the microstructural constituents ((AF+PF(I)) and ((PF(G)+FS) on the impact transition temperature $T_{50\%}$ of the CGHAZ (CG) and ICCGHAZ (ICCG) specimens.

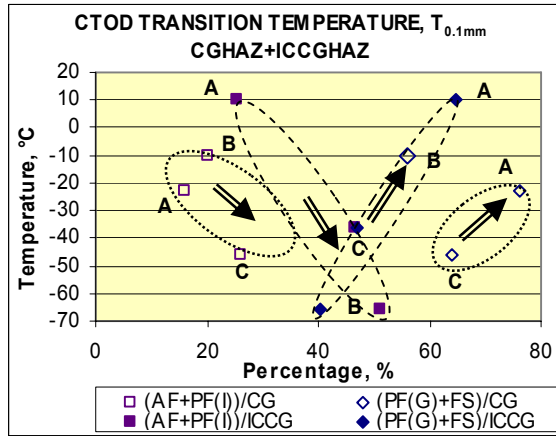


Fig. 40. Influence of microstructural constituents ((AF+PF(I)) and ((PF(G)+FS) on the CTOD transition temperature $T_{0.1mm}$ of the CGHAZ (CG) and ICCGHAZ (ICCG) specimens.

The test results from the ICHAZ of test plates A, B and C showed a similar relationship between toughness and the microconstituents (Figs 41–43). However, the effect is opposite, if the heat treated specimen D1 is taken into consideration (Figs 41–42). The heat treated test pieces D1 and D2 indicated that the other factors such as ferrite grain size, bainite packet size and M-A constituents had a stronger influence on toughness than the intragranularly nucleated microconstituents (AF+PF(I)) and primary grain boundary ferrite plus ferrite with second phase microconstituents (PF(G)+FS), as will be presented in the following paragraphs.

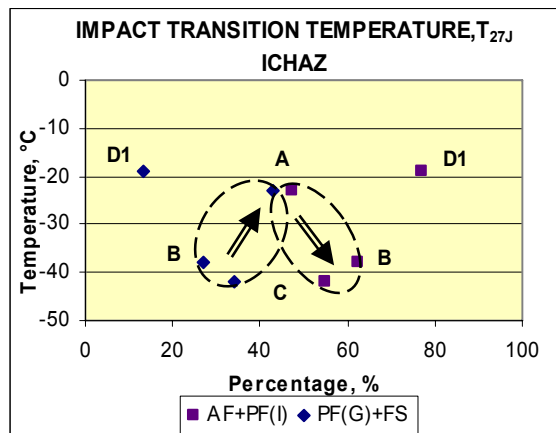


Fig. 41. Influence of the microstructural constituents ((AF+PF(I)) and ((PF(G)+FS) on the impact transition temperature T_{27J} of the ICHAZ specimens.

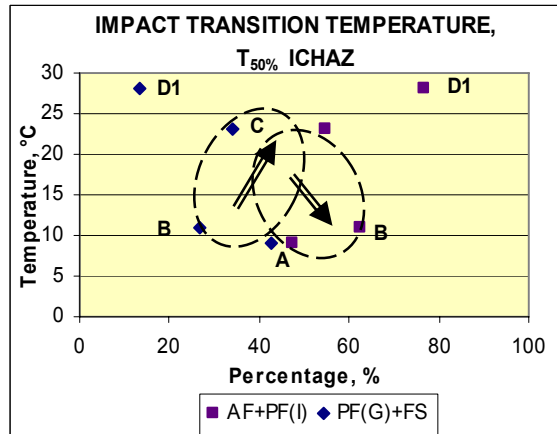


Fig. 42. Influence of the microstructural constituents ((AF+PF(I)) and ((PF(G)+FS) on the impact transition temperature $T_{50\%}$ of the ICHAZ specimens.

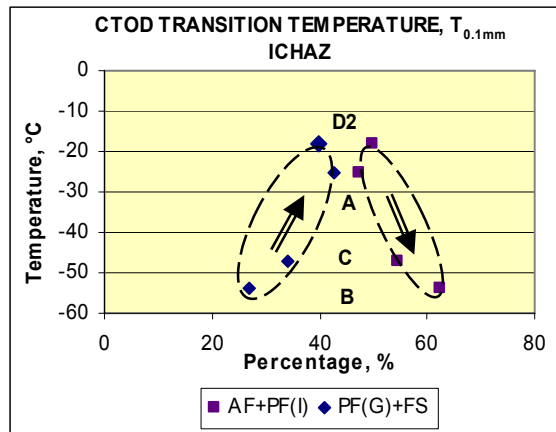


Fig. 43. Influence of the microstructural constituents ((AF+PF(I)) and ((PF(G)+FS) on the CTOD transition temperature $T_{0.1\text{mm}}$ of the ICHAZ specimens.

6.3.4 Summary of paragraph 6.3

In summary, evaluation of the microstructural constituents showed that in the CGHAZ ferrite with non-aligned second phase (FS(NA)) and primary grain boundary ferrite PF(G) were the main microconstituents in test plates A, B and C in addition to ferrite with aligned second phases FS(A) in plate A, martensite in plate B and acicular ferrite in

plate C as a result of a significant increase of them compared with the base plates. The intercritical thermal cycle of the CGHAZ increased intragranularly nucleated microconstituents ((AF+PF(I)) and decreased grain boundary ferrite plus ferrite with second phase microconstituents (PF(G)+FS) in all test plates. Similarly, the intercritical thermal cycle of the base plate increased intragranularly nucleated polygonal ferrite PF(I) and decreased ferrite with non-aligned microconstituents FS(NA) in test plates A, B C and in the heat treated test pieces D1 and D2 in addition to an increase of acicular ferrite (AF) in plate B and to a decrease of it in the heat treated test pieces D1 and D2.

The trend curves from the test results showed that the impact and fracture toughness of the most critical sub-zones CGHAZ, ICCGHAZ and ICHAZ of the weld HAZ were improved by an increase of intragranularly nucleated microconstituents (AF+PF(I)) and impaired by an increase of primary grain boundary ferrite plus ferrite with second phase microconstituents (PF(G)+FS). However, the ICCGHAZ and ICHAZ were more critical sub-zones of the weld HAZ than CGHAZ in spite of the higher content of intragranularly nucleated microconstituents (AF+PF(I)) and a smaller content of primary grain boundary ferrite plus ferrite with second phase microconstituents (PF(G)+FS) than in the CGHAZ. This indicated that factors such as ferrite grain size, bainite packet size and M-A constituents, had a stronger influence on toughness than the intragranularly nucleated microconstituents (AF+PF(I)) and primary grain boundary ferrite plus ferrite with second phase microconstituents (PF(G)+FS), as will be presented in the following paragraphs.

6.4 Grain sizes and their influence on impact and fracture toughness

6.4.1 Austenite grain size and ferrite grain and bainite packet sizes

In this research work the largest and average austenite grain sizes were measured from the base plate and the ICCGHAZ also representing those in the CGHAZ. The effective grain size including the largest ferrite grain and bainite packet sizes was assumed to have a significant influence on toughness and measured from the most critical sub-zones CGHAZ, ICCGHAZ and ICHAZ of the weld HAZ (Figs 44–46, Appendices 6–7, Tables 13–14).

The test results showed that titanium precipitates were effective in preventing austenite grain growth in the CGHAZ of plates A and C, but less effective in plate B. Titanium plus niobium precipitates (68%Ti+28%Nb) prevented austenite grain coarsening in the ICCGHAZ of plate A. But titanium plus vanadium precipitates (70%Ti+25%V) and titanium oxides suppressed austenite grain coarsening only partly in the ICCGHAZ of plate C (Appendices 8–9, Table 15, Figs 91–93). However, these precipitates and inclusions could not prevent austenite grain coarsening in the heat treated test pieces D1 and D2 from plate D by heating for 1 h at 1300 °C (Fig. 44). In the ICCGHAZ from plate B, austenite grain sizes were about twice as large as in the base plate due to a relatively high proportion of large (>100 nm) titanium precipitates (87% Ti) (Appendix 8, Table 15, Appendices 9–10, Figs 92 and 95).

The titanium based precipitates analysed from the ICCGHAZ of the test plates were probably nitrides of titanium, vanadium and niobium conducted on the general basis of the precipitation of titanium nitrides at higher temperatures and the shape of the precipitates (Appendices 8–9, Figs 91–93).

The largest ferrite grain and bainite packet sizes were smaller in the ICCGHAZ of plates B and C than in plate A due to the more effective grain coarsening of the CGHAZ in plate A than in plates B and C as a result of an intercritical thermal cycle. Post weld heat treatment (PWHT) of the ICCGHAZ increased the largest ferrite grain and bainite packet sizes in test plates A, B and C (Figs 45–46, Appendices 6–7, Tables 13–14).

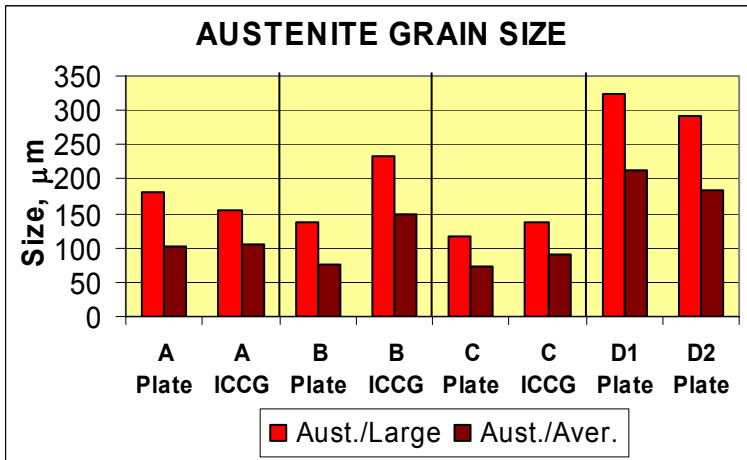


Fig. 44. Austenite grain sizes of the base plate and simulated ICCGHAZ specimens of plates A, B and C and the heat treated test pieces D1 and D2 (ICCG=ICCGHAZ).

The intercritical thermal cycle decreased ferrite grain and bainite packet sizes in the ICHAZ of plates A, B and D, but increased them in the ICHAZ of plate C. Post weld heat treatment (PWHT) of the ICHAZ increased ferrite grain and bainite packet sizes in plates A and B. Ferrite grain and bainite packet sizes of the heat treated test pieces D1 and D2 were higher than in plates A, B, C and D and in their ICHAZ areas. The intercritical thermal cycle decreased the ferrite grain and bainite packet size of the heat treated test piece D1, but increased it in test piece D2 (Fig. 46, Appendices 6–7, Tables 11–12).

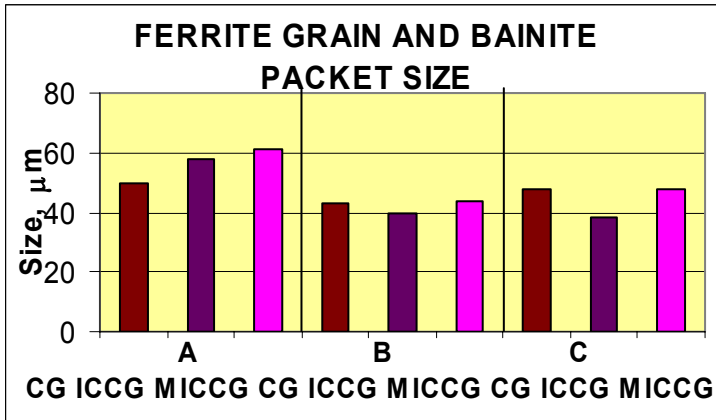


Fig. 45. The largest ferrite grain and bainite packet sizes of the simulated CGHAZ, ICCGHAZ and the post weld heat treated ICCGHAZ specimens of plates A, B and C (CG=CGHAZ, ICCG=ICCGHAZ and MICCG=ICCGHAZ+PWHT).

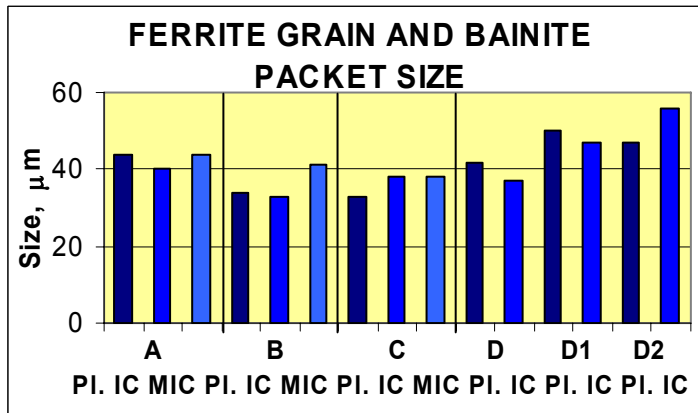


Fig. 46. The largest ferrite grain and bainite packet sizes of the base plates/the test pieces and simulated ICHAZ and the post weld heat treated ICHAZ specimens of plates A, B, C and D and the heat treated test pieces D1 and D2 (PI=plate/test piece, IC=ICHAZ and MIC=ICHAZ+PWHT).

6.4.2 Grain orientation analyses

The measured orientation differences of the adjacent grains using line plot analyses showed that the ICCGHAZ of plate A contained a higher proportion of low angle boundaries (differences of the orientation angle $\leq 15^\circ$) and a little lower proportion of the highest angle boundaries (differences of the orientation angle $\geq 41^\circ$) than that of plates B

and C. However, the lowest proportion of low angle boundaries and the highest proportion of high angle boundaries contained the ICCGHAZ of plate C (Fig. 47, Appendix 12, Figs 98–99). In the area plot analyses of the ICCGHAZ the differences between the specimens were minimal (Fig. 48, Appendix 13, Figs 100–101). The ICHAZ of plate C also contained a lower proportion of low angle boundaries than that of the heat treated specimens D1 and D2 in the line plot analyses, but the distribution of the highest angle boundaries was close to the same in all specimens. The intercritical thermal cycle of the heat treated specimens D1 and D2 increased the proportion of low angle boundaries and slightly decreased the highest angle boundaries (Figs 47–48, Appendix 14, Figs 102–103).

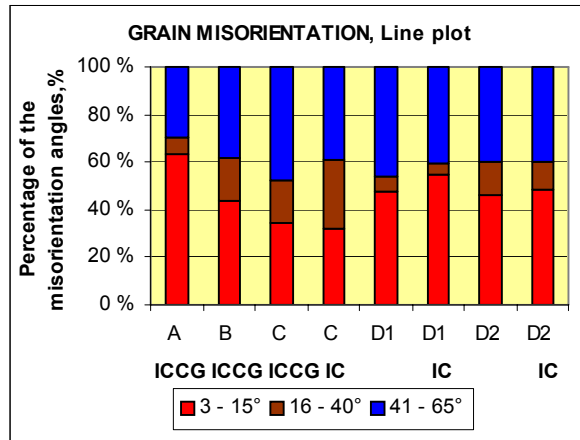


Fig. 47. Line plot misorientation of adjacent grains of the ICCGHAZ of plates A, B, C and ICHAZ of plate C and the heat treated test pieces D1 and D2 (ICCG=ICCGHAZ and IC=ICHAZ).

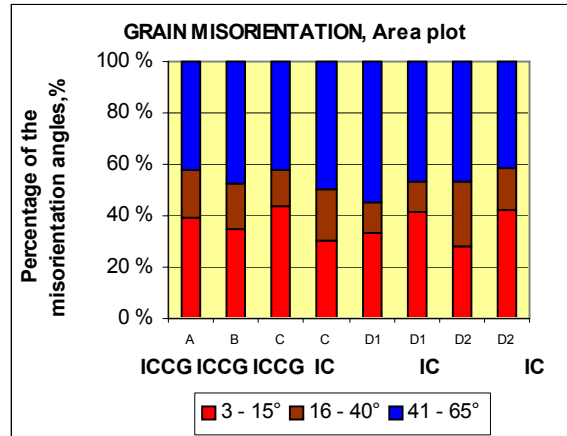


Fig. 48. Area plot misorientation of adjacent grains of the ICCGHAZ of plates A, B, C and ICHAZ of plate C and the heat treated test pieces D1 and D2 (ICCG=ICCGHAZ and IC=ICHAZ).

The distributions of grain misorientations were close the same order in line plot and in area plot analyses, but the percentages of low misorientation angles ($\leq 15^\circ$) were higher in the line plot than in the area plot analyses. However, an example of a long period area plot analysis increased low misorientation angles ($\leq 15^\circ$) and decreased the highest misorientation angles ($\geq 41^\circ$) compared to a short period analysis (Appendix 15, Figs 104–105). A remarkable amount of non-identified misorientations caused a scatter of the test results particularly in the line plot analyses. However, these relatively small amounts of test results gave a rough estimation of grain structures of the specimens.

The average grain size of ferrite and bainite was measured according to area plot misorientation measurements. The test results were classified according to the misorientation angles due to the increase of the average grain size with increasing the misorientation angle (Table 9).

Table 9. Distribution of the average grain sizes and the largest ferrite grain and bainite packet sizes (effective grain size) using the area plot misorientation measurements and optical microscope.

Test specimen	Average grain size (μm)			Eff. grain size (μm)
	Misor.angle $\geq 5^\circ$	Misori.angle $\geq 15^\circ$	Misor.angle $\geq 40^\circ$	
A ICCGHAZ	8.4	11.1	18.2	58
B ICCGHAZ	7.2	11.5	16.8	40
C ICCGHAZ	2.8	3.9	5.1	38
C ICHAZ	6.5	8.1	13.1	38
D1	6.8	10.0	11.7	50
D1 ICHAZ	11.9 ¹⁾	10.9 ¹⁾	13.9	47
D2	7.3	8.8	15.5	47
D2 ICHAZ	11.5	13.0	18.2	56

¹⁾Grain size (misorient. $\geq 5^\circ$) should be smaller than grain size (misorient. $\geq 15^\circ$)

The test results showed that the average grain size of the high angle boundaries (misorient. $\geq 15^\circ$) were lower in the ICCGHAZ of plate C than in that of the other test plates A and B. Also, a smaller fraction of the low angle boundaries in the ICHAZ of plate C was lower than in that of the heat treated test pieces D1 and D2. The intercritical thermal cycle of the heat treated specimens D1 and D2 increased the average sizes of all tested misorientation angles ($\geq 5^\circ$, $\geq 15^\circ$ and $\geq 40^\circ$). The average sizes in the high angle boundary ($\geq 15^\circ$) grains and the largest ferrite grain and bainite packet sizes in the ICCGHAZ and ICHAZ of plate C were smaller than in the other test plates and test pieces indicating a direct correlation between the microscopical investigation and the grain misorientation analyses (Table 9). However, this relatively limited amount of test results and the small total analysed area gave only a rough estimation of the grain structures of the specimens.

6.4.3 Relationship between the largest ferrite grain and bainite packet sizes and the cleavage facet size

A good correlation between the largest ferrite grain and bainite packet sizes and cleavage facet sizes in the ICCGHAZ and ICHAZ of the test plates has been observed in this research work (Figs 49–50).

The correlation curves (Fig. 49) of the impact test specimens systematically showed that in the ICCGHAZ ferrite grain and bainite packet sizes were higher than cleavage facet sizes, whereas in the ICHAZ cleavage facet sizes were higher than ferrite grain and bainite packet sizes. In the CTOD tests the differences of the ICCGHAZ and ICHAZ specimens were not as systematic as in the impact tests. Exceptionally high cleavage facet size, compared with ferrite grain and bainite packet sizes, was observed in the ICCGHAZ of plate C which contained a higher fraction of M-A constituents than that of plates A and B (Fig. 50).

transition temperatures T_{27J} , $T_{50\%}$ and $T_{0.1mm}$ of the ICCGHAZ caused by an increase in ferrite grain and bainite packet sizes as a result of the intercritical thermal cycle of the CGHAZ of plate A. However the differences in the transition temperatures T_{27J} , $T_{50\%}$ and $T_{0.1mm}$ of the CGHAZ and ICCGHAZ of plates B and C and particularly in $T_{50\%}$ of the CGHAZ were insignificant (Figs 51–53, Appendices 6–7, Tables 13–14).

Also, the ICHAZ of plates A, B and C showed that an increase of ferrite grain and bainite packet sizes elevated the impact and CTOD transition temperatures T_{27J} and $T_{0.1mm}$ in spite of small differences between the test plates (Figs 51 and 53), but there was no visible effect in the impact transition temperature $T_{50\%}$ (Fig. 52). Particularly, a little higher transition temperatures for T_{27J} and $T_{0.1mm}$ and larger ferrite grain and bainite packet sizes in the ICHAZ of plate A than in those from the other plates B and C, supported this opinion. The increase of ferrite grain and bainite packet sizes in the ICHAZ of the heat treated test pieces D1 and D2 elevated the transition temperatures T_{27J} , $T_{50\%}$ and $T_{0.1mm}$ only a little higher than in the ICHAZ of plates A, B and C. However, the higher transition temperatures T_{27J} , $T_{50\%}$ and $T_{0.1mm}$ in the ICHAZ of plate D than in that of plates A, B and C demonstrated a detrimental influence of M-A constituents on impact and fracture toughness (Figs 51–53).

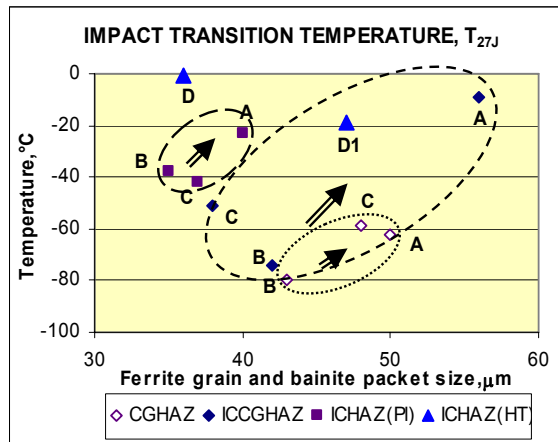


Fig. 51. Influence of ferrite grain and bainite packet sizes on impact transition temperature T_{27J} of the simulated CGHAZ, ICCGHAZ and ICHAZ specimens (PI=plate, HT=heat treated).

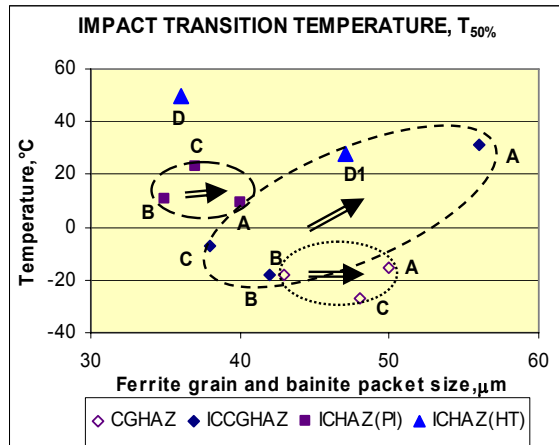


Fig. 52. Influence of ferrite grain and bainite packet sizes on impact transition temperature $T_{50\%}$ of the simulated CGHAZ, ICCGHAZ and ICHAZ specimens (PI=plate, HT=heat treated).

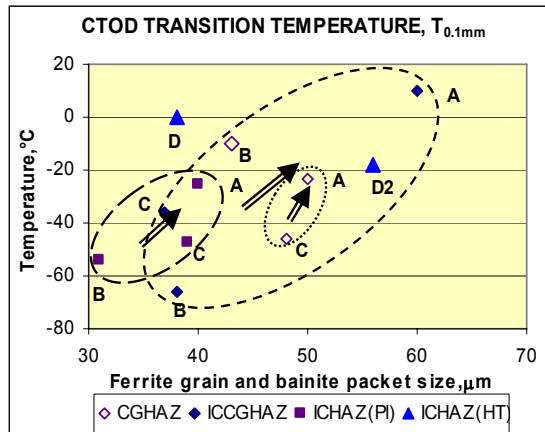


Fig. 53. Influence of ferrite grain and bainite packet sizes on CTOD transition temperature $T_{0.1mm}$ of the simulated CGHAZ, ICCGHAZ and ICHAZ specimens (PI=plate, HT=heat treated).

6.4.5 Summary of paragraph 6.4

In summary, the investigation of ferrite grain and bainite packet sizes of the CGHAZ, ICCGHAZ and ICHAZ of the test plates showed that an increase in ferrite grain and bainite packet sizes elevated the impact and CTOD transition temperatures T_{27J} , $T_{50\%}$ and $T_{0.1mm}$ particularly remarkably in the ICCGHAZ of plate A. However, small differences in

ferrite grain and bainite packet sizes in the ICCGHAZ plates B and C and in the CGHAZ and ICHAZ of all test plates called this into question.

In the ICHAZ of the heat treated test pieces D1 and D2, the increased ferrite grain and bainite packet sizes elevated the transition temperatures T_{27J} , $T_{50\%}$ and $T_{0.1mm}$ only a little higher than in the ICHAZ of plates A, B and C. However, the higher transition temperatures T_{27J} , $T_{50\%}$ and $T_{0.1mm}$ in the ICHAZ of plate D than that of plates A, B and C demonstrated a detrimental influence of M-A constituents on impact and fracture toughness.

6.5 Investigations of M-A constituents and their influence on impact and fracture toughness

The presence of M-A constituents is generally regarded as the major factor which reduces the fracture toughness of weld HAZ particularly with low heat input welding (Kweon *et al.* 2000). It has been reported that the loss of toughness is not solely due the total amount of M-A constituents, but is related to the distribution and morphology of them and the microstructure of the matrix.

6.5.1 Amount and size of M-A constituents

The chemical composition of steel and the welding thermal cycle are the major factors in the formation of M-A constituents, which are significantly formed in the ICCGHAZ and ICHAZ as a result of the intercritical thermal cycles of the CGHAZ and base plate. It is well-known that carbon and alloy contents of steel have the key compositional factors affecting a fraction of M-A constituents.

In this research work the area fraction of M-A constituents increased with the carbon content in the ICHAZ, but in the ICCGHAZ the area fraction of M-A constituents increased with the carbon contents of plates A and C (0.074–0.087%) and decreased with the highest carbon plate B (0.1%). Similarly, the lower area fraction of M-A constituents in the ICHAZ from the heat treated test pieces D1 and D2, compared with those from plate D, showed a reduction in the amount of M-A constituents between intragranularly nucleated ferritic microstructure (Fig. 54).

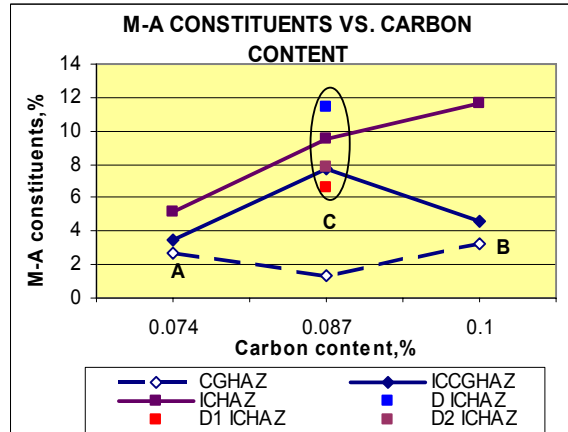


Fig. 54. Influence of carbon content of the test plates on the fraction of M-A constituents in the CGHAZ, ICCGHAZ and ICHAZ.

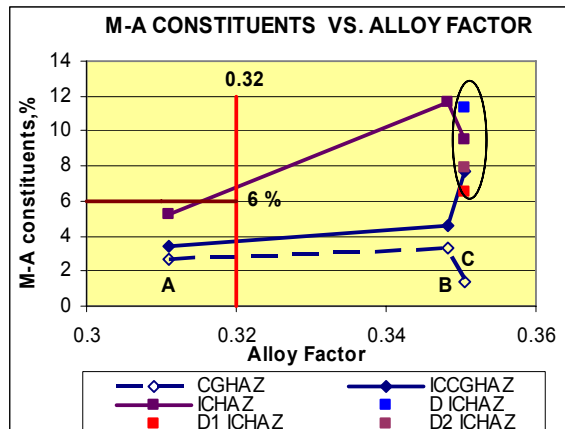


Fig. 55. Influence of alloy factor of the test plates on the fraction of M-A constituents in the CGHAZ, ICCGHAZ and ICHAZ.

The dependence of the area fraction of M-A constituents on alloy contents can be evaluated using alloy factor (AlF) (9) defined by Harrison and Webster (1994) and Harrison and Wall (1996). In the ICCGHAZ and ICHAZ the area fraction of M-A constituents increased by the increasing of an alloy factor exceeding the toughness deterioration limit of 6% (Akselsen *et al.* 1988) in an alloy factor of 0.35 in the ICCGHAZ and 0.32 in the ICHAZ. In the CGHAZ the area fraction of M-A constituents remained below 6% (Fig. 55).

Table 10. Area fraction and equivalent diameter of M-A constituents in ICCGHAZ and ICHAZ of test plates and the heat treated specimens.

Specimen	Area fraction (%)	Equivalent diameter, max. (μm)
A ICCGHAZ	3.47	$>5 \leq 10$
B ICCGHAZ	4.55	$>5 \leq 10$
C ICCGHAZ	7.73	$>5 \leq 10$
A ICHAZ	5.23	$>1 \leq 5$
B ICHAZ	11.67	$>5 \leq 10$
C ICHAZ	9.47	$>5 \leq 10$
D ICHAZ	11.35	$>20 \leq 50$
D1 ICHAZ	6.57	$>10 \leq 15$
D2 ICHAZ	7.86	$>10 \leq 15$

The test results showed that a higher area fraction of M-A constituents in the ICCGHAZ of test plates had an insignificant influence on their equivalent diameter (Table 10, Appendix 16, Figs 106–107). However, in the ICHAZ of normalized rolled plate D and the heat treated test pieces D1 and D2, the sizes of M-A constituents were larger than those in plates A, B and C, although the total area fraction of M-A constituents in the ICHAZ of plate B was equal to or higher than those in plate D. The total area of M-A constituents was higher in the ICHAZ of plate C than in that of the heat treated test pieces D1 and D2. The finest M-A constituents were observed in the ICHAZ of plate A (Table 10, Appendices 17–18, Figs 108–111).

6.5.2 Type and distribution of M-A constituents

The test results of the ICCGHAZ demonstrated significant differences between test plates concerning the morphology and distribution of M-A constituents. In the ICCGHAZ of plate A, the massive blocky-type M-A constituents were observed along the prior austenite grain boundaries together with elongated stringer type M-A constituents situated between lath boundaries of large ferrite grains and bainite packets (Fig. 56). However, in the ICCGHAZ of plate B the blocky-type M-A constituents were smaller than in the ICCGHAZ of plate A, and the small stringer-type M-A constituents were mainly between ferrite-bainite laths (Fig. 57). The post weld heat treatment of 4 h at 600 °C of the ICCGHAZ of plate A caused a decomposition of M-A constituents into carbides (Fig. 58).

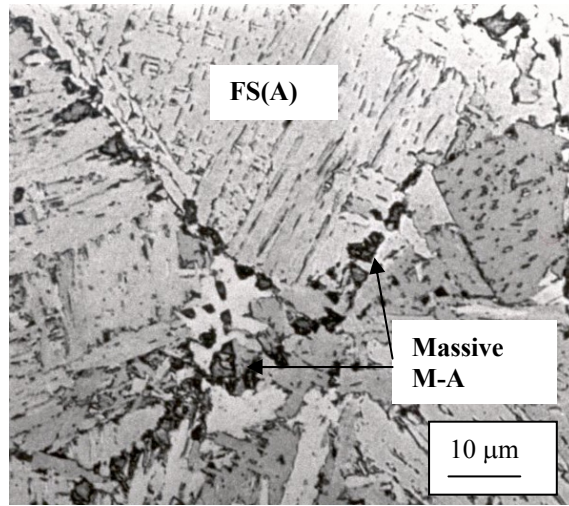


Fig. 56. Type and distribution of M-A constituents in the ICCGHAZ of plate A, 1% Na₂HSO₃ etching.

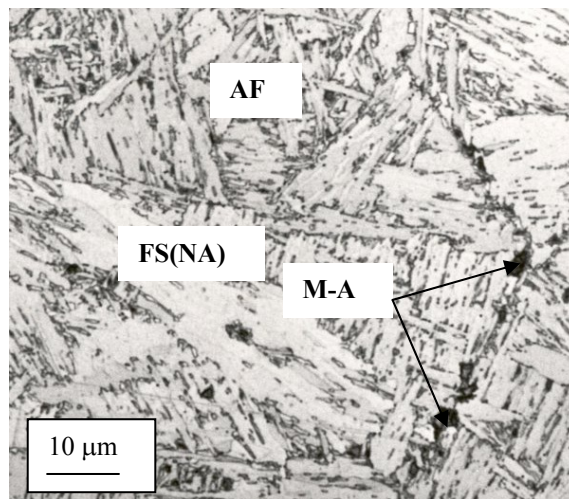


Fig. 57. Type and distribution of M-A constituents in the ICCGHAZ of plate B, 1% Na₂HSO₃ etching.

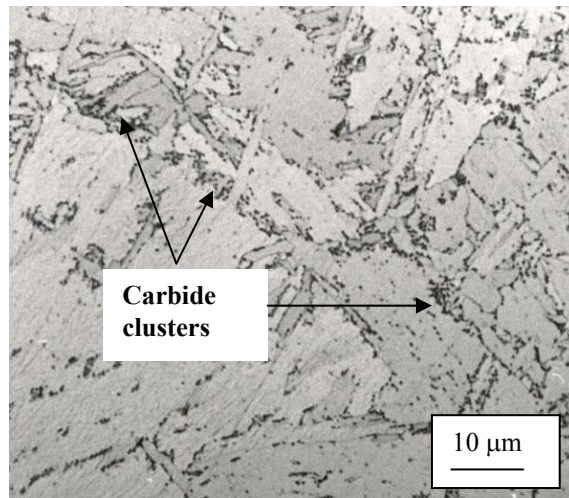


Fig. 58. Decomposition of M-A constituents in the post weld heat treated ICCGHAZ specimens from plate A, 1% Na_2HSO_3 etching.

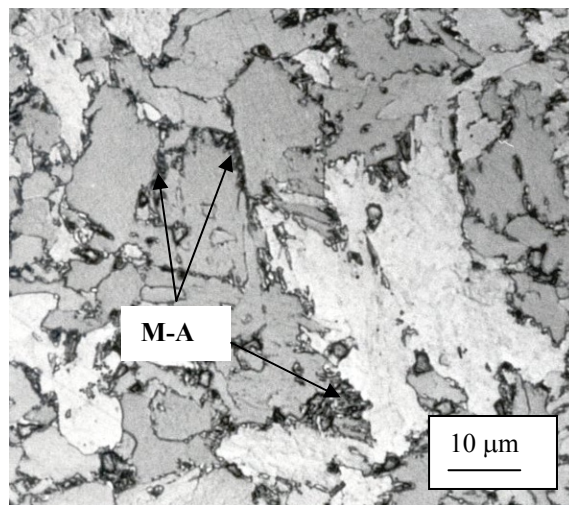


Fig. 59. Type and distribution of M-A constituents in the ICHAZ specimens from plate C, 1% Na_2HSO_3 etching.

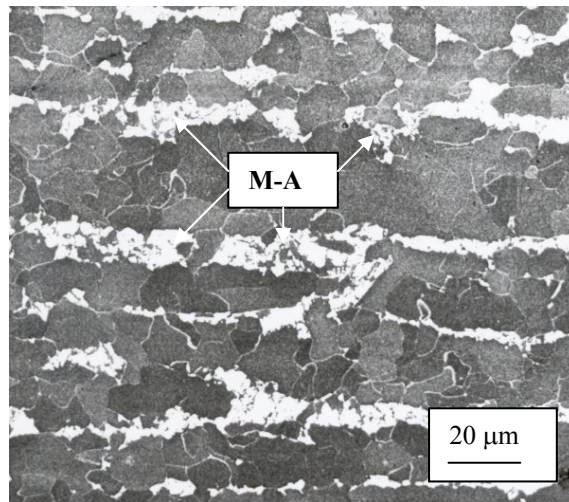


Fig. 60. Distribution of M-A constituents in the ICHAZ of plate D, LePera etching.

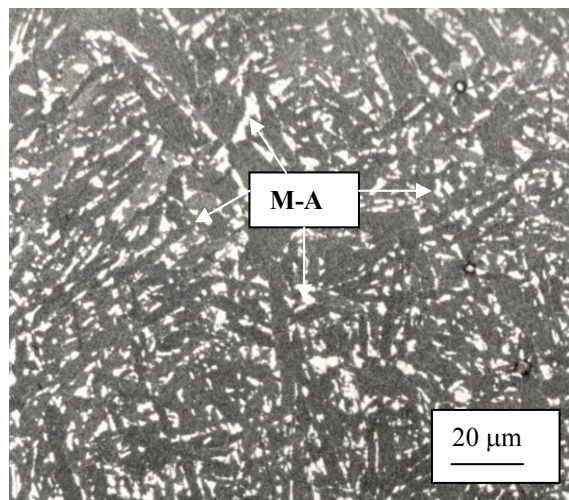


Fig. 61. Type and distribution of M-A constituents in the ICHAZ of the heat treated test piece D2, LePera etching.

In the ICHAZ of plate C, M-A constituents were the blocky-types and situated along the ferrite grain boundaries (Fig. 59). The M-A constituents formed as a result of the intercritical thermal cycle of ferritic-pearlitic microstructure contained in plate D were situated along the previous pearlite bands. The total percentage of M-A constituents was equal to the pearlite content (11–12%) of the plate (Table 10, Fig. 60). In the ICHAZ of the heat treated test piece D2 the total area fraction of M-A constituents was lower and the distribution of the blocky- and stringer-types of M-A constituents in the ferrite-bainite grain boundaries was more even than in the ICHAZ specimens from plate D (Fig. 61).

6.5.3 Influence of M-A constituents on impact and fracture toughness

The impact and CTOD test results of the ICCGHAZ showed that the increase of the area fraction of M-A constituents elevated the impact and CTOD transition temperatures T_{27J} , $T_{50\%}$ and $T_{0.1mm}$. However, the highest transition temperatures T_{27J} , $T_{50\%}$ and $T_{0.1mm}$ in the ICCGHAZ of plate A, in spite of its lowest area fraction of M-A constituents, showed that the other factors such as the distribution of M-A constituents and the ferrite grain and bainite packet sizes had a more significant influence on toughness of these specimens than the area fraction of M-A constituents (Figs 62–64).

The increase of M-A constituents elevated the impact and CTOD transition temperatures T_{27J} , $T_{50\%}$ and $T_{0.1mm}$ in the ICHAZ of plates A and D and the heat treated test pieces D1 and D2. However, the relatively low transition temperatures T_{27J} and $T_{0.1mm}$ in the ICHAZ of plates B and C, compared with the high area fraction of M-A constituents, demonstrates the beneficial influence of their even distribution relating to toughness (Figs 62–64).

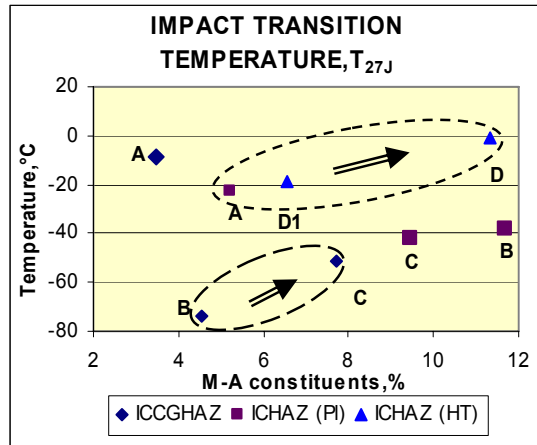


Fig. 62. Influence of M-A constituents on impact transition temperature T_{27J} of the ICCGHAZ and ICHAZ (PI=plate, HT=heat treated).

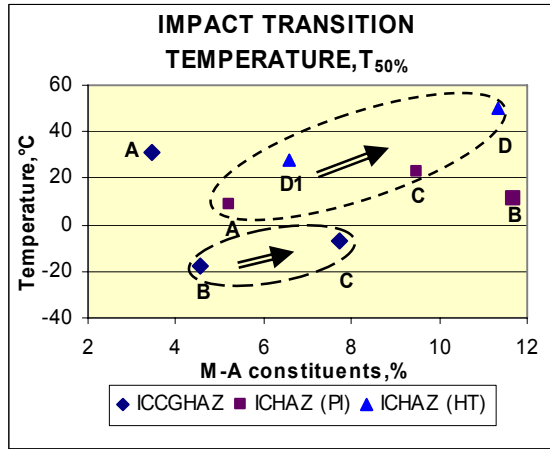


Fig. 63. Influence of M-A constituents on impact transition temperature $T_{50\%}$ of the ICCGHAZ and ICHAZ (PI=plate, HT=heat treated).

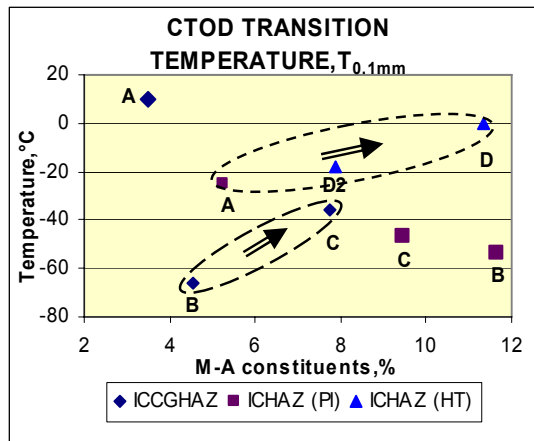


Fig. 64. Influence of M-A constituents on CTOD transition temperature $T_{0.1mm}$ of the ICCGHAZ and ICHAZ (PI=plate, HT=heat treated).

6.5.4 Summary of paragraph 6.5

In summary, the ICCGHAZ of plates A and C and the ICHAZ of all test plates supported the opinion that the area fraction of M-A constituents increased as a result of an increase in carbon content and alloy factor (AIF). The toughness deterioration limit of 6% M-A constituents was exceeded, when alloy factor exceeded 0.35 in the ICCGHAZ and 0.32 in the ICHAZ. The area fraction of M-A constituents had an insignificant influence on their

size in the ICCGHAZ and ICHAZ of plates A, B and C. However, in the ICHAZ of plate D and the heat treated test pieces D1 and D2, the increase of the area fraction of M-A constituents also increased their size.

The test results demonstrated the significant differences in the type and distribution of M-A constituents in the ICCGHAZ and ICHAZ of the test plates. In the ICCGHAZ of plate A, the massive blocky-type M-A constituents were observed along the prior austenite grain boundaries together with the elongated stringer type of M-A constituents in lath boundaries, whereas in the ICCHAZ of plate B the smaller blocky-type M-A constituents at the prior austenite grain boundaries, together with the small stringer-type M-A constituents were found. In the ICHAZ of plate C and the heat treated test pieces D1 and D2, M-A constituents were the blocky- and stringer-type and were situated along the ferrite-bainite grain boundaries. However, in the ICHAZ of ferritic-pearlitic microstructure contained plate D they were situated along the previous pearlite bands. The total percentage of M-A constituents was equal as the pearlite content (11–12%) of the plate.

The impact and CTOD test results from the ICCGHAZ of plates B and C, ICHAZ of plates A and D and the heat treated test pieces D1 and D2 showed that the increase of the area fraction of M-A constituents elevated the impact and CTOD transition temperatures T_{27J} , $T_{50\%}$ and $T_{0.1mm}$. However, the highest transition temperatures T_{27J} , $T_{50\%}$ and $T_{0.1mm}$ in the ICCGHAZ of plate A, in spite of the lowest area fraction of M-A constituents, showed that the distribution of M-A constituents had a more significant influence on toughness than their area fraction. In addition, the relatively low transition temperatures T_{27J} and $T_{0.1mm}$ of the ICHAZ of plates B and C, compared with the high area fraction of M-A constituents, demonstrates the beneficial influence of their relatively even distribution on toughness.

6.6 Crack initiation and propagation

Evaluation of crack initiation and propagation mechanisms completes the understanding of the relationship between microstructural features and toughness. There is a general agreement that M-A constituents, being harder than the matrix, act as a site of crack initiation impairing toughness at ambient, as well as at low temperatures. On the contrary, the microstructure of the matrix plays a significant role in crack propagation.

6.6.1 Crack initiation mechanisms

In this research work crack initiation mechanisms have been evaluated using secondary cracks from the specimens tested below the ductile-brittle impact and CTOD transition temperatures T_{27J} and $T_{0.1mm}$, when the evaluation mainly represented cleavage fracture. In the ICCGHAZ of plate A (Figs 65–66) a secondary crack has been assumed to nucleate M-A/ferrite-bainite interfaces or between two massive M-A constituents with sizes of 2–5 μm at the prior austenite grain boundaries (point A).

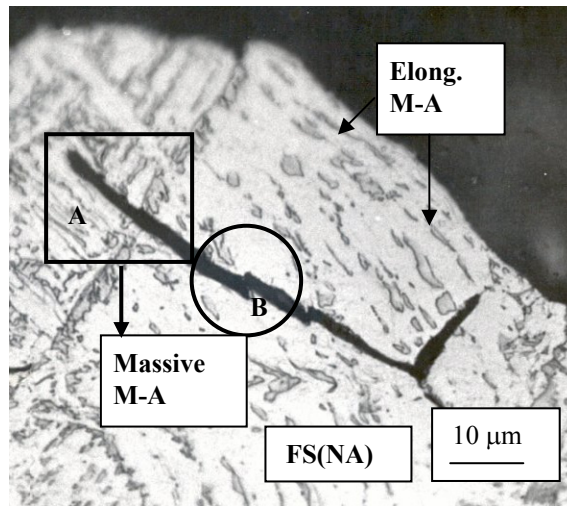


Fig. 65. Secondary crack initiation caused by M-A constituents at the prior austenite grain boundary (point A) and propagation in the ferrite with non-aligned second phase in the ICCGHAZ of plate A tested in Charpy V test at $-40\text{ }^{\circ}\text{C}$, 2% Nital etching.

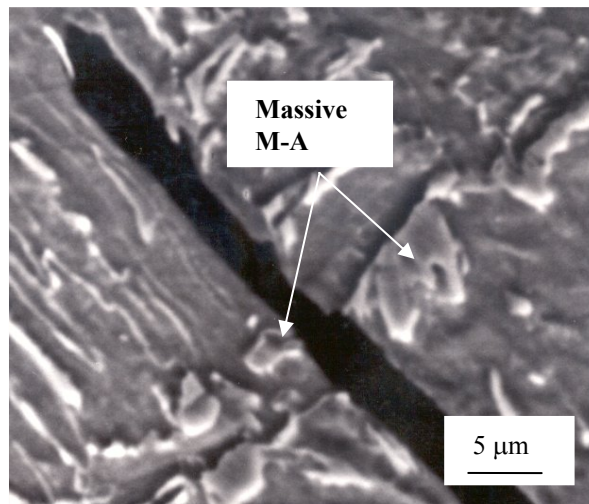


Fig. 66. Scanning electron microscope picture from crack nucleation point A in the previous Fig. 65, 2% Nital etching.

On the contrary, in the ICCGHAZ of plate B, the proposed mechanism consists of nucleation of microvoids at numerous sites of M-A/ferrite boundaries in small ferrite or bainite laths followed by cracking of stringer-type M-A constituents between ferrite or bainite laths and coalescence of microvoids to microcracks. Then the microcracks were joined together for a final crack crossing the prior austenite grain boundaries, where M-A constituents can promote crack propagation. The plastic deformation in the cracked

edges, before final cracking and elaborated cracking paths, indicate ductile crack growth before final fracture.

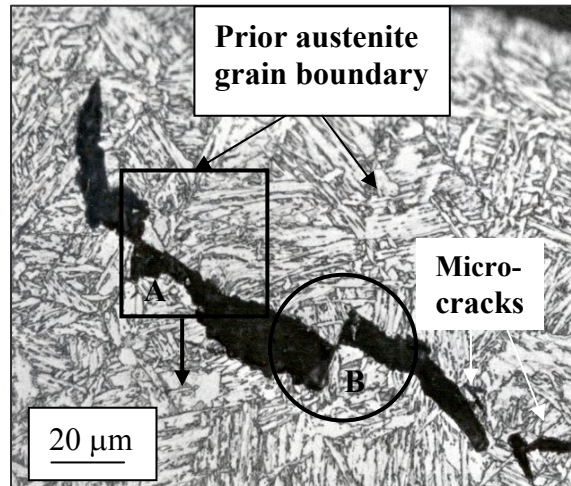


Fig. 67. Secondary crack nucleation (points A and B), microcracks and crack propagation path cross the prior austenite grain boundaries in points A and B of the ICCGHAZ of plate B tested in Charpy V tests at $-80\text{ }^{\circ}\text{C}$, 2% Nital etching.

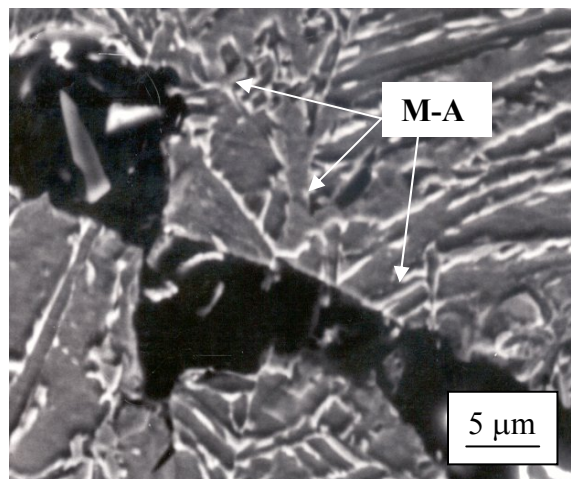


Fig. 68. Scanning electron microscope picture from crack nucleation both sides of the prior austenite grain boundary in point A in the previous Fig. 67, 2% Nital etching.

In the post weld heat treated ICCGHAZ of plate A, clusters of carbides induced stress-strain concentrations in ferrite close to ferrite/carbide interfaces causing the initiation of microcracks at many points (points A, B, C in Figs 69–70). Plastic deformation of

microcracks and their limited propagation showed a stress relaxation in the ferritic-bainitic matrix in addition to a decomposition of M-A constituents.

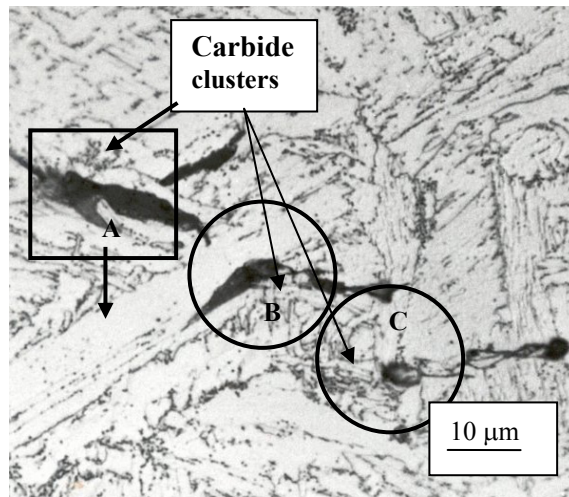


Fig. 69. Nucleation of secondary microcracks in ferrite close to carbide clusters (points A, B and C) in the post weld heat treated ICCGHAZ of plate A tested in Charpy V test at $-60\text{ }^{\circ}\text{C}$, 2% Nital etching.

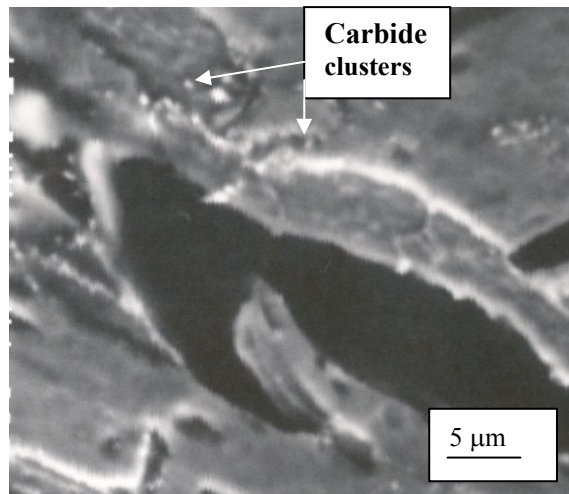


Fig. 70. Scanning electron microscope picture from crack nucleation in ferrite close to carbide clusters in point A in the previous Fig. 69, 2% Nital etching.

6.6.2 Crack propagation mechanisms

It has been observed that crack propagation is controlled by crack growth from one ferrite grain, bainite packet or prior austenite grain boundary to another along the dominant cleavage lattice plane $(100)_\alpha$. In Fig. 65 the primary crack has propagated through a large ferrite grain and bainite packet (FS(NA)) from one prior austenite grain boundary to another, which deflected the fracture path from its direction, as presented before. M-A constituents inside the ferrite grains or bainite packets caused small kinks (point B) in secondary crack paths.

In the post weld heat treated ICCGHAZ of plate A (Fig. 69), microcracks nucleated in clusters of carbides at prior austenite grain boundaries (point A) or between ferrite-bainite laths, joined together propagating through large ferrite grains and bainite packets. Carbide clusters in ferrite grains and bainite packets and in lath boundaries can cause kinks in (point A) and branching (point B) of the crack (Fig. 71).

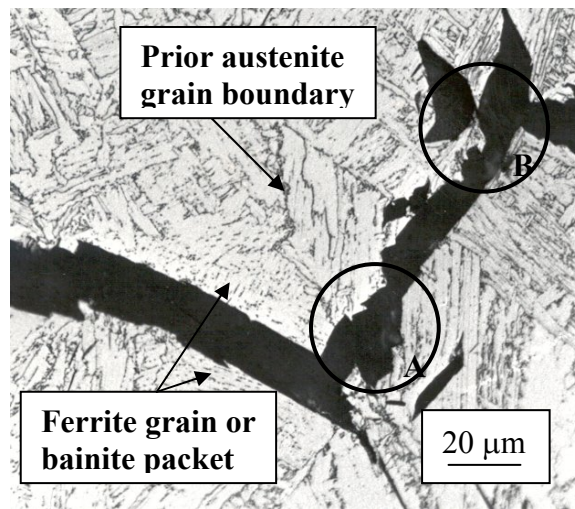


Fig. 71. Secondary crack propagation through a large a ferrite grain or bainite packet and branching of crack in the post weld heat treated ICCGHAZ of plate A after tested with the Charpy V test at $-60\text{ }^\circ\text{C}$, 2% Nital etching.

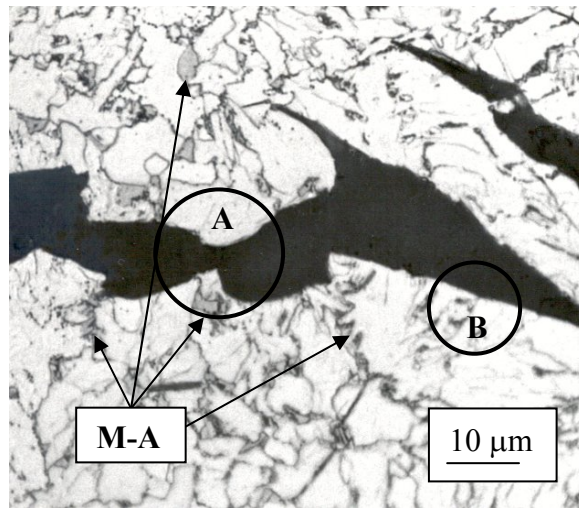


Fig. 72. Secondary crack nucleation in both side of M-A constituents (point A) and propagation through large ferrite grain (point B) in the ICHAZ of plate A tested with the Charpy V test at $-40\text{ }^{\circ}\text{C}$, 2% Nital etching.

In the ICHAZ specimens of plate A (Fig. 72), M-A constituents induced microcracks in ferrite grains causing plastic deformation (point A) before cracking. Cracks propagated through a large ferrite grain without significant plastic deformation (point B).

In the ICHAZ of plate C (Figs 73–74), microcracks induced by M-A constituents were found in ferrite grains. Larger secondary cracks were propagated directly through larger ferrite grains. M-A constituents in ferrite grain boundaries deflected cracks from their original direction or even obstructed them (point A).

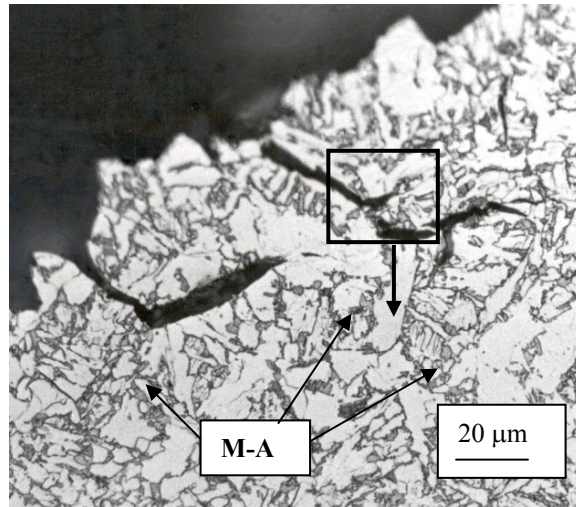


Fig. 73. Primary crack and secondary cracks propagation through ferrite grains and bainite packets in the ICHAZ of plate C tested with the Charpy V test at -60°C , 2% Nital etching.

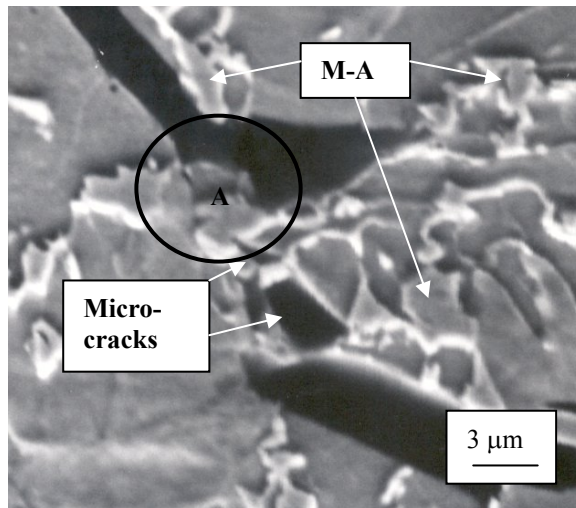


Fig. 74. Scanning electron microscope picture of secondary cracks and their propagation through ferrite grains and M-A constituents in the ICHAZ of plate C in the previous Fig. 73, 2% Nital etching.

In the intragranularly nucleated acicular and polygonal ferritic microstructure in the ICHAZ of heat treated test piece D2 (Figs 75–76), microcracks induced by M-A constituents in ferrite grain boundaries were joined together into zig-zag cracks. M-A constituents in ferrite grain boundaries deflected cracks from their direction (point A) and finally prevented (point B) their propagation.

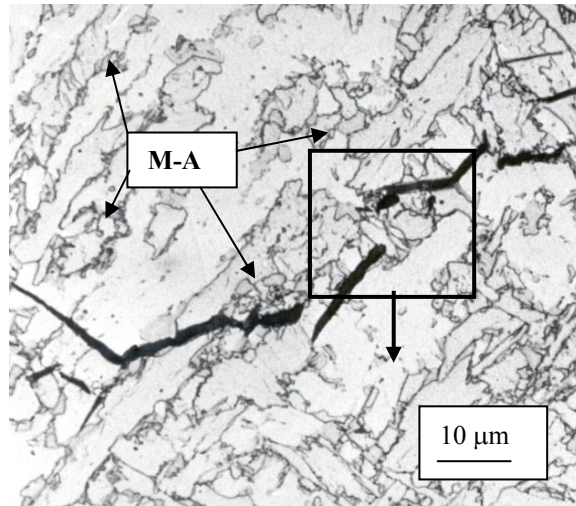


Fig. 75. Secondary crack propagation through ferrite grains and bainite packets in the ICHAZ of heat treated test piece D2 tested in CTOD test at $-60\text{ }^{\circ}\text{C}$, 2% Nital etching.

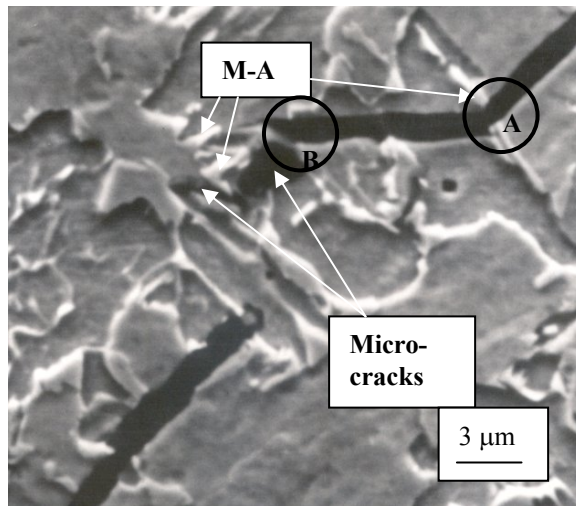


Fig. 76. Scanning electron microscope picture of secondary cracks and their propagation through ferrite grains and M-A constituents in the ICHAZ of plate C in the previous Fig. 75, 2% Nital etching.

In the ICHAZ of plate D (Figs 77–78) a high fraction of M-A constituents (11.35%) contained in original pearlite bands caused a nucleation of microvoids in M-A/ferrite boundaries and their coalescence by cracking of M-A particles into microcracks (Point A). They were then propagated through large ferrite grains from one M-A band to another. Obviously, M-A constituents or microvoids in M-A/matrix interfaces enhanced crack reinitiation and propagation.

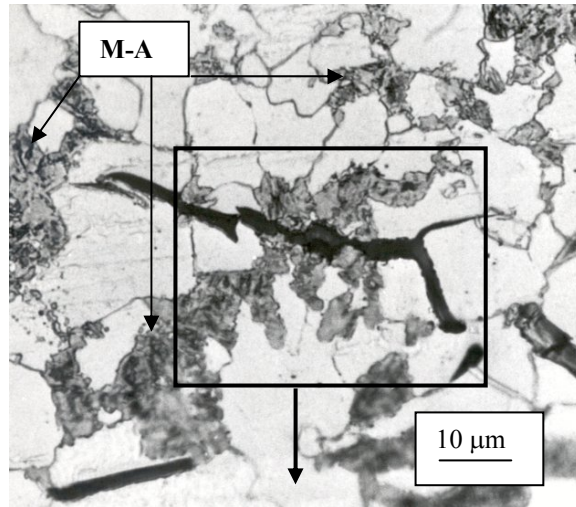


Fig. 77. Secondary crack nucleation between M-A constituents and propagation through ferrite grains in the ICHAZ specimens of plate D tested in Charpy V test at $-40\text{ }^{\circ}\text{C}$, 2% Nital etching.

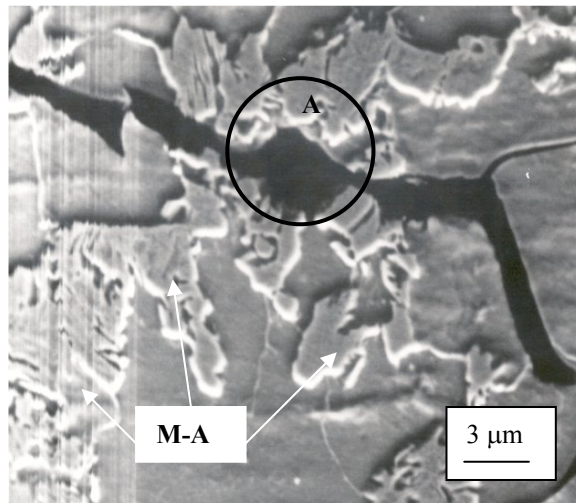


Fig. 78. Scanning electron microscope picture of a secondary crack nucleated in point A and propagated through M-A constituents and ferrite grains in the ICHAZ of plate D in the previous Fig. 77, 2% Nital etching.

6.6.3 Summary of paragraph 6.6

In summary, continuous sheets of massive M-A constituents observed along the prior austenite grain boundaries of the ICCGHAZ of plate A can be assumed to enhance crack nucleation in M-A/ferrite-bainite interfaces and large ferrite grains and bainite packets crack propagation. On the contrary, in the ICCGHAZ of plate B, nucleation of microcracks between many small ferrite or bainite laths was induced by a relatively even distribution of M-A constituents and crack propagation by joining them together, resulting in cracking. M-A constituents between ferrite or bainite laths and inside ferrite grains and bainite packets caused kinks, deflecting cracks from their original direction, branching or even obstructing them. In the post weld heat treated ICCGHAZ of plate A, clusters of carbides induced nucleation of cracks, deflected cracks from their original direction and branched them.

In the ICHAZ from plates A and C, M-A constituents along ferrite or bainite grain boundaries induced nucleation of microcracks in ferrite or bainite grains and deflected cracks from their original direction or even obstructed them. In the intragranularly nucleated acicular and polygonal ferritic microstructure in the ICHAZ of the heat treated test piece D2, microcracks induced by M-A constituents in ferrite grain boundaries joined together into zig-zag cracks arresting or finally preventing the propagation of microcracks. A high fraction of large M-A constituents (11.35%) in original pearlite bands in the ICHAZ of plate D promoted nucleation of microvoids in M-A/ferrite boundaries, coalesced them into microcracks by cracking of M-A particles and propagated them through large ferrite grains from one M-A band to another.

6.7 Multiple linear regression analyses

The main factors affecting the impact and CTOD transition temperatures T_{27J} , $T_{50\%}$ and $T_{0.1mm}$ were evaluated using the multiple linear regression analysis, which was carried out using Microsoft Exel 97 with a confidence level of 95%, consisting of two groups of the test results on the basis of the most critical sub-zones in the weld HAZ. The first group consisted of the test results from the CGHAZ and ICCGHAZ and the second group from the base plate and the ICHAZ. At the first stage the independent variables such as grain boundary ferrite plus ferrite with second phases (PF(G)+FS) and intragranularly nucleated ferrite and bainite (AF+PF(I)), the largest ferrite grain and bainite packet sizes (Packet), the area fraction of M-A constituents (M-A) and hardness (Hardn.) were analysed. Then the variables, which had the greatest p-values, i.e. the lowest significant levels of probability, were rejected. Generally, in a confidence level of 95% the variables with p-values greater than 0.05 have a mutual dependence, or there are the other influencing variables, which impair the independence of the variables. In these analyses the best combination of the variables, such as the largest ferrite grain and bainite packet sizes, the area fraction of M-A constituents and hardness, in view of the highest correlation coefficients, were included in the final equations of the transition temperatures T_{27J} , $T_{50\%}$ and $T_{0.1mm}$ for the parity check (Figs 79–84, Appendices 19–24).

6.7.1 CGHAZ and ICCGHAZ

The regression equations (17)-(18) with correlation coefficients of 0.87 and 0.90 demonstrated that the largest ferrite grain and bainite packet sizes and the area fraction of M-A constituents had the most significant influence on impact transition temperatures T_{27J} and $T_{50\%}$. Variations of the largest ferrite grain and bainite packet sizes (18 μm) and the area fraction of M-A constituents (6.34%) in the coarse grained region, elevated the transition temperatures T_{27J} and $T_{50\%}$ by 86 $^{\circ}\text{C}$ and 70 $^{\circ}\text{C}$ respectively caused by (Packet) and by 64 $^{\circ}\text{C}$ and 59 $^{\circ}\text{C}$ caused by (M-A) respectively. This means that the largest ferrite grain and bainite packet sizes had a more significant influence on the impact toughness than the area fraction of M-A constituents in the CGHAZ and ICCGHAZ of the weld HAZ.

$$T_{27J} (^{\circ}\text{C}) = 4.79x\text{Packet} + 10.03x(\text{M} - \text{A}) - 315 , \quad (17)$$

$$\sigma = 11.5 ^{\circ}\text{C}, R^2 = 0.87$$

$$T_{50\%} (^{\circ}\text{C}) = 3.89x\text{Packet} + 9.38x(\text{M} - \text{A}) - 225 , \quad (18)$$

$$\sigma = 8.5 ^{\circ}\text{C}, R^2 = 0.90$$

where Packet= largest ferrite grain and bainite packet size (μm) and (M-A)= area fraction of M-A constituents (%)

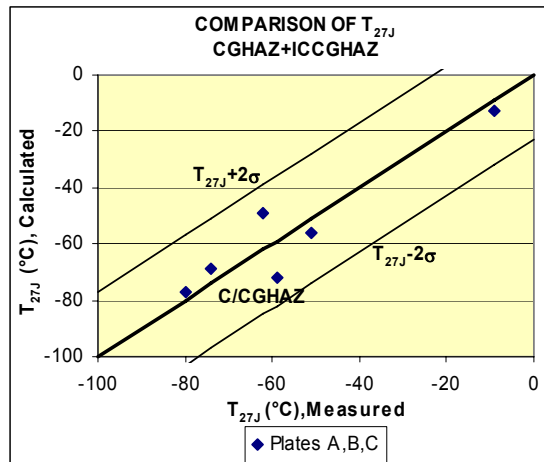


Fig. 79. Results of multiple linear regression analyses between the largest ferrite grain and bainite packet sizes, the area fraction of M-A constituents and the impact transition temperature T_{27J} of the CGHAZ and ICCGHAZ.

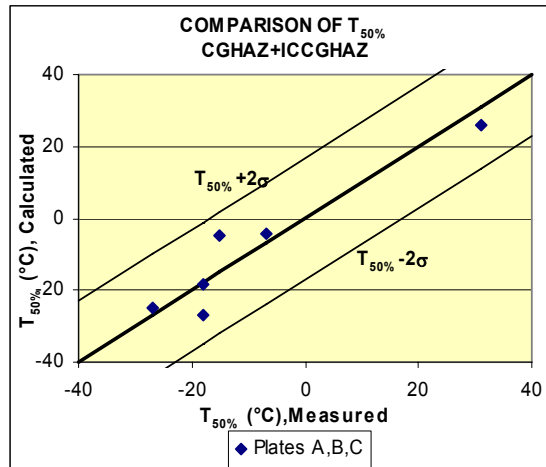


Fig. 80. Results of multiple linear regression analyses between the largest ferrite grain and bainite packet sizes, the area fraction of M-A constituents and the impact transition temperature $T_{50\%}$ of the CGHAZ and ICCGAZ.

Multiple linear regression equation (19) with a correlation coefficient of 0.92 showed that the largest ferrite grains and bainite packets, the area fraction of M-A constituents and hardness were the dominating factors affecting the CTOD transition temperature $T_{0.1mm}$. Variations of the largest ferrite grain and bainite packet sizes (23 μm), the area fraction of M-A constituents (6.34%) and hardness (60 HV) elevated the CTOD transition temperature $T_{0.1mm}$. The following temperature increases were recorded: an increase of 96 °C caused by the largest ferrite grain and bainite packet sizes, an increase of 84 °C caused by the area fraction of M-A constituents and an increase of 50 °C caused by hardness. Thus, the largest ferrite grain and bainite packet sizes and the area fraction of M-A constituents had a more significant influence on the fracture toughness than impact toughness of the CGHAZ and ICCGAZ of the weld HAZ than hardness. On the other hand, p-values of 0.09 (> 0.05) for M-A constituents and 0.11 (> 0.05) for hardness impaired the independence of these variables (Appendix 21). Anyway, the area fraction of M-A constituents elevated the CTOD transition temperature $T_{0.1mm}$ more than the impact transition temperatures T_{27J} and $T_{50\%}$.

$$T_{0.1mm} (\text{°C}) = 4.19xPacket + 13.27x(M - A) + 0.83xHardn. - 485 \quad (19)$$

$$\sigma = 11.8, R^2 = 0.92$$

where Packet= largest ferrite grain and bainite packet size (μm), (M-A)= area fraction of M-A constituents (%) and Hardn.= hardness (HV)

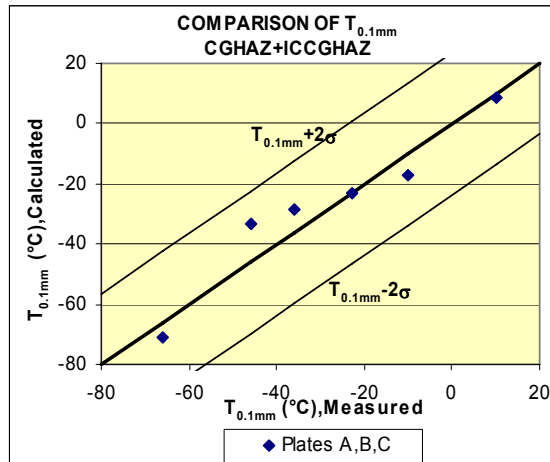


Fig. 81. Results of multiple linear regression analyses between the largest ferrite grain and bainite packet sizes, the area fraction of M-A constituents, hardness (Hardn.) and the CTOD transition temperature $T_{0.1mm}$ of the CGHAZ and ICCGHAZ.

6.7.2 Plate and ICHAZ

In the ICHAZ of the weld HAZ, multiple linear regression equations (20)-(21) with the correlation coefficients of 0.76 and 0.90 showed that the area fraction of M-A constituents and hardness dominated regarding their impact on transition temperatures T_{27J} and $T_{50\%}$. The largest ferrite grain and bainite packet sizes only had influence on the impact transition temperature T_{27J} , although p-value of 0.31 (>0.05) for the largest ferrite grain and bainite packet sizes impaired the independence of the variable (Appendix 22). Variations of the area fraction of M-A constituents (11.23%) and hardness (48 HV) in the ICHAZ of the weld HAZ elevated the transition temperature T_{27J} by 59 °C and $T_{50\%}$ by 111 °C caused by M-A constituents and $T_{50\%}$ by 74 °C caused by hardness.

In the heat treated test pieces D1 and D1/ICHAZ, the impact transition temperatures T_{27J} were situated close the mean correlation line, but the impact transition temperatures $T_{50\%}$ close the lower line ($T_{50\%}-2\sigma$) in the scatter band (Figs 82–83).

$$T_{27J} (\text{°C}) = 2.57x\text{Packet} + 5.23x(M - A) - 181 , \quad (20)$$

$$\sigma = 19.4 \text{ °C}, R^2 = 0.76$$

$$T_{50\%} (\text{°C}) = 9.87x(M - A) + 1.55x\text{Hardn.} - 391 , \quad (21)$$

$$\sigma = 17.3 \text{ °C}, R^2 = 0.90$$

where Packet= largest ferrite grain and bainite packet size (μm), (M-A)= area fraction of M-A constituents (%) and Hardn.= hardness (HV)

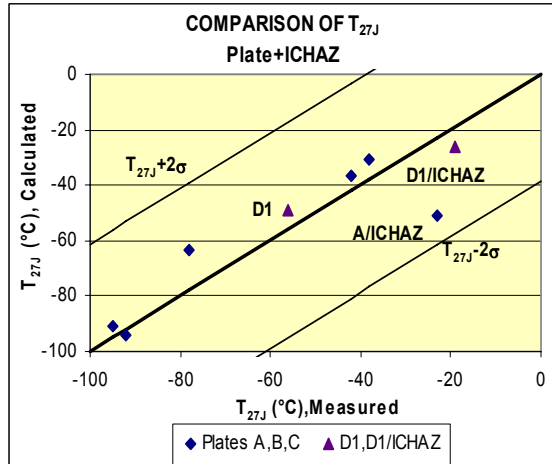


Fig. 82. Results of multiple linear regression analyses between the largest ferrite grain and bainite packet sizes, the area fraction of M-A constituents and the impact transition temperature T_{27J} of the plate and ICHAZ.

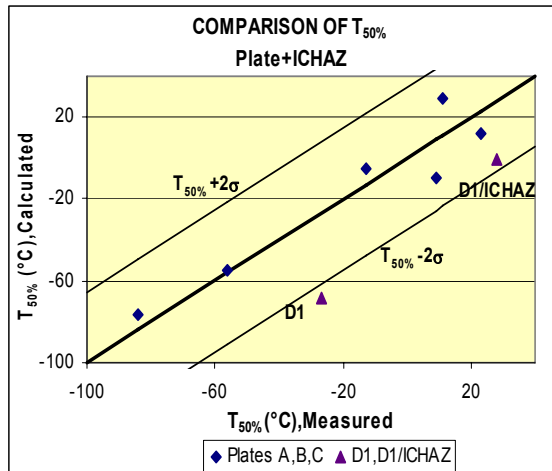


Fig. 83. Results of multiple linear regression analyses between the area fraction of M-A constituents, hardness and the impact transition temperature $T_{50\%}$ of the plate and ICHAZ.

Equation (22) with a correlation coefficient of 0.71 demonstrated that the area fraction of M-A constituents and hardness had a significant influence on the CTOD transition temperature $T_{0.1\text{mm}}$ in the ICHAZ of the weld HAZ. Variation of the area fraction of M-A constituents (11.23%) and hardness (48 HV) in the ICHAZ of the weld HAZ elevated the

CTOD transition temperature $T_{0.1mm}$ by 68 °C and 72 °C respectively. On the other hand, p-values of 0.09 (> 0.05) for M-A constituents and 0.11 (> 0.05) for hardness impaired the independence of these variables (Appendix 24).

The test result from the heat treated test pieces D2 and D2/ICHAZ were situated between the main and the lower lines ($T_{0.1mm}-2\sigma$) in the scatter band of the CTOD transition temperatures $T_{0.1mm}$ (Fig. 84).

$$T_{0.1mm} (\text{°C}) = 6.08x(M - A) + 1.51xHardn. - 409, \quad (22)$$

$$\sigma=22.5, R^2=0.71$$

where M-A= area fraction of M-A constituents (%) and Hardn.= hardness (HV)

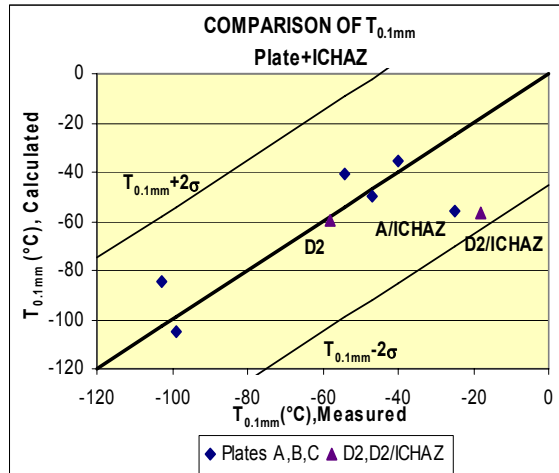


Fig. 84. Results of multiple linear regression analyses between the area fraction of M-A constituent, hardness and the CTOD transition temperature $T_{0.1mm}$ of the plate and ICHAZ.

6.7.3 Summary of paragraph 6.7

In summary, the multiple linear regression analyses calculated on the basis of the impact and CTOD transition temperatures T_{27J} , $T_{50\%}$ and $T_{0.1mm}$ of the CGHAZ and ICCGHAZ showed that the largest ferrite grain and bainite packet sizes (Packet) and the area fraction of M-A constituents (M-A) had the most significant influence on the impact and fracture toughness of the CGHAZ and ICCGHAZ in the weld HAZ. Elevation of the CTOD transition temperatures $T_{0.1mm}$ caused by the largest ferrite grain and bainite packet sizes and the area fraction of M-A constituents completed by hardness was more significant than that of the impact transition temperatures T_{27J} and $T_{50\%}$.

In the ICHAZ of the weld HAZ the multiple linear regression analyses calculated on the basis of the base plate and the ICHAZ showed that the area fraction of M-A constituents and hardness had the most significant influence on impact and fracture toughness. An increase of the area fraction of M-A constituents elevated the impact transition temperature $T_{50\%}$ more significantly than T_{27J} and the CTOD transition temperature $T_{0.1mm}$. Elevation of the CTOD transition temperature $T_{0.1mm}$ caused by M-A constituents and hardness was equal.

In the heat treated test pieces D1 and D1/ICHAZ the dots of the impact transition temperature T_{27J} were situated close the mean correlation line, but those of the $T_{50\%}$ were close the lower line ($T_{50\%}-2\sigma$) in the scatter band. The dots of the CTOD transition temperature $T_{0.1mm}$ of the heat treated test pieces D2 and D2/ICHAZ were situated between the mean and the lower lines ($T_{0.1mm}-2\sigma$) in the scatter band.

7 Discussion

Improvement of the toughness of the low heat input weld HAZ is based on the microstructure of the most critical sub-zones ICCGHAZ and ICHAZ formed as a result of intercritical heating of the CGHAZ and the base plate. However, at low heat input welding the ICHAZ stretches through the whole plate thickness and has a more significant influence on toughness than the ICCGHAZ, which is very limited in size. Thus, the microstructure of the base plate has a significant influence on the toughness of the weld HAZ.

The ideal microstructure in the base plate regarding the toughness of the weld HAZ would be intragranular acicular ferritic or bainitic microstructure with evenly distributed high carbon microconstituents such as fine dispersion of isolated carbides and carbide colonies between acicular ferritic or bainitic laths. Such microstructure would lead to the formation of evenly distributed M-A constituents between acicular ferritic or bainitic laths in the ICHAZ as a result of the intercritical thermal cycle (Akselsen *et al.* 1988). Although a reduction of carbon and alloy contents of a steel reduces the area fraction of M-A constituents, their use is necessary to achieve the strength and toughness properties of the base plate. Thus, the size and distribution of M-A constituents play a key role in deterioration of toughness in addition to the area fraction of M-A constituents at areas of low heat input welding.

7.1 Intragranular nucleation of ferrite and bainite

Although the intragranular nucleation of acicular ferrite or bainite in the base plate and CGHAZ has an indirect influence on the toughness of the weld HAZ at low heat input welding, it has a central position regarding the formation of a uniform distribution of relatively small isolated martensite microconstituents due to the fine interlocking character of intragranularly nucleated microstructure. Normally, intragranularly nucleated acicular ferritic microstructure has been achieved in the weld metal, the CGHAZ of high heat input welding and the rolling simulation specimens, but not in rolled plates (Shim J-D *et al.* 1999, Shim *et al.* 2000). The main factors affecting the formation of intragranular ferritic or bainitic microstructure such as the chemical composition of steel; the type,

amount, distribution and size of inclusions; austenite grain size; cooling rate and finish cooling temperature are discussed in the following paragraphs.

7.1.1 Chemical composition of steel

The choice of the chemical composition (Table 3) of titanium killed plate C, regarding the formation of acicular ferritic microstructure, was based on titanium oxide inclusions for nucleation of intragranular ferrite according to the recommendations in the course of a European Coal and Steel (ECSC) R&D project "*Heterogenous nucleation of acicular ferrite for toughness of HSLA steels*" (Anelli *et al.* 2002). The suitable contents of titanium and oxygen of 0.014% and 48 ppm, a low aluminium content of below 0.002%, so that the Al/O ratio did not exceed unity, and relatively high manganese and sulphur contents of 1.57% and 0.005% respectively, were expected to promote the formation of suitable titanium oxide inclusions with manganese sulphides on them (Cochrane & Senogles 1994, Francis-Schrutton 1995a,b, Ishikawa & Takahashi 1995, Zhang & Farrar 1996). Furthermore, alloying of nickel and copper of 0.40% and 0.29%, as well as manganese, was assumed to contribute the intragranular nucleation of ferrite and bainite due to a decrease of austenite-ferrite transformation temperature. In addition, vanadium microalloying of 0.074% was expected to promote the formation of intragranularly nucleated ferrite and bainite in the ICCGHAZ due to the formation of polygonal ferrite along the austenite grain boundaries in the CGHAZ (Harrison & Webster 1994, Hart & Mitchell 1995, Harrison & Wall 1996, Li *et al.* 2000, Li *et al.* 2001) and the intragranular nucleation of ferrite on VN precipitates (Kimura *et al.* 1997). On the other hand, vanadium has been observed to enhance the formation of M-A constituents and increase hardness by precipitation hardening (Haze & Aihara 1987, Fairchild *et al.* 1991, Harrison & Webster 1994, Harrison & Wall 1996, Matsuda *et al.* 1996, Tian 1998).

In aluminium killed conventional thermomechanically processed plate A, titanium microalloying of 0.016% was expected to prevent austenite grain coarsening during rough rolling and niobium microalloying of 0.039% to elevate the austenite recrystallization temperature T_{NR} contributing to a deformation below it for the formation of deformation bands inside austenite grains for the nucleation of ferrite. However, several research works have postulated that an addition of niobium more than 0.01% in titanium microalloyed steels enhances the formation of coarse ferrite side plates or ferrite with aligned second phase microconstituents (FS(A)) (Yamamoto *et al.* 1989, Tomita *et al.* 1994, Manochar *et al.* 1996). In addition, niobium microalloying can promote a deterioration of toughness of the ICCGHAZ due to its attribution of martensite hardness (Haze & Aihara 1987, Lee *et al.* 1992, Matsuda *et al.* 1996).

In aluminium killed and titanium microalloyed recrystallization controlled rolled plate B with copper and nickel alloying of 0.30% and 0.34% respectively, were selected for testing on the basis of good impact and fracture toughness of simulated test specimens according to higher heat input ($t_{8/5}=30$ s). A relatively high carbon, manganese, copper and nickel content in steel can decrease the austenite-ferrite transformation temperature contributing the intragranular nucleation of ferrite or bainite without the increase of

hardness of M-A constituents in the weld HAZ caused by niobium and vanadium microalloying.

7.1.2 Type, amount, distribution and size of inclusions

The chemical composition of the inclusions in titanium killed plate C containing 34% TiO₂, 34% MnS and 32% MnO (Fig. 28) was suitable for the nucleation of acicular ferrite representing a type of inclusions in higher oxygen steels. High manganese contents in the inclusion analyses are consistent with the observation concerning the formation of a manganese depleted zone in the surrounding matrix of the inclusions. However, in an aluminium killed plate from the same charge as plate A, inclusions contained 30–35% Al₂O₃, 20–30% TiO₂, 20–25% MnS and 15–25% MnO (Fig. 29) and inclusions in plate B containing a significant amount of aluminium and calcium oxides were not so favourable for the intragranular nucleation of ferrite as were inclusions in titanium killed plate C due to thermodynamically more stable aluminium calcium oxysulphides probably formed in the liquid state. (Gladman & Senogles 1994, van der Eijk *et al.* 2000, Anelli *et al.* 2002).

The amount of inclusions of 303–751 particles/mm² in the SEM/EDS analyses and 69 particles/mm² in the optical microscope analysis of titanium killed plate C exceeded the minimum amount of 10–50 particles/mm² for the formation of acicular ferritic microstructure in the HAZ of high heat input welded joints. In the SEM/EDS analyses, the amount of inclusions exceeded the minimum amount of 50–250 particles/mm² (about 200 particles/mm² in this type of steel) for the formation of acicular ferritic microstructure in the base plate. Thus, the high amount of predominantly small inclusions, revealed in the SEM/EDS analysis at the University of Oulu, was expected to enhance the intragranular nucleation of acicular ferrite in titanium killed plate C. The higher amount of large inclusions (average length of 2.7 μm) of 142 particles/mm² in aluminium killed plate B, than 69 particles/mm² in titanium killed plate C, did not have such a significant influence on the formation of acicular ferrite as did small inclusions in titanium killed plate C. In the aluminium killed plate from the same charge as plate A, the amount of inclusions of 119 particles/mm² also exceeded the minimum amount of particles, but was not high enough for the nucleation of acicular ferrite (Chijiwa *et al.* 1988, Yamamoto *et al.* 1989, Yamamoto *et al.* 1996, van der Eijk *et al.* 2000, Anelli *et al.* 2002).

The average size of inclusions of 0.8–3.7 μm in titanium killed plate C was roughly the same as 0.2–4.0 μm measured from titanium killed plates and the weld HAZ in the several research works. The relatively large inclusions promote the nucleation of ferrite on them within a diffusion controlled reconstructive reaction with star like ferrite indicating its nucleation in manganese depletion zones around the inclusions (Figs 30 and 31), but small inclusions promote the nucleation of ferrite using a displacive reaction. In aluminium killed plate B and the plate from the same charge as plate A, the average size of inclusions of 2.3–2.7 and 1.9 μm respectively was larger than in titanium killed plate C (Chijiwa *et al.* 1988, Yamamoto *et al.* 1989, Gladman & Senogles 1994, Yamamoto *et al.* 1996, Zhang & Farrar 1996, Haaland *et al.* 1997, van der Eijk *et al.* 2000, Thewlis 2001, Anelli *et al.* 2002).

The average size and the inclusion volume fraction in all test plates determined using the SEM/EDS analysis at CSM were relatively high compared with the calculated values based on the oxygen and sulphur contents (1) indicating a too high penetration depth in the SEM/EDS analysis. This observation is also supported by the measurements from plate B carried out using the SEM/EDS and the optical microscope analyses at the University of Oulu. But in the analyses from plate C the inclusion volume fraction was a little higher than calculated according to (1). However, the evaluation of the results was carried out according to the SEM/EDS analysis at CSM completed by the SEM/EDS and the optical microscope analyses at the University of Oulu due to a large variation of test results from this type of steel in a European Coal and Steel (ECSC) R&D project “*Heterogenous nucleation of acicular ferrite for toughness improvement of HSLA steels*” (Anelli *et al.* 2002).

7.1.3 Austenite grain size

The amount of acicular ferritic microstructure of 6% in titanium killed plate C (Table 7) with an austenite grain size of 50–90 μm (average about 70 μm and the largest 116 μm) and mainly acicular microstructure with an austenite grain size of about 120–180 μm (simulation heat treatments of 20 min at 1250 $^{\circ}\text{C}$ or 3 min at 1300 $^{\circ}\text{C}$, followed by cooling at 10 $^{\circ}\text{C}/\text{s}$ to 500 $^{\circ}\text{C}$ of the specimens from plate C) showed that the austenite grain size of the plate was too small for the intragranular nucleation of acicular ferrite in the rolled plate. This observation also supported the opinion that the minimum austenite grain size for the formation of a significant amount of acicular ferrite in this type of steel is 100 μm (Anelli *et al.* 2002). On the other hand, some research works have shown that the intragranular nucleation of ferrite or acicular ferrite is achieved in titanium killed steels containing titanium oxides, when the prior austenite grain sizes were 50–90 μm (Lee & Pan 1991, Shim J-D *et al.* 1999, Shim *et al.* 2000). In weld metals containing a greater amount of smaller inclusions than base plates, the minimum austenite grain size for the nucleation of acicular ferrite has been reported to be 50–60 μm and in weld metals containing boron even as low as 20 μm (Thewlis 1994, Thewlis 2000).

Even the aluminium killed plates A and B contained higher amounts of acicular ferrite than plate C: 8% in plate A and 11% in plate B (Table 7). Probably, the largest austenite grain sizes of 181 μm and an average of 101 μm for plate A and of 136 μm and of 76 μm for plate B respectively (Fig. 44), were not high enough for the formation of more acicular ferrite with a relatively low amount of favourable inclusions.

The achievement of intragranular ferrite of more than 60% (26–32% acicular ferrite (AF) and 32–36% intragranular polygonal ferrite PF(I)) in the heat treated test pieces D1 and D2 (Table 7) from titanium killed plate D with the largest prior austenite grain size of 323 and 293 μm and with the average of 212 and 183 μm respectively, also evidenced a significant influence of the prior austenite grain size on intragranular nucleation of ferrite (Fig. 44). In comparison with the microstructure in test plate C, the intragranular nucleation of ferrite in the heat treated test pieces took place at the expense of primary grain boundary ferrite PF(G) and ferrite with non-aligned second phases (FS(NA)). Probably, a larger increase of the prior austenite grain size in the heat treated test pieces

D1 and D2 than in the rolled plate C, increased the amount of intragranular polygonal ferrite PF(I) and caused ferrite grain coarsening, as was observed by the increased ferrite grain and bainite packet sizes in the heat treated test pieces D1 and D2, compared with those in plate C. Thus, it is obvious that an increase of the prior austenite grain size to over 200 μm , the intergranular ferrite nucleation of ferrite increases at the expense of the intragranular nucleation of ferrite with this number density of suitable titanium-manganese oxide/manganese sulphide inclusions.

7.1.4 Hot deformation and cooling rate

The microconstituents in test plates A, B and C provide evidence that acicular ferritic microstructure is very difficult to achieve in TMCP or RCR plates, at least for a number density of inclusions that can be achieved with titanium killing. It is impossible to achieve sufficiently large austenite grain sizes under the restraints of practical plate rolling mill conditions. Furthermore, possibilities to achieve acicular ferritic microstructure in titanium killed plate C were probably impaired by an inadequate hot deformation in plate rolling in the 50 mm thick plate compared with the recent research works. For example in the Korean research work, 60% acicular ferrite was achieved in wrought steel containing fine (0.1–5 μm) Ti_2O_3 inclusions with high manganese contents of 2.3–2.5% using slab heating temperatures of 1150–1250 $^\circ\text{C}$ followed by rolling deformation of 50% at 1050–1150 $^\circ\text{C}$ and cooling at 1–30 $^\circ\text{C}/\text{s}$ (Shim J-D *et al.* 1999, Shim *et al.* 2000). Furthermore, acicular ferritic microstructure has been achieved after austenite deformation in its recrystallization temperature range followed by controlled cooling at 10–30 $^\circ\text{C}/\text{s}$ (Zhao & Boyd 2000, Zhao *et al.* 2003). Also, a strong deformation in the austenite recrystallization temperature T_{NR} region or a two stage rolling deformation, including the first stage in the austenite recrystallization temperatures followed by the second stage below it, increased dislocations in austenite grains for intragranular nucleation sites. In addition, a high cooling rate increased the thermodynamic driving force for nucleation and growth of intragranular ferrite. (Yakubtsov *et al.* 2000, Yakubtsov & Boyd 2001, Zhao *et al.* 2003, Yakubtsov *et al.* 2004).

Although intragranular nucleation of acicular ferrite has been reported as being possible in titanium killed plates over a wide range of cooling rates of 0.3–54 $^\circ\text{C}/\text{s}$, the accelerated cooling rate of 10 $^\circ\text{C}/\text{s}$ was selected for the heat treated test pieces from titanium killed plate D on the basis of the several research works and the simulation heat treatment studies. The variation of accelerated cooling rates between 1000 and 500 $^\circ\text{C}$ from 11.2 $^\circ\text{C}/\text{s}$ for test piece D1 to 6.8 $^\circ\text{C}/\text{s}$ for test piece D2 were derived from variations in the laboratory process. However, the test pieces contained over 60% intragranularly nucleated ferrite (26–32% acicular ferrite and 32–36% polygonal ferrite) as expected (Barbaro *et al.* 1989, Yamamoto *et al.* 1989, Shim J-D *et al.* 1999, Yakubtsov *et al.* 2000, Zhao *et al.* 2003, Yakubtsov *et al.* 2004).

7.1.5 Finish cooling temperature

For the rolling simulated specimens from plate C and the heat treated test pieces from plate D, a finish cooling temperature of 500 °C was selected to achieve the maximum amount of acicular ferrite, when the cooling rate was 10 °C/s ($t_{8/5}=30$ s), although lower finish cooling temperatures, even as low as 200 °C, have been proposed for the formation of acicular ferritic microstructure, but then the amount of M-A constituents is increased (Yamamoto *et al.* 1989, Suh *et al.* 2000, Yakubtsov *et al.* 2000, Yakubtsov *et al.* 2004). Probably, the M-A constituents in the laboratory heat treated test piece D2, instead of the ferrite carbide-aggregates in test piece D1, was caused by a lower finish cooling temperature of D2 due to variations in the laboratory accelerated cooling process.

7.1.6 Summary of paragraph 7.1

In summary, the test results from titanium killed plate C showed that no significant amount of acicular ferritic microstructure was achieved under the restraints of practical plate rolling mill conditions, in spite of the suitable chemical composition and the inclusion content. Alloying of nickel and copper of 0.40% and 0.29% respectively, for a decrease of the austenite-ferrite transformation temperature, was expected to enhance the intragranular nucleation of ferrite. In addition, vanadium microalloying of 0.074% was assumed to promote the formation of acicular ferrite in the ICCGHAZ due to the formation of polygonal ferrite along the austenite grain boundaries in the CGHAZ and the intragranular nucleation of ferrite on VN precipitates.

Although the advantageous chemical composition of inclusions (34% TiO₂, 34% MnS and 32% MnO) and the amount of 303–751 particles/mm² (≥ 200 particles/mm²) in titanium killed plate C promoted the formation of acicular ferritic microstructure, only 6% of it could be achieved in the rolled plate due to too small a prior austenite grain size of 50–90 μm (average about 70 μm and the largest 116 μm) compared with a number density of suitable titanium-manganese oxide/manganese sulphide inclusions.

However, mainly acicular ferritic microstructure was achieved using the rolling simulation heat treatments of 20 min at 1250 °C or 3 min at 1300 °C and cooling at 10 °C/s to 500 °C of test specimens from titanium killed plate C, when the prior austenite grain size coarsened from 50–90 μm in plates to about 120–180 μm in the simulated specimens. Similarly, over 60% intragranularly nucleated ferrite (26–32% acicular ferrite and 32–36% polygonal ferrite), achieved in the laboratory heat treated test pieces D1 and D2 from titanium killed plate D, with the largest prior austenite grain size of 323 μm and 293 μm and the average of 212 μm and 183 μm respectively, demonstrated the significant influence of the prior austenite grain size on the intragranular nucleation of acicular and polygonal ferrite.

7.2 Toughness of the CGHAZ and ICCGHAZ

It has been stated in the previous paragraphs that the ICHAZ was the most critical sub-zone of the weld HAZ regarding the toughness of the low heat input welded joints. However, the test results showed that the CGHAZ and ICCGHAZ also had a significant influence on toughness due to the area fraction, size and distribution of M-A constituents, which dominate crack nucleation (Kweon *et al.* 2000). Normally, the type of microstructures and the sizes of the largest ferrite grains and bainite packets resulting grain coarsening also have a significant influence on the toughness of the CGHAZ and ICCGHAZ due to their enhancement of crack propagation. In addition, hardness reflecting the contribution of dislocation, solid solution and precipitation strengthening in high heat input HAZs should be taken into consideration (Harrison & Webster 1994, Harrison & Wall 1996).

7.2.1 Type of microstructures

The trend curves (Figs 38–40) from the microstructural investigations of the CGHAZ showed that an increase of intragranular microconstituents ((AF)+PF(I)) and a decrease of primary grain boundary ferrite plus ferrite with second phase microconstituents (PF(G)+FS) improved toughness. However, the individual test results outside the trend curves showed that there were also other factors, which had a significant influence on the toughness of the CGHAZ. In addition, the influence of the largest ferrite grain and bainite packet sizes outweighed that of microstructure type on toughness in the multiple linear regression analyses in paragraph 6.7.1.

The low fracture toughness of the CGHAZ (Figs 36–37 and 40) made it the most critical sub-zone in the weld HAZ of plate B. This was probably due to a 24% proportion of martensite, although the CGHAZ thermal cycle of the base plate elevated the impact and CTOD transition temperatures T_{27J} , $T_{50\%}$ and $T_{0.1mm}$ of plate B less than those of plates A and C. This was due to the higher transition temperatures $T_{50\%}$ and $T_{0.1mm}$ in the base plate B compared to plates A and C. However, the improvement of impact toughness of the CGHAZ of plate B compared to plate A demonstrated that increasing P_{cm} improved impact toughness (Harrison & Hart 1990). In the CGHAZ of plate A the increase of ferrite with second phase microconstituents (FS(A) and FS(NA)) and local martensite (M) together with a decrease of intragranular polygonal ferrite (PF(I)), compared with those of the base plate (Table 7), indicated an enhancement of 0.039% niobium microalloying for formation of FS(A) and FS(NA) and their detrimental influence on toughness (Yamamoto *et al.* 1989, Tomita *et al.* 1994, Li *et al.* 2001). On the contrary, the lower transition temperatures $T_{50\%}$ of $-27\text{ }^{\circ}\text{C}$ and $T_{0.1mm}$ of $-46\text{ }^{\circ}\text{C}$ in the CGHAZ of plate C than in plates A and B indicated an improvement of toughness caused by intragranularly nucleated acicular ferrite that was probably enhanced by 0.074% vanadium microalloying (Ishikawa & Takahashi 1995, Kimura *et al.* 1997, Li *et al.* 2000, Li *et al.* 2001).

The impact and fracture toughness trend curves of the ICCGHAZ (Figs 38–40) showed that an increase of a relative proportion of intragranularly nucleated microconstituents (AF+PF(I)), particularly in the ICCGHAZ of plates B and C (14–31%)

and a decrease of ferrite with non-aligned second phases FS(NA), improved toughness significantly as expected according to the studies focusing on high heat input welding (Harrison & Webster 1994, Harrison & Wall 1996). However, there is no clear theoretical evidence concerning the transformation of ferrite with non-aligned second phase FS(NA) in the CGHAZ of plate B into intragranularly nucleated microconstituents (AF+PF(I)) as a result of the intercritical thermal cycle (Table 7). Furthermore, no significant elevation of the transition temperatures T_{27J} , $T_{50\%}$ and $T_{0.1mm}$ in the ICCGHAZ of plates B and C, regardless of the increase of M-A constituents, also indicated that the formation of relatively homogeneously distributed M-A constituents was caused by high carbon microstructures interposed between intragranularly nucleated ferrite and bainite plates as a result of the intercritical thermal cycle of the CGHAZ.

In the ICCGHAZ of plate A, the significant elevation of the transition temperatures T_{27J} , $T_{50\%}$ and $T_{0.1mm}$ (33–53 °C) compared with those in the CGHAZ specimens, despite a 17% decrease of ferrite with non-aligned second phase microstructures FS(NA) and a small increase of intragranularly nucleated polygonal ferrite PF(I). This demonstrated that a high proportion of primary grain boundary ferrite plus ferrite with second phase microconstituents (PF(G)+FS) and the formation of M-A constituents during the intercritical thermal cycle between Ac_1 and Ac_3 impaired toughness, as is presented in the following paragraphs.

7.2.2 Ferrite grain and bainite packet sizes

The trend curves (Figs 51–53) and the multiple linear regression analyses (6.7.1) of the CGHAZ and ICCGHAZ provide evidence that an increase of the effective grain size, i.e. the largest ferrite grain and bainite packet sizes, decreased toughness significantly by allowing crack propagation across longer distances from one high angle boundary to another on a dominant cleavage plane $(100)_\alpha$. The enhancement of crack propagation caused by the increased ferrite grain and bainite packet sizes also supported the opinion that the arrest capability of bainite packet boundaries decreases when the temperature decreases. Crack propagation has been claimed to be dominant at ductile-brittle temperatures. Cleavage crack initiation was proposed to be critical only at temperatures below –150 °C (Tian *et al.* 1996, Lambert *et al.* 2000b, Lambert *et al.* 2000c).

Elevation of the impact and CTOD transition temperatures T_{27J} by 4.8 °C/ μm , $T_{50\%}$ by 3.9 °C/ μm and $T_{0.1mm}$ by 4.2 °C/ μm calculated according to the multiple linear regression analyses (6.7.1) of the CGHAZ and ICCGHAZ, showed that the increased largest ferrite grain and bainite packet sizes had an even more detrimental influence on toughness than the measured changes in the percentage of M-A constituents. However, a significantly smaller elevation of the impact transition temperature $T_{50\%}$, from 0.6 to 1.0 °C/ μm , was calculated according to (10) using the coefficient of d from 10 to 16 °C/ \sqrt{mm} in ferrite grain and bainite packet sizes ranging from 30 to 60 μm (Yamamoto *et al.* 1989, Lee & Pan 1991, François 2001). This great difference is probably a consequence of the way in which the ferrite grain and bainite packet sizes were characterised; the largest values were used in the present research work, but average values were used in the referenced work.

A remarkable elevation of the impact and CTOD transition temperatures T_{27J} , $T_{50\%}$ and $T_{0.1mm}$ in the ICCGHAZ of plate A, by increase in ferrite grain and bainite packet sizes as a result of the intercritical thermal cycle of the CGHAZ and nearly direct propagation of a crack through a large ferrite grain (Figs 65–66), showed that a high proportion of primary grain boundary ferrite plus ferrite with second phase microconstituents (PF(G)+FS) had a detrimental influence on toughness. On the contrary, a small decrease of ferrite grain and bainite packet sizes without significant changes in impact toughness and with improvement of fracture toughness of the ICCGHAZ of plate B, as a result of the intercritical thermal cycle of CGHAZ, showed an improvement of toughness caused by intragranularly nucleated microconstituents (AF+PF(I)). Thus, the type of microstructure has a significant influence on ferrite grain and bainite packet sizes, which has been used in the multiple linear regression analyses in this research work (6.7.1).

7.2.3 Amount, size, type and distribution of M-A constituents

The presence of M-A constituents has been regarded as the major factor reducing the toughness of low heat input welded joints (Kweon *et al.* 2000) due to their enhancement of crack initiation. However, it has been suggested that they decrease both crack initiation and propagation energy. Crack initiation energy is decreased by an increase in the area fraction of the massive M-A constituents and crack propagation energy by an increase in the interfacial area between the M-A constituent and the matrix. Thus, the area fraction and distribution of M-A constituents dominate in crack initiation, but their size and distribution dominate in crack propagation (Okada *et al.* 1994, Tian *et al.* 1996, Li *et al.* 2001, Liu *et al.* 2002).

The trend curves (Figs 62–64) and the multiple linear regression analyses (6.7.1) showed that the total area fraction of M-A constituents decreased the toughness of the CGHAZ and ICCGHAZ at low heat input welding more significantly than that of the CGHAZ at high heat input (7.5 kJ/mm) welding (Harrison & Webster 1994, Harrison & Wall 1996, Kweon *et al.* 2000). Elevation of the impact and CTOD transition temperatures T_{27J} by 10.0 °C/%, $T_{50\%}$ by 9.4 °C/% and $T_{0.1mm}$ by 13.3 °C/% increase M-A constituents of the CGHAZ and ICCGHAZ of test plates A, B and C according to the multiple linear regression analyses supporting the above-mentioned observation. The highest elevation in the $T_{0.1mm}$ evidenced that M-A constituents had a more detrimental influence on toughness in CTOD tests than in Charpy V impact tests due to the smaller root radius in CTOD test specimens than in Charpy V impact test specimens (Harrison & Webster 1994, Harrison & Wall 1996, Matsuda *et al.* 1996, Li *et al.* 2001). Also, a decrease of the impact and CTOD transition temperatures in the post weld heat treated ICCGHAZ (PWHT) specimens from all test plates, roughly to the same level as those of the CGHAZ specimens, evidenced a detrimental influence of M-A constituents on impact and fracture toughness. Transformation of M-A constituents into carbides or carbide clusters and a stress relaxation of the ferrite-bainite matrix improved toughness significantly in the post weld heat treated ICCGHAZ (PWHT) regardless of a small increase of ferrite-bainite packet size (5–15 µm), which confirmed a significant enhancement of M-A constituents on crack nucleation at low heat input welding (Okada

et al. 1994, Tian *et al.* 1996, Kweon *et al.* 2000). However, the impairment of fracture toughness in the ICCGHAZ of plate C, as a result of post weld heat treatment (PWHT), was probably caused by a coarsening of TiV precipitates as can be seen from the increased fraction of coarse precipitates (Appendix 11, Figs 96–97) and their vanadium content (Appendix 8, Table 15) as a result of PWHT.

However, the trend curves of the impact and CTOD transition temperatures (Figs 62–64) showed that only a slightly higher area fraction of M-A constituents (7.73%) in the ICCGHAZ of plate C compared to that of plate B (4.55%) increased the impact and CTOD transition temperatures indicating a degradation of toughness in excess of 6% of M-A constituents (Akselsen *et al.* 1987, Akselsen *et al.* 1988, Harrison & Webster 1994, Harrison & Wall 1996). This also indicates that the vanadium content of 0.074% in plate C promoted the formation of M-A constituents due to an excess of the optimum vanadium content of 0.050% regarding toughness improvement of the CGHAZ and ICCGHAZ proposed by Li *et al.* (2000) and Li *et al.* (2001). On the other hand, the smaller fraction of M-A constituents in the ICCGHAZ of steel B, compared with the carbon contents of test plates (Fig. 54), could be as a result of evenly distributed M-A constituents between mostly intragranularly nucleated microconstituents (AF+(PF(I))) (Chijiwa *et al.* 1988, Yamamoto *et al.* 1989, Yurioka 1995) or a failure to identify them in the image analysis. Consequently, the above-mentioned limit concerning a degradation of toughness in excess of 6% M-A constituents is disproved in the present research work.

The highest deterioration of the impact and fracture toughness of the ICCGHAZ of plate A compared with that of plates B and C demonstrates the significant influence of the distribution of M-A constituents on toughness (Figs 62–64). Investigations of the cracks in the ICCGHAZ of plate A revealed, like many other investigations, that cracks are nucleated at the M-A/ferrite-bainite interfaces or between two massive blocky-type M-A constituents with sizes of 2–5 μm situated in continuous sheets along the prior austenite grain boundaries and propagated nearly direct through a large ferrite packet (Figs 65–66). Although M-A particles on one hand assisted crack initiation and propagation decreasing crack initiation and propagation energies, on the other hand they hindered, crack propagation causing kinks on the fracture surface (Chen *et al.* 1984, Tian 1988, Hrivnak *et al.* 1992a,b, Davis & King 1993, Davis & King 1994, Hrivnak *et al.* 1995, Hrivnak *et al.* 1996, Tian *et al.* 1996, Li *et al.* 2000, Li *et al.* 2001). However, the negative contribution of M-A constituents to crack initiation and propagation outweighs the small positive contribution caused by kinking. Also, niobium microalloying of 0.039%, together with a carbon content of 0.074% in TMCP plate A, probably promoted a deterioration of toughness in the ICCGHAZ due to its contribution to martensite hardness (Haze & Aihara 1987, Lee *et al.* 1992, Matsuda *et al.* 1996, Tian 1998).

The investigation of the secondary cracks in the ICCGHAZ of plate B showed that microvoids were nucleated at numerous sites of M-A/ferrite boundaries or bainite interfaces in small ferrite or bainite laths. The nucleation of microvoids was followed by the cracking of M-A constituents between ferrite or bainite laths and their coalescence into final cracks as expected according to the observations concerning crack nucleation at the ends of aligned M-A particles and their cracking (Figs 67–68) (Kim *et al.* 1991, Hrivnak *et al.* 1992a). Consequently, it can be assumed that the coalescence of microvoids and microcracks and their growth into the critical size becomes more difficult

in a case of many small microcracks between fine ferrite-bainite laths compared with few large microcracks between coarse ferrite grains and bainite packets.

7.2.4 Hardness

Hardness measurements revealed relatively high elevations of hardness in the CGHAZ of all test plates compared to base plates. This was caused by an increase of bainitic ferrite with second phase microconstituents (FS(A)+FS(NA)) in plate A and local martensitic microconstituents in plates B and C. These martensitic microconstituents probably elevated the impact and fracture toughness transition temperatures $T_{50\%}$ and $T_{0.1\text{mm}}$ of the base plate and the CGHAZ of plate B as expected according to numerous research works (Haze & Aihara 1987, Harrison & Hart 1990, Harrison & Webster 1994, Harrison & Wall 1996). However, the low impact energy transition temperature T_{27J} of plate B demonstrated the improvement of impact toughness of the low heat input welded joints by an increase in the hardness of the CGHAZ (Harrison & Hart 1990). On the contrary, in this research work the multiple linear regression analyses showed that hardness of the CGHAZ and the ICCGAZ had an insignificant influence on the toughness of low heat input welding simulated specimens. Of course, toughness test results cannot be explained by hardness alone. The microstructural factors discussed in paragraphs 7.2.1–7.2.3 need to be taken into consideration.

7.2.5 Summary of paragraph 7.2

In summary, the trend curves and the multiple linear regression analyses showed that an increase of the largest ferrite grain and bainite packet sizes, the area fraction of M-A constituents and hardness elevated the impact and CTOD transition temperatures T_{27J} , $T_{50\%}$ and $T_{0.1\text{mm}}$ of the CGHAZ and ICCGAZ of the test plates as the main factors. However, the individual test results were influenced by the chemical composition of steel, the type of microstructures and the size and distribution of M-A constituents, as explained below.

Titanium killing, together with vanadium microalloying of plate C, was a potential method for improving the toughness of the CGHAZ due to the formation of a significant amount of intragranularly nucleated ferrite (20% acicular ferrite) and bainite. A little higher carbon, aluminium killed and copper plus nickel alloyed plate B impaired the toughness of the CGHAZ compared to the titanium killed plate C due to a 24% proportion of martensite. Niobium microalloyed (0.039% niobium) and aluminium killed steel A impaired the toughness of the CGHAZ compared to the titanium killed plate C due to the increase of ferrite with second phase microconstituents FS(A) and FS(NA).

The significant improvement of the toughness of the ICCGAZ was achieved in aluminium killed and copper plus nickel alloyed plate B and titanium killed plate C. This was due to the formation of relatively evenly distributed M-A constituents mainly between an intragranularly nucleated ferritic-bainitic microstructure, followed by the nucleation of microcracks at numerous sites of M-A/ferrite boundaries or bainite

interfaces and crack propagation joining separate microcracks together and cracking of M-A constituents. On the contrary, the significant degradation of the toughness of the ICCGHAZ was observed in the aluminium killed and niobium microalloyed plate A. This was due to the formation of continuous sheets of the massive blocky-type M-A constituents with sizes of 2–5 μm along the prior austenite grain boundaries and the large ferrite grain and bainite packet sizes significantly promoting crack nucleation and propagation.

Post weld heat treatment (PWHT) improved toughness of the ICCGHAZ roughly to the same level as that of the CGHAZ. This was a result of dispersion of M-A constituents into carbides or carbide clusters and stress relaxation in the ferritic-bainitic matrix regardless of a small increase of ferrite grain and bainite packet sizes, which demonstrated a significant enhancement of M-A constituents on crack nucleation and propagation.

7.3 Toughness of the ICHAZ

In many research works, a degradation of toughness of the ICHAZ was believed to be insignificant compared to that of the CGHAZ and ICCGHAZ (Harrison & Hart 1990), but normally at low heat input welding, the overmatched weld metal and HAZ concentrate cracking in the ICHAZ (Laitinen 1998). However, in this research work the ICHAZ was observed to be the most critical sub-zone of the weld HAZ of all test plates evaluated in regard to impact toughness of the simulated specimens. And in real welds the ICHAZ extends throughout the plate, whereas the other critical sub-zone, the ICCGHAZ, is restricted to small isolated strips. However, the toughness differences of the ICHAZ of test plates A, B and C were relatively small. Therefore, the discussion of the toughness of the ICHAZ will concentrate on the heat treated test pieces from plate D in which the area fraction, size, type and above all distribution of M-A constituents can be expected to play a key role in toughness in addition to the type of microstructures, ferrite grain and bainite packet sizes and hardness (Akselsen *et al.* 1987, Akselsen *et al.* 1988, Harrison & Hart 1990).

7.3.1 Type of microstructures

The trend curves (Figs 41–43) showed that the impact and fracture toughness of the ICHAZ of test plates A, B and C was improved by an increase in intragranularly nucleated microconstituents (AF+PF(I)). On the other hand, they were impaired by an increase in primary grain boundary ferrite plus ferrite with second phase microconstituents (PF(G)+FS). It is well known that the microstructure of the base plate, particularly the type of ferrite or bainite and the distribution of high carbon microconstituents, determines the microstructure of the ICHAZ (Akselsen *et al.* 1987, Akselsen *et al.* 1988, Fairchild *et al.* 1991). However, in this research work the microstructural differences in the TMCP and RCR test plates and in their ICHAZs were relatively small. Only a slightly higher proportion of intragranularly nucleated

microconstituents (17% AF plus 46% PF(I)), and a slightly lower proportion of primary grain boundary ferrite PF(G) in the ICHAZ of plate B than in those of the other test plates A and C, appeared to improve toughness. However, the high elevation of the impact and CTOD transition temperatures of the ICHAZ of the test plates was observed as a result of the intercritical thermal cycle of the base plate regardless of the significant decrease of ferrite with second phase microconstituents (FS(A) plus FS(NA)) and the increase of intragranular polygonal ferrite PF(I). This demonstrated a lesser influence of the type of microstructure than ferrite grain and bainite packet sizes, M-A constituents and hardness on toughness (Harrison & Webster 1994, Harrison & Wall 1996).

In addition, the lower impact and fracture toughness of the heat treated test pieces D1 and D2 from plate D and their ICHAZ areas compared to the ICHAZ of plate C, regardless of their higher proportion of intragranularly nucleated microconstituents (AF+PF(I)) and their lower proportion of primary grain boundary ferrite PF(G) plus ferrite with second phase microconstituents (PF(G)+FS), indicated a lesser influence of microstructure on toughness compared to that of the largest ferrite grain and bainite packet sizes and M-A constituents (Figs 41–43, 51–53, 62–64).

The multiple linear regression analyses from the test results also supported the observation that microstructure had a minor influence on impact and fracture toughness. Anyhow, the largest ferrite grain and bainite packet sizes (20) and hardness (21)-(22) reflected the microstructural aspects and the contribution of dislocation, solid solution and precipitation strengthening on toughness (Harrison & Webster 1994, Harrison & Wall 1996).

7.3.2 Ferrite grain and bainite packet sizes

The test results illustrated in trend curves (Figs 51–53) showed that an increase of the largest ferrite grain and bainite packet sizes of plates A, B and C impaired toughness, although the differences of the toughness between test plates A, B and C were small. However, the microstructural investigations indicated that the largest ferrite grains and bainite packets promoted crack propagation (Figs 73–76). Also, the multiple linear regression analyses with respect to elevation of the impact transition temperature T_{27J} by $2.6\text{ }^{\circ}\text{C}/\mu\text{m}$ increase in ferrite grain and bainite packet sizes provided evidence of a detrimental influence of increased ferrite grain and bainite packet sizes on impact toughness (Harrison & Webster 1994, Harrison & Wall 1996). However, the collective influence of the largest ferrite grain and bainite packet size on the toughness of the ICHAZ was smaller than that of the CGHAZ and ICCGHAZ, as the reduced influence of this variable in the multiple linear regression analyses also showed.

The effect of ferrite grain and bainite packet sizes on the toughness of the ICHAZ can be evaluated by comparing the test results from the ICHAZ of plate C and the heat treated test pieces D1 and D2. This comparison showed that 10 to 20 μm larger ferrite grain and bainite packet sizes in the ICHAZ of the heat treated test pieces D1 and D2 compared with those of plate C apparently impaired toughness because of their higher impact and CTOD transition temperatures (5–29 $^{\circ}\text{C}$) regardless of their higher proportion of intragranularly nucleated microconstituents (AF+PF(I)) and their lower area fraction and

more evenly distributed M-A constituents (Figs 46, 51–53, Appendices 6–7, Tables 13–14).

7.3.3 *Amount, size, type and distribution of M-A constituents*

The trend curves (Figs 62–64) in this research work based on the test results from plates A and D and the heat treated test pieces D1 and D2, equally showed (as in numerous other studies) that an increase in the area fraction of M-A constituents impaired toughness. Elevation of the transition temperatures T_{27J} by 5.2 °C/%, $T_{50\%}$ by 9.9 °C/% and $T_{0.1mm}$ by 6.1 °C/% an increase in the area fraction of M-A constituents according to the multiple linear regression analyses also supported this evidence, but was lower than in the CGHAZ and ICCGAZ. On the other hand, a higher area fraction of M-A constituents in the ICHAZ than in the ICCGAZ increased the total influence of M-A constituents on the toughness of the ICHAZ roughly to the similar level as that of the ICCGAZ. Also, a decrease of the impact transition temperature T_{27J} of the ICHAZ of all test plates and the CTOD transition temperature $T_{0.1mm}$ of the ICHAZ of plates B and C, at least to the same level as those of the base plate, as a result of post weld heat treatment (PWHT) is conclusive evidence of a loss of toughness caused by M-A particles.

The larger elevation of the impact transition temperatures T_{27J} and $T_{50\%}$ in the ICHAZ of ferritic-pearlitic plate D than in the ICHAZ of the heat treated test piece D1 demonstrated a significant degradation of toughness, when the area fraction of M-A constituents increased 11.00% and 5.87% respectively as a result of the intercritical thermal cycle (Appendix 1, Table 12). This also indicated that the excess of 6% M-A constituents decreased toughness significantly (Akselsen *et al.* 1987, Akselsen *et al.* 1988, Harrison & Webster 1994, Harrison & Wall 1996). Furthermore, the presence of approximately twice as much as M-A constituents in the ICHAZ of plate D compared with the ICHAZ of the heat treated test pieces D1 and D2 showed that the formation of M-A constituents was reduced in intragranularly nucleated ferritic-bainitic microstructure, as expected according to some research works (Chijiwa *et al.* 1988, Yamamoto *et al.* 1989, Yurioka 1995).

The lower impact and CTOD transition temperatures T_{27J} , $T_{50\%}$ and $T_{0.1mm}$ in the ICHAZ of plates A, B, C, which contained smaller M-A constituents than the ICHAZ of plate D and the heat treated specimens D1 and D2, was evidence of a detrimental influence of large M-A particles on toughness (Table 10).

The improvement of toughness in the ICHAZ of the heat treated test pieces D1 and D2 caused by smaller and more evenly distributed M-A constituents, compared with larger and in continuous band situated M-A constituents in the ICHAZ of plate D, evidenced a significant influence of the distribution of M-A constituents on the toughness of the ICHAZ (Figs 60–61). Also, the improved toughness of the ICHAZ in plates A, B and C containing the more evenly distributed M-A constituents compared with those in plate D and above all, the comparison of 11.67 and 11.35% M-A constituents contained ICHAZ of plates B and D respectively supported this evidence. The significant influence of the distribution of M-A constituents on toughness of the ICHAZ disproved the above-

mentioned assumption of a degradation of toughness caused by the excess of 6% M-A constituents.

Microstructural investigation of secondary cracks confirmed the evidence that microcracks, often nucleated at M-A/ferrite boundaries and propagated joining together separate microcracks into zig-zag cracks in the ICHAZ specimens from the heat treated test piece D2, contained relatively evenly distributed M-A constituents. In the ICHAZ of plate D microcracks nucleated at M-A/ferrite boundaries situated in continuous bands and propagated through ferrite grains followed by cracking of the M-A bands (Figs 77–78). Although a high proportion of preferable intragranularly nucleated ferritic-bainitic microstructure and evenly distributed M-A constituents between ferrite-bainite laths achieved in the ICHAZ of the heat treated test pieces D1 and D2, the impact and fracture toughness were lower than in the ICHAZ of plate C. This indicated a detrimental influence of the increased ferrite grains and bainite packet sizes and the large M-A constituents on the toughness of the ICHAZ of heat treated test pieces D1 and D2 (paragraph 7.3.2) (Table 10).

7.3.4 Hardness

Normally, microhardness measurements have been used for identification of microstructural constituents and normal hardness measurements for evaluation the contribution of dislocation, solid solution and precipitation strengthening (Harrison & Webster 1994, Harrison & Wall 1996). Microstructural investigations in this research work, based on the normal hardness measurements, showed that ferrite-bainite microconstituents were dominating in base plates A, C and D and in the heat treated test pieces D1 and D2, but bainite and local martensite (hardness 245 HV 10) in plate B were the main microconstituents calculated according to equations (14)-(16) (Kojima *et al.* 1999). A hardness of 180 HV 10 in plate D and 202 HV 10 in the heat treated test pieces D1 and D2 showed that mainly intragranularly nucleated acicular and polygonal ferritic microstructure increased hardness by about 20 HV 10 compared with ferritic-pearlitic banded microstructure. The difference is smaller than would be measured using microhardness measurements, due to a larger extent of microstructures in the vertex of normal hardness than microhardness measurements.

Hardness of the ICHAZ exhibited that the intercritical heat treatment of the base plate did not increase hardness of the ICHAZ of plates A and C and even decreased it in the ICHAZ of plate B regardless of a significant increase in M-A constituents (from 4.24 to 11.05%). The increase of hardness by 1.7 HV 10/% increase in M-A constituents in the ICHAZ of plate D and by 1.0 HV 10/% increase in M-A constituents in the ICHAZ of the heat treated specimen D1 indicated a significant influence of M-A constituents on elevation of hardness. Apparently, loading stresses at the interface of M-A/ferrite, caused by the higher hardness of M-A constituents than ferrite and transformation stresses, caused by the formation of martensite increased hardness (Chen *et al.* 1984, Davis & King 1993, Tian *et al.* 1996).

The influence of hardness on the toughness of the ICHAZ was apparent in the linear regression analyses. The impact and CTOD transition temperatures $T_{50\%}$ and $T_{0.1\text{mm}}$

increased by 1.5–1.6 °C/ HV 10 increase in hardness. However, p-values for hardness of 0.058 and 0.11 (Appendices 23–24) in the regression equations of $T_{50\%}$ (21) and $T_{0.1\text{mm}}$ (22) respectively greater than 0.05 in a confidence level of 95%, showed that there is a mutual dependence of M-A constituents and hardness or there are other factors impairing the independence of particularly the regression equation of $T_{0.1\text{mm}}$ (22).

7.3.5 Summary of paragraph 7.3

In summary, the ICHAZ was observed to be the most critical sub-zone of the weld HAZ due to a significant degradation of toughness by an intercritical thermal cycle applied to the base plate of test plates A, B, C, D and the heat treated test pieces D1 and D2. The test results exhibited that the area fraction, size, type and distribution of M-A constituents, completed with the ferrite-bainite packet size and hardness, were the dominating factors affecting the toughness of the ICHAZ.

The significant elevation of the impact and CTOD transition temperatures T_{27J} , $T_{50\%}$ and $T_{0.1\text{mm}}$ of the ICHAZ by increase in the area fraction of M-A constituents in the trend curves and in the multiple linear regression analyses evidenced a key role of M-A constituents in the degradation of toughness. Similarly, a significant improvement in toughness as a result of post weld heat treatment (PWHT) followed by a dispersion of M-A constituents demonstrated the significance of M-A constituents on toughness properties.

However, the significant improvement of the toughness of the ICHAZ was observed in the test results from the aluminium killed and copper plus nickel alloyed RCR test plate B and the heat treated test piece D1 and D2 from titanium killed NR plate D compared with those from the original titanium killed NR plate D. In the ICHAZ of plate B and the heat treated test pieces D1 and D2, relatively evenly distributed M-A constituents between mainly intragranularly nucleated acicular and polygonal ferrite caused the nucleation of microcracks at numerous sites in M-A/ferrite boundaries or bainite interfaces and their zig-zag propagation. But, in the ICHAZ of titanium killed NR plate D containing ferritic-pearlitic band microstructure, the nucleation of microcracks in M-A/ferrite boundaries in the continuous bands located M-A constituents and their direct propagation through ferrite grains decreased toughness.

A lower toughness of the ICHAZ of the heat treated test pieces D1 and D2 from titanium killed NR plate D than that of plate C showed that the increased size of ferrite grains and bainite packets and M-A constituents decreased toughness regardless of the more evenly distributed M-A constituents between intragranularly nucleated ferrite grains and bainite packets in the ICHAZ of the heat treated test pieces D1 and D2.

7.4 Evaluation of testing and analyzing methods

In this research work toughness properties of the low heat input weld HAZ have been evaluated using simulated specimens of the most critical sub-zone in the weld HAZ, such as the coarse grained HAZ (CGHAZ), intercritically reheated coarse grained HAZ

(ICCGHAZ) and intercritical HAZ (ICHAZ). Evaluation of toughness based on the determination of the impact and CTOD transition temperatures, microstructural investigations and calculation of the multiple linear regression analyses using the type of microstructures, the largest ferrite grain and bainite packet sizes, the area fraction of M-A constituents and hardness as the independent variables (Harrison & Webster 1994, Harrison & Wall 1996).

7.4.1 Simulated weld HAZ specimens

Thermal simulation of the most critical sub-zones such as the CGHAZ, ICCGHAZ and ICHAZ in the specimens opens up a useful, fast and relatively reliable tool to compare microstructures and toughness properties of the weld HAZ of steels without actual welding. Although the simulated wide sub-zones predominantly characterize the properties of the microstructure, not the actual properties of the weld HAZ, the simulated weld HAZ tests give the same toughness ranking of steels with different chemical compositions, as those on actual weld HAZ (Qiu *et al.* 2000). Normally, the toughness properties tested using the simulated CGHAZ, ICCGHAZ and ICHAZ specimens are poorer than when tested using real welds due to a more extensive distribution of brittle microstructures ahead of the notch tip of the simulated specimens compared with specimens from the real weld HAZ. There is also a lack of residual stresses, weld mismatch, constraint effects etc., in the simulated specimens.

7.4.2 Microstructural investigations and hardness measurements

The present and numerous other investigations have demonstrated, on one hand, the improvement of toughness caused by intragranularly nucleated microconstituents (AF+PF(I)) and, on the other hand, the degradation of toughness caused by primary grain boundary ferrite plus ferrite with second phase microconstituents (PF(G)+FS). However, in the multiple linear regression analyses these types of microstructures had a minor influence on toughness compared to the largest ferrite grain and bainite packet sizes, the area fraction of M-A constituents and hardness. This apparent discrepancy can be explained by a mutual interdependence of these variables. The largest ferrite grain and bainite packet sizes and hardness have been postulated to dominate toughness characteristics of the CGHAZ, the largest ferrite grain and bainite packet sizes and M-A constituents those of the ICCGHAZ and M-A constituents and hardness those of the ICHAZ.

In this research work the slower heating rate of max. 100 °C/s in the simulated CGHAZ specimens than in a real weld and the absence of the steep temperature gradient that exists in the real weld HAZ, is apt to increase the prior austenite grain size in the simulated specimens (Cardinal 1996). However, ferrite grain and bainite packet sizes of simulated CGHAZ specimens have been observed to be similar to real welds over the whole cooling rate range due to the lower peak temperature in simulated specimens than in a real weld (Cardinal 1996). Also, the actual limitation is a power of Gleeble machines,

i.e. their ability to heat and cool quickly enough (Gliha *et al.* 2004). However, it is apparent that the difference in ferrite grain and bainite packet sizes between a real weld and the simulated CGHAZ specimens is smaller at low heat input welding than at higher input welding (Cardinal 1996). This is probably due to smaller grain and packet sizes at low heat input welding than at high heat input welding.

The multiple linear regression analyses on the simulated CGHAZ and ICCGHAZ specimens in this research work showed that the largest ferrite grain and bainite packet sizes decreased the toughness of the low heat input weld HAZ more significantly than in the high heat input weld HAZ studied by Harrison and Webster (1994) and Harrison and Wall (1996). The influence of ferrite grain and bainite packet sizes on toughness is based the Griffith criterion (12) concerning a critical cleavage stress σ_f and its inverse square root of a particle and grain, size followed by a linear logarithm function of the packet or cleavage facet size (Yamamoto *et al.* 1989, Lee & Pan 1991, Li *et al.* 2001). There is a general agreement that ferrite grain and bainite packet sizes have a direct correlation with cleavage facet size (Figs 49–50). However, the linear relationship between the ductile-brittle transition temperatures and the largest ferrite grain and bainite packet sizes were applied in the multiple linear regression analyses of the present research in the limited ferrite grain and bainite packet size range between 30–60 μm .

It has been generally established that M-A constituents dominate the toughness of the ICCGHAZ and ICHAZ due to their formation in high carbon areas as a result of the intercritical thermal cycle. The area fraction of M-A constituents in the multiple linear regression analyses supported this opinion, but the p values for the coefficients of M-A constituents (M-A) were greater than 0.05 in the correlation equations of $T_{0.1\text{mm}}$ indicating that there is a mutual dependence of variables or other influencing factors, for example the size and distribution of M-A constituents. The influence of M-A constituents on toughness is emphasized in simulated specimens compared with a real weld due to the larger prior austenite grain size and slower heating rate in thermal simulation than in real welding (Cardinal 1996). Thus, the more massive, blocky type M-A constituents are apt to form along the prior austenite grain boundaries of the simulated ICCGHAZ specimens than prior austenite grain boundaries of a real weld.

7.4.3 Charpy V impact energy transition temperature T_{27J}

The Charpy V impact test has been developed to evaluate toughness in a simple way and can be regarded as more versatile and better for ranking of materials from the viewpoint of resistance to brittle fracture (Dziubin'ski & Adamiec 2001). Crack initiation in impact tests depends predominantly on the distribution of brittle microstructures ahead of the notch tip. However, the relatively large notch root radius (0.25 mm) in the Charpy V impact test specimens does not enhance the formation of microcracks caused by the local brittle phase as effectively as the smaller radius ahead of the fatigue crack in CTOD specimens (Li *et al.* 2001). Crack propagation in the dynamically loaded impact test takes place so fast, that there is not sufficient time for cracks to find the weakest planes in adjacent grains and packets. Consequently, cracks propagate from one grain or packet to another on the same cleavage plane until a prior austenite grain boundary is reached (Qiu

et al. 2000). However, high angle grains or packet boundaries can cause kinks in crack propagation.

In this research work impact test results, evaluated according to the generally agreed ductile-brittle impact energy transition temperature of 27 J, supported the evidence that the Charpy V impact test took more preferential ferrite grain and bainite packet sizes into consideration in the multiple linear regression analyses of the simulated CGHAZ and ICCGHAZ specimens than expected in the research works of Harrison and Webster (1994), Harrison and Wall (1996) and Matsuda *et al.* (1996). The lowest transition temperature T_{27J} of the simulated CGHAZ specimens from plate B compared with those from the other test plates showed a beneficial influence of fine lath upper bainitic plus martensitic micro-structure on Charpy V impact toughness. However, the continuous sheets of massive blocky-type M-A constituents at the prior austenite grain boundaries in the ICCGHAZ specimens from plate A, and in the continuous bands situated M-A constituents in the ICHAZ specimens from plate D, elevated the impact transition temperature T_{27J} .

7.4.4 50% ductile fracture transition temperature $T_{50\%}$ in Charpy V impact tests

It is well-known that in the plate and the simulated HAZ specimens the 50% ductile fracture transition temperature $T_{50\%}$ is higher than the transition temperature T_{27J} (23) (Fig 85). This is due to relatively high upper shelf energy of the ferritic-bainitic steels and their HAZ, coupled with the high crack initiation energy of these steels, in relation to the propagation energy (Wallin *et al.* 2001). The difference between the transition temperatures T_{27J} and $T_{50\%}$ depends on the microstructure of steel, being 40–60 °C in the simulated HAZ specimens of the test plates. This is regarded as a demonstration of comparatively high crack initiation toughness in the investigated steels. However, the difference in the transition temperatures were smaller in the test plates than in the simulated specimens, except for in the more martensite containing plate B where the upper shelf energy was smaller than in the ferritic-bainitic microstructure contained plates A and C (Table 4). Thus, the transition temperature $T_{50\%}$ demonstrates more ductile crack appearance than the T_{27J} . In the ductile fracture temperature range, final cracking is controlled by formation of microvoids as a result of de-bonding of the M-A/matrix interfaces, growth of these voids and their coalescence to deep holes finally joining together to the final cracking. Deformation of ductile ferritic or ferritic-bainitic matrix prevents crack propagation and hard M-A constituents promote it (Chen *et al.* 1984, Hrivnak *et al.* 1992a, Hrivnak *et al.* 1992b, Davis & King 1994, Hrivnak 1995, Hrivnak 1996).

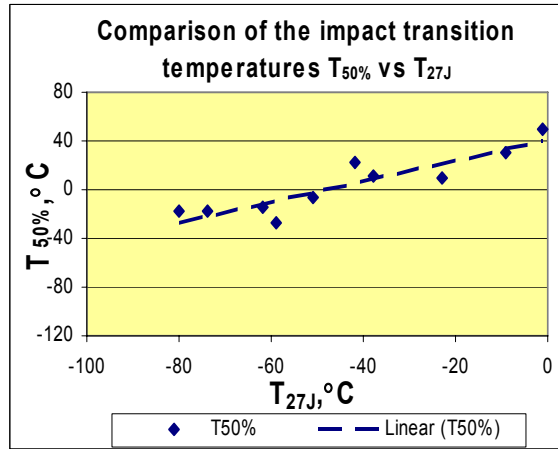


Fig. 85. Comparison of the impact transition temperatures $T_{50\%}$ vs T_{27J} of the simulated CGHAZ, ICCGAZ and ICHAZ specimens.

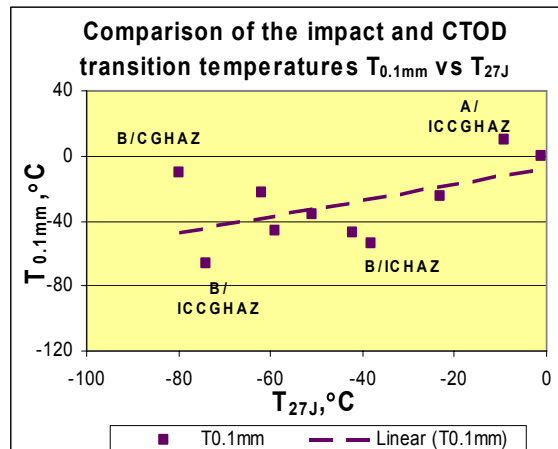


Fig. 86. Comparison of the impact and CTOD transition temperatures $T_{0.1mm}$ vs T_{27J} of the simulated CGHAZ, ICCGAZ and ICHAZ specimens.

The linear 50% regression curves in Figs 85–86 are as follows:

$$T_{50\%} (\text{°C}) = 0.86xT_{27J} + 42, \quad (23)$$

$$R^2=0.82$$

$$T_{0.1mm} (\text{°C}) = 0.49xT_{27J} - 8, \quad (24)$$

$$R^2=0.28$$

A good correlation of the impact transition temperatures T_{27J} and $T_{50\%}$ (correlation coefficient $R^2=0.82$) was found. Also, almost the same coefficients of the largest ferrite grain and bainite packet sizes (Packet) and M-A constituents (M-A) in the multiple linear regression analyses for the transition temperatures T_{27J} and $T_{50\%}$ of the simulated CGHAZ and ICCGHAZ ((17)-(18)) showed that both impact transition temperatures are usable for evaluation of the toughness of these sub-zones of the weld HAZ. In general, the transition temperature T_{27J} characterises crack initiation and propagation, but the fracture appearance transition temperature $T_{50\%}$ additionally showed crack arrest properties. In the multiple linear regression analyses of the base plate and ICHAZ specimens the impact energy transition temperature T_{27} was controlled by ferrite grain and bainite packet sizes (Packet) and the area fraction of M-A constituents (M-A), but the fracture appearance transition temperature $T_{50\%}$ by the area fraction of M-A constituents (M-A) and hardness (Hardn.).

7.4.5 Crack tip opening displacement (CTOD) tests

The sharp crack tip in the fatigue pre-cracked CTOD specimen makes it more sensitive for crack initiation than the Charpy V test with a 'blunt' notch. The CTOD test results in the numerous investigations have demonstrated the significant role of M-A constituents in deteriorating toughness by decreasing particularly crack initiation, but also propagation energy (Okada *et al.* 1994, Harrison & Webster 1994, Harrison & Wall 1996, Matsuda *et al.* 1996, Tian *et al.* 1996, Tian 1998). In this research work a low correlation coefficient of 0.28 between the relationship of the transition temperatures $T_{0.1mm}$ and T_{27J} demonstrated differences between the toughness responses of these two very different toughness tests in terms of sampling inhomogeneous substructures from the simulated HAZ specimens. The toughness of the HAZ thereby depends on the inherent toughness of the substructure influenced by a relation between a volume of the substructure and the dimensions of the notch tip, degree of mismatch between the substructure and the matrix and micromechanism of fracture. In general, a descriptive potential of equation (24) is probably poor due to the influence of the other above-mentioned parameters on the correlation in equation (24), even though a correlation coefficient would be high.

The individual test results in Fig. 86 demonstrated the more significant influence of martensitic microstructure and the distribution of M-A constituents on the toughness in the CTOD test than in the Charpy V impact test. Relatively low transition temperatures $T_{0.1mm}$ of the ICCGHAZ and ICHAZ specimens of plate B compared with the trend line showed the improvement of the toughness in the CTOD test caused by evenly distributed M-A constituents. On the contrary, 24% martensite in the CGHAZ of plate B and continuous sheets of blocky M-A constituents in the ICCGHAZ of plate A impaired the toughness in the CTOD tests more than in the impact tests. Apparently, the CTOD transition temperature $T_{0.1mm}$ is more sensitive to the distribution of M-A constituents than the impact transition temperatures T_{27J} and $T_{50\%}$.

The multiple linear regression analyses showed that the largest ferrite grain and bainite packet sizes (Packet) and M-A constituents (M-A) were the main factors affecting the transition temperature $T_{0.1mm}$ of the CGHAZ and ICCGHAZ, as well as the transition

temperatures T_{27J} and $T_{50\%}$. In the CGHAZ and ICCGHAZ specimens almost the same coefficient of the largest ferrite grain and bainite packet sizes (Packet) of the transition temperatures T_{27J} , $T_{50\%}$ and $T_{0.1mm}$, and a little higher coefficient of M-A constituents (M-A) of the transition temperatures $T_{0.1mm}$ than the impact transition temperatures T_{27J} and $T_{50\%}$, showed that the area fraction of M-A constituents had a more significant influence on toughness in the CTOD tests than in the Charpy V impact tests. In the ICHAZ specimens the area fraction of M-A constituents (M-A) and hardness (Hardn.) were the main factors affecting the CTOD transition temperature $T_{0.1mm}$, as well as the impact transition temperature $T_{50\%}$.

7.4.6 Summary of paragraph 7.4

In summary, thermal simulation of the most critical sub-zones, such as the coarse grained HAZ (CGHAZ), the intercritically reheated coarse grained HAZ (ICCGHAZ) and the intercritical HAZ (ICHAZ), provides a useful, fast and relatively reliable tool for comparing microstructures and toughness properties of the weld HAZ of steels without actual welding. An evaluation of toughness properties based on the relationship between the impact and CTOD transition temperatures and the type of microstructures, the largest ferrite grain and bainite packet sizes, the area fraction of M-A constituents and hardness has been carried out using multiple linear regression analysis.

The larger prior austenite grain size, as a result of lower heating rate of max. 100 °C/s in the simulated specimens than in real welds, enhances the formation of the higher fraction of M-A constituents particularly at the prior austenite grain boundaries in the simulated CGHAZ and ICCGHAZ specimens emphasizing their detrimental influence on toughness.

Since M-A constituents play a key role regarding the toughness of the ICCGHAZ and ICHAZ, the distribution of M-A constituents should be taken into consideration in addition to the area fraction of M-A constituents used in the multiple linear regression analyses.

The dynamically loaded impact test using the Charpy V specimens with a notch root radius of 0.25 mm opens up a versatile evaluation of resistance to brittle fracture. The impact energy transition temperature T_{27J} is mainly influenced by ferrite grain and bainite packet sizes and M-A constituents in the simulated CGHAZ and ICCGHAZ characterizing brittle cracks initiation and propagation.

A good correlation of the impact transition temperatures T_{27J} and $T_{50\%}$ was found in the simulated CGHAZ and ICCGHAZ specimens. However, the 40–60 °C higher area fraction transition temperature $T_{50\%}$ represents a more ductile fracture mechanism and reveals more crack arrest properties than the impact energy transition temperature T_{27J} .

The sharp crack tip in the fatigue cracked CTOD specimens indicates the great sensitivity of the transition temperature $T_{0.1mm}$ to microconstituents such as martensitic microstructure and the distribution of M-A constituents.

8 Conclusions

This research work regarding the toughness of the weld HAZ of RCR and TMCP steels welded using a low heat input consisted of three main topics: 1) evaluation of the intragranular nucleation of ferrite and bainite, 2) improvement of the toughness of the CGHAZ, the ICCGHAZ and the ICHAZ and 3) an evaluation of the testing and analyzing methods used.

The first topic dealt with the clarification of a theoretical background for the intragranular nucleation of acicular ferrite in weld metal, the weld HAZ and the base plate, and the preparation of laboratory test pieces containing the maximum amount of intragranularly nucleated microconstituents as was possible. Since intragranularly nucleated acicular ferritic microstructure is crucial to the improvement of weld HAZ toughness, extensive studies were carried out with the aim of achieving acicular ferrite even in the base plate of titanium killed steel. In spite of wide ranging theoretical studies and technological trials, no significant amount of acicular ferrite and bainite could be achieved in a 50 mm thick titanium killed plate rolled on a full-scale rolling mill. However, the following main conclusions about the formation of intragranularly nucleated ferritic and bainitic microstructures can be drawn:

1. The largest recrystallized austenite grain size that can be achieved after rolling titanium killed steel is 50–90 μm (average about 70 μm). This is too small for the formation of significant amounts of acicular ferrite despite the presence of suitable titanium-manganese oxide/manganese sulphide inclusions with a number density of about 300–750 particles/ mm^2 , and an optimum accelerated cooling rate after rolling of 7 $^{\circ}\text{C}/\text{s}$ down to 580 $^{\circ}\text{C}$.
2. Mainly acicular ferritic microstructures can be obtained from the same steel when the prior austenite grain size is coarsened to an average size of more than about 120 μm and the cooling rate to 500 $^{\circ}\text{C}$ is in the range 6–11 $^{\circ}\text{C}/\text{s}$.
3. The above effects are explained by the competition between grain boundary and inclusion nucleated microstructural constituents.

The second topic covered the improvement of the impact and fracture toughness of the most critical sub-zones of the weld HAZ using the simulated CGHAZ, ICCGHAZ and ICHAZ specimens at a cooling time $t_{8/5}$ of 5 s. At this rapid cooling rate the area fraction,

size and distribution of M-A constituents and the largest ferrite grain and bainite packet sizes, as well as the microstructure of the matrix, play key roles in determining the toughness of the weld HAZ.

The toughness of the CGHAZ, ICCGHAZ and ICHAZ under these circumstances can be improved by the formation of significant amounts of intragranularly nucleated ferritic-bainitic microstructure. In the case of the ICCGHAZ and ICHAZ, the intercritical thermal cycle then leads to an even distribution of M-A constituents between ferrite and bainite laths. The formation of these favourable microstructures can be achieved using a suitable chemical composition of steel and steelmaking process as follows:

4. A significant amount of intragranularly nucleated ferritic-bainitic microstructure for the improvement of the toughness of the CGHAZ can be achieved using titanium killing and vanadium microalloying.
5. Relatively evenly distributed M-A constituents between intragranularly nucleated ferritic-bainitic microstructure in the ICCGHAZ and ICHAZ are obtained by using aluminium killed steel with copper plus nickel alloying and titanium micro-alloying, or titanium killed steel with vanadium microalloying.
6. The toughness improvement in the latter case is caused by crack nucleation at numerous sites such as M-A/ferrite boundaries or bainite packet interfaces and crack propagation through the linking of separate microcracks.

The third topic was an evaluation of toughness testing using thermal simulation of the most critical heat affected sub-zones, i.e. the CGHAZ, the ICCGHAZ and the ICHAZ. This led to the following conclusions:

7. Evaluation of the toughness at low heat input welding using simulated specimens is apt to emphasize the detrimental influence of M-A constituents on the toughness of the ICCGHAZ due to a lower heating rate (100 °C/s) of the simulations of the CGHAZ compared to real welds. This enhances the formation of the massive blocky-type M-A constituents at the prior austenite grain boundaries decreasing the toughness of the ICCGHAZ.
8. Linear regression equations reveal the influence of the largest ferrite grain and bainite packet sizes, the area fraction of M-A constituents and hardness on the toughness of weld HAZ. The spatial distribution of M-A constituents also has a clear effect on toughness, but it has not been possible to include this in a quantitative way in the regression equations.
9. The CTOD transition temperature $T_{0.1\text{mm}}$ (determined using fatigue cracked CTOD specimens with the sharp crack tip) shows a greater sensitivity to microconstituents such as martensitic microstructure and the distribution of M-A constituents than the transition temperature T_{27J} (determined using the Charpy V specimens with the notch root radius of 0.25 mm).

9 Future research

9.1 Improvement of toughness of the most critical sub-zones CGHAZ, ICCGHAZ and ICHAZ of the low heat input weld HAZ

The test results from this and previous research works showed that it is possible to achieve a significant improvement in the toughness of the low heat input weld HAZ by intragranularly nucleated acicular ferritic-bainitic microstructure in the base plate. In the ICHAZ, intragranularly nucleated acicular ferritic-bainitic microstructure in the base plate enhances the formation of evenly distributed M-A constituents between the ferrite or bainite laths. So, investigation of the suitable chemical composition, inclusions and precipitations for the preferred intragranular nucleation sites, rolling deformation, cooling rate and finish cooling temperature open up possibilities for toughness improvement. In the CGHAZ and the ICCGHAZ, the toughness improvement can be achieved using a suitable chemical composition and steelmaking process for the formation of favourable inclusions and precipitations for intragranular nucleation of ferrite or bainite and evenly distributed M-A constituents between ferrite or bainite laths.

The formation of M-A constituents as a result of an intercritical thermal cycle has a significant influence on the toughness of the ICCGHAZ and ICHAZ. In this research work a decrease of ferrite with non-aligned second phases (FS(NA)) and martensite and an increase of intragranularly nucleated microconstituents (AF+PF(I)) in the ICCGHAZ of plate B, as a result of intercritical thermal cycle, was theoretically unclear. Thus, the mechanism of the transformation of FS(NA) to (AF+PF(I)) and the formation of M-A constituents from high carbon microconstituents such as martensite, precipitates, carbides in bainite and pearlite, as a result of the intercritical thermal cycle, would be worth further studies.

9.2 Practical consequences of this work for steelmaking

Improvement of the toughness of the CGHAZ and ICCGHAZ at low heat input is based on a fine effective grain size, i.e. small ferrite grain and bainite packet sizes and fine and evenly distributed M-A constituents between intragranularly nucleated ferritic or bainitic laths. Thus, a steelmaking process including titanium killing and vanadium microalloying together with low carbon, niobium and aluminium contents opens up a potential possibility for improvement of toughness provided a sufficient density of favourable inclusions and a sufficiently large austenite grain size can be achieved. Inoculation of inclusions with a suitable chemical composition into the steel melt instead of titanium killing will be challenging.

At low heat input the ICHAZ plays a key role for improvement of the toughness of the weld HAZ. A fine intragranularly nucleated ferritic-bainitic microstructure with fine and evenly distributed M-A constituents between ferrite laths is the optimal microstructure for improvement of toughness. Titanium killing together with low carbon and aluminium content ($Al/O \leq 1$) and a suitable alloying content and/or a strong deformation below austenite recrystallization temperature, followed by accelerated cooling at rates of 10–30 °C/s are potential methods to achieve favourable nucleation sites for intragranularly nucleation of ferrite or bainite. Such a strong hot deformation of 0.6–0.7 in austenite non-recrystallization temperatures in final rolling, followed by accelerated cooling, is possible in hot strip rolling. However, in plate rolling, titanium killing together with a low carbon and aluminium content ($Al/O \leq 1$) and suitable alloying seems to be a preferential method for increasing toughness of steel.

References

- Akhlaghi S, Ivey DG & Collins L (2000) Microstructural study of grade 100 steel. Proc. The 42nd mechanical Working and Steel Processing Conference, Toronto, Ontario, Canada, 22–25 October 2000. Eds. Canary D.L., Fuga D.J. & Baker M.A. Iron & Steel Society (ISS), Vol XXXVII: 419–428.
- Akselsen OM, Grong Ø & Solberg JK (1987) Structure-property relationship in inter-critical heat affected zone of low-carbon microalloyed steels. *Materials Science and Technology* 3(8): 649–655.
- Akselsen OM, Solberg JK & Grong Ø (1988) Effect of martensite-austenite (M-A) islands on intercritical heat-affected zone toughness of low carbon microalloyed steels. *Scandinavian Journal of Metallurgy* 17: 194–200.
- Anelli E, Matera S, Harrison P, Gutiérrez I, Díaz-Fuentes M, Porter D, Hutchinson B, Zajac S & Siwecki T (2002) Heterogenous nucleation of acicular ferrite for toughness improvement of HSLA steels. European Commission, Report EUR 20215 EN, ECSC- EC-EAEC, Brussels, Luxembourg, 221.
- Babu SS, Reidenbach F, David SA, Böllinghaus Th & Hoffmeister H (1999) Effect of high energy density welding processes on inclusion and microstructure formation in steel welds. *Science and Technology of Welding and Joining* 4 (2): 63–73.
- Barbaro FJ, Kraukalis P & Easterling KE (1989) Formation of acicular ferrite at oxide particles in steels. *Materials Science and Technology* 5 (11): 1057–1068.
- Bhadeshia HKDH (1992) Modelling of steel welds. *Materials Science and Technology* 8(2): 123–133.
- Bhadeshia HKDH & Svensson L-E (1993) Modelling the evolution of microstructure in steel weld metal. Eds. Cerjak H & Easterling KE.: MATHEMATICAL MODELLING OF WELD PHENOMENA, The Institute of Materials, Cambridge, 109–180.
- Boyd JD & Zhao P (2000) Microstructure-property relationships in thermomechanically processed forgings. Proc. The 42nd Mechanical Working and Steel Processing Conference, Toronto, Ontario, Canada, 22–25 October 2000. Eds. Canary D.L., Fuga D.J. & Baker M.A. Iron & Steel Society (ISS), Vol XXXVII: 799–810.
- Boyd JD, Zhao P, Liu T & Gyorffy M (2000) Thermomechanical processing in hot forging. Proc. 39th Annual Conference of Metallurgists of CIM, Ottawa, Ontario, Canada, 20–23 August 2000. Eds. Yue S. & Essadiqi E: J. J. Jonas Symposium on Thermomechanical Processing of Steel, MET SOC: 475–488.
- Bramfit BL. (1970) The effect of carbide and nitride additions on the heterogenous nucleation behaviour of liquid iron. *Metallurgical Transactions* 1 July: 1987–1995.

- BS 7448-1:1991 (1991) Fracture mechanics toughness tests-Part 1: Method for determination of K_{IC} , critical CTOD and critical J values of metallic materials. British Standard Institution (BSI): 31 + Apps 7.
- BS 7448-2:1997 (1997) Fracture mechanics toughness tests-Part 2: Method for determination of K_{IC} , critical CTOD and critical J values of metallic materials. British Standard Institution (BSI): 16 + Apps 14.
- Cardinal N (1996) Factors affecting thermally simulated HAZ microstructures. OMAE '96, 15th International Conference on Offshore. MECHANICS & ARCTIC ENGINEERING, Florence, Italy, 16–20 June 1996. The American Society of Mechanical Engineers (ASME), Vol. III: 35–44.
- Chaouadi R & Fabry A (2001) On the utilization of the instrumented Charpy V impact test for characterizing the flow and fracture behaviour of reactor pressure vessel steels. Proc. The Charpy Centenary Conference, Poitiers, France, 2–5 October 2001. Eds. François D. & Pineau A: From Charpy to Present Impact Testing,ESIS Publication 30, 2002: 103–117.
- Chen JH, Kikuta Y, Araki T, Yoneda M & Matsuda Y (1984) Micro-fracture behaviour induced by M-A constituent (island martensite) in simulated welding heat affected zone of HT 80 high strength low alloy steel. *Acta metallurgica* 32 (10): 1779–1788.
- Chijiwa R, Tamehiro H, Hirai M, Matsuda H & Mimura H (1988) Extra high toughness titanium oxide steel plates for offshore structures and line pipe. Proc. 7th International Conference on Offshore Mechanics and Arctic Engineering, Houston, Texas, 7–12 February 1988. Eds. Salama M. et al. U.S.A. The American Society of Mechanical Engineers (ASME), Vol. III: 165–172.
- Cochrane RC & Senogles DJ (1994) The effect of Ti additions on the microstructure of autogenous laser welds. Proc. of a Conference Titanium Technology in Microalloyed Steels Held at the University of Sheffield December 1994. Ed. Baker T.N. The Institute of Materials, Cambridge, 1997: 207–223.
- Couque H., Asaro RJ, Duffy J & Lee SH (1988) Correlations of microstructure with dynamic and quasi-static fracture in a plain carbon steel. *Metallurgical Transactions A* 19A September: 2179–2206.
- Davis CL & King JE (1993) Effect of cooling rate on intercritically reheated microstructure and toughness in high strength low alloy steel. *Materials Science and Technology* 9 January: 8–15.
- Davis CL & King JE (1994) Cleavage initiation in intercritically reheated coarse-grained heat-affected zone: Part I. Fractographic evidence. *Metallurgical and Materials Transactions A* 25A March: 563–573.
- Davis CL & King JE (1996) Cleavage initiation in intercritically reheated coarse-grained heat affected zone: Part II. Failure criteria and statistical effects. *Metallurgical and Materials Transactions A* 27A October: 3019–3029.
- Díaz-Fuentes M, Madariaga I & Gutiérrez I (1998) Acicular ferrite microstructure and mechanical properties in a low carbon wrought steel. *Materials Science Forum* 284–286: 245–252.
- Díaz-Fuentes M, Madariaga I & Gutiérrez I (2000) Acicular ferrite microstructure formation in low and medium carbon steels. Proc. 39th Annual Conference of Metallurgists of CIM, Ottawa, Ontario, Canada, 20–23 August 2000. Eds. Yue S. & Essadiqi E: J. J. Jonas Symposium on Thermomechanical Processing of Steel, MET SOC: 489–500.
- Dziubin'ski J & Adamiec P (2001) Correlation between Charpy V and crack tip opening displacement as well as drop weight tear test results. Proc. The Charpy Centenary Conference, Poitiers, France, 2–5 October 2001. Eds. François D. & Pineau A.: From Charpy to Present Impact Testing,ESIS Publication 30, 2002: 349–355.
- EN 10025-3:2004 (2004) Hot rolled product of structural steels-Part 3: Technical delivery conditions for normalized/normalized rolled weldable fine grain structural steels, ECIS/TC10, CEN: 21 + Apps 3.

- EN 10025-4:2004 (2004) Hot rolled product of structural steels-Part 4: Technical delivery conditions for thermomechanical rolled weldable fine grain structural steels, ECISS/TC10, CEN: 21 + Apps 3.
- EN 10225:2001 (2001) Weldable structural steels for fixed offshore structures-Technical delivery conditions, ECISS/TC 10, CEN: 49 + Apps 40.
- Enomoto M (1997) The mechanisms of ferrite nucleation at intragranular inclusions in steel. Proc. THERMEC'97 International Conference on Thermomechanical Processing of Steels and Other Material, Wollongong, Australia, 7–11 July 1997. Eds. Chandra T. & Sakai T. The Minerals, Metals & Materials Society: 427–433.
- Evans GM (1996) Microstructure and properties of ferritic steel welds containing Ti and B. *Welding Journal* 75 August: 251-s-260-s.
- Evans GM (1998) Effect of nitrogen on C-Mn steel welds containing titanium and boron. *Welding Journal* 77 June: 239-s-248-s.
- Fairchild DP, Bangary NV, Koo JY, Harrison PL & Ozekcin A (1991) A study concerning intercritical HAZ microstructure and toughness in HSLA steels. *Welding Journal* 70 December: 321-s-329-s.
- Francis-Scrutton N (1995a) Further studies of microstructural development in low oxygen steel weld metal: effect of Al, Ti and V in TIG and laser weld metal. TWI Members Report 514/1995, TWI, Abington Hall, Abington Cambridge CB1 6AL, United Kingdom: 17 + Apps 32.
- Francis-Scrutton N (1995b) Effect of Al, Ti and V on microstructural development in laser and electron beam steel weld metal. TWI Members Report 531/1995, TWI, Abington Hall, Abington Cambridge CB1 6AL, United Kingdom: 19 + Apps 22.
- François D (2001) Micromechanisms and the Charpy transition curve. Proc. The Charpy Centenary Conference, Poitiers, France, 2–5 October 2001. Eds. François D. & Pineau A: From Charpy to Present Impact Testing,ESIS Publication 30, 2002: 21–32.
- Fukuda Y & Komizo Y (1992) Effect of Al content on critical CTOD properties in heat affected zone of C-Mn microalloyed steel. *Quarterly J. Japan Welding Society* 10 (3): 409–415 (in Japanese).
- Furuhara T & Maki T (2000) Acceleration of intragranular nucleation of ferrite and pearlite at inclusions by hot deformation of Austenite. Proc. 39th Annual Conference of Metallurgists of CIM, Ottawa, Ontario, Canada, 20–23 August 2000. Eds. Yue S. & Essadiqi E: J. J. Jonas Symposium on Thermomechanical Processing of Steel, MET SOC: 465–473.
- Furuya H, Uehimori R, Tomita Y, Aihara S & Hagiwara Y (2000) Effect of carbon and niobium content on HAZ toughness of HT 590 steel. Proc. The 42nd Mechanical Working and Steel Processing Conference, Toronto, Ontario Canada, 22–25 October 2000. Eds. Canary D.L., Fuga D.J. & Baker M.A. Iron & Steel Society (ISS), Vol XXXVII: 351–364.
- Gladman T & Senogles DJ (1994) Grain refinement of low carbon structural steels by titanium oxide particles. Proc. of a Conference Titanium Technology in Microalloyed Steels Held at the University of Sheffield December 1994. Ed. Baker T.N. The Institute of Materials, Cambridge, 1997: 83–97.
- Gliha V, Vuherer T, Ule B & Vojvodi'c-Tuma J (2004) Fracture resistance of simulated heat affected zones areas in HSLA structural steel. *Science and Technology of Welding and Joining* 9 (5): 399–406.
- Gourgues A-F, Flower HM & Lindley TC (2000) Electron backscattering diffraction study of acicular ferrite, bainite and martensite steel microstructure. *Material Science and Technology* 16 January: 26–40.
- Grong Ø (1994) Metallurgical modelling of welding. Materials modelling Series. Ed. Bhadeshia H.K.D. The Institute of Materials, Cambridge: 581.
- Grong Ø, Kluken AO, Nylund HK, Dons AL & Hjelen J (1995) Catalyst effect in heterogenous nucleation of acicular ferrite. *Metallurgical and Materials Transactions A* 26A March: 525–534.

- Guide to the light microscope examination of ferritic steel weld metals (1991). *Welding in the World* 29 (7/8): 160–176.
- Haaland D, van der Eijk C & Grong Ø (1997) The role of interactive particles in steel. Proc. Safety in Application of High Strength Structural Steel Symposium Held at Statoil Research Centre, Trondheim, Norway, 1–2 July 1997. Publisher: Statoil Research Centre, Trondheim Norway.
- Harrison PL & Hart PHM (1990) Influence of steel composition and welding procedure on the HAZ toughness of thick section structural steels. Proc. of Conference on Metallurgy, Welding and Qualification of Microalloyed (HSLA) Steel Weldments, American Welding Society, Miami, Florida: 605–637.
- Harrison PL & Webster SE (1994) HAZ microstructure and toughness in single pass welds. Proc. The 36th Mechanical Working and Steel Processing Conference, Baltimore, Maryland, USA: 551–559.
- Harrison P & Wall P (1996) Effect of alloying elements on HAZ microstructure and toughness. European Commission, Report EUR 15834 EN, ECSC-EC-EAEC, Brussels, Luxembourg: 79.
- Hart PHM & Mitchell PS (1995) The effect of vanadium on toughness of weld in structural and pipeline steels. *Welding Journal* 74 July: 239-s-248-s.
- Haze T & Aihara S (1988) Influence of toughness and size of local brittle zone on HAZ toughness of HSLA steels. Proc. 7th International Conference on Offshore Mechanics and Arctic Engineering, Houston, Texas, 7–12 February 1988. Eds. Salama M. et al. U.S.A. The American Society of Mechanical Engineers (ASME), Vol. III.: 515–523.
- He K & Edmonds DV (2000) The promotion of acicular ferrite microstructure in C-Mn steel by vanadium. Proc. HSLA Steels 2000- The 4th International Conference on High Strength Low Alloy Steels, Xián, China. Eds. Liu G., Wang F., Wang Z. & Zhang H. The Chinese Society for Metals, Beijing: 260–266.
- He K & Edmonds DV (2002) Formation of acicular ferrite and influence of vanadium alloying. *Materials Science and Technology* 18 March: 289–296.
- Hickson MR, Gibbs RK & Hodgson PD (1999) The effect of chemistry on formation of ultrafine ferrite in steel. *ISIJ International* 39 (11): 1176–1180.
- Homma H, Ohkita S, Matsuda S & Yamamoto K (1987) Improvement of HAZ toughness in HSLA steel by introducing finely dispersed Ti-oxide. *Welding Journal* 66 October: 301-s-309-s.
- Howe AA (2000) Ultrafine grained steels. Industrial prospects. *Materials Science and Technology* 16 November-December: 1264–1266.
- Hrivnak I, Matsuda F & Ikeuchi K (1992a) Investigation of M-A constituent in high strength welds. *Transactions of Japan Welding Institute* 21 (2): 9–31.
- Hrivnak I, Matsuda F, Li Z, Ikeuchi K & Okada H (1992b) Investigation of metallography and behaviour of M-A constituent in weld HAZ of HSLA steels. *Transactions of Japan Welding Institute* 21 (2): 101–110.
- Hrivnak I (1995) Weldability of modern steel materials. *ISIJ International* 35 (10): 1148–1156.
- Hrivnak I & Matsuda F (1996) The M-A constituent and its decomposition products in HSLA steel welds. Proc. The International Welding Conference, High-Tatras Mountains, Slovakia: 55–58.
- Ikawa H, Oshige H & Tanoe T (1980) Effect of martensite-austenite constituent on HAZ toughness of high strength steel. *Transactions of the Japan Welding Society* 11 October: 3–12.
- Ishikawa F & Takahashi T (1995) The formation of intragranular ferrite plates in medium-carbon steels for hot-forging and its effect on the toughness. *ISIJ International* 35 (9): 1128–1133.
- Karjalainen LP, Porter D, Xu Z & Guo Y (1995) Influence of steel composition on impact toughness of simulated high energy welds. Proc. The International Conference on the Joining of Materials, JOM-7, Helsingør, Denmark, 31 May-2 June 1995: 83–94.
- Kim BC, Lee S, Kim NJ & Lee DY (1991) Microstructure and local brittle zone phenomena in high-strength low-alloy steel welds. *Metallurgical Transactions A* 22A January: 139–149.

- Kimura T, Ohimori A, Kawabata F & Amano K (1997) Ferrite grain refinement through intragranular ferrite transformation on VN precipitates in TMCP of HSLA steel. Proc. THERMEC'97 International Conference on Thermomechanical Processing of Steels and Other Material, Wollongong, Australia, 7–11 July 1997. Eds. Chandra T. & Sakai T., The Minerals, Metals & Materials Society: 645–651.
- Kojima T, Yurioka N, Kasuya T, Shiga C, Ikeuchi K & Takahashi M (1999) Result of Round Robin Test on HAZ microstructure. IIW Doc. No. IX-1929-99, IIW Commission IX, July 1999: 13.
- Koseki T, Ohkita S & Yurioka N (1997) Thermodynamic study of inclusion formation in low alloy steel weld metals. *Science and Technology of Welding and Joining* 2 (2): 65–69.
- Kweon KS, Kim JH, Hong JH & Lee CH (2000) Microstructure and toughness of intercritically reheated heat affected zone in reactor pressure vessel steel weld. *Science and Technology of Welding and Joining* 5 (3): 161–167.
- Laitinen R (1998) Koostumuksen ja valmistustavan vaikutus lujien terästen hitsausliitoksen murtumissitkeyteen. *Lisensiaatin työ, Oulun yliopisto, Konetekniikan osasto, Materiaalitekniikan laboratorio: 118 + Aps 88.* (in Finnish).
- Lambert A, Drillet J, Gourgues A-F, Sturel T & Pineau A (2000a) Microstructure of martensite-austenite constituents in heat affected zones of high strength low alloy steel welds in relation to toughness properties. *Science and Technology of Welding and Joining* 5 (3): 168–173.
- Lambert A, Garat X, Sturel T, Gourgues A-F & Gingell A (2000b) Application of acoustic emission to study of cleavage fracture mechanism in a HSLA steel. *Scripta materialia* 43 (2): 161–166.
- Lambert A, Gourgues A-F, Sturel T & Pineau A (2000c) Fracture toughness of simulated HAZ in HSLA steel welds. *EUROMAT 2000 Conference on Advanced in Mechanical Behaviour, Plasticity and Damage, 7–9 Nov 2000, Tours, France.* Eds. Miannay D., Costa P., François D. & Pineau A., Elsevier: 97–102.
- Lanzilotto CAN & Pickering FB (1982) Structure-property relationship in dual-phase steels. *Metals Science* 16 August: 371–382.
- Lee JL & Pan YT (1991) Microstructure and toughness of simulated heat-affected zone in Ti- and Al-killed steels. *Materials Science and Engineering A* 136 (4): 109–119.
- Lee JL & Pan YT (1993) Effect of sulphur content on the microstructure and toughness of simulated heat-affected zone in Ti-killed steels. *Metallurgical Transactions A* 24A June: 1399–1408.
- Lee JL & Pan YT (1995) The formation of intragranular acicular ferrite in simulated heat-affected zone. *ISIJ International* 35 (8): 1027–1033.
- Lee S, Kim BC & Kwon D (1992) Correlation of microstructure and fracture properties in weld heat-affected zones of thermomechanically controlled processed steels. *Metallurgical Transactions A* 23A October: 2803–2816.
- Leinonen J (2001) Processing steel for higher strength. *Advanced Materials & Processes (USA)* 159 November: 31–33.
- Leinonen J (2002) A novel process results in ultra-fine structures and improved properties. 2nd International Symposium on High Strength Steel, Stiklestad, Verdal, 23–24 April 2002: 10.
- LePera FS (1980) Improved etching technique to emphasize martensite and bainite in high-strength Dual-Phase steels. *Journal of Metals* March: 38–39.
- Li Y, Crowther DN, Green MJW, Mitchell PS & Baker TN (2000) The influence of vanadium in microalloyed steels on properties and microstructure of the intercritically reheated coarse grained heat affected zone. Proc. Thermomechanical Processing of Steels conference, London, UK, 24–26 May 2000. The Institute of Materials: 69–78.

- Li Y, Crowther DN, Green MJW, Mitchell PS & Baker TN (2001) The effect of vanadium and niobium on properties and microstructure of intercritically reheated coarse grained heat affected zone in low carbon microalloyed steels. *ISIJ International*, 41 (1): 46–55.
- Liao J, Ikeuchi K & Matsuda F (1996) Effect of cooling time on HAZ toughness and microstructure: Simulated HAZ toughness of low-alloy SQV-2A pressure vessel steel (1st Report). *Welding International* 10 (7): 552–558.
- Liu C, Zhao Z-B & Northwood DO (2002) Mechanical properties of heat affected zone bainitic high strength low alloy steel. *Material Science and Technology* 18 November: 1325–1328.
- Lou D & Holappa L (2001) Microstructure property control steels by inclusions. SINTEF Report no. STF24 AO1295: 40.
- Mabuchi H & Nakao H (1981) The effect of excess aluminium on low-temperature toughness in A302C steels. *Transactions of ISIJ* 21: 495–501.
- Mabuchi H & Nakao H (1983) The effects of excess aluminium on mechanical properties of Mn-Mo, Mn-Mo-Ni and Mn-Mo-Ni-Cr with regard to solute interactions. *Transactions of ISIJ* 23: 504–512.
- Mabuchi H, Uemori R & Fujioka M (1996) The role of Mn depletion in intra-granular ferrite transformation in the heat affected zone of welded joints with large heat input in structural steels. *ISIJ international* 36 (11): 1406–1412.
- Madariaga I, Romero JL & Gutiérrez I (1998) Upper acicular ferrite formation in medium-carbon microalloyed steel by isothermal transformation: Nucleation enhancement by CuS. *Metallurgical and Materials Transactions A* 29A March: 1003–1015.
- Manohar PA & Chandra T (1997) Effect of TMP and Mn content on the CCT behaviour of Ti-Nb-Mo microalloyed steels. *Proc. THERMEC'97 International Conference on Thermomechanical Processing of Steels and Other Material*, Wollongong, Australia, 7–11 July 1997. Eds: Chandra T. & Sakai T. *The Minerals, Metals & Materials Society*: 749–755.
- Manohar PA & Chandra T (1998) Continuous cooling transformation behaviour of high strength microalloyed steels for linepipe applications. *ISIJ International* 38 (7): 766–774.
- Manohar PA, Chandra T & Killmore CR (1996) Continuous cooling transformation behaviour of microalloyed steels containing Ti, Nb, Mn and Mo. *ISIJ International* 36 12: 1486–1493.
- Mannsfeld A, Langenberg P & Dahl W (2001) Statistical treatment of fracture mechanics data and correlation with Charpy energy. *Proc. The Charpy Centenary Conference*, Poitiers, France, 2–5 October 2001. Eds. François D. & Pineau A: *From Charpy to Present Impact Testing*, ESIS Publication 30, 2002: 357–364.
- McRobie DE & Knott JF (1985) Effect of strain ageing on fracture toughness of C-Mn weld metal. *Material Science and Technology* 1 May: 357–365.
- Matsuda F, Li Z, Bernasovsky P, Ishihara K & Okada H (1991) An investigation on the behaviour of the M-A constituent in simulated HAZ of HSLA steels. *Welding in the World* 29 (9/10): 307–313.
- Matsuda F, Fukuda Y, Okada H, Shiga C, Ikeuchi K, Horii Y, Shiwaku T & Suzuki S (1996) Review of mechanical and metallurgical investigations of martensite-austenite constituent in welded joints in Japan. *Welding in the World* 37 (3): 134–154.
- Nagel M, Langenberg P, Lüder F, Bleck W & Dilthey U (2001) Discussion of testing procedures for determination of toughness properties of laser welded joints. *Proc. The Charpy Centenary Conference*, Poitiers, France, 2–5 October 2001. Eds. François D. & Pineau A.: *From Charpy to Present Impact Testing*, ESIS Publication 30, 2002: 253–261.
- NORSOK STANDARD (2004) Material data sheets for structural steel, M-120, Rev. 4, June 2004. Standard Norge: 5 + Apps 35.
- Obara M & Wallach ER (1999) Improvement of weld microstructure at very low oxygen levels *IIW Doc. IX-1936-99*: 17.

- Ohkita S & Horii Y (1995) Recent development in controlling the microstructure and properties of low alloy steel weld metals. *ISIJ International* 35 (10): 1170–1182.
- Oikawa K, Ishida K & Nishizawa T (1997a) Effect of titanium addition on the formation and distribution of MnS inclusions in steel during solidification. *ISIJ International* 37 (4): 332–338.
- Oikawa K, Ohuchi Y & Ishida K (1997b) Effect of Ti and Al addition on distribution of MnS inclusion in steel during solidification. Proc. THERMEC'97 International Conference on Thermomechanical Processing of Steels and Other Material, Wollongong, Australia, 7–11 July 1997. Eds handra T. & Sakai T. The Minerals, Metals & Materials Society: 859–865.
- Okada H, Matsuda F, Ikeuchi K & Hrivnak I (1994) Effect of M-A constituent on fracture behaviour of weld HAZ with high heat input in 780 and 980 MPa class HSLA steels. Proc. 2nd Workshop on Constraint Effect on the Structural Performance of Welded Joints, 1–2 September 1994, Osaka, Japan, IIW Doc. X-1300-94: 131–141.
- Pan L.(2004) Two methods for processing an ultrafine ferritic grain size in steels and the thermal stability of the structure. Doctoral Thesis, Department of Mechanical Engineering, University of Oulu, Finland. *Acta Universitatis Ouluensis C Technica* 211: 125.
- Powel GLF, Lloyd PG & Bee JV (1998) Hetrogeneity of coarsened oxide inclusions in C-Mn steel welds. *Science and Technology of Welding and Joining* 3 (1): 9–11.
- Priester R & Ibraheem AK (2000) Processing of steel for ultrafine ferrite grain structures. *Materials Science and Technology* 16 November-December: 1267–1272.
- Qiu H, Mori H, Enoki M & Kishi T (2000) Fracture mechanism and toughness of welding heat-affected zone in structural steel under static and dynamic loading. *Metallurgical and Materials Transactions A* 31A November: 2785–2791.
- Ricks RA, Howell PR & Barritte GS (1982) The nature of acicular ferrite in HSLA steel weld metals. *Journal of Materials Science* 17: 732–740.
- San Martin I & Rodriguez-Ibabe JM (1999) Effect of Ti addition on toughness improvement of as-rolled microalloyed vanadium steels. Proc. Conference from Materials Solutions '99, 1–4 November 1999, Cincinnati, Ohio. Eds. Asfahani R. & Bodnar R.: *International Symposium on Steel for Fabricated Structures*, ASM International: 146–153.
- Senogles D (1998) A steel composition for laser welding. UK Patent application GB 2341613 A: 36 + Apps 17.
- Shiga C (1994) Application of TMCP to high strength steels with excellent weld properties. IIW Doc. IX-1746–94: 6.
- Shim J-D, Cho YW & Shim J-H (1999) Carbon-manganese wrought steel with inoculated acicular ferrite microstructure. *CAMP-ISIJ* 12: 1120–1122.
- Shim J-H, Byun J-S, Cho YW, Oh Y-J, Shim J-D & Lee DN (2000) Hot deformation and acicular ferrite microstructure in C-Mn steel containing Ti₂O₃ inclusions. *ISIJ international* 40 (8): 819–823.
- Shim J-H, Byun J-S, Cho YW, Oh Y-J, Shim J-D & Lee DN (2001) Effect of Si and Al on acicular ferrite formation in C-Mn steel. *Metallurgical and Materials Transactions A* 32A January: 75–83.
- Shim J-H, Cho YW, Chung SH, Shim J-D & Lee DN (1999) Nucleation of intragranular ferrite at Ti₂O₃ particle in low carbon steel. *Acta mater.* 47 (9): 2751–2760.
- Suh J-Y, Byun J-S, Shim J-H, Oh Y-J, Cho YW, Shim J-D & Lee DN (2000) Acicular ferrite microstructure in titanium bearing low carbon steels. *Metallurgical modelling of welding. Materials Science and Technology* 16 November-December: 1277–1281.
- Suzuki S, Bessyo K, Toyota M & Minami F (1996) Morphology and fracture properties of martensitic islands in a multipass weld HAZ: Study of microcrack initiation properties of a steel HAZ having microscopic strength inhomogenities (1st Report). *Welding International* 10 (1): 27–35.

- Svensson L-E & Gretoft B (1990) Microstructure and impact toughness of C-Mn weld metals. *Welding Journal* 69 December: 454-s-461-s.
- Tanguy B, Piques R & Pineau A (2001) Experimental analysis of Charpy V-notch specimens. Proc. The Charpy Centenary Conference, Poitiers, France, 2–5 October 2001. Eds. François D. & Pineau A.: From Charpy to Present Impact Testing, ESIS Publication 30, 2002: 453–460.
- Terada Y, Chijiwa R, Tamemiro H, Kikuma T & Funato K (1992) Titanium-oxide bearing steels for offshore structures. Proc. 2nd International Conference on HSLA Steels, Beijing, 1990. Eds. Tither G. & Shouma Z. The Minerals, Metals & Materials Society: 519–524.
- Terada Y, Kojima A, Hara T, Morimoto H, Tsuru E, Asahi H, Kiyose A, Sugiyama M, Nakashima T, Doi N, Murata M & Ayukawa N (2004) Recent development of high-strength linepipes in hostile environments. Proc. International Pipeline Technology Conference, Ostend, Belgium, 9–13 May 2004. Eds. Denys R. & Tiratsoo J. Pipeline World and The Journal of Pipeline Integrity, Volume IV: 1603–1617.
- Thewlis G (1994) Transformation kinetics of ferrous weld metals. *Materials Science and Technology* 10 February: 110–125.
- Thewlis G, Whiteman JA & Segnoles DJ (1997) Dynamics of austenite to ferrite phase transformation in ferrous metals. *Materials Science and Technology* 13 March: 257–274.
- Thewlis G (2000) Weldability of X100 linepipe. *Science and Technology of Welding and Joining* 5 (6): 365–377.
- Thewlis G (2001) Steel composition and microstructure. International Application Published under the Patent Cooperation Treaty (PCT), WO 01/66813 A1 (CORUS UK LIMITED): 16 + Apps 17.
- Thewlis G (2004) Classification and qualification of microstructures in steels. *Materials Science and Technology* 20 February: 143–160.
- Tian D (1998) Microstructure, cleavage fracture and toughness of granular bainite in simulated coarse-grained heat-affected zones of low-carbon high-strength steels. Doctoral Thesis, Department of Mechanical Engineering, University of Oulu, Finland. *Acta Universitatis of Ouluensis C Technica* 113: 120 + Apps 10.
- Tian D, Karjalainen LP, Qian B & Chen X (1996) Correlation between microstructure features of granular bainite, roughness of fracture surface and toughness of simulated CGHAZ in QT type HSLA steels. *Scandinavian Journal of Metallurgy* 25: 87–94.
- Tomita Y, Saito N, Tsuzuki T, Tokunaga Y & Okamoto K (1994) Improvement in HAZ toughness of steel by TiN-MnS addition. *ISIJ International* 34 (10): 829–835.
- Tweed JH & Knott JF (1987) Micromechanisms on failure in C-Mn weld metals. *Acta metallurgica* 35 (7): 1401–1414.
- Van der Eijk C, Grong Ø & Walmsley J (2000) Mechanisms of inclusion formation in low alloy steels deoxidised with titanium. *Materials Science and Technology* 16 January: 55–64.
- Verrier P, Maurickx T, Taillard R & Garrigues G (1989) Effect of HAZ microstructure on fracture toughness of offshore microalloyed structural steels. Proc. The 8th International Conference on Offshore Mechanics and Arctic Engineering, Hague, 19–23 March 1989: 641–647.
- Wallin K, Nevasmaa P, Planman T & Valo M (2001) Evolution of Charpy V test from a quality control test to a materials evolution tool for structural integrity assessment. Proc. The Charpy Centenary Conference, Poitiers, France, 2–5 October 2001. Eds. François D. & Pineau A.: From Charpy to Present Impact Testing, ESIS Publication 30, 2002: 57–68.
- Weng Y & Dong H (2000) Ultra fine grain steels and their properties. Proc. The 42nd Mechanical Working and Steel Processing Conference, Toronto, Ontario, Canada, 22–25 October 2000. Eds. Canary D.L., Fuga D.J. & Baker M.A. Iron & Steel Society (ISS), Vol XXXVII: 533–545.
- Wistance W, Pumphrey PH & Howarth DJ (2001) Material qualification for shipbuilding industry. Proc. The Charpy Centenary Conference, Poitiers, France, 2–5 October 2001. Eds. François D. & Pineau A.: From Charpy to Present Impact Testing, ESIS Publication 30, 2002: 393–400.

- Xu XX, Su Y, Zhou W & Piao HL (1993) A study of cleavage/fibrous transition temperature of 15MnVN steel weld metal. *Welding Journal* 72 June: 257-s-262-s.
- Yakubtsov IA, Boyd JD, Liu WJ & Essadiqi E (2000) Strengthening mechanism in dual-phase acicular ferrite+M/A microstructures. Proc. The 42nd Mechanical Working and Steel Processing Conference, Toronto, Ontario, Canada, 22–25 October 2000. Eds. Kanary D.L., Fuga D.J. & Baker M.A. Iron & Steel Society (ISS), Vol XXXVII: 429–439.
- Yakubtsov IA & Boyd JD (2001) Bainite transformation during continuous cooling of low carbon microalloyed steel. *Materials Science and Technology* 17 March: 296–301.
- Yakubtsov I, Boyd D, Turi T and Emadi D (2004) Processing and properties of ultrafine bainitic plate steels. Proc. 2nd International Conference Thermomechanical Processing of Steels TMP '2004, Liège, Belgium, 15–17 June, 2004. Eds. Lamberigts M.. Centre de Recherches Métallurgiques (CRM): 303–310.
- Yamamoto K, Matsuda S, Haze T, Chijiwa R & Mimura H (1989) A new developed Ti-oxide bearing steel having high HAZ toughness. Proc. Symposium on Residual and Unspecified Elements in Steel, ASTM STP 1042, Philadelphia 1989. Eds. Melilli A.S. & Nisbett E.G. American Society for Testing and Materials: 266–284.
- Yamamoto K, Hasegawa T & Takamura J (1996) Effect of boron on intra-granular ferrite formation in Ti-oxide bearing. *ISIJ International* 36 (1): 80–86.
- Yang Z, Zhao Y, Chen Q, Gao H, Wang R & Ma Y (2000) Formation of ultra-fine ferrite grains in common carbon steels through low temperature heavy deformation. Proc. The 42nd Mechanical Working and Steel Processing Conference, Toronto, Ontario, Canada, 22–25 October 2000. Eds. Kanary D.L., Fuga D.J. & Baker M.A. Iron & Steel Society (ISS), Vol XXXVII: 505–513.
- Yokoyama K & Nagumo M (1998) Brittle fracture initiation associated with the strain localization a heat-affected zone of low carbon steel. *Metallurgical and Materials Transactions A* 29A February: 551–558.
- Yoshida Y, Tamehiro H, Chijiwa R, Funato K, Doi N, Tanaka K, Kibe M & Watanabe K (1998) High strength TMCP steel plate for offshore structures (Titanium oxide bearing steel plate). *Nippon Steel Corporation*, May 1998: 8.
- Yurioka N (1995) TMCP steels and their welding. *Welding in the World* 35 (6): 375–390.
- Zhang Z & Farrar RA (1996) Role of non-metallic inclusions in formation of acicular ferrite in low alloy weld metals. *Materials Science and Technology* 12 March: 237–260.
- Zhang Z & Farrar RA (1997) Influence of Mn and Ni on the microstructure and toughness of C-Mn-Ni weld metals. *Welding Journal* 76 May: 183-s-196-s.
- Zhang XZ & Knott JF (1999) Cleavage fracture in bainitic and martensitic microstructures. *Acta materialia* 47 (12): 3483–3495.
- Zhao P & Boyd JD (2000) Mechanism of intragranular ferrite nucleation in microalloyed medium carbon steels. Proc. HSLA Steels 2000- The 4th International Conference on High Strength Low Alloy Steels, Xián, China. Eds. Liu G., Wang F., Wang Z. & Zhang H. The Chinese Society for Metals, Beijing: 130–132.
- Zhao M-C, Shan Y-Y, Xiao F-R & Yang K (2003) Acicular ferrite formation during hot plate rolling for pipeline steels. *Materials Science and Technology* 19 March: 355–359.

Appendices

Appendix 1

Table 11. Impact and CTOD transition temperatures T_{27J} , $T_{50\%}$ and $T_{0.1mm}$ of the base plates, the simulated CGHAZ, ICCGHAZ and ICHAZ specimens in the as-simulated and PWHT state ($^{\circ}\text{C}$).

Steel	CGHAZ, $t_{8/5}=5$ s			ICCGHAZ, $t_{8/5}=5$ s			ICGHAZ, $t_{8/5}=5$ s			ICHAZ, $t_{8/5}=5$ s								
	Simulated			Simulated			Simulated			Simulated								
	T_{27J}	$T_{50\%}$	$T_{0.1mm}$	T_{27J}	$T_{50\%}$	$T_{0.1mm}$	T_{27J}	$T_{50\%}$	$T_{0.1mm}$	T_{27J}	$T_{50\%}$	$T_{0.1mm}$						
A	-78	-56	-103	-62	-15	-23	-9	+31	+10	-58	-23	-49	-23	+9	-25	-94	-43	-39
B	-95	-13	-40	-80	-18	>-10	-74	-18	-66	-80	-30	-91	-38	+11	-54	-100	-40	<-110
C	-92	-84	-99	-59 ¹⁾	-27 ¹⁾	-46 ¹⁾	-51	-7	-36	-72	-22	-24	-42	+23	-47	-74	-27	-103
D	-68	-32	-99	-	-	-	-	-	-	-	-	-	-1	>+50	± 0	-	-	-
D1	-56	-27	-	-	-	-	-	-	-	-	-	-	-19	+28	-	-	-	-
D2	-	-	-58	-	-	-	-	-	-	-	-	-	-	-	-18	-	-	-

¹⁾ Plate no. 11172-21 or no. 11172-31

Table 12. Maximum hardness and M-A constituents (M-A) of the base plate, the simulated CGHAZ, ICCGHAZ and ICHAZ specimens in the as-simulated and PWHT state (HV, %).

Steel	CGHAZ, $t_{8/5}=5$ s			ICCGHAZ, $t_{8/5}=5$ s			ICGHAZ, $t_{8/5}=5$ s			ICHAZ, $t_{8/5}=5$ s			
	Simulated			Simulated			Simulated			Simulated			
	HV	M-A(%)	M-A(%)	HV	M-A(%)	M-A(%)	HV	M-A(%)	M-A(%)	HV	M-A(%)	M-A(%)	
A	211	0.99	2.67	262	2.67	3.47	233	0.92	0.92	213	5.23	202	0.33
B	245	0.62	3.26	295	3.26	4.55	217	1.41	1.41	197	11.67	175	0.79
C	200	0.44	1.39 ¹⁾	280 ¹⁾	1.39 ¹⁾	7.73	231	1.01	1.01	200	9.47	180	2.82
D	180	0.35	-	-	-	-	-	-	-	197	11.35	-	-
D1	204	0.70	-	-	-	-	-	-	-	210	6.57	-	-
D2	202	7.29	-	-	-	-	-	-	-	202	7.86	-	-

¹⁾ Plate no. 11172-21 or no. 11172-31

Appendix 2

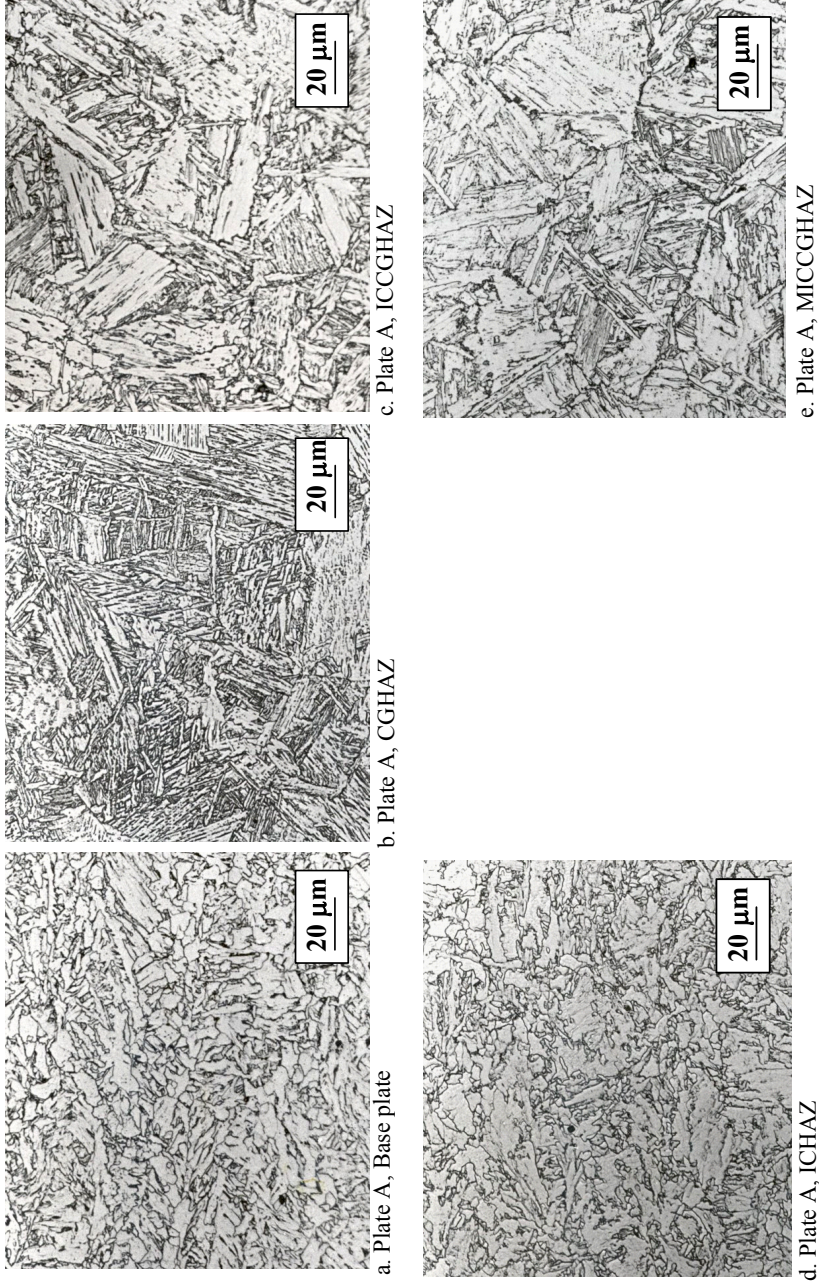


Fig. 87. Microstructures of plate A: base plate (a), CGHAZ (b), ICCGHAZ (c), ICHAZ (d) and MICCGHAZ (e), 2% Nital etching.

Appendix 3

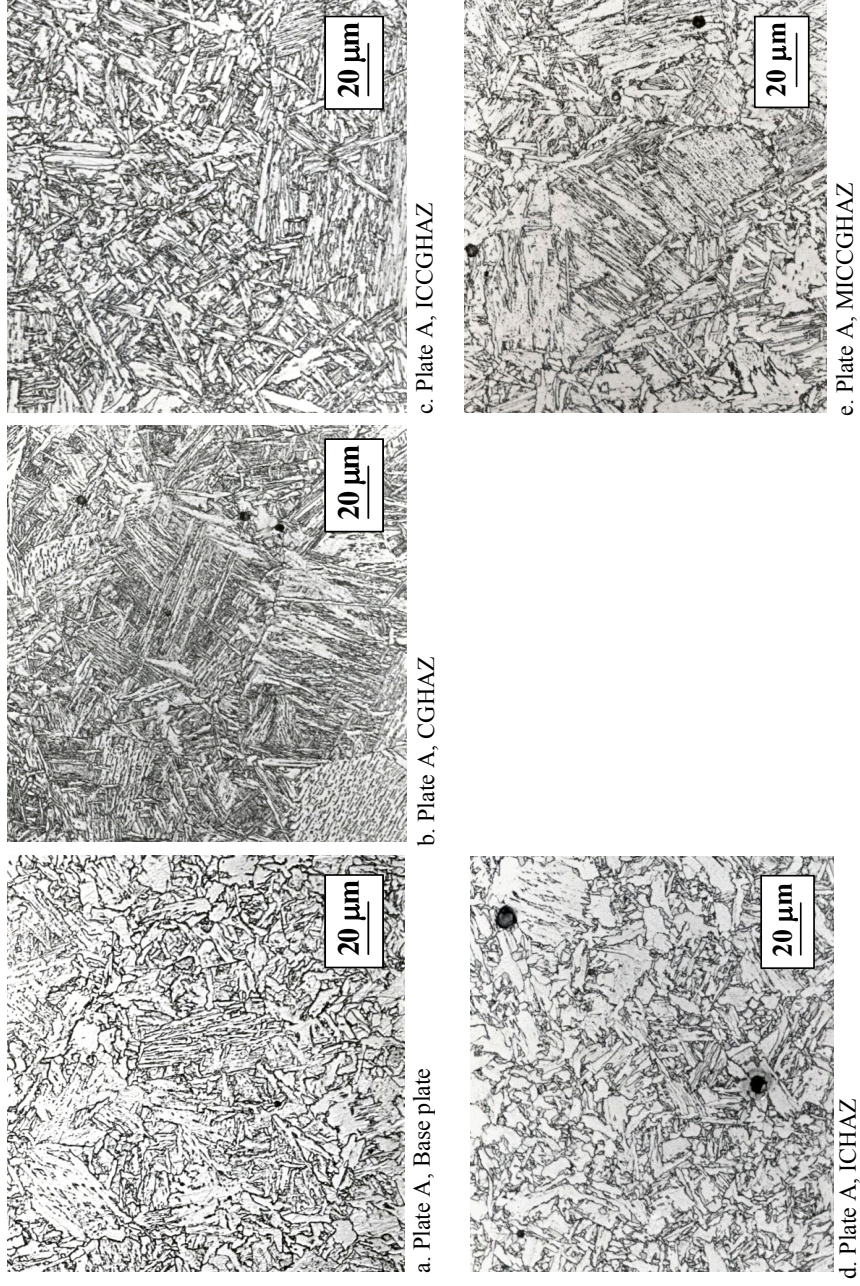


Fig. 88. Microstructures of plate B: base plate (a), CGHAZ (b), ICCGHAZ (c), ICHAZ (d) and MICCGHAZ (e), 2% Nital etching.

Appendix 4

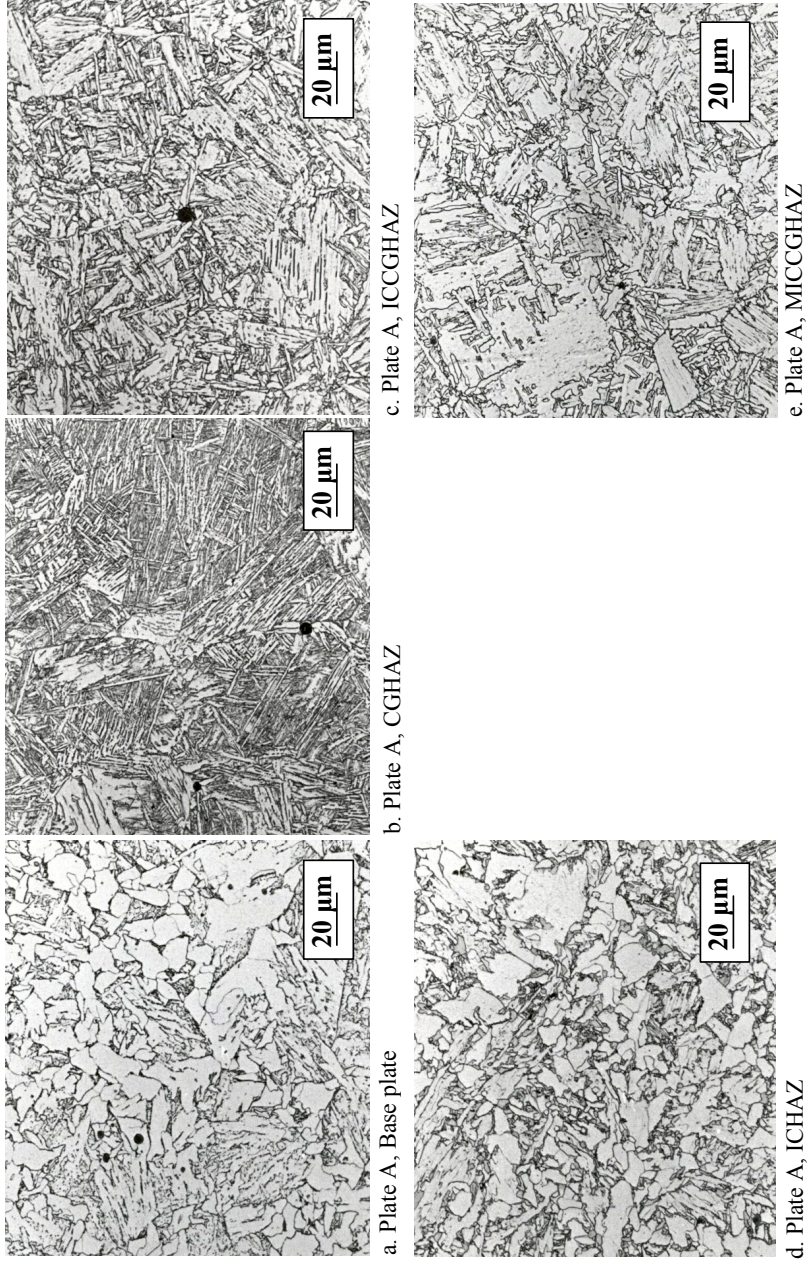
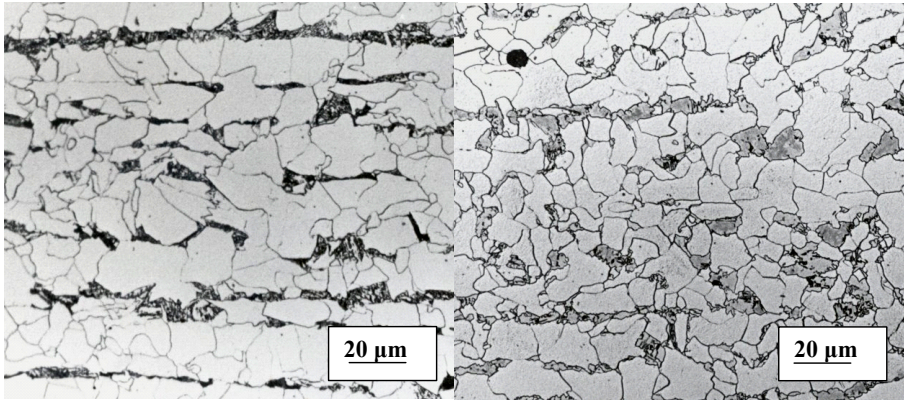


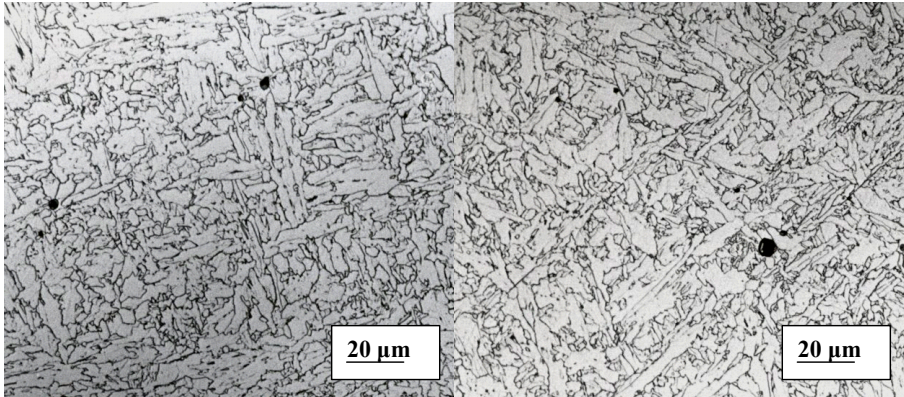
Fig. 89. Microstructure of plate C:base plate (a), CGHAZ (b), ICCGHAZ(c), ICHAZ (d) and MICCGHAZ (e), 2% Nital etching.

Appendix 5



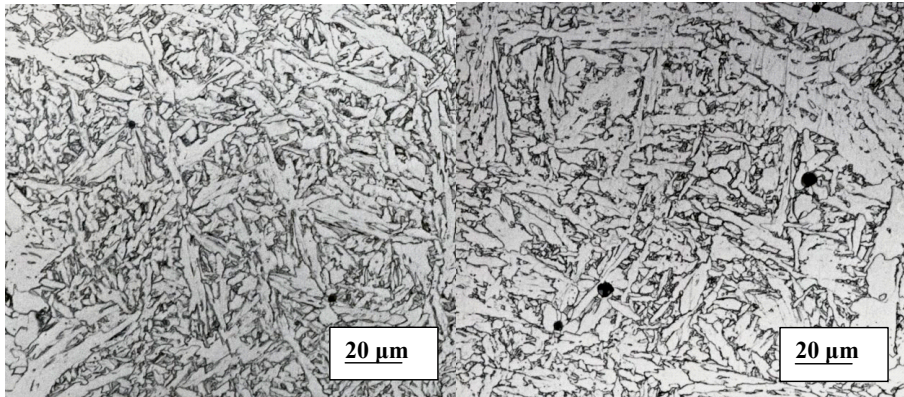
a. Plate D, Base plate

b. Plate D, ICHAZ



c. Test piece D1

d. Test piece D1, ICHAZ



e. Test piece D2

f. Test piece D2, ICHAZ

Fig. 90. Microstructures of plate D and the heat treated test pieces D1 and D2, 2% Nital etching.

Appendix 6

Table 13. Ferrite grain, bainite packet and fracture facet sizes defined from the Charpy V specimens.

Test specimen	Test. temp. (°C)	Ferrite grain-bainite packet size (µm)			Cleavage facet size (µm) Fracture profiles		
		Min.	Aver.±1σ	Max.	Min.	Aver.±1σ	Max.
A Base plate	-	29	44±7	66	-	-	-
A CGHAZ	-	30	50±11	80	-	-	-
A ICCGHAZ	-40	34	56±11	92	37	55±15	90
A MICCGHAZ	-60	33	61±11	83	42	56±9	76
A ICHAZ	-40	27	40±8	69	27	47±12	69
A MICHAZ	-80	29	43±11	88	40	50±8	64
B Base Plate	-	16	34±8	53	-	-	-
B CGHAZ	-	28	43±10	69	-	-	-
B ICCGHAZ	-80	25	42±10	63	23	39±8	53
B MICCGHAZ	-100	33	47±9	73	27	41±7	54
B ICHAZ	-60	25	35±6	49	26	41±7	55
B MICHAZ	-100	25	39±7	55	31	42±8	59
C Base Plate	-	25	33±6	50	-	-	-
C CGHAZ	-	26	48±12	75	-	-	-
C ICCGHAZ	-60	29	38±7	57	29	41±12	82
C MICCGHAZ	-40	28	51±11	83	32	49±9	61
C ICHAZ	-60	23	37±7	56	32	47±9	64
C MICHAZ	-60	24	37±6	49	32	43±7	59
D Base Plate	-70	31	45±12	101	30	45±9	66
D ICHAZ	-40	28	36±7	57	29	38±5	48
D1 Base Plate	-60	31	50±14	90	32	54±12	81
D1 ICHAZ	-40	28	47±14	93	36	56±19	93

Appendix 7

Table 14. Ferrite grain, bainite packet and fracture facet sizes defined from the CTOD specimens.

Test specimen	Test. temp. (°C)	Ferrite grain-bainite packet size (μm)			Cleavage facet size (μm) Fracture profiles		
		Min.	Aver.±1σ	Max.	Min	Aver.±1σ	Max.
A ICCGHAZ	-40	42	60±11	86	31	56±17	90
A MICCGHAZ	-80	40	62±13	98	39	63±18	118
A ICHAZ	-60	23	40±8	57	35	47±12	87
A MICHAZ	-100	29	44±9	65	32	44±11	76
B ICCGHAZ	-100	23	38±10	76	19	38±11	60
B MICCGHAZ	-100	28	41±8	71	19	39±9	56
B ICHAZ	-100	20	31±6	46	23	34±6	44
B MICHAZ	-110	26	42±9	67	19	35±11	62
C ICCGHAZ	-80	21	37±7	57	20	49±16	73
C MICCGHAZ	-40	29	45±11	70	36	47±7	59
C ICHAZ	-80	19	39±8	60	29	39±7	54
C MICHAZ	-120	26	39±7	57	24	42±13	77
D Base Plate	-110	24	38±7	63	30	43±9	63
D ICHAZ	-60	27	38±8	79	32	45±9	65
D2 Base Plate	-80	31	47±12	101	39	59±12	86
D2 ICHAZ	-60	26	56±18	103	44	60±10	89

Appendix 8

Table 15. Chemical composition of the precipitations (wt-%).

Specimen	Titanium	Niobium	Vanadium	Form
A ICCGHAZ	68.3	28.0	-	Rectangular
B ICCGHAZ	86.8	-	6.5	Diamond
C ICCGHAZ	70.4	-	25.3	Square/Circle
C MICCGHAZ	68.3	-	31.8	Square/Circle

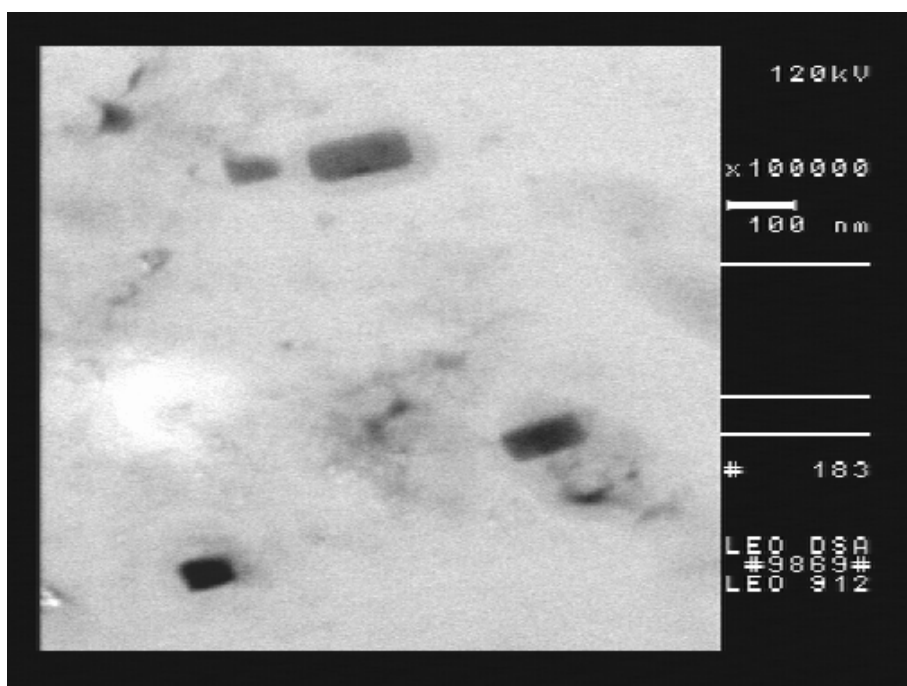


Fig. 91. TiNb precipitations in the simulated ICCGHAZ specimens of plate A, approximately 5–340 nm in size.

Appendix 9

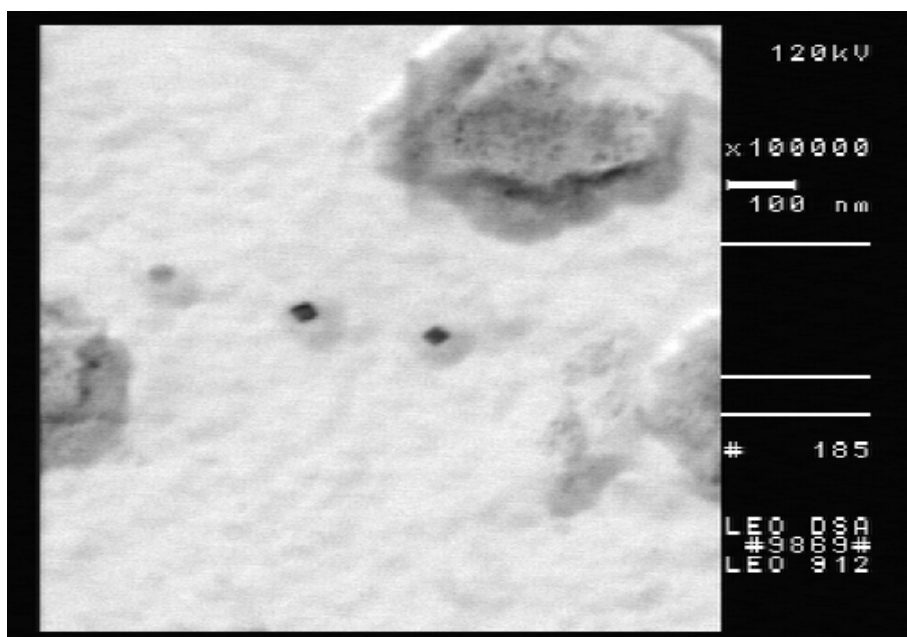


Fig. 92. Ti precipitations in the simulated ICCGHAZ specimen of plate B, approximately 5–350 nm in size.

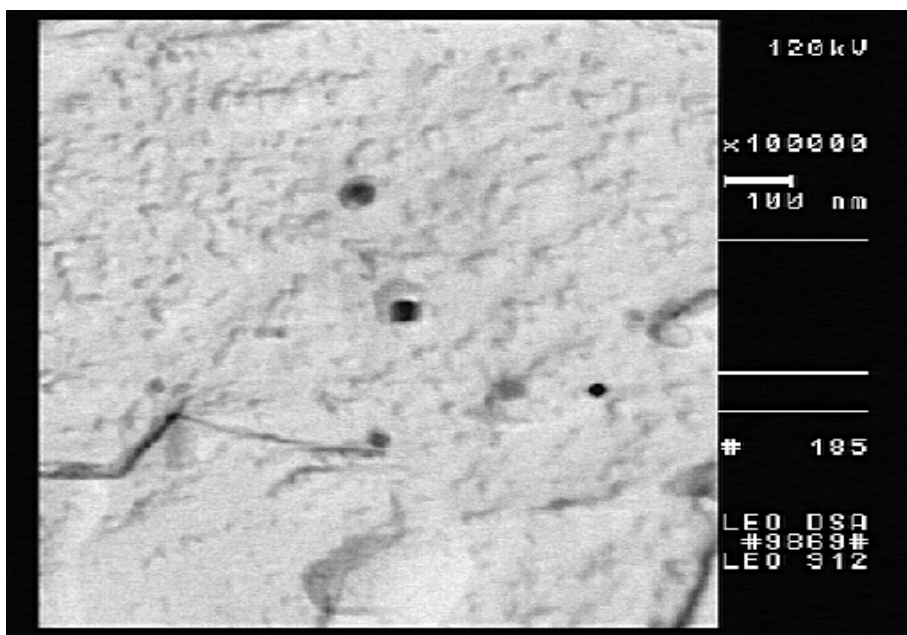


Fig. 93. TiV precipitations in the simulated ICCGHAZ specimen of plate C, approximately 6–85 nm in size.

Appendix 10

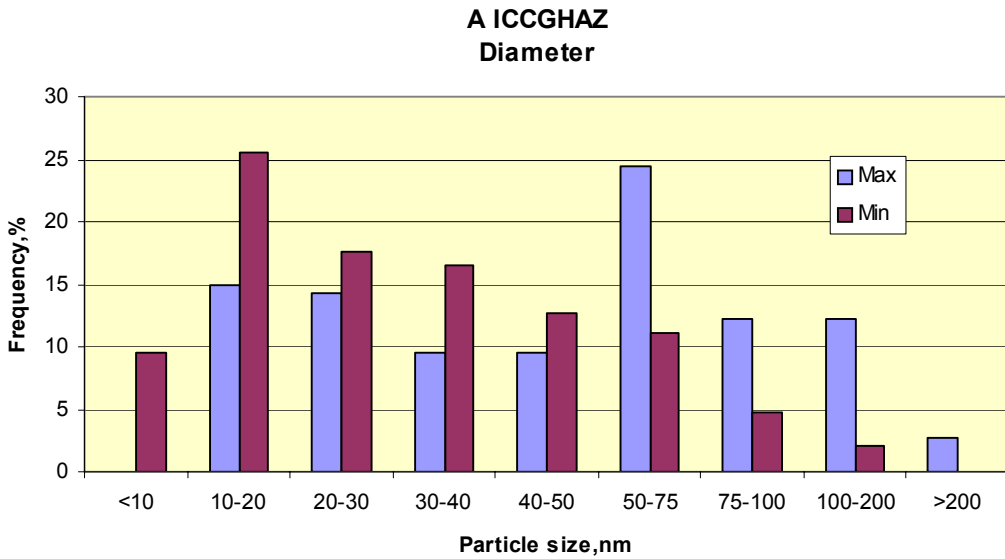


Fig. 94. Distribution of the diameter of TiNb precipitations in the simulated ICCGHAZ specimens from plate A.

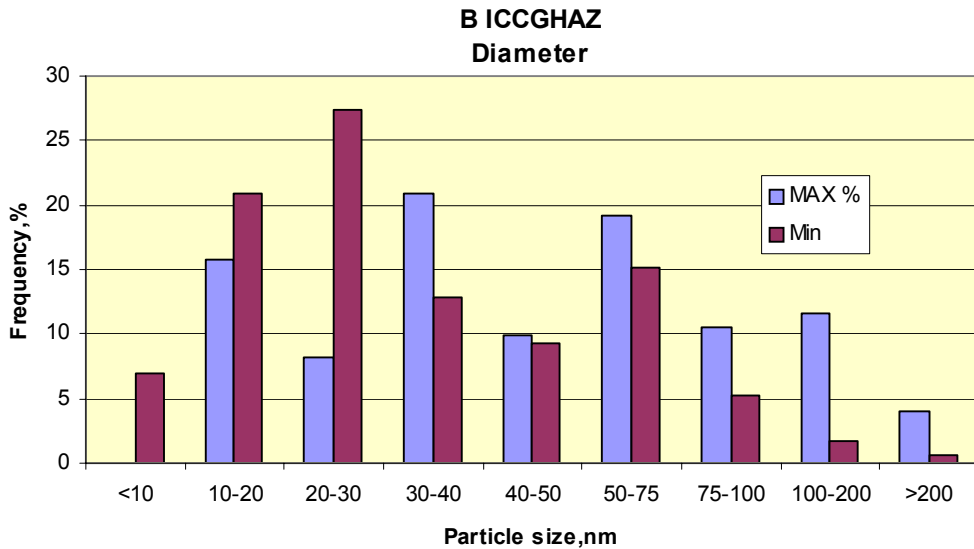


Fig. 95. Distribution of the diameter of Ti precipitations in the simulated ICCGHAZ specimens from plate B.

Appendix 11

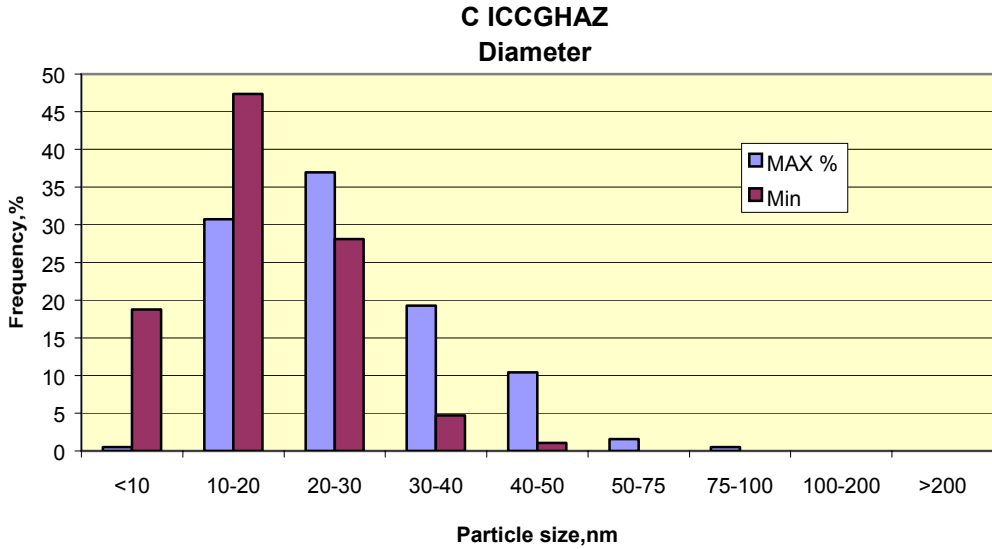


Fig. 96. Distribution of the diameter of TiV precipitation in the simulated ICCGHAZ specimens from plate C.

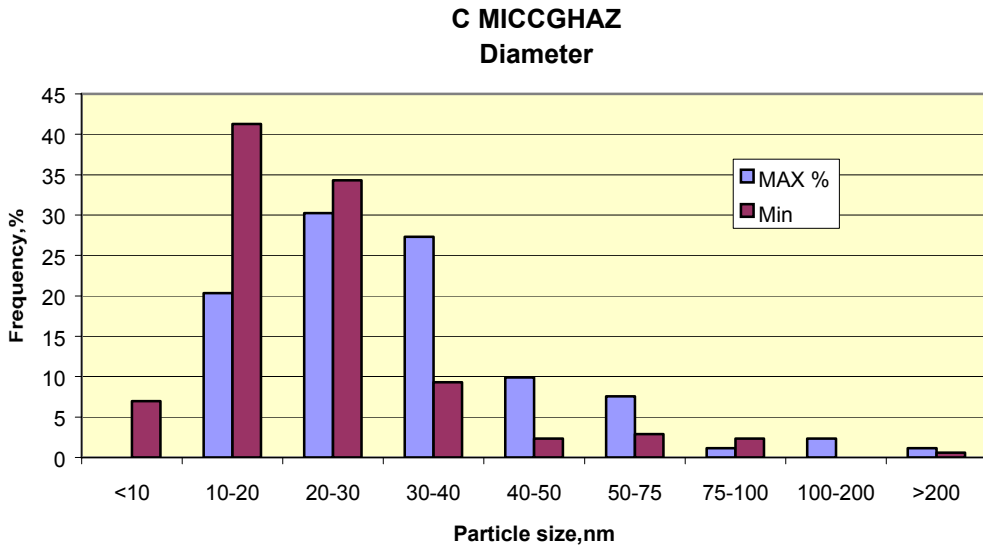


Fig. 97. Distribution of the diameter of TiV precipitation in the simulated ICCGHAZ specimens from plate C after PWHT.

Appendix 12

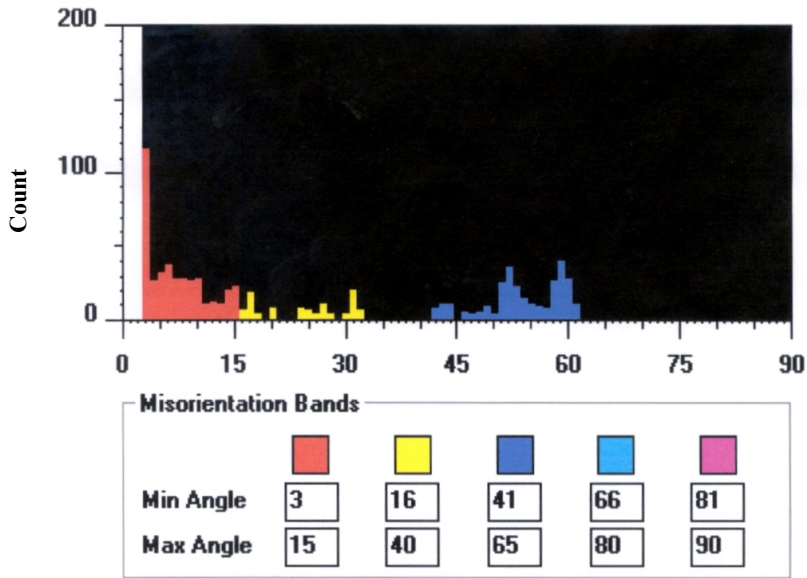


Fig. 98. Line plot histogram of adjacent grain misorientations in the simulated ICCGHAZ specimen from plate B, 44% (3–15°), 18% (16–40°), 38% (41–65°).

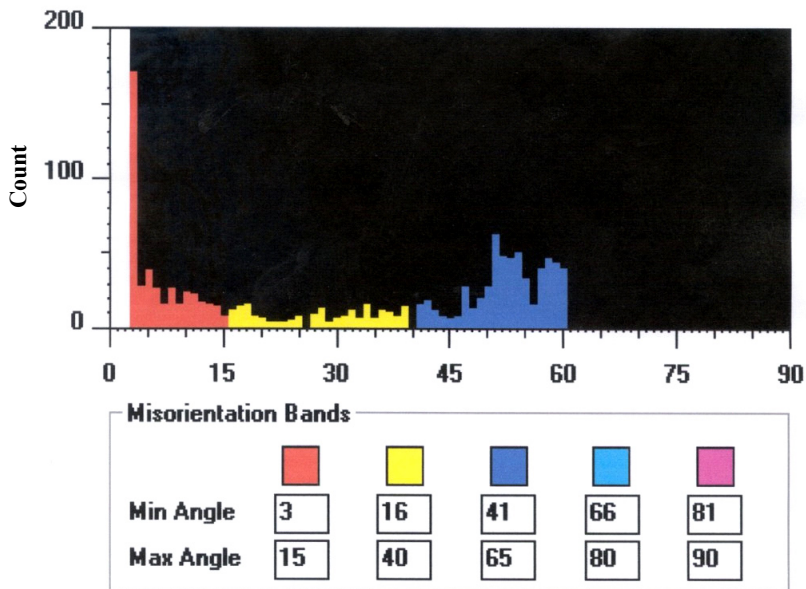


Fig. 99. Line plot histogram of adjacent grain misorientations in the simulated ICCGHAZ specimen from plate C, 34% (3–15°), 18% (16–40°), 48% (41–65°).

Appendix 13

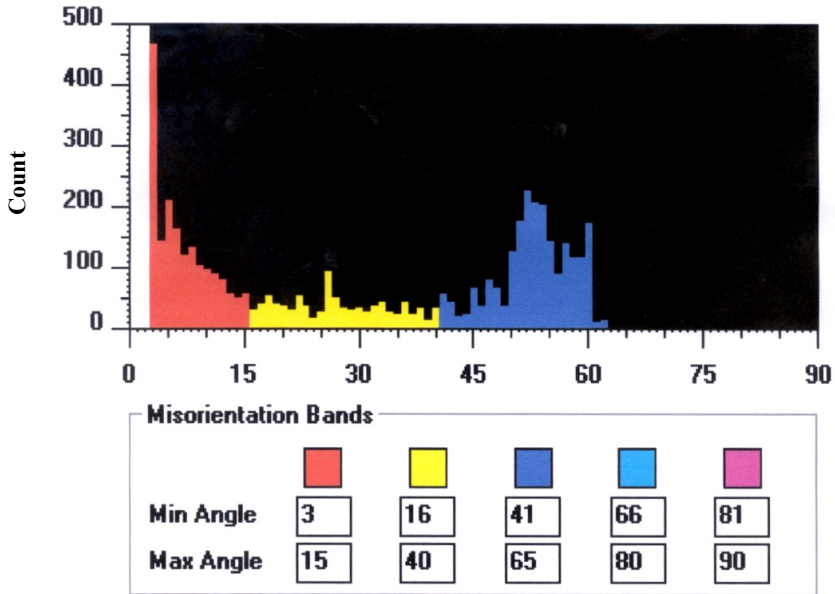


Fig. 100. Area plot histogram of adjacent grain misorientations in the simulated ICCGHAZ specimen from plate A, 39% (3–15°), 18% (16–40°), 43% (41–65°).

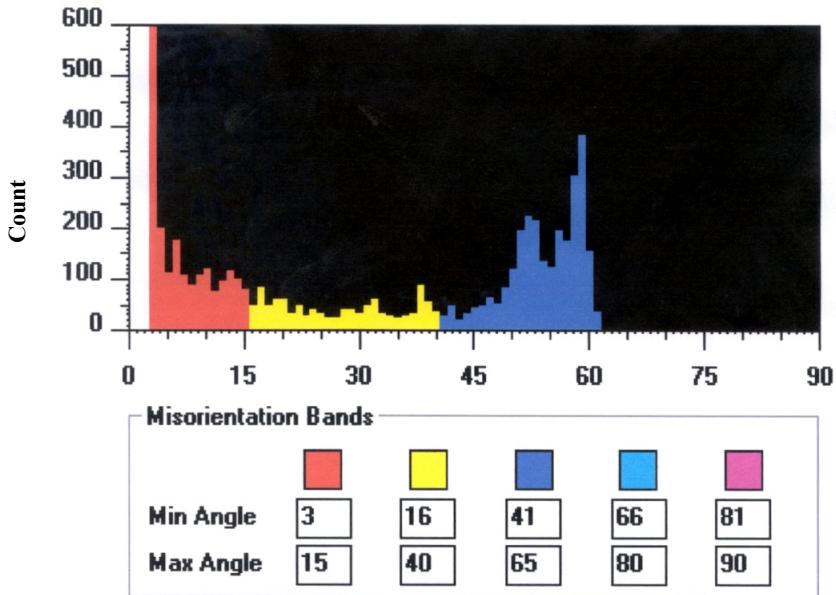


Fig. 101. Area plot histogram of adjacent grain misorientations in the simulated ICCGHAZ specimen from plate B, 35% (3–15°), 18% (16–40°), 47% (41–65°).

Appendix 14

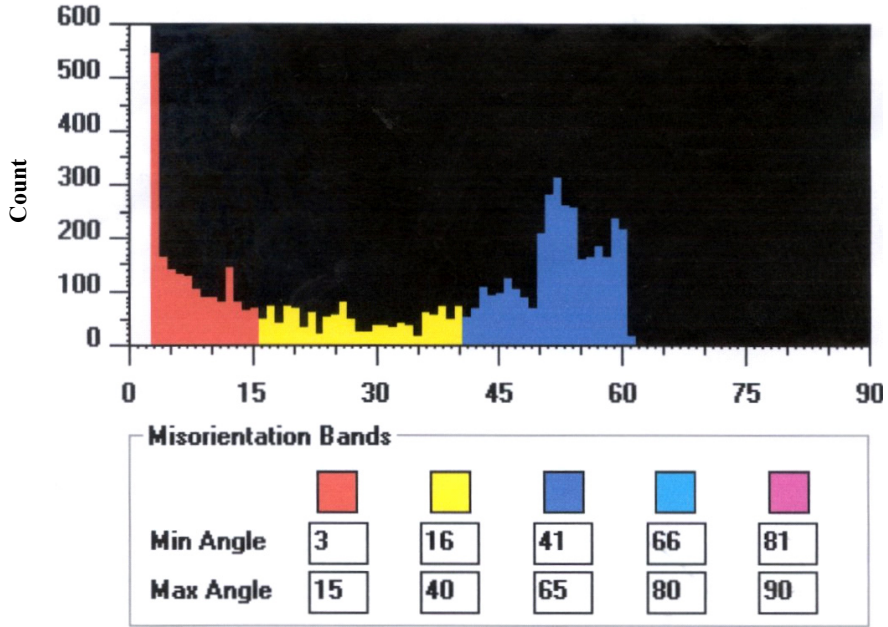


Fig. 102. Area plot histogram from adjacent grain misorientations in the simulated ICHAZ specimen of plate C, 30% (3–15°), 20% (16–40°), 50% (41–65°).

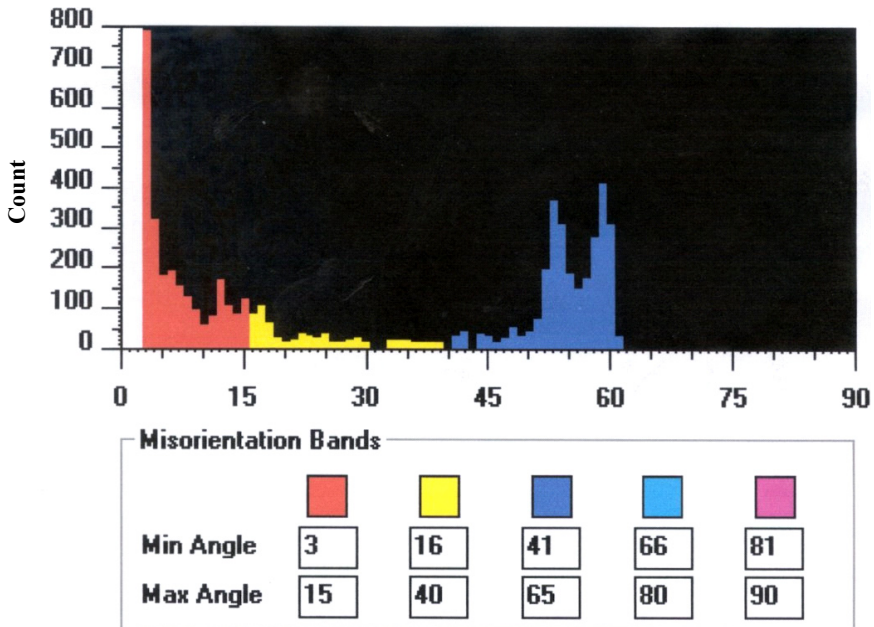


Fig. 103. Area plot histogram of adjacent grain misorientations in the simulated ICHAZ specimen from heat treated test piece D1, 41% (3–15°), 12% (16–40°), 47% (41–65°).

Appendix 15

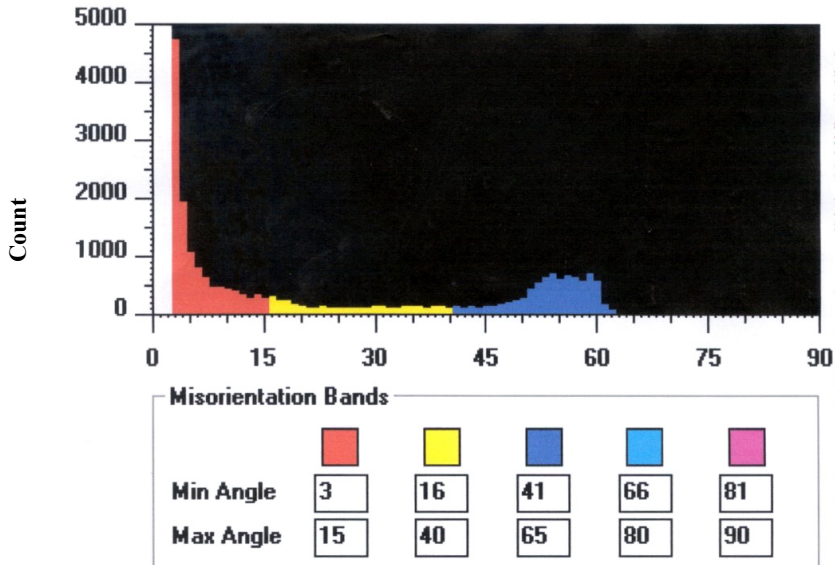


Fig. 104. Area plot histogram of adjacent grain misorientations in the heat treated test piece D2 (long period analysis), 49.5% (3–15°), 17.4% (16–40°), 33.1% (41–65°).

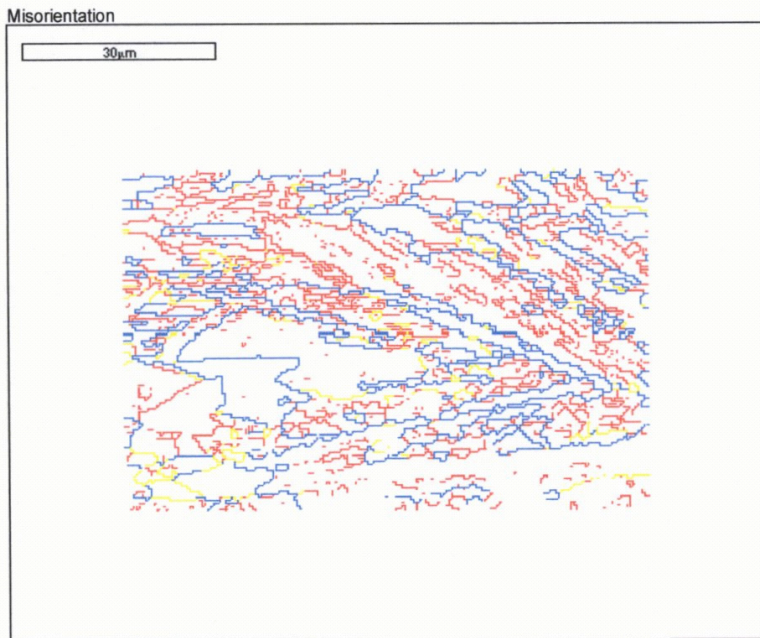


Fig. 105. Distribution of adjacent grain misorientations in the heat treated test piece D2 (long period analysis).

Appendix 16

A ICCGHAZ / Martensite-austenite, 3.47%

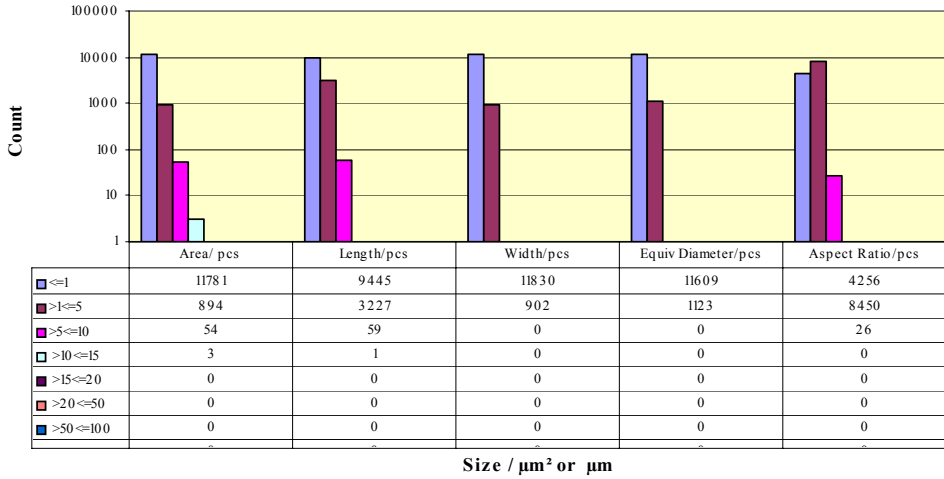


Fig. 106. Size distribution of M-A constituents in the simulated ICCGHAZ specimens from plate A.

C ICCGHAZ / Martensite-austenite, 7.73%

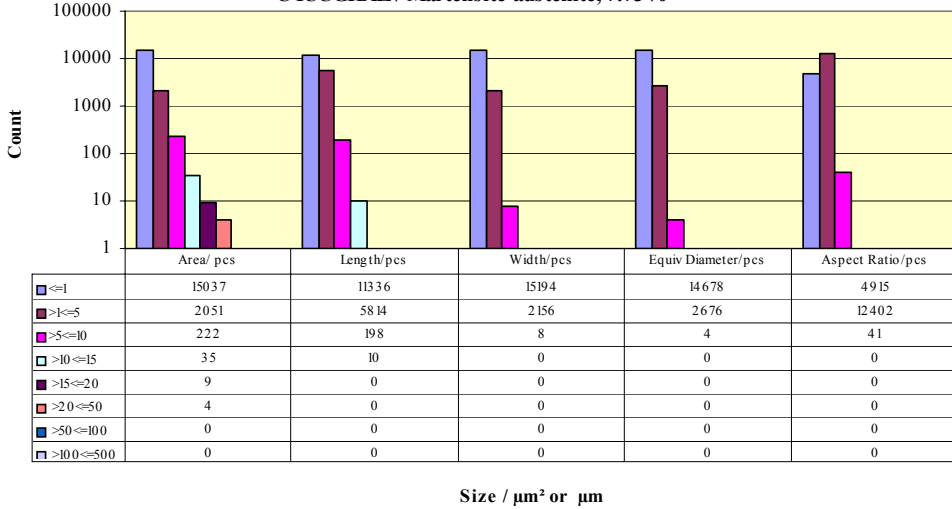


Fig. 107. Size distribution of M-A constituents in the simulated ICCGHAZ specimens from plate C.

Appendix 17

A ICHAZ/ Martensite-austenite, 5.23%

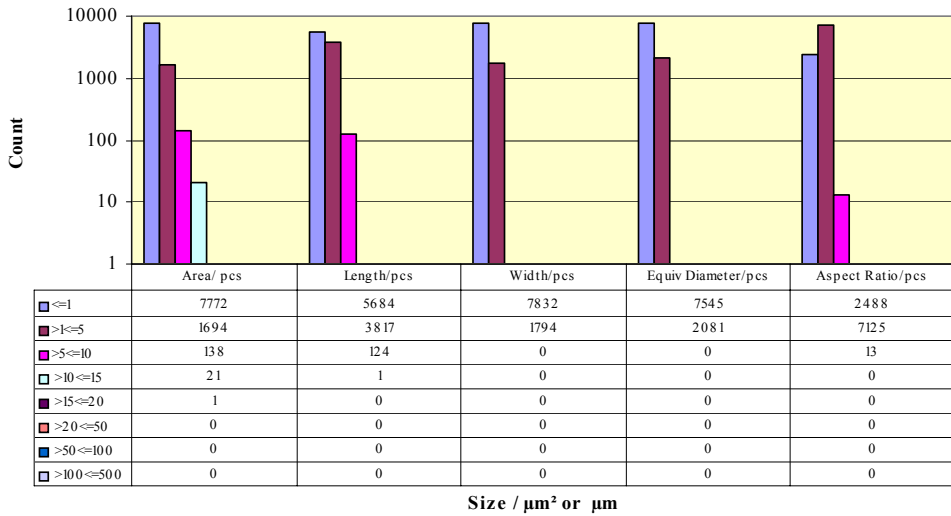


Fig. 108. Size distribution of M-A constituents in the simulated ICHAZ specimens from plate A.

B ICHAZ/ Martensite-austenite, 11.67%

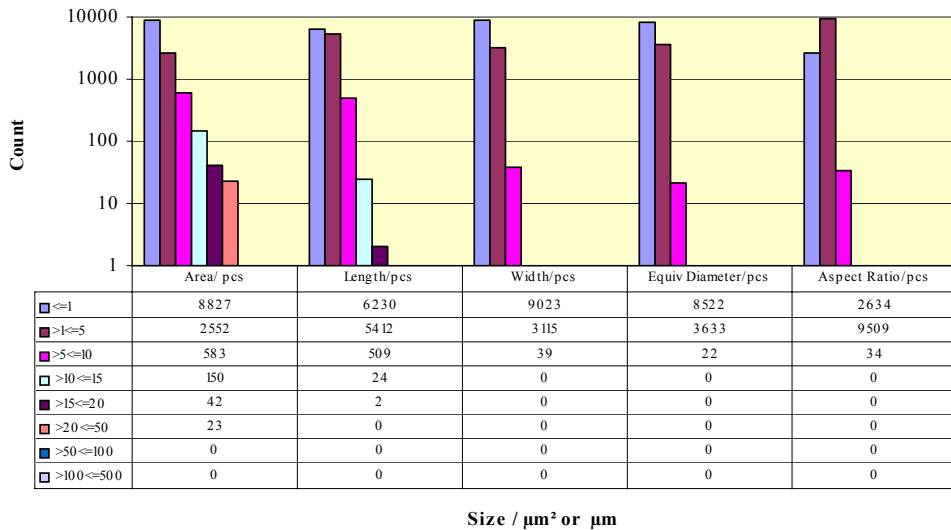


Fig. 109. Size distribution of M-A constituents in the simulated ICHAZ specimens from plate B.

Appendix 18

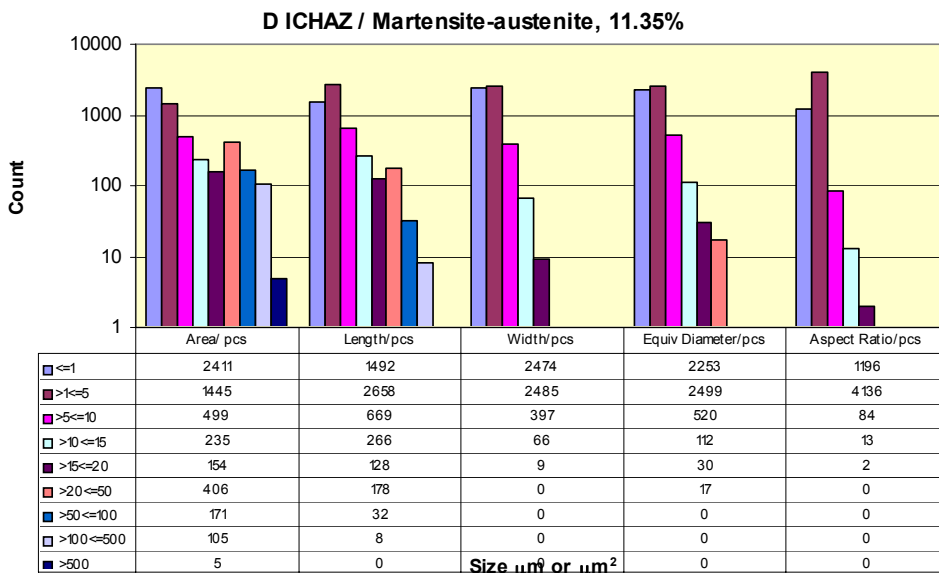


Fig. 110. Size distribution of M-A constituents in the simulated ICHAZ specimens from plate D.

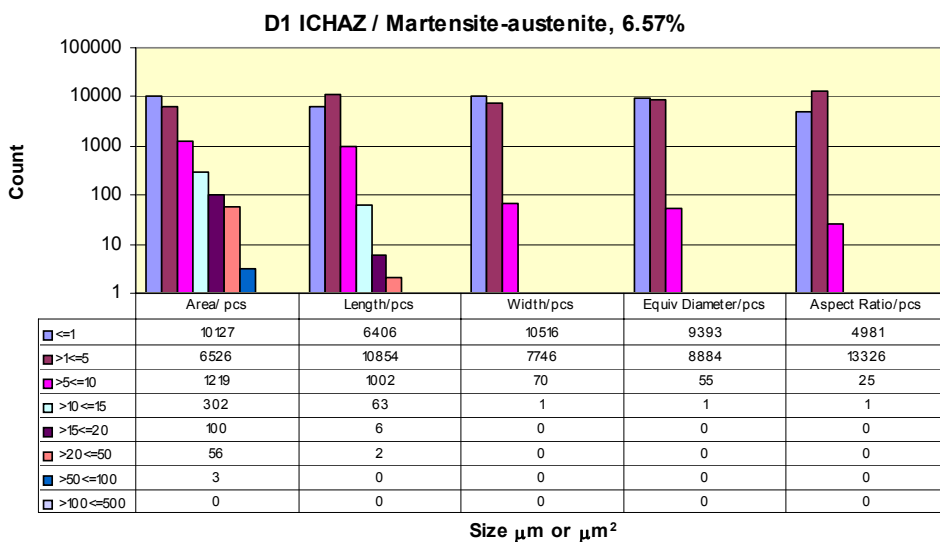


Fig. 111. Size distribution of M-A constituents in the simulated ICHAZ specimens from the heat treated test piece D1.

Appendix 19

T_{27J} CGHAZ+ICCGHAZ

SUMMARY OUTPUT

<i>Regression Statistics</i>	
Multiple R	0.935343
R Square	0.874867
Adjusted R	0.791445
Standard E	11.51487
Observatio	6

ANOVA

	<i>df</i>	<i>SS</i>	<i>MS</i>	<i>F</i>	<i>ignificance F</i>
Regressor	2	2781.057	1390.528	10.48726	0.044265
Residual	3	397.7764	132.5921		
Total	5	3178.833			

	<i>Coefficient</i>	<i>standard Err</i>	<i>t Stat</i>	<i>P-value</i>	<i>Lower 95%</i>	<i>Upper 95%</i>	<i>ower 95.0%</i>
Intercept	-315.5315	57.14156	-5.521927	0.011699	-497.3816	-133.6814	-497.3816
Packet	4.78983	1.048341	4.568963	0.019668	1.453539	8.126121	1.453539
M-A	10.03061	3.126413	3.208344	0.049018	0.080958	19.98026	0.080958

$$T_{27J}(^{\circ}\text{C}) = 4.79 \times \text{Packet} + 10.03 \times \text{M-A} - 315.53, R^2 = 0.87$$

Appendix 20

T_{50%} CGHAZ+ICCGHAZ

SUMMARY OUTPUT

<i>Regression Statistics</i>	
Multiple R	0.948089
R Square	0.898872
Adjusted R	0.831453
Standard E	8.465582
Observatio	6

ANOVA

	<i>df</i>	<i>SS</i>	<i>MS</i>	<i>F</i>	<i>ignificance F</i>
Regressor	2	1911.002	955.5009	13.33268	0.032159
Residual	3	214.9983	71.66609		
Total	5	2126			

	<i>Coefficients</i>	<i>standard Err</i>	<i>t Stat</i>	<i>P-value</i>	<i>Lower 95%</i>	<i>Upper 95%</i>	<i>ower 95.0%</i>	<i>pper 95.0%</i>
Intercept	-224.9974	42.00974	-5.35584	0.012735	-358.6913	-91.30357	-358.6913	-91.30357
Packet	3.897329	0.770727	5.056694	0.014924	1.44453	6.350127	1.44453	6.350127
M-A	9.381214	2.298499	4.081452	0.026566	2.066357	16.69607	2.066357	16.69607

$$T_{50\%}(^{\circ}\text{C}) = 3.89 \times \text{Packet} + 9.38 \times \text{M-A} - 225.00, R^2 = 0.90$$

Appendix 21

T_{0.1mm} CGHAZ+ICCGHAZ

SUMMARY OUTPUT

<i>Regression Statistics</i>	
Multiple R	0.960632
R Square	0.922813
Adjusted R	0.807033
Standard E	11.82553
Observatio	6

ANOVA

	<i>df</i>	<i>SS</i>	<i>MS</i>	<i>F</i>	<i>ignificance F</i>
Regressior	3	3343.814	1114.605	7.970394	0.113516
Residual	2	279.6862	139.8431		
Total	5	3623.5			

	<i>Coefficient</i>	<i>standard Error</i>	<i>t Stat</i>	<i>P-value</i>	<i>Lower 95%</i>	<i>Upper 95%</i>	<i>ower 95.0%</i>	<i>pper 95.0%</i>
Intercept	-485.4361	117.0484	-4.147309	0.053515	-989.0552	18.18305	-989.0552	18.18305
Packet	4.189412	0.870524	4.81252	0.040568	0.443849	7.934975	0.443849	7.934975
M-A	13.27329	4.249734	3.123322	0.089033	-5.011856	31.55843	-5.011856	31.55843
Hardn.	0.825774	0.299263	2.759356	0.110072	-0.461853	2.113401	-0.461853	2.113401

$$T_{0.1mm}(^{\circ}C) = 4.19 \times \text{Packet} + 13.27 \times \text{M-A} + 0.83 \times \text{Hardn.} - 485.44, R^2 = 0.92$$

Appendix 22

T_{27J} Plate+ICHAZ

SUMMARY OUTPUT

<u>Regression Statistics</u>	
Multiple R	0.873144
R Square	0.76238
Adjusted R	0.603966
Standard E	19.37492
Observatio	6

ANOVA

	<i>df</i>	<i>SS</i>	<i>MS</i>	<i>F</i>	<i>ignificance F</i>
Regressor	2	3613.171	1806.586	4.81259	0.115831
Residual	3	1126.162	375.3874		
Total	5	4739.333			

	<i>Coefficients</i>	<i>standard Err</i>	<i>t Stat</i>	<i>P-value</i>	<i>Lower 95%</i>	<i>Upper 95%</i>	<i>ower 95.0%</i>	<i>pper 95.0%</i>
Intercept	-181.4593	79.17297	-2.291935	0.105768	-433.4232	70.50468	-433.4232	70.50468
Packet	2.565737	2.087459	1.22912	0.306642	-4.077495	9.208968	-4.077495	9.208968
M-A	5.228586	1.774486	2.946535	0.060192	-0.418626	10.8758	-0.418626	10.8758

$$T_{27J}(^{\circ}\text{C}) = 2.57 \times \text{Packet} + 5.23 \times \text{M-A} - 181.46, R^2 = 0.76$$

Appendix 23

T_{50%} Plate+ICHAZ

SUMMARY OUTPUT

<i>Regression Statistics</i>	
Multiple R	0.94923
R Square	0.901038
Adjusted R	0.835063
Standard E	17.30237
Observatio	6

ANOVA

	<i>df</i>	<i>SS</i>	<i>MS</i>	<i>F</i>	<i>ignificance F</i>
Regressor	2	8177.218	4088.609	13.65729	0.031132
Residual	3	898.1158	299.3719		
Total	5	9075.333			

	<i>Coefficients</i>	<i>standard Err</i>	<i>t Stat</i>	<i>P-value</i>	<i>Lower 95%</i>	<i>Upper 95%</i>	<i>ower 95.0%</i>	<i>pper 95.0%</i>
Intercept	-391.2933	114.7011	-3.411416	0.042107	-756.3239	-26.26269	-756.3239	-26.26269
M-A	9.871234	1.889374	5.224605	0.01364	3.858396	15.88407	3.858396	15.88407
Hardn.	1.545987	0.518105	2.983923	0.058413	-0.102857	3.194831	-0.102857	3.194831

$$T_{50\%}(^{\circ}\text{C}) = 9.87 \times \text{M-A} + 1.55 \times \text{Hardn.} - 391.29, R^2 = 0.90$$

Appendix 24

T_{0.1mm} Plate+ICHAZ

SUMMARY OUTPUT

<i>Regression Statistics</i>	
Multiple R	0.841122
R Square	0.707486
Adjusted R	0.512477
Standard E	22.49409
Observatio	6

ANOVA

	<i>df</i>	<i>SS</i>	<i>MS</i>	<i>F</i>	<i>ignificance F</i>
Regressor	2	3671.381	1835.691	3.627962	0.158205
Residual	3	1517.952	505.984		
Total	5	5189.333			

	<i>Coefficients</i>	<i>standard Err</i>	<i>t Stat</i>	<i>P-value</i>	<i>Lower 95%</i>	<i>Upper 95%</i>	<i>ower 95.0%</i>	<i>pper 95.0%</i>
Intercept	-409.336	149.1182	-2.745044	0.071037	-883.897	65.22509	-883.897	65.22509
M-A	6.084005	2.456297	2.476902	0.089515	-1.733035	13.90105	-1.733035	13.90105
Hardn.	1.512724	0.673567	2.245839	0.110363	-0.63087	3.656317	-0.63087	3.656317

$$T_{0.1mm}(^{\circ}C) = 6.08 \times M - A + 1.51 \times \text{Hardn.} - 409.34, R^2 = 0.71$$

217. Nyberg, Jens (2004) Characterisation and control of the zinc roasting process
218. Sfakiotaki, Despina (2005) Analysis of movement in sequential space. Perceiving the traditional Japanese tea and stroll garden
219. Phan, Vinh V. (2005) Smart packet access and call admission control for efficient resource management in advanced wireless networks
220. Ylianttila, Mika (2005) Vertical handoff and mobility — system architecture and transition analysis
221. Typpö, Asser (2005) Pellon alarajan muutos ja sen vaikutukset viljelyyn ja ympäristöön Keski-Pohjanmaalla ja Pohjois-Pohjanmaan eteläosassa
222. Jokelainen, Janne (2005) Hirsirakenteiden merkitys asema-arkkitehtuurille 1860–1950
223. Hadid, Abdenour (2005) Learning and recognizing faces: from still images to video sequences
224. Simola, Antti (2005) Turvallisuuden johtaminen esimiestyönä. Tapaustutkimus pitkäkestoisen kehittämishankkeen läpiviennistä teräksen jatkojalostustehtaassa
225. Pap, Andrea Edit (2005) Investigation of pristine and oxidized porous silicon
226. Huhtinen, Jouni (2005) Utilization of neural network and agent technology combination for distributed intelligent applications and services
227. Ojala, Satu (2005) Catalytic oxidation of volatile organic compounds and malodorous organic compounds
228. Sillanpää, Mervi (2005) Studies on washing in kraft pulp bleaching
229. Lehtomäki, Janne (2005) Analysis of energy based signal detection
230. Kansanen, Kimmo (2005) Wireless broadband single-carrier systems with MMSE turbo equalization receivers
231. Tarkkonen, Juhani (2005) Yhteistoiminnan ehdoilla, ymmärryksen ja vallan rajapinnoilla. Työsuojeluvaltuutetut ja -päälliköt toimijoina, työorganisaatiot yhteistoiminnan areenoina ja työsuojelujärjestelmät kehittämisen kohteina
232. Ahola, Timo (2005) Intelligent estimation of web break sensitivity in paper machines
233. Karvonen, Sami (2006) Charge-domain sampling of high-frequency signals with embedded filtering

Book orders:
OULU UNIVERSITY PRESS
P.O. Box 8200, FI-90014
University of Oulu, Finland

Distributed by
OULU UNIVERSITY LIBRARY
P.O. Box 7500, FI-90014
University of Oulu, Finland

S E R I E S E D I T O R S

A
SCIENTIAE RERUM NATURALIUM
Professor Mikko Siponen

B
HUMANIORA
Professor Harri Mantila

C
TECHNICA
Professor Juha Kostamovaara

D
MEDICA
Professor Olli Vuolteenaho

E
SCIENTIAE RERUM SOCIALIUM
Senior assistant Timo Latomaa

E
SCRIPTA ACADEMICA
Communications Officer Elna Stjerna

G
OECONOMICA
Senior Lecturer Seppo Eriksson

EDITOR IN CHIEF
Professor Olli Vuolteenaho

EDITORIAL SECRETARY
Publication Editor Kirsti Nurkkala

ISBN 951-42-8000-8 (nid.)
ISBN 951-42-8001-6 (PDF)
ISSN 0355-3213

